Forschungsbericht 2021-15

Global modelling of ice nucleating particles and their effects on cirrus clouds

Christof Gerhard Beer

Deutsches Zentrum für Luft- und Raumfahrt
Institut für Physik der Atmosphäre
Oberpfaffenhofen

Dissertation
an der Fakultät für Physik
der Ludwig-Maximilians-Universität
München

ISSN 1434-8454

ISRN DLR-FB--2021-15

C. G. Beer

ISRN DLR-FB--2021-15

Deutsches Zentrum
DLR für Luft- und Raumfahrt

Herausgeber
Deutsches Zentrum
für Luft- und Raumfahrt e. V.
Bibliotheks- und
Informationswesen
D-51170 Köln
Porz-Wahnheide
Linder Höhe
D-51147 Köln

Telefon (0 22 03) 6 01 - 44 44
Telefax (0 22 03) 6 01 - 47 47

ISSN 1434-8454

Globales Klima-Chemie-Modell, atmosphärisches Aerosol, Aerosolmodellierung, Aerosol-Wolken-Wechselwirkung, eisbildende Aerosole, Zirruswolken, Strahlungsantrieb

(Veröffentlicht in Englisch)

Christof Beer
Institut für Physik der Atmosphäre des DLR, Oberpfaffenhofen

Globale Modellierung eisbildender Partikel und deren Effekte auf Zirruswolken

Dissertation Ludwig-Maximilians-Universität München
DLR-Forschungsbericht 2021-15, 2021, 186 Seiten, 55 Bilder, 8 Tabellen, 308 Literaturstellen, 39,00 € zzgl. MwSt.

Eisbildende Aerosolpartikel in der globalen Atmosphäre, auch Eiskerne genannt, können durch Beeinflussung von Wolkeneigenschaften und damit verbundenen Modifikationen des Strahlungshaushaltes wichtige Klimaänderungen bewirken. Aerosol-Wolken-Wechselwirkungen, besonders im Hinblick auf Zirruswolken, sind allerdings mit großen Unsicherheiten behaftet. In dieser Dissertation werden Eiskern-Effekte auf Zirruswolken und Strahlung mithilfe des globalen Klima-Chemie Modells EMAC analysiert, welches das Aerosol-Mikrophysik Modul MADE3 beinhaltet.

Zur Analyse der globalen Eiskerneffekte wird die Modelldarstellung eisbildender Aerosole weiterentwickelt und, neben Mineralstaub und Ruß, um zusätzliche Eiskerntypen erweitert: kristallines Ammoniumsulfat und hochviskose organische Partikel.

Eine globale Klimatologie der verschiedenen Eiskern-Typen wird präsentiert und globale Effekte auf Zirruswolken-Eigenschaften und Strahlungsbilanz werden quantifiziert. Sensitivitäten im Hinblick auf die Gefriereigenschaften der Eiskerne, die Vertikalgeschwindigkeiten und die Effekte anthropogener Eiskerne werden analysiert.

Global atmospheric chemistry-climate model, atmospheric aerosol, aerosol modelling, aerosol-cloud-interaction, ice-nucleating particles, cirrus clouds, radiative forcing

Christof Beer
Institut für Physik der Atmosphäre des DLR, Oberpfaffenhofen

Global modelling of ice nucleating particles and their effects on cirrus clouds

Doctoral Thesis Ludwig-Maximilians-Universität München
DLR-Forschungsbericht 2021-15, 2021, 186 pages, 55 figs., 8 tabs., 308 refs., 39.00 €

Atmospheric ice nucleating aerosol particles (INPs) can influence the climate system by modifying cloud properties and consequently the Earth's radiation budget. However, these aerosol-cloud interactions and their effects on the global scale, especially regarding cirrus clouds, are still only poorly understood, and subject to large uncertainties. In this thesis INP-induced modifications of cirrus clouds are analysed by employing the atmospheric chemistry general circulation model EMAC, including the aerosol microphysics submodel MADE3.

To facilitate the analysis of INP-effects, model improvements and developments with respect to the representation of ice nucleating particles are applied. Besides mineral dust and soot aerosols, additional types of INPs are implemented, i.e. crystalline ammonium sulfate and glassy organic particles.

A global climatology of the different INP-types is presented and global effects on cirrus coud properties and the radiative balance are quantified. Sensitivities with respect to the freezing efficiency of INPs, to the vertical velocities, and the effects of anthropogenic INPs are analysed.

Forschungsbericht 2021-15

Global modelling of ice nucleating particles and their effects on cirrus clouds

Christof Gerhard Beer

Deutsches Zentrum für Luft- und Raumfahrt
Institut für Physik der Atmosphäre
Oberpfaffenhofen

Dissertation
an der Fakultät für Physik
der Ludwig-Maximilians-Universität
München

186 Seiten
55 Bilder
8 Tabellen
308 Literaturstellen

Deutsches Zentrum
DLR für Luft- und Raumfahrt

Global modelling of ice nucleating particles and their effects on cirrus clouds

Christof Gerhard Beer

München 2021

Erstgutachter: Prof. Dr. Robert Sausen
Zweitgutachter: Prof. Dr. George Craig
Tag der Abgabe: 17.05.2021
Tag der mündlichen Prüfung: 07.07.2021

Global modelling of ice nucleating particles and their effects on cirrus clouds

Christof Gerhard Beer

Dissertation
an der Fakultät für Physik
der Ludwig–Maximilians–Universität
München

vorgelegt von
Christof Gerhard Beer
aus München

München, Juli 2021

Kurzfassung

Eisbildende Aerosolpartikel in der globalen Atmosphäre, auch Eiskerne genannt, können durch Beeinflussung von Wolkeneigenschaften und damit verbundenen Modifikationen des Strahlungshaushaltes wichtige Klimaänderungen bewirken. Allerdings sind Aerosol-Wolken-Wechselwirkungen, besonders im Hinblick auf Zirruswolken, noch wenig verstanden und bisherige Analysen globaler Effekte sind mit großen Unsicherheiten behaftet. In dieser Dissertation werden globale Eiskern-Effekte auf Zirruswolken und Strahlung mithilfe des globalen Klima-Chemie Modells EMAC (ECHAM/MESSy Atmospheric Chemistry model) analysiert, welches das Aerosol Mikrophysik Modul MADE3 (Modal Aerosol Dynamics model for Europe, angepasst für globale Anwendungen, dritte Generation) beinhaltet.

Zur Analyse der globalen Eiskern-Effekte werden in einem ersten Schritt wichtige Weiterentwicklungen des EMAC-MADE3 Modells vorgenommen. Diese betreffen die Darstellung von Mineralstaub und Ruß-Partikeln im Modell, beides wichtige Typen eisbildender Aerosole. Indem eine Online-Berechnung der windgetriebenen Staubemissionen verwendet wird, im Gegensatz zu einer Offline-Klimatologie basierend auf Monatsmitteln eines spezifischen Jahres, kann eine verbesserte Übereinstimmung der Modellergebnisse verglichen mit bodengestützten Stationsmessungen erzielt werden. Des Weiteren führt eine Erhöhung der horizontalen und vertikalen Modellauflösung zu Verbesserungen der atmosphärischen Verteilung von Mineralstaub und Ruß-Aerosolen verglichen mit verschiedenen flugzeuggestützten Messkampagnen. Weitere Modellentwicklungen beinhalten die Implementierung zusätzlicher Eiskerntypen in EMAC-MADE3 (zusätzlich zu Mineralstaub und Ruß): kristallines Ammoniumsulfat und hochviskose organische Partikel.

Aufbauend auf diesen Modell-Weiterentwicklungen wird die globale Verteilung der Eiskerne im Detail analysiert und eine globale Klimatologie der verschiedenen Eiskern-Typen präsentiert. Außerdem werden Eiskern-Effekte auf Zirruswolken und deren mikrophysikalische Eigenschaften ermittelt. Diese Analyse zeigt eine deutliche Abnahme der Eiskristallzahlen durch den Effekt der Eiskerne. Diese Ausdünnung der Zirruswolken führt zu einem kühlenden globalen Strahlungseffekt im Bereich zwischen -100 und $-40\,\mathrm{mW\,m^{-2}}$. Hochviskose organische Partikel und kristallines Ammoniumsulfat zeigen vergleichbar große Effekte wie Mineralstaub und Ruß (ungefähr 50 % des gesamten Eiskern-Effekts). Anthropogene Eiskerne, z.B. Ruß und Ammoniumsulfat aus der Verbrennung fossiler Brennstoffe, führen zu großen Effekten in den nordhemisphärischen Extratropen ($-100\,\mathrm{mW\,m^{-2}}$). Die Simulationsergebnisse zeigen eine deutliche Abhängigkeit der Eiskern-Effekte von den Modellannahmen der Gefriereigenschaften der Partikel und besonders von der Darstellung der Vertikalgeschwindigkeiten, welche die adiabatischen Kühlraten bei der Wolkenbildung bestimmen. Idealisierte Experimente unter Verwendung einer räumlich homogenen, globalen Vertikalgeschwindigkeit zwischen 1 und $50\,\mathrm{cm\,s^{-1}}$ führen zu globalen Strahlungseffekten

im Bereich von $(-260, +40)$ mW m^{-2}. Des Weiteren werden Effekte hocheffizienter Eiskerne analysiert, welche z.B. für das „Impfen“ von Zirruswolken als Möglichkeit, die globale Erwärmung durch Geo-Engineering abzuschwächen, vorgeschlagen werden. Die Ergebnisse zeigen allerdings, dass solche Eiskerne den gegenteiligen Effekt bewirken können, indem sie zu einer Erhöhung der Eiskristallzahlen und der Zirrusbedeckung und in der Folge einem ausgeprägten wärmenden Effekt von bis zu 300 mW m^{-2} führen.

Insgesamt zeigen die Ergebnisse dieser Doktorarbeit, dass Eiskerne zu deutlichen Zirrus-Modifikationen führen und das Potenzial haben, anthropogene Klimaveränderungen zu beeinflussen. Beispielsweise tragen die hier quantifizierten Eiskern-Effekte anthropogener Eiskerne zu etwa 10 % des gesamten anthropogenen Aerosoleffekts bei. Die hier gezeigten Effekte sind jedoch oft kleiner als in einigen früheren Studien postuliert. Bisherige Modellstudien beinhalteten meist nur Mineralstaub- und Ruß-Eiskerne; die Ergebnisse dieser Arbeit zeigen jedoch, dass die neu implementierten Eiskerntypen (kristallines Ammoniumsulfat und hochviskose organische Partikel) ebenso wichtig sind und für zukünftige Modellstudien berücksichtigt werden sollten.

Abstract

Atmospheric ice nucleating aerosol particles (INPs) can influence the climate system by modifying cloud properties and consequently the Earth's radiation budget. However, these aerosol-cloud interactions and their effects on the global scale, especially regarding cirrus clouds, are still only poorly understood, and subject to large uncertainties. In this thesis INP-induced modifications of cirrus clouds are analysed by employing the atmospheric chemistry general circulation model EMAC (ECHAM/MESSy2 Atmospheric Chemistry model), including the aerosol microphysics submodel MADE3 (Modal Aerosol Dynamics model for Europe, adapted for global applications, third generation).

First, to facilitate the analysis of INP-effects, model developments with respect to the representation of mineral dust and soot aerosols, both important types of INPs, are applied. Using an online calculation scheme for wind-driven mineral dust emissions, instead of a prescribed monthly-mean climatology representing a specific year, leads to an improved agreement with ground-based station observations. Additionally, increasing the horizontal and vertical model resolution, improves the simulated atmospheric dispersion of mineral dust and soot compared with various aircraft-based field-campaigns. Further model developments include the implementation of other INP-types, in addition to mineral dust and soot, i.e. crystalline ammonium sulfate and glassy organics.

Building on these model developments the global distribution of INPs is analysed and a global climatology considering all different INP-types is compiled. In addition, INP-induced modifications of cirrus microphysical properties are evaluated, showing reduced ice crystal numbers in the presence of INPs. This cirrus cloud thinning leads to a total global radiative effect ranging between -100 and $-40\,\mathrm{mW\,m^{-2}}$, which represents a global cooling. Glassy organics and crystalline ammonium sulfate show comparable effects as mineral dust and soot, i.e. about 50 % of the total INP-effect. Anthropogenic INPs, e.g. soot and ammonium sulfate from the combustion of fossil fuels, have largest effects at northern extratropical latitudes of about $-100\,\mathrm{mW\,m^{-2}}$. Additionally, results show a pronounced dependence of simulated effects on the freezing efficiency of INPs, and especially on the representation of the vertical velocity, which influences the adiabatic cooling rates in the model. Using idealized experiments with prescribed, globally homogeneous updraft speeds ranging between 1 and $50\,\mathrm{cm\,s^{-1}}$, global radiative effects in the range of $(-260, +40)\,\mathrm{mW\,m^{-2}}$ are simulated. Moreover, highly efficient INPs are analysed, e.g. proposed for cirrus cloud seeding to reduce global warming via climate engineering. However, results show that such INPs can have the opposite effect as they increase ice crystal numbers and cirrus coverage and result in a pronounced positive radiative effect of up to $300\,\mathrm{mW\,m^{-2}}$, leading to a warming of the climate system.

In general, the results of this thesis show that INPs can lead to considerable cirrus modifications and have the potential to influence climate change, e.g. the effect of anthropogenic INPs is about 10 % of the total anthropogenic aerosol effect. The INP-effects quantified here are, however, smaller compared to some previous global model studies. Importantly, newly implemented INP-types, i.e. crystalline ammonium sulfate and glassy organics, which were not considered in most previous model studies, show notable effects and need to be taken into account in future model applications.

Publications

Parts of the results presented in this thesis were previously published in:

C. G. Beer, J. Hendricks, M. Righi, B. Heinold, I. Tegen, S. Groß, D. Sauer, A. Walser, and B. Weinzierl. Modelling mineral dust emissions and atmospheric dispersion with MADE3 in EMAC v2.54. *Geosci. Model Dev.*, 13(9):4287–4303, 2020. doi:10.5194/gmd-13-4287-2020

C. Beer conceived the study, implemented the method for tuning online dust emissions at low model resolutions, designed and performed the simulations, analysed the data, evaluated and interpreted the results, and wrote the paper. J. Hendricks contributed to conceiving the study and to the model evaluation, the interpretation of the results, and the text. M. Righi assisted in preparing the simulation setup, helped designing the evaluation methods, and contributed to the interpretation of the results and to the text. B. Heinold and I. Tegen assisted in implementing the method for tuning online dust emissions at low model resolutions. S. Groß provided data from ground-based lidar observations and assisted in the corresponding model evaluation. D. Sauer, A. Walser, and B. Weinzierl provided data from aircraft-based observations and assisted in the corresponding model evaluation.

Contents

Chapter 1

Introduction

1.1 Motivation

Atmospheric aerosol particles can influence the climate system in various ways. Aerosols directly change the Earth's radiation budget by interactions with solar and terrestrial radiation through absorption and scattering (e.g., Boucher et al., 2013). Importantly, aerosol particles can also act as cloud condensation nuclei and ice nucleating particles, consequently influencing the formation of cloud droplets and ice crystals. These indirect effects lead to cloud perturbations and result in additional climate modifications (e.g., Boucher et al., 2013; Mülmenstädt and Feingold, 2018).

On the global scale, direct and indirect aerosol effects are assumed to result in a cooling of the present day climate (Boucher et al., 2013; Bellouin et al., 2020), with anthropogenic aerosols partly masking the strong global warming induced by greenhouse gases. In the fifth assessment report of the IPCC (Intergovernmental Panel on Climate Change) the term of "Effective Radiative Forcing" (ERF) was introduced to characterize the change in the Earth's radiation budget with respect to pre-industrial conditions, also including the effects of rapid adjustments due to cloud modifications (Boucher et al., 2013). The total, present-day ERF due to anthropogenic aerosols (direct and indirect effect) was recently estimated as $(-2.0, -0.4)$[1] Wm^{-2} by Bellouin et al. (2020), basically confirming the estimate presented in Boucher et al. (2013). This cooling effect of aerosols partly compensates the strong positive forcing due to greenhouse gases, e.g. CO_2, CH_4 and N_2O, of about $2.8\,\mathrm{Wm}^{-2}$ for the time period 1750–2011 (Myhre et al., 2013). However, climate forcings of aerosols, especially the indirect effects resulting from cloud modifications are still highly uncertain. Most observations are limited in space and time, complicating interpretations on a global scale (e.g., Ghan and Schwartz, 2007), while simulations of aerosol-cloud interactions in global models are challenging, as these processes occur at the scale of clouds and are difficult to resolve with the relatively coarse model resolution (e.g., Fan et al., 2016).

Especially, the effects of ice-nucleating aerosol particles (INPs) on cirrus clouds are only poorly understood and subject of ongoing research activities. Cirrus clouds are cold ice clouds that frequently occur at temperatures below $-38\,^{\circ}\mathrm{C}$, mainly in the upper troposphere (Heymsfield et al., 2017). Cirrus clouds are estimated to have a pronounced

[1] This notation characterizes the range between the values in brackets.

warming effect on the global climate due to their strong absorption of outgoing terrestrial radiation (e.g., Chen et al., 2000; Gasparini and Lohmann, 2016). INPs have the potential to change these climatic impacts substantially by influencing the microphysical properties of cirrus clouds, e.g. via changes in ice crystal number concentrations. However, recent studies show conflicting results concerning the importance of aerosol-cirrus interactions, ranging from statistically insignificant effects (Hendricks et al., 2011; Gettelman et al., 2012), to small or rather large coolings (Zhou and Penner, 2014; Penner et al., 2018; Zhu and Penner, 2020), or even small warming effects (Liu et al., 2009). In order to reduce these uncertainties, this thesis provides an additional step towards elucidating climate modifications induced by aerosol-cirrus interactions.

Here, ice nucleating aerosol particles and corresponding climate modifications are simulated by applying the atmospheric chemistry general circulation model (AC-GCM) EMAC (ECHAM/MESSy2 Atmospheric Chemistry model; Jöckel et al., 2010), including the dedicated aerosol microphysics submodel MADE3 (Modal Aerosol Dynamics model for Europe, adapted for global applications, third generation; Kaiser et al., 2014, 2019).

In order to analyse the effects of ice nucleating aerosol particles on cirrus clouds, several model developments have been applied with respect to previous model versions of EMAC-MADE3 (Kaiser et al., 2019; Righi et al., 2020). As mineral dust is one of the most effective ice nucleating particle types in the atmosphere (Hoose and Möhler, 2012; Kanji et al., 2017), its correct representation in the model is highly important. It has been argued that using prescribed monthly-mean dust emission fields representative of a specific year could lead to a misrepresentation of the temporal variability of mineral dust in the model (Aquila et al., 2011; Huneeus et al., 2011; Kaiser et al., 2019). To improve mineral dust emissions and its atmospheric dispersion, an online calculation of wind-driven dust emissions is applied (Tegen et al., 2002), in contrast to the offline emission setup employed in previous studies (Aquila et al., 2011; Righi et al., 2013; Kaiser et al., 2019). Additionally, an increased vertical and horizontal model resolution has been employed, to further improve the simulated atmospheric dispersion of mineral dust, but also of other aerosol particles, e.g. soot, which can also act as ice nucleating particles (e.g., Kulkarni et al., 2016).

From recent laboratory studies on INPs, other particle types than mineral dust and soot were observed to efficiently nucleate ice at cirrus temperatures, i.e. crystalline ammonium sulfate (Abbatt et al., 2006; Wise et al., 2009; Baustian et al., 2010; Ladino et al., 2014), and high-viscosity, glassy organic particles (Murray et al., 2010; Ignatius et al., 2016; Wagner et al., 2017). However, their potential for global climate perturbations is still uncertain, as only few studies consider them as ice nucleating particles (at temperatures below $-38\,^{\circ}\mathrm{C}$) in global models (e.g., Abbatt et al., 2006; Penner et al., 2018; Zhu and Penner, 2020). Additionally, the correct representation of phase states is essential for these particles as only the solid or glassy state, respectively, facilitates ice nucleation. Here, crystalline ammonium sulfate and glassy organic particles are implemented as INPs in the framework of EMAC-MADE3 and their effects on cirrus clouds and the global climate system are analysed.

1.2 Science Questions

The objective of this work is to provide an assessment of the importance of global climate modifications through aerosol-cirrus cloud interactions induced by ice nucleating particles, by means of global modelling. This includes model improvements with regard to simulations of the classical ice nucleating aerosols, i.e. mineral dust and soot, which have already been considered in the model, as well as the addition of new ice nucleating particles, i.e. ammonium sulfate and organics. The main scientific questions, this study aims to answer, are:

Q.1 What is the global distribution of the different ice nucleating particles?

Q.2 To what extent do ice nucleating particles change the microphysical properties of cirrus clouds?

Q.3 What are the magnitude and sign of the climatic effect of cirrus cloud modifications induced by ice nucleating particles compared with previous studies?

Q.4 How large is the contribution of previously not considered particles, i.e. ammonium sulfate and organic particles to the climatic impact of aerosol-cirrus interactions?

Q.5 What are possible contributions of anthropogenic aerosols with regard to the climate effects of ice nucleating particles?

The questions above are addressed by means of global modelling using the EMAC-MADE3 model system. In order to develop a global climatology of the different INPs (question Q.1) several model improvements are applied. On the one hand, an online calculation of wind-driven dust emissions (Tegen et al., 2002) is employed, to improve the representation of mineral dust emissions in the model. Differences with respect to the offline emission setup, as applied in previous studies, are evaluated. Additionally, the horizontal and vertical model resolution is increased to improve the simulated dispersion of dust and soot aerosols in EMAC-MADE3. Furthermore, new types of ice nucleating particles in addition to mineral dust and soot, i.e. crystalline ammonium sulfate and glassy organics, are implemented in the model to include their effects for the simulated aerosol-cirrus interactions. To quantify INP-induced cirrus modifications and resulting climate effects (questions Q.2 to Q.5) a dedicated microphysical cloud-scheme is applied (Kuebbeler et al., 2014; Righi et al., 2020), which is adapted to include also the coupling of newly implemented INP-types to the freezing mechanisms in cirrus clouds.

This thesis is organized as follows: Chapter 2 presents the fundamental scientific background and state of the science related to this work. Methods and details on the model system and the simulation setups are described in Chapter 3. The results of this work are presented and discussed in detail in Chapter 4. Finally, Chapter 5 presents a summary of important results and conclusions of this work and gives an outlook for possible future developments and applications.

Chapter 2

Scientific background

This chapter provides a detailed overview of the scientific background of this thesis. It is organized as follows: The properties and relevant processes of atmospheric aerosols are described in Sect. 2.1. Additionally, the representation of atmospheric aerosols in numerical models is outlined. Possible impacts of aerosols on the global climate are highlighted in Sect. 2.2. Section 2.3 focuses on ice-nucleation mechanisms and pathways, including a brief review of important ice nucleating particle types and cirrus cloud modifications.

2.1 The global aerosol

An aerosol is defined as a suspension of solid particles or solution droplets in a gas, usually in air. In the atmospheric sciences community the term aerosol refers often to the particulate phase only, i.e. aerosol particles. Aerosol particles are ubiquitous in the Earth's atmosphere and play an important role for various processes influencing the global climate. They show a large variety of compositions, shapes and sizes as can be seen in Fig. 2.1, where scanning electron microscopy images of several ambient aerosol particles collected at Xi'an City in China (Li et al., 2016) are shown.

In this section an overview of atmospheric aerosol particles is presented, including the properties and relevant processes of the atmospheric aerosol, as well as their relevance for the Earth's climate. A detailed review on the atmospheric aerosol, aerosol related processes and climate effects is presented in e.g. Fuzzi et al. (2015). Additionally, a short review of the representation of aerosols in numerical computer models is provided, mainly based on the textbook by Seinfeld and Pandis (2016).

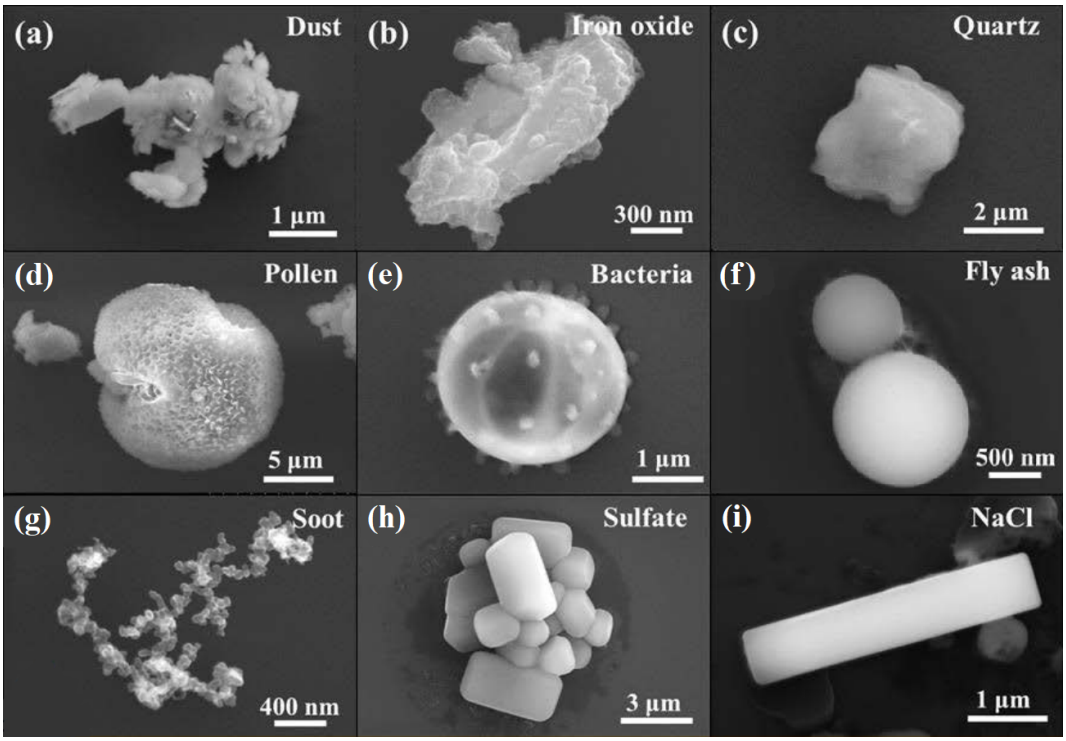

Figure 2.1: Examples of scanning electron microscopy images of airborne particulates collected at Xi'an Jiaotong University (China). Shown are (a) dust, (b) iron oxide, (c) quartz, (d) pollen, (e) bacteria, (f) fly ash, (g) soot, (h) sulfate, and (i) sodium chloride particles, respectively (Li et al., 2016, adapted from their Fig. 1).

2.1.1 Aerosol properties

2.1.1.1 Aerosol sizes

Atmospheric aerosol particles can occur in a large variety of different sizes, with particle diameters ranging from a few nanometers to several tens of micrometers. As most solid aerosol particles are not spherical but have irregular shapes, their size is usually defined by diameters or radii of equivalent spheres (e.g., Seinfeld and Pandis, 2016, Ch.9). For example, the volume equivalent diameter is the diameter of a sphere of equivalent volume as the irregularly shaped particle. As several definitions of equivalent diameters exist (e.g. aerodynamic diameter, Stokes diameter), it has to be stated which definition is used in the corresponding context. However, for this general overview different equivalent diameters will not be distinguished for the sake of simplicity.

Aerosols are commonly grouped into different size modes, namely the Aitken mode (tens of nanometers), the accumulation mode (up to around 1 micrometer), and the coarse mode (micrometers and larger) (e.g., Seinfeld and Pandis, 2016, Ch.8). Occasionally, a nucleation mode may be present with particles smaller than 10 nanometers. An example of the number distribution of ambient aerosol particles of different sizes measured at a boreal forest station in Finland (Dal Maso et al., 2005) is shown in Fig. 2.2. There, the number distributions were calculated from lognormal distribution functions fitted to the measurement data. A detailed description of lognormal size distributions can be found in Sect. 2.1.3. Typically, the smallest particles have the largest contribution to the total number of particles. The Aitken and nucleation modes often dominate particle number concentrations in the atmosphere, with concentrations of in some cases up to $10^5\,\mathrm{cm}^{-3}$. On the other hand, the particle volume or mass concentrations are typically dominated by coarse mode particles, whereas medium sized particles in the accumulation mode often contribute the largest fraction to the particle surface area concentration.

The size of aerosol particles influences their residence time in the atmosphere, thus there exists a wide range of atmospheric lifetimes of aerosols (Boucher et al., 2013; Kristiansen et al., 2016). Nucleation and Aitken mode particles typically exist only for a duration of a few hours or days after their formation, as they efficiently coagulate with larger particles or quickly take up condensable matter and grow to accumulation mode sizes. Atmospheric coarse mode particles are also rather short-lived, as they are efficiently removed by sedimentation. Particles in the accumulation mode typically have the longest residence times of up to a few weeks.

2.1.1.2 Aerosol composition and sources

The chemical composition of aerosol particles plays a key role for understanding their climatic effects. The most important aerosol species are: marine aerosol or sea spray (SS), mineral dust (DU), black carbon (BC), organic aerosol (OA), sulfate (SO_4), ammonium (NH_4), nitrate (NO_3), and aerosol water (H_2O). For simplicity, ion charges will be omitted here. Aerosol particles can either be directly emitted into the atmosphere as primary aerosol or formed in secondary processes from precursor gases. Furthermore, they may have a natural or anthropogenic origin. In the atmosphere aerosol particles are often mixtures of several components, as they undergo various atmospheric processes. One differentiates between a particle ensemble that is internally mixed, i.e. individual particles

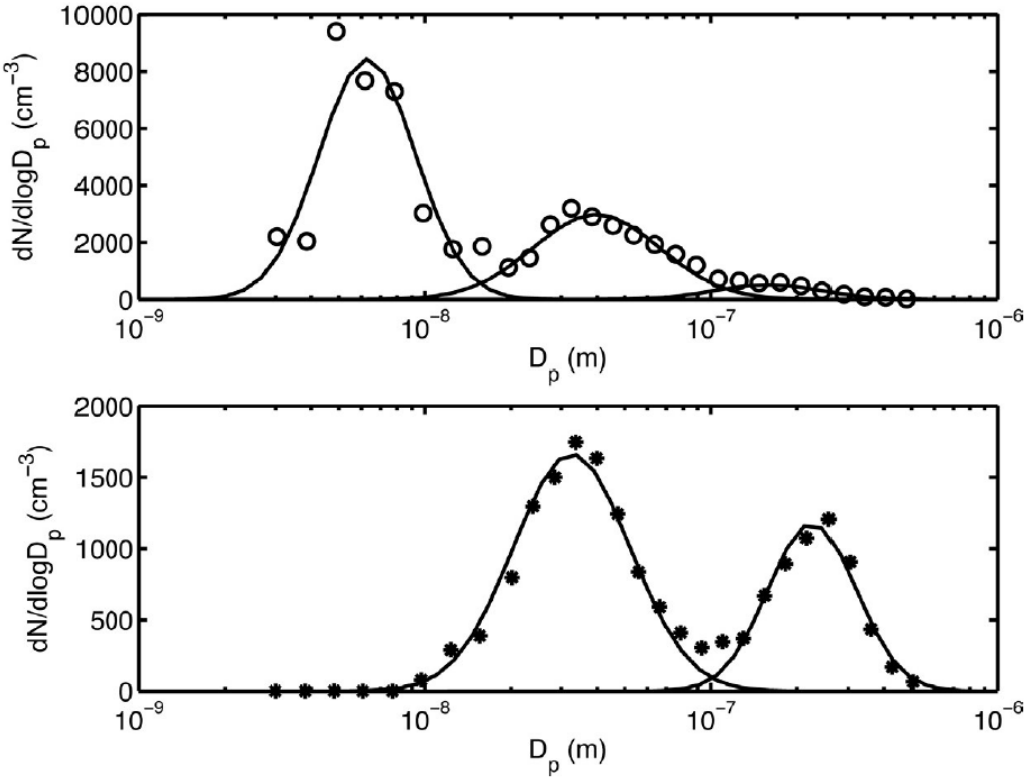

Figure 2.2: Examples of number size distributions of aerosol particles measured at a station in Hyytiälä, Finland between 1996 and 2003. (Top) Tri-modal distribution with nucleation, Aitken and accumulation mode. (Bottom) Bi-modal distribution with Aitken and accumulation mode. The markers represent measured data points, the solid lines show log-normal fits (see also Sect 2.1.3). Taken from Dal Maso et al. (2005, their Fig. 1).

that are composed of different chemical components, and an externally mixed ensemble, where each particle consists of only one chemical species. Many primary particles are transformed from an external to an internal mixture during their residence time in the atmosphere. For example, dust particles may acquire a coating of organic or inorganic substances (Kojima et al., 2006; Kanji et al., 2019). Table 2.1 shows global average emission fluxes and atmospheric burdens of different aerosol species, as simulated by the models participating in the AeroCom model intercomparison project (Aerosol Comparison between Observations and Models; Textor et al., 2006).

Sea spray (SS) is an important natural aerosol component. It dominates the marine boundary layer (MBL) and has the largest emission fluxes in the troposphere compared to other aerosol types. The majority of SS particles reside in the coarse mode and many particles have diameters larger than 10 µm and are thus quickly removed via deposition and sedimentation processes (Quinn et al., 2015). SS is mainly composed of sodium chloride (NaCl), but can also consist of other substances like magnesium, calcium and sulfate. The SO_4 component in SS particles may also originate from the oxidization of dimethyl sulfide (DMS) emitted by phytoplankton at the sea surface (Yang et al., 2011). Sulfuric acid and nitric acid can displace the chlorine in SS, resulting in a sink for SO_4 and NO_3 and a source of reactive chlorine to the atmosphere (Chameides and Stelson, 1992). Another important feature of sea spray aerosol is its organic component. Ocean-derived organic aerosol (OA) stems from the incorporation of organic matter from marine organisms into primary SS particles, but can also be formed as secondary organic aerosol

Table 2.1: Global average mass emission fluxes and atmospheric burdens of different aerosol species, as estimated by the AeroCom project (Textor et al., 2006).

Aerosol species	Emission [Tg a^{-1}]	Burden [Tg]
Sea spray (SS)	16600	7.52
Mineral dust (DU)	1840	19.2
Sulfate (SO_4)	179	1.99
Particulate organic matter (POM)	96.6	1.7
Black carbon (BC)	11.9	0.24

(SOA) via oxidation of volatile organic compounds (VOCs). Primary SS particles are mainly generated by the bursting of air bubbles from breaking waves due to the wind stress at the ocean surface. The generation of SS is therefore strongly related to the wind speed.

Mineral dust (DU) aerosol is one of the main aerosol types in the troposphere and often dominates aerosol concentrations in large parts of the globe. DU particles are mainly emitted from dry, arid regions with reduced vegetation cover and from deserts. Most dust source regions are located in the Northern Hemisphere, where the Sahara Desert is the largest dust source on Earth, providing at least half of the globally emitted dust (Huneeus et al., 2011). It is estimated that around 75 % of the global dust emissions are produced from natural sources while 25 % have anthropogenic origin (Ginoux et al., 2012). DU aerosol particles are formed via the process of saltation, as larger particles (100 µm - 200 µm diameter) start moving close to the ground forced by strong winds. These saltating particles can break apart and eject smaller particles that are entrained in the planetary boundary layer and can subsequently be transported over long distances (Mahowald et al., 2014). As is the case with SS, the emission of DU is strongly related to the wind speed. The mineralogy of DU particles in the troposphere varies according to source regions and atmospheric processing. DU aerosol typically consists of insoluble clay silicates like quartz, clay minerals, or feldspar. It often contains iron, phosphorous and other micronutrients that are deposited with the dust aerosol and are essential for the growth of tropical rainforests, as well as oceanic life (Chadwick et al., 1999; Jickells et al., 2005; Nenes et al., 2011; Yu et al., 2015).

Black carbon (BC) aerosol is emitted into the atmosphere in the form of soot particles by the incomplete combustion of fossil fuels, biofuels and biomass. Natural BC emission sources include biomass burning during forest fires, often together with emissions of organic aerosol. However, a major fraction of atmospheric BC is of anthropogenic origin, e.g. combustion processes in road traffic, aviation, and shipping, residential heating, biofuel cooking, industrial processes, and power generation from fossil fuels. Most anthropogenic BC particles reside in the Aitken and accumulation modes, sometimes also referred to as fine particulate matter (e.g. $PM_{2.5}$ with diameters smaller than 2.5 µm).

A significant source of atmospheric particulate organic matter (POM) is the formation of secondary organic aerosol (SOA) from precursor gases of both natural and anthropogenic origin. These precursor vapours can be transformed to low and semi-volatile species, which can condense on existing aerosols or contribute to new particle formation, thereby generating SOA (e.g., Carlton et al., 2009). Precursors include for example

volatile organic compounds (VOCs) emitted from the oceans and the biosphere (Guenther et al., 1995), as well as anthropogenic SOA precursors from emissions of Diesel engines (Gentner et al., 2012). Atmospheric POM can also consist of a variety of biological components like bacteria, algae, fungal spores, viruses, pollen, and plant fragments ranging from sizes of tens of nanometers (viruses) to hundreds of micrometers (pollen).

Atmospheric sulfate (SO_4) occurs mainly in the form of solution droplets of sulfuric acid (H_2SO_4), which is produced from the oxidation of sulfur dioxide (SO_2). SO_2 is emitted naturally by volcanic activity but is predominantly produced anthropogenically by the combustion of sulfur-containing fossil fuels and during industrial processes. SO_4 is also produced from the oxidation of dimethyl sulfide (DMS), which is emitted from the world's oceans by marine organisms, in particular, phytoplankton (Yang et al., 2011). Aerosol nitrate (NO_3) is formed from gaseous nitric acid (HNO_3), which is a product of the photo-oxidation of nitrous oxides (NO_x), primarily generated during combustion processes but also naturally by biomass burning and lightning activity. Aerosol phase ammonium (NH_4) is generated from gaseous ammonia (NH_3). A major fraction of NH_3 emissions are of anthropogenic origin, such as the production and use of ammoniacal fertilizers and animal husbandry. A smaller fraction of NH_3 is produced naturally via volatilization from soils and oceans or biomass burning (Behera et al., 2013). NH_4, SO_4, and NO_3 can also occur in the atmosphere as crystalline salts, e.g. ammonium sulfate ($(NH_4)_2SO_4$) and ammonium nitrate ($(NH_4)_2NO_4$). Their formation and phase state is strongly related to temperature and humidity (Martin et al., 2003). Also the amount of available NH_3 is often a limiting factor for the formation of ammonium salts, as NH_3 is the most abundant alkaline gas in the atmosphere.

Aerosol water (H_2O) is an important component of the atmospheric aerosol, as it affects both the size and composition of atmospheric particles, thereby influencing particulate mass and its optical and chemical properties. The abundance of H_2O is related to the relative humidity (RH), which is defined as the ratio of the partial pressure of H_2O vapour to the saturation pressure of liquid H_2O at the prevalent temperature, and is usually expressed in percent. At high RH, water starts to condense on preexisting aerosol particles to form cloud condensation nuclei (CCN) and subsequently cloud droplets. The ability of aerosol particles to take up water is termed hygroscopicity and can be expressed with the hygroscopicity parameter κ (Petters and Kreidenweis, 2007). κ relates the dry particle volume of a particle with a specific chemical composition to the water uptake at a given RH. High κ values indicate highly hygroscopic particles, also termed hydrophilic. Inorganic salts like NaCl are of that category, with κ values between approximately 0.5 and 1.4 (Petters and Kreidenweis, 2007). Water repelling substances are termed hydrophobic ($\kappa = 0$). Many organic aerosols typically have a low hygroscopicity. Insoluble particles like DU and BC generally have very small κ values upon emission, but can be transformed into a hydrophilic state during atmospheric processing by developing a coating of hygroscopic material (Kojima et al., 2006; Herich et al., 2009; Motos et al., 2019).

2.1.2 Aerosol processes and life cycle

In Fig. 2.3, a summary of the different atmospheric aerosol processes is presented. Aerosols can be directly emitted as primary particles both naturally (e.g. mineral dust, sea spray) and anthropogenically (e.g. soot). In addition, secondary aerosols can be formed via nucleation of low-volatility materials produced from the oxidation of aerosol precursor gases (e.g. SO_2, DMS, VOCs). The process of the nucleation of molecular clusters and subsequent growth of these clusters to detectable sizes is called new particle formation (NPF). While the process of NPF is still a focus of current research, there is a general consensus that gaseous sulfuric acid plays a key role in atmospheric nucleation (Kulmala et al., 2014). Besides H_2SO_4, other constituents like oxidized organic compounds (e.g., Metzger et al., 2010; Riccobono et al., 2012; Bianchi et al., 2016; Tröstl et al., 2016), gaseous ammonia and amines (e.g., Kurtén et al., 2008; Berndt et al., 2010), and ions (e.g., Hirsikko et al., 2011; Kirkby et al., 2016) are believed to be relevant for NPF. Gaseous H_2SO_4 is produced from the oxidation of SO_2, which is directly emitted into the atmosphere, mainly by the combustion of fossil fuels and by volcanoes, or through the oxidation of dimethyl sulfide (DMS). The hydroxyl radical (OH) is considered as the main atmospheric oxidant, but other compounds like O_3, H_2O_2, NO_3, and VOCs are also thought to be responsible for atmospheric oxidation (Kulmala et al., 2014).

After their formation and release into the atmosphere, aerosol particles are transported with their surrounding air parcel. During this transport they are subjected to various processes that influence their mass and number concentration, as well as their size and composition.

The condensation of low- or semi-volatile gases on preexisting particles leads to the reversible growth of aerosols. Evaporation of semi-volatile vapours, on the other hand, results in a reduction of particle mass. Similarly, particles can grow or shrink by condensation or evaporation of water vapour. These processes depend on atmospheric parameters like temperature and relative humidity (Bones et al., 2012).

Coagulation processes only influence the number, size and composition of particles. As coagulation rates depend on the diameter difference of the involved particles, coagulation with larger particles is a very efficient sink for small, often newly formed particles (Seinfeld and Pandis, 2016, Ch.13).

Aerosols can change the Earth's energy budget both directly (via radiation interactions) and indirectly (via cloud interactions). Typically, such changes are termed radiative forcings (RF), i.e. perturbations of incoming solar and outgoing terrestrial radiation (Boucher et al., 2013; Bellouin et al., 2020). Positive forcings lead to a warming of the climate system, while negative forcings result in a global cooling. Aerosols interact with solar and terrestrial radiation through absorption and scattering, thus directly changing the Earth's radiation budget. This process is known as the direct aerosol effect (Boucher et al., 2013). Additionally, aerosol particles can act as cloud condensation nuclei (CCN) and ice nucleating particles (INPs), consequently influencing the formation of cloud droplets and ice crystals, resulting in additional climate modifications (e.g., Hendricks et al., 2011; Boucher et al., 2013; Fan et al., 2016; Mülmenstädt and Feingold, 2018). This effect is known as the indirect aerosol effect. A detailed description of climate forcings due to atmospheric aerosols is presented in Sect. 2.2.

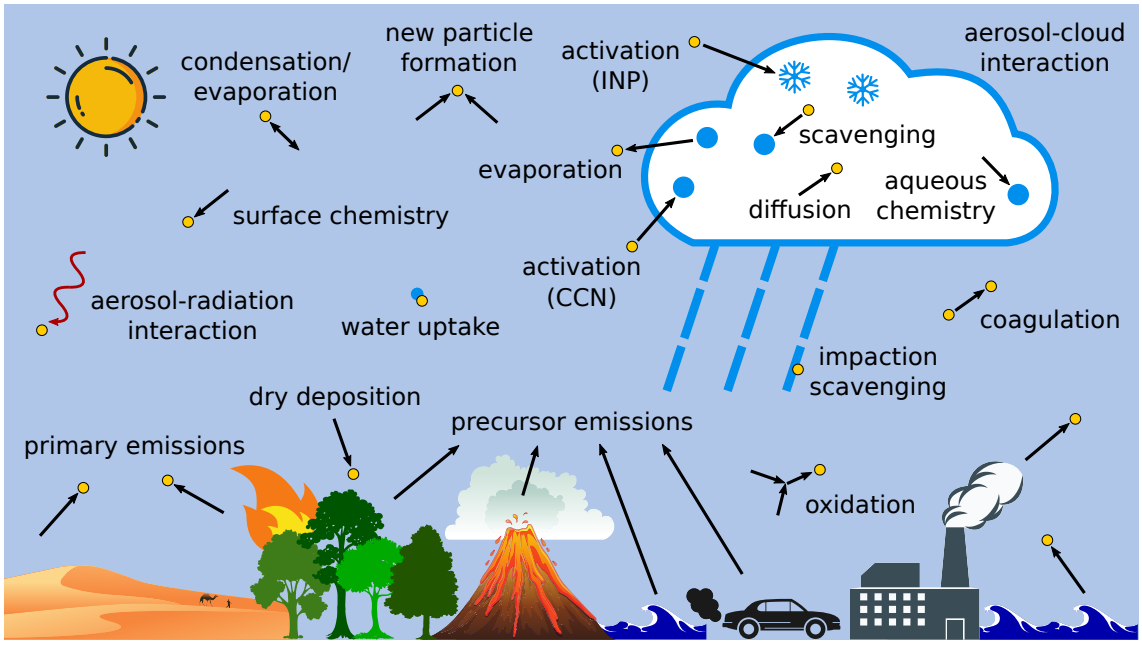

Figure 2.3: Aerosol processes in the atmosphere (adapted from Ghan and Schwartz, 2007, their Fig. 1).

Inside clouds, aqueous-phase chemical reactions can take place in cloud and fog droplets. In case of evaporation of the droplets this results in a gain of additional mass onto the residual aerosol particles due to aqueous-phase oxidation of precursor gases.

Cloud droplets and ice crystals that do not evaporate or melt can remove particulate matter from the atmosphere. This scavenging process is known as wet deposition. It can be initiated by cloud condensation or ice nucleation on aerosol particles (nucleation scavenging) and can be further enhanced by the scavenging due to impacting hydrometeors within and below the cloud (impaction scavenging). In addition to nucleation scavenging, cloud droplets can collect particles via Brownian diffusion (Fowler et al., 2009).

Other sinks for atmospheric aerosol particles include dry deposition, i.e. removal of particles through the contact with soils, vegetation, or water surfaces. Smaller particles travel through the turbulent surface layer by Brownian diffusion, while super-micron particles are efficiently removed by gravitational settling or sedimentation (Fowler et al., 2009).

2.1.3 Modelling the atmospheric aerosol

Over the last decades numerical computer models of the Earth system have rapidly evolved and are able to simulate a multitude of atmospheric processes. An important aspect of such models is the representation of aerosol microphysical processes in the atmosphere. Ghan and Schwartz (2007) present a comprehensive overview of the requirements, challenges, approaches and applications of aerosol models. Although in situ measurements and ground-based and satellite remote-sensing provide detailed and essential information about the distribution and properties of aerosols in the climate system, these observations are typically limited in space and time. Therefore, a major application for aerosol models – especially when they are part of global atmospheric chemistry general circulation models (AC-GCMs) – is the interpretation of past climate, as well as the prediction (up to several days or weeks) and projection (up to decades or centuries) of the properties of

the atmospheric aerosols. Typical use cases for aerosol models include the investigation of climatic and health effects related to atmospheric aerosol particles, or the contribution of sources (e.g. natural versus anthropogenic) or types of aerosol particles to climate perturbations. Additionally, the effect of different processes can be analysed, as these can be simply switched on or off in the model. Aerosol models can be very detailed, e.g. focusing on single clouds (e.g., Shpund et al., 2019; Ahola et al., 2020) or emission plumes (e.g., Riemer et al., 2009), or more simplified for the application as part of regional climate models or global AC-GCMs (e.g., Nabat et al., 2012; Kaiser et al., 2019).

2.1.3.1 Aerosol size distribution

An aerosol population can be defined by a size distribution function $n_N(D,t)$ [1], such that $n_N(D,t)\ \mathrm{d}D$ is equal to the number of particles per unit volume of air and with diameters in the range of D to $D+\mathrm{d}D$, at time t (Seinfeld and Pandis, 2016, Ch.8). The total number concentration of particles $N(t)$ is then given by

$$N(t) = \int_0^\infty n_N(D,t)\ \mathrm{d}D \quad . \tag{2.1}$$

Typically, the assumption of spherical particles is introduced, as this simplifies the mathematical representation. In general, the moments of a size distribution are defined as

$$M_k(t) = \int_0^\infty n_N(D,t)\ D^k\ \mathrm{d}D \quad , \tag{2.2}$$

where $M_k(t)$ is the k^{th} moment of the distribution. According to this definition the zeroth moment $M_0(t)$ is equal to the total particle number concentration $N(t)$. The particle surface area concentration $S(t)$ is related to the second moment, while the particle volume concentration $V(t)$ is related to the third moment, via

$$S(t) = \pi\ M_2(t) \quad , \tag{2.3a}$$

$$V(t) = \frac{\pi}{6}\ M_3(t) \quad . \tag{2.3b}$$

Many aerosol models solve prognostic equations for the moments of a size distribution corresponding to changes of these moments due to different atmospheric processes, e.g. atmospheric transport, emission, wet and dry deposition, nucleation, coagulation, condensation and evaporation:

$$\begin{aligned}\frac{\partial M_k}{\partial t} = &\left.\frac{\partial M_k}{\partial t}\right|_{\mathrm{transp}} + \left.\frac{\partial M_k}{\partial t}\right|_{\mathrm{emis}} + \left.\frac{\partial M_k}{\partial t}\right|_{\mathrm{depo}} + \left.\frac{\partial M_k}{\partial t}\right|_{\mathrm{nucl}} + \\ &+ \left.\frac{\partial M_k}{\partial t}\right|_{\mathrm{coag}} + \left.\frac{\partial M_k}{\partial t}\right|_{\mathrm{cond}} + \left.\frac{\partial M_k}{\partial t}\right|_{\mathrm{evap}}\end{aligned} \tag{2.4}$$

Here, as in the following, time dependencies are not stated explicitly for the sake of simplicity in this chapter.

[1] The N in n_N illustrates that this is a number distribution, in contrast to surface area and volume distributions.

2.1.3.2 The lognormal distribution

As the diameters of atmospheric aerosol particles span several orders of magnitude from a few nanometers to several tens of micrometers, the numerical representation of the complete aerosol size distribution is a challenging problem. Therefore, different numerical representations exist that approximate the particle number size distribution. One approach is the discrete approximation, where the size range of particles is divided into discrete intervals or size bins. However, this approach suffers from relatively high demands on computational resources and also from the loss of the distribution structure in each bin. A different very efficient approach relies on representing the size distribution by continuous analytical functions. A widely used mathematical function that covers a wide range of diameters and fits many aerosol measurements reasonably well is the lognormal distribution (Whitby and McMurry, 1997; Seinfeld and Pandis, 2016, Ch.8):

$$n_N(D) = \frac{N}{\sqrt{2\pi} D \ln \sigma_g} \exp\left(-\frac{(\ln D - \ln \tilde{D}_g)^2}{2 \ln^2 \sigma_g}\right) \quad , \tag{2.5}$$

where the parameters describing the distribution are the total number of particles N, the median particle diameter $\tilde{D}_g$, and the geometric standard deviation σ_g describing the width of the distribution. Unlike the usual arithmetic standard deviation the geometric standard deviation is a dimensionless multiplicative factor. Formally, the logarithm of a dimensional quantity does not exist ($\ln D$ in Eq. 2.5). Thus, $\ln D$ is in fact $\ln (D/1\mu\text{m})$, but this reference diameter is not stated explicitly. Sometimes, the size distribution (Eq. 2.5) is represented based on the independent variable $\ln D$ instead of D, i.e. $n^\star_N(\ln D)$. Since the number of particles $\mathrm{d}N$ in the infinitesimal size range between diameters D and $\mathrm{d}D$ is independent of the representation of the size distribution function,

$$n_N(D)\ \mathrm{d}D = n^\star_N(\ln D)\ \mathrm{d}\ln D \quad , \tag{2.6}$$

the distribution with respect to $\ln D$ is related to that with respect to D by

$$n^\star_N(\ln D) = D\ n_N(D) = \frac{N}{\sqrt{2\pi} \ln \sigma_g} \exp\left(-\frac{(\ln D - \ln \tilde{D}_g)^2}{2 \ln^2 \sigma_g}\right) \quad . \tag{2.7}$$

With the lognormal distribution function (Eq. 2.5) the cumulative size distribution $F_N(D^*)$, i.e. the number concentration of all particles in the population with diameters below or equal to D^* (Seinfeld and Pandis, 2016, Ch.8) is given by

$$F_N(D^*) = \int_0^{D^*} n_N(D)\ \mathrm{d}D = \frac{N}{\sqrt{2\pi} \ln \sigma_g} \int_0^{D^*} \frac{1}{D} \exp\left(-\frac{(\ln D - \ln \tilde{D}_g)^2}{2 \ln^2 \sigma_g}\right) \mathrm{d}D \quad . \tag{2.8}$$

This integral can be evaluated as

$$F_N(D) = \frac{N}{2} + \frac{N}{2}\ \mathrm{erf}\left(\frac{\ln (D/\tilde{D}_g)}{\sqrt{2} \ln \sigma_g}\right) \quad , \tag{2.9}$$

renaming $D^* = D$ in the end. The error function $\mathrm{erf}\, x$ is defined as

$$\mathrm{erf}\, x = \frac{2}{\sqrt{\pi}} \int_0^x e^{-\eta^2}\ \mathrm{d}\eta \quad . \tag{2.10}$$

For $D = \tilde{D}_g$, since $\mathrm{erf}\,(0) = 0$, it is $F_N(\tilde{D}_g) = N/2$, which corresponds to the definition of the median diameter, for which one half of the particles are smaller and one half are larger. Considering a diameter D_σ, for which $\sigma_g = D_\sigma/\tilde{D}_g$, it follows from Eq. 2.9

$$F_N(D_\sigma) = N\left[\frac{1}{2} + \frac{1}{2}\,\mathrm{erf}\left(\frac{1}{\sqrt{2}}\right)\right] = 0.841N \quad . \tag{2.11}$$

Therefore, the geometric standard deviation σ_g is the ratio of that diameter to the median diameter below which 84.1 % of the particles reside.

In aerosol models, the particle population is typically described as a superposition of several lognormal functions (of the form of Eq. 2.5) also known as modes. This modal approach relies on the central assumption that the aerosol population can be viewed as a superposition of several populations of particles with different sizes and chemical populations (Whitby and McMurry, 1997). Consequently the distribution of a multimodal aerosol population consisting of K modes is given by:

$$n_N(D) = \sum_{k=0}^{K} n_{N,k}(D) = \sum_{k=0}^{K} \frac{N_k}{\sqrt{2\pi}D\ln\sigma_{g,k}} \exp\left(-\frac{(\ln D - \ln \tilde{D}_{g,k})^2}{2\ln^2\sigma_{g,k}}\right) \quad , \tag{2.12}$$

with the corresponding parameters N_k, $\sigma_{g,k}$, and $\tilde{D}_{g,k}$ of mode k. In the majority of modal aerosol models the mode widths are fixed so that only two parameters of the distribution, the number and the median diameter of the modes, have to be predicted by the model. This further reduces the computational requirements.

2.2 Climate effects of aerosols

In this section a brief overview of climate modifications induced by atmospheric aerosol particles is presented. Firstly, interactions between aerosols and solar and terrestrial radiation as well as the resulting direct aerosol effect are described. Secondly, indirect aerosol effects, like aerosol-cloud interactions are summarized.

Generally, the term "Radiative Forcing" (RF) characterizes the net change of the Earth's energy balance, i.e. downward shortwave plus upward longwave radiative flux, due to some imposed perturbation (Myhre et al., 2013). It is usually expressed in units of Wm^{-2} and defined at the top of the atmosphere (TOA). The RF typically characterizes the net radiative flux change between pre-industrial and present-day conditions. Often, the term "Radiative Effect" (RE) of aerosols is used to describe the instantaneous radiative impact of all atmospheric aerosol particles on the Earth's energy balance (e.g., Heald et al., 2014). The RF, in this context, can be regarded as the change in RE from pre-industrial to present-day conditions.

As described previously in Sect. 2.1.2, the aerosol RF can be splitted in a component representing the radiative forcing due to aerosol-radiation interactions ($\mathrm{RF}_{\mathrm{ari}}$) and a component including aerosol-cloud interactions ($\mathrm{RF}_{\mathrm{aci}}$), as defined by Boucher et al. (2013) in the fifth assessment report of the IPCC (Intergovernmental Panel on Climate Change). There, the authors also introduced the concept of the effective radiative forcing (ERF), which adds the effects of rapid adjustments to the RF. These rapid adjustments are mainly caused by cloud changes, e.g. modifications of cloud cover and cloud lifetime. In contrast to other slow climate feedbacks like the melting of continental ice sheets or oceanic processes these adjustments are rapid, as they are not controlled by the change in the global mean temperature (ΔT), which is slow because of the massive heat capacity of the oceans.

Overall, models and observations indicate that the total effect of anthropogenic aerosols (i.e. $\mathrm{ERF}_{\mathrm{ari}}$ + $\mathrm{ERF}_{\mathrm{aci}}$) cools the climate system, partially masking the global warming due to greenhouse gases. The total aerosol effective radiative forcing is estimated to be in the range of -1.5 to $-0.4\,\mathrm{Wm}^{-2}$ (Boucher et al., 2013). A more recent review by Bellouin et al. (2020) provides an interval of -2.0 to $-0.4\,\mathrm{Wm}^{-2}$ with a 90 % likelihood.

2.2.1 Aerosol-radiation interactions

Aerosol particles can interact with solar and terrestrial radiation through scattering and absorption. The effects on solar or shortwave radiation are typically more pronounced than interactions with long-wave terrestrial radiation (Zhou and Savijärvi, 2014). Scattering particles in the atmosphere generally have a cooling effect, as less sunlight reaches the Earth's surface. Absorbing aerosols, on the other hand, tend to warm the climate system, as they absorb solar radiation, which heats the aerosol layer locally and leads to a warming of the atmosphere via the redistribution of thermal energy. The balance between cooling and warming is determined by the composition and the optical properties of the aerosols. Examples for scattering atmospheric particles include mineral dust, sea spray and sulfate aerosols, while black carbon mainly absorbs solar radiation. Additionally, environmental conditions influence the radiative effects, e.g. the distribution and relative position of cloud and aerosol layers (Zarzycki and Bond, 2010) or surface albedo (Zhou, 2005).

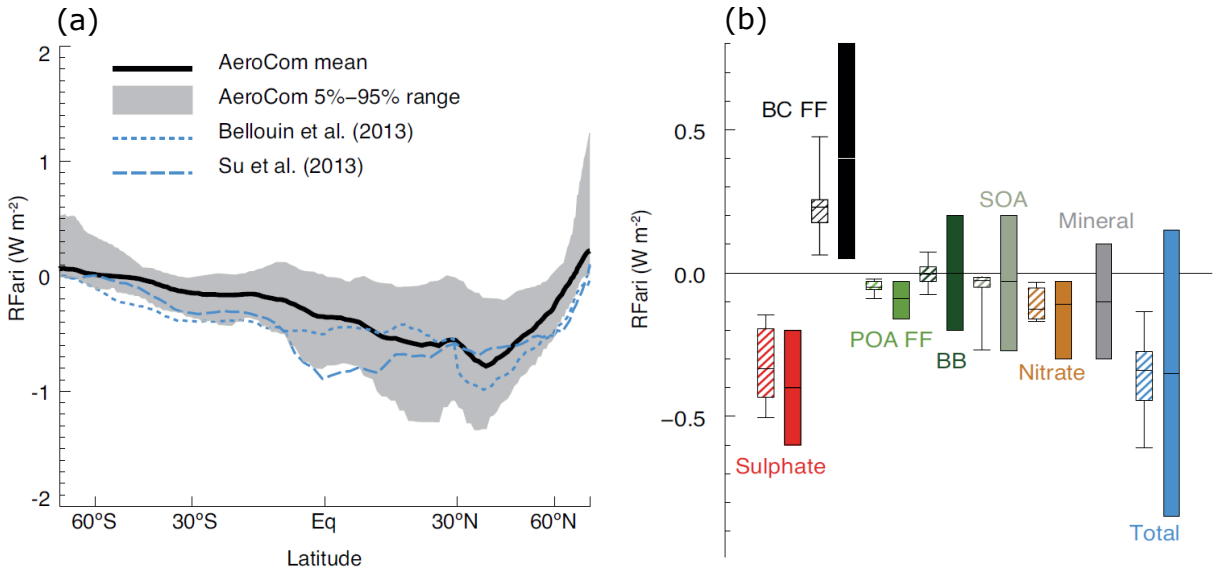

Figure 2.4: (a) Annual zonal-mean radiative forcing due to aerosol-radiation interactions (RF_{ari}) at the top of the atmosphere in units of Wm^{-2} due to all anthropogenic aerosols (Boucher et al., 2013, their Fig. 7.17). The black solid line and the grey shading represent the multi-model mean and the 5th to 95th percentile range of the AeroCom II models (Myhre et al., 2013). Blue dotted and dashed lines show results from Bellouin et al. (2013) and Su et al. (2013), respectively. The forcings are for the 1850 to 2000 period. (b) Annual mean top of the atmosphere RF_{ari} due to different anthropogenic aerosol types (Boucher et al., 2013, their Fig. 7.18). Hatched boxes represent median (line), 5th to 95th percentile range (box) and min/max values (whiskers) from AeroCom II models (Myhre et al., 2013). Solid coloured boxes show the best estimates and 90 percent uncertainty range from the IPCC report (Boucher et al., 2013).

Fig. 2.4 shows annual zonal-mean RF_{ari}, as well as its species breakdown (Boucher et al., 2013). The maximum negative RF is found around the northern midlatitudes, where the aerosol concentrations are highest. The global mean RF_{ari} is estimated as $-0.35\,Wm^{-2}$. Differences in the estimated RF ranges per species (see Fig. 2.4b) between AeroCom II models Myhre et al. (2013) and the IPCC judgement (Boucher et al., 2013) are related to the intercomparison of different sets of models and to different uncertainty estimates. In addition to these aerosol-radiation interactions, absorbing aerosol particles embedded in cloud droplets can lead to increased cloud dissipation (Koren, 2004; Feingold, 2005), but the contribution to RF_{ari} is small (Ghan et al., 2012). Furthermore, deposition of BC on snow or ice leads to surface albedo changes and the corresponding RF is estimated to be in the range of +0.02 to $+0.09\,Wm^{-2}$ (Bond et al., 2013).

2.2.2 Aerosol-cloud interactions

Aerosol particles can influence cloud properties via several different pathways. These mechanisms may interact and compensate each other, further complicating the assessment of the corresponding effects. The total effective radiative forcing of aerosol-cloud interactions is termed ERF_{aci}, including modifications of cloud reflectivity or albedo and cloud lifetime (Boucher et al., 2013). Global forcings are primarily quantified using satellite-based remote sensing, global modelling, or a combination of both.

In warm, liquid clouds ($T > 0\,°C$) aerosols can act as CCNs resulting in the formation of cloud droplets. In warm clouds the cloud albedo effect, also known as Twomey effect (Twomey, 1977) is the mechanism by which an increase in CCN concentration results

in an enhanced cloud albedo due to an increased cloud droplet number concentration (CDNC) and a decreased droplet size if the liquid water content (i.e. liquid water mass per unit mass of air; LWC) remains constant. This increases the total droplet surface area and the reflectivity of the cloud. The physical basis of this albedo effect is fairly well developed from observations and model simulation studies (e.g., Fountoukis et al., 2007; Lu et al., 2007; Werner et al., 2014). Evidence for this effect can for example be seen in satellite images of ship tracks, where a strong increase in CCN concentration leads to enhanced cloud albedo along shipping routes (Durkee et al., 2000).

In addition to the Twomey effect, aerosols are hypothesized to induce cloud modifications by increasing cloud amount or cloud lifetime. Decreasing cloud droplet size in the presence of high CCN concentrations may lead to reduced precipitation, as smaller droplets have a smaller collection efficiency (Albrecht, 1989; Stevens and Feingold, 2009). However, this effect is difficult to quantify, as observations generally include both the albedo effect and secondary adjustments that influence cloud lifetime. Some results from satellite observations or small scale studies confirm that an increase in aerosol tends to increase cloud amount by suppressing precipitation (Lebsock et al., 2008; Xue et al., 2008; Yuan et al., 2011; Gryspeerdt et al., 2016). However, these effects are strongly influenced by cloud properties and satellite retrieval biases and controversial results exist (e.g., Jiang et al., 2006; Lebsock et al., 2008; Small et al., 2009; Dey et al., 2011; Small et al., 2011). Therefore, the significance of the cloud lifetime effect is not clearly established.

In cold clouds liquid water droplets freeze spontaneously below temperatures of $-38\,^{\circ}\mathrm{C}$ at atmospheric conditions (see Sect. 2.3). For larger temperatures ($-38\,^{\circ}\mathrm{C} < T < 0\,^{\circ}\mathrm{C}$) ice crystal formation depends on the presence of aerosol particles that act as INPs. This temperature threshold of $-38\,^{\circ}\mathrm{C}$ marks the difference between mixed-phase and cirrus clouds. Mixed phase clouds exist between temperatures of $0\,^{\circ}\mathrm{C}$ and $-38\,^{\circ}\mathrm{C}$ and contain both supercooled liquid water droplets and ice crystals. At colder temperatures liquid water freezes homogeneously and cirrus clouds consist only of ice crystals (see Sect. 2.3). Despite the low concentration of INPs (of the order of 10 per litre, e.g. DeMott et al., 2010) they have an important influence on mixed phase and cirrus clouds. However, the simulation of aerosol-cloud interactions in global climate models is challenging, as the key physical processes are occurring at the relatively small cloud-scale (of the order of 1 km), which cannot be resolved in current global climate models. Such models therefore have to rely on assumptions and parametrizations to represent these processes at large-scale global model resolutions (Mülmenstädt and Feingold, 2018). Thus, ice nucleation effects of aerosols on cold clouds and especially cirrus are highly uncertain and the subject of ongoing research activities. A comparison of different studies on the effects of INPs on cirrus clouds and resulting climate modifications is presented in Sect. 2.3.3. A more detailed overview of ice nucleation processes in cirrus clouds is presented in the following section (Sect. 2.3).

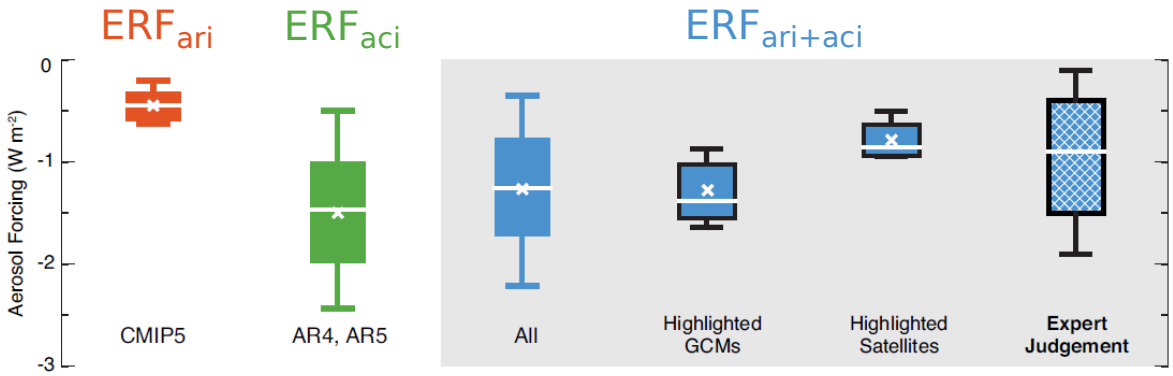

Figure 2.5: (a) $\mathrm{ERF_{ari}}$ (red), $\mathrm{ERF_{aci}}$ (green) and the total $\mathrm{ERF_{ari+aci}}$ (blue) estimated from GCM studies and satellite observations. Estimates of $\mathrm{ERF_{ari}}$ are from CMIP5 models (Coupled Model Intercomparison Project Phase 5), $\mathrm{ERF_{aci}}$ values stem from GCM studies presented before (AR4) and after the 4th assessment report (AR5). Estimates of $\mathrm{ERF_{ari+aci}}$ include both GCM and satellite studies. Results from selected (highlighted) GCM studies include additional adjustments including aerosol-cloud interactions in mixed-phase and in convective clouds. Selected model and satellite estimates were used for the expert judgment in the IPCC-AR5 report (Boucher et al., 2013). The box-whisker plots are displaying averages (cross sign), median values (middle line), 17th to 83th percentile range (box boundaries), and 5th to 95th percentile range (whiskers). Adapted from Boucher et al. (2013, their Fig. 7.19).

In Fig. 2.5 estimates for $\mathrm{ERF_{aci}}$ are shown together with $\mathrm{ERF_{ari}}$ and the combined forcing of both effects $\mathrm{ERF_{ari+aci}}$, as presented in Boucher et al. (2013). Median $\mathrm{ERF_{aci}}$ from GCMs is estimated as $-1.4\,\mathrm{Wm^{-2}}$ and uncertainties span a much larger range than for $\mathrm{ERF_{ari}}$. These estimates to some extent include effects of ice nucleating aerosols on mixed-phase clouds but cirrus modifications are only scarcely considered. The combined $\mathrm{ERF_{ari+aci}}$ is assessed as $-0.9\,\mathrm{Wm^{-2}}$ with a 5 to 95 percent uncertainty range of -1.9 to $-0.1\,\mathrm{Wm^{-2}}$. A more recent review by Bellouin et al. (2020) estimates a similar range of the total aerosol ERF, i.e. -2.0 to $-0.4\,\mathrm{Wm^{-2}}$, albeit shifted towards more negative forcings.

2.3 Cirrus clouds and ice nucleation

In this section a brief overview of ice nucleation processes and pathways in cold clouds, especially cirrus, is presented. First, ice nucleation processes are reviewed, with a focus on ice nucleating aerosol particles. A comprehensive and detailed review about cirrus cloud formation and ice nucleation can also be found in Heymsfield et al. (2017) and Kanji et al. (2017). Secondly, an overview of cirrus clouds is presented, including their formation, occurrence and resulting climate effects. A detailed cirrus cloud review is also given in Heymsfield et al. (2017).

2.3.1 Ice nucleation processes

In general ice particles form when a moist air parcel cools to a temperature at which the water vapour is supersaturated with respect to ice. The supersaturation is typically produced by the vertical motion of the air parcel. This updraft can occur on large scales (e.g. along frontal boundaries) or by small scale vertical perturbations (e.g. due to turbulence, convective systems, or gravity waves). Ice particles in cirrus clouds can form via homogeneous freezing, i.e. the spontaneous freezing of a supercooled cloud droplet or a liquid aerosol particle. Solution droplets can freeze spontaneously at temperatures below $-38\,°C$ (Koop et al., 2000). The process of homogeneous freezing is well defined and has been shown to be solely dependent on particle volume and water activity, i.e. the ratio between the water vapour pressures of the solution and of pure water under the same conditions (Koop et al., 2000). At sufficiently high supersaturations all solution droplets would freeze homogeneously, but supersaturations are driven by the updraft speed and the temperature of an air parcel. The number of homogeneously formed ice crystals was shown to increase with increasing updraft speed and decreasing temperature (Kärcher and Lohmann, 2002).

Some aerosol particles can serve as ice nucleating particles (INPs). They lower the energy barrier for the formation of a critical ice embryo, thus facilitating ice formation at temperatures below $0\,°C$, when the saturation of water vapour with respect to ice is exceeded. In cirrus clouds heterogeneous ice nucleation can occur also below $-38\,°C$ together with homogeneous freezing, but above a supersaturation threshold of $RH_i = 140\,\% - 150\,\%$ homogeneous nucleation rates dominate the freezing process (Spichtinger and Cziczo, 2010). As heterogeneous freezing can occur at higher temperatures and lower supersaturations with respect to ice than homogeneous nucleation, these two mechanisms compete for the available supersaturated water vapour during the lifting-up of an air parcel. If the concentration of INPs is sufficiently high, homogeneous freezing could be attenuated or even suppressed.

Heterogeneous ice nucleation is less clearly understood than homogeneous freezing, as there exist several pathways by which ice is formed in the presence of INPs. Different freezing mechanisms are relevant for the mixed-phase ($-38\,°C < T < 0\,°C$) and the cirrus regime ($T < -38\,°C$), respectively. Fig. 2.6 depicts a schematic representation of different freezing pathways in cold clouds.

For the case of mixed-phase clouds, ice nucleation requires the presence of cloud droplets. Contact freezing happens when an INP collides with the air-water interface of a supercooled cloud droplet. This can occur from the outside of the droplet but also

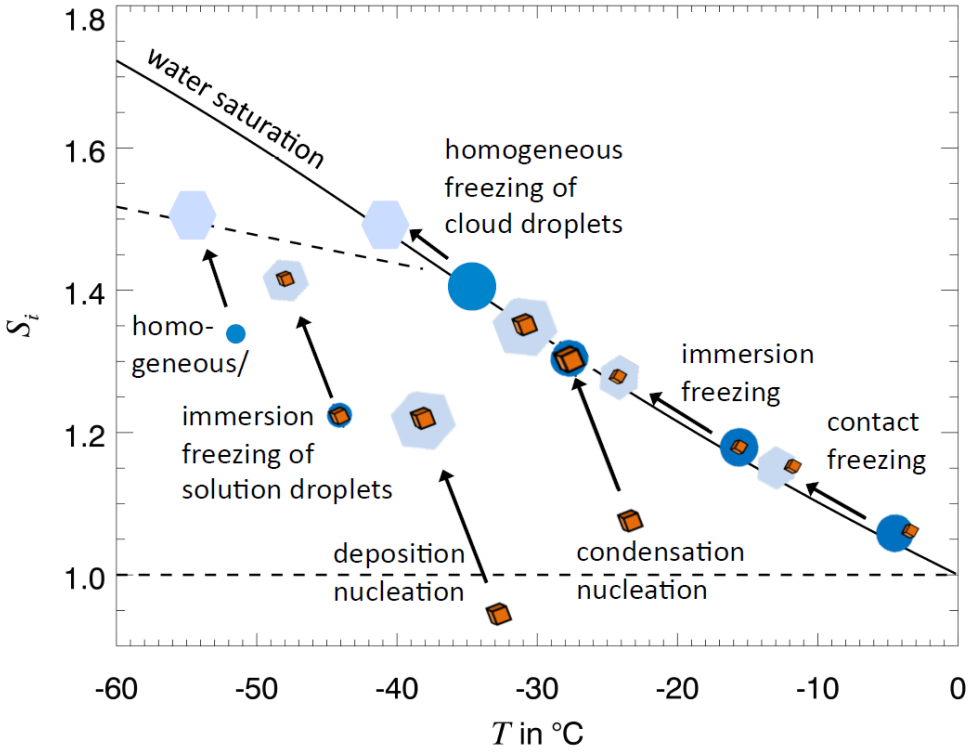

Figure 2.6: Different ice nucleation mechanisms and formation pathways possible in the atmosphere, depicted in the ice supersaturation versus temperature space. The solid diagonal line represents ice saturation ratio at liquid water saturation, where supercooled liquid water is in equilibrium with the vapour phase. Above $S_i = 1$, ice is the stable phase. At temperatures below $-38\,°C$ liquid solution particles and cloud droplets freeze homogeneously (dashed line at high saturation ratios). Taken from Hoose and Möhler (2012, their Fig. 1).

from "inside-out", when an INP touches the droplet surface from within the droplet, e.g. if the droplet evaporates. Immersion freezing refers to ice nucleation initiated by an INP immersed inside a cloud droplet. This can happen via activation of CCN, such that some CCN could also be efficient INPs. Condensation freezing is defined as freezing being initiated concurrently with CCN activation, but is not fully established as a separate mechanism because of its similarities with immersion freezing (Vali et al., 2015).

In the cirrus regime, where no cloud droplets are present, immersion freezing can also occur for INPs immersed inside liquid solution droplets. However, immersion freezing was found to be most important for mixed-phase clouds (Murray et al., 2012). Deposition ice nucleation is the process of ice nucleating directly from water vapour supersaturated with respect to ice, without the involvement of liquid water. Laboratory studies recently suggested that deposition nucleation may in fact be pore condensation and freezing (PCF), i.e. condensation of water in cavities on the surface of porous INPs, which subsequently freezes homogeneously at $T < -38\,°C$ (Marcolli, 2014; Wagner et al., 2016). The different heterogeneous freezing mechanisms compete with homogeneous freezing for the available supersaturated water vapour. This competition typically results in a reduction of the overall ice crystal number and is strongly dependent on the number concentration of INPs, their freezing properties, and the updraft speed (Kärcher et al., 2006). Additionally, deep convection detraining at the top of convective clouds can be a source for ice crystals in the cirrus regime, mainly in the tropical tropopause layer (TTL) (e.g., Jensen et al., 2018; Ueyama et al., 2020; Krämer et al., 2020).

2.3.1.1 Ice nucleating aerosol particles

In this section, a brief overview of some of the most important types of INPs and their properties and freezing efficiencies is presented. In general, concentrations of INPs in the global atmosphere are rather low, 1-100 per litre (e.g., Rogers et al., 2001a; DeMott et al., 2010), much lower than CCN concentrations. However, measurements of INP concentrations in the cirrus regime are very limited. Additionally, INP concentrations of the past have been estimated from recent ice core analyses (e.g. Hartmann et al., 2019; Schrod et al., 2020), shedding light on possible differences between pre-industrial and present-day conditions. INP number concentrations are typically presented as counts per litre of air (L^{-1}), as this is a common unit in this research field[1] (e.g., Kärcher, 2017; Chen et al., 2018).

How efficiently INPs nucleate ice depends on their size, composition and surface morphology. Ice nucleation is often initiated at certain locations at the surface of a solid INP, such as cracks or lattice mismatches. These sites occur with a higher probability on particles with a larger surface area. Thus, the ice nucleation ability for insoluble, solid particles scales with particle size. Additionally, the presence of functional groups (e.g. OH) at a particle's surface was found to play a role in promoting ice nucleation, as these are able to form hydrogen bonds with water molecules (Kanji et al., 2008; Freedman, 2015).

The ice nucleation ability of different INP-types was investigated in various laboratory studies, e.g. in experiments with cloud or ice nucleation chambers, external parameters like temperature, pressure and humidity can be controlled, in order to study ice nucleation events (e.g., Möhler et al., 2008; Paramonov et al., 2018). The main factors that determine ice nucleation are temperature (T) and saturation ratio with respect to ice (S_i). For $S_i > 1$, the system is supersaturated with respect to ice and ice is the stable phase. Most laboratory studies report temperatures and saturation ratios for the "onset" of ice nucleation. This onset is not well defined and corresponds either to the detection limit of the instrument or to the point when a critical active fraction (f_{act}) of particles has been activated. Often the onset f_{act} is chosen as 0.1 %, in laboratory experiments.

Fig. 2.7 summarizes results from many laboratory studies corresponding to different INP-types and freezing modes. Some particle types are more efficient INPs than others, i.e. they initiate ice formation at lower supersaturations and higher temperatures. This can also lead to a competition mechanism between different INPs.

Additionally, different INP-types are important for the mixed-phase and cirrus regime, respectively, and their freezing potential may vary according to the temperature regime. Mineral dust and soot are important INP-types in both regimes. Bioaerosols (e.g. pollen or fungal spores) mainly serve as ice nuclei in mixed-phase clouds. For example, certain proteins in the cell membrane of some bacteria (e.g. *Pseudomonas syringae*) promote ice nucleation (Pandey et al., 2016), resulting in freezing temperatures $T < -5\,°C$. Marine diatoms or diatom exudates were also observed to form ice at temperatures below $-15\,°C$ (Knopf et al., 2011; Wilson et al., 2015). Generally, the importance of bioaerosol-INPs is limited by their smaller emission rates compared with other aerosol types like mineral dust (Després et al., 2012). Furthermore, NaCl salt particles, a main component of sea spray aerosol, can serve as ice nuclei in mixed-phase clouds. NaCl particles were observed

[1] The capital letter L is used here to avoid confusion with the digit 1.

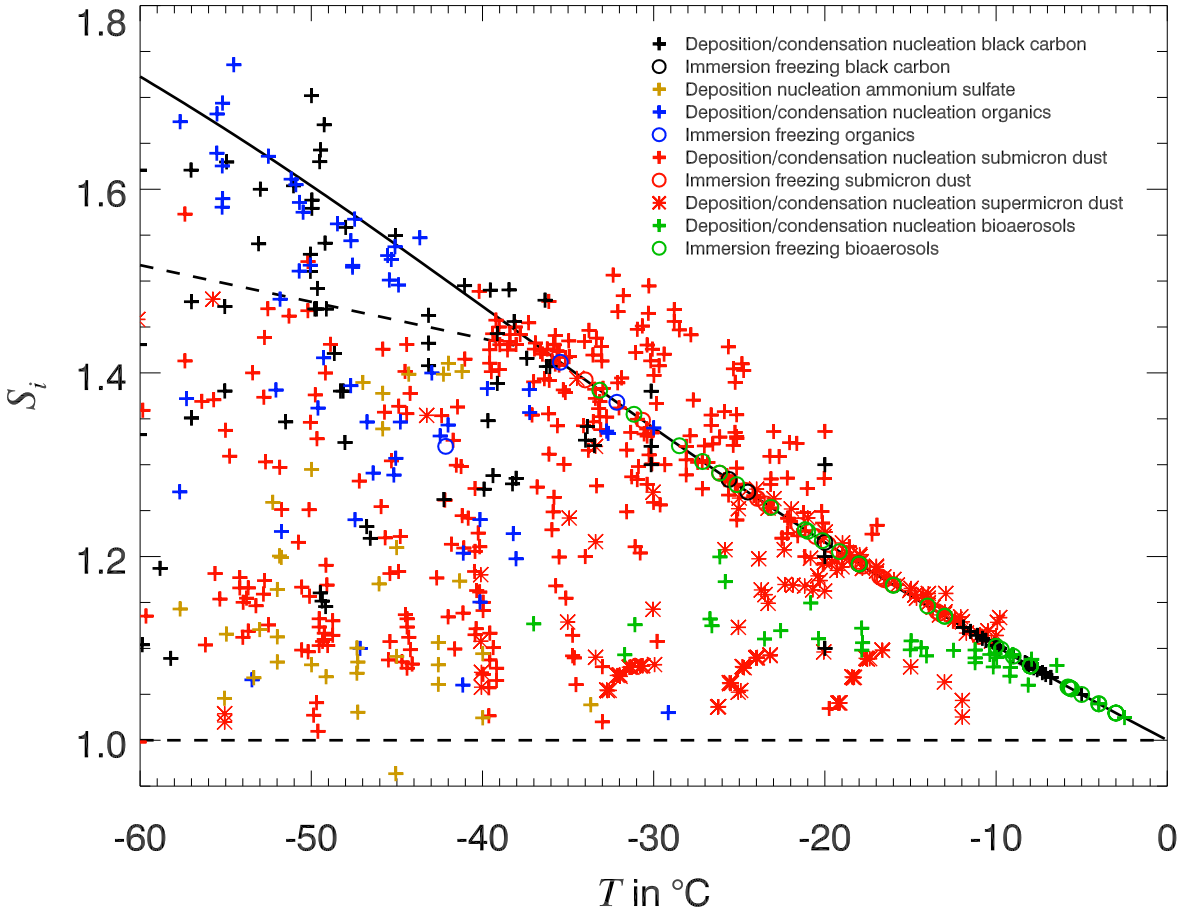

Figure 2.7: Ice nucleation onset temperatures and saturation ratios for different INPs, as observed in several laboratory measurements. The solid diagonal line represents ice saturation ratio at liquid water saturation, where supercooled liquid water is in equilibrium with the vapour phase. Above $S_i = 1$, ice is the stable phase. The dashed line at high supersaturation ratios represents the heterogeneous freezing threshold for temperatures below −38 °C. Taken from Hoose and Möhler (2012, their Fig. 2).

in a large quantity of ice residuals collected in cirrus clouds over the oceans (Cziczo et al., 2013) and large NaCl particles were found to nucleate ice via contact freezing at temperatures of up to −7 °C in laboratory experiments (Niehaus and Cantrell, 2015).

In the cirrus regime, besides mineral dust and soot INPs, organic particles that are transformed into a glassy, high-viscosity state, as well as crystalline ammonium sulfate ($(NH_4)_2SO_4$) particles, were observed as INPs at temperatures below −38 °C. These types of ice nucleating particles are described in the following.

Mineral dust

Mineral dust is widely recognized as the most important type of INPs, due to its very strong ice nucleation ability and its abundance in the atmosphere. DU particles were found to effectively nucleate ice at $T < -38$ °C (Möhler et al., 2006, 2008) but also at higher temperatures in the mixed-phase regime (Harrison et al., 2016; Peckhaus et al., 2016). However, not all mineral dust INPs are equal, and their ice nucleation potential largely depends on their composition. Silicate clay minerals like kaolinte, montmorillonite and illite were observed to be efficient ice nuclei at cirrus (Welti et al., 2009) and mixed-phase

temperatures (Wex et al., 2014), but potassium rich K-feldspars have been identified as the most ice active components of DU particles in the cirrus (Kiselev et al., 2016) and mixed-phase (Harrison et al., 2016; Kumar et al., 2018) regimes. Importantly, dust particles often develop surface coatings during their atmospheric lifetime (e.g. sulfuric acid coatings) that may impede ice nucleation (Möhler et al., 2008; Cziczo et al., 2009; Kulkarni et al., 2014).

Black carbon

Soot and ash particles produced from biomass burning or from incomplete combustion of fossil fuels may play an important role for ice nucleation, due to their high emission rates and atmospheric concentrations. However, it is unclear whether these particles are efficient INPs, as there exists contradictory evidence from laboratory and field experiments (e.g., Bond et al., 2013). Only few studies have shown ice nucleation by soot particles for $T > -40\,°C$ (Chou et al., 2013; Grawe et al., 2016). At cirrus conditions, below $-40\,°C$, several studies show BC-induced ice nucleation (e.g., Koehler et al., 2009; Chou et al., 2013; Kulkarni et al., 2016), while the ice nucleation ability of these particles appears to be related to the fuel source and mixing state (Kulkarni et al., 2016; Möhler et al., 2005). It was hypothesized that cloud processing of soot particles, i.e. particles involved in one or more cloud formation cycles that are subsequently released back into the atmosphere, may enhance their ice nucleation potential (Kärcher et al., 2007; Marcolli, 2014; Mahrt et al., 2020). This preactivation could be an important process for possible aircraft-induced cirrus modifications, if the ice nucleation ability of soot particles is enhanced after contrail ice sublimation. Recent studies have shown that cloud processing can indeed increase the ice nucleation abilities of soot aerosol, and this process was attributed to the PCF mechanism (Mahrt et al., 2018; David et al., 2019; Nichman et al., 2019; Mahrt et al., 2020). However, this process is mostly limited to larger particles of several hundreds of nanometers (e.g., Mahrt et al., 2020), which occur only rarely at cirrus altitudes.

Glassy organics

Recently, several studies have reported on the ice nucleation potential of glassy SOA particles (Murray et al., 2010; Ignatius et al., 2016; Wagner et al., 2017). Atmospheric SOA particles can exist in a highly viscous, amorphous state, depending on ambient temperature and humidity. If the temperature decreases below the glass transition temperature (T_g), a liquid solution particle vitrifies and is transformed into a semi-solid, glassy phase (Reid et al., 2018). For increasing temperatures, the reverse process, i.e. the glass-to-liquid transition, occurs at the same specific temperature. T_g depends on the composition of the organic compound and increases with decreasing relative humidity. For small humidities ($< 10\,\%$), Koop et al. (2011) describe a T_g for a SOA estimate of around -3 °C. Common biogenic SOA precursors are terpenes, a class of organic compounds produced by various plants, especially in boreal forest regions, e.g. the monoterpene pinene (Laaksonen et al., 2008). Another typical SOA precursor is isoprene, mainly emitted from tropical rainforests (Guenther et al., 1995, 2006).

Crystalline ammonium sulfate

Several studies show that crystalline $(NH_4)_2SO_4$ can serve as efficient INPs under cirrus conditions (Abbatt et al., 2006; Wise et al., 2009; Baustian et al., 2010; Ladino et al., 2014). As these salt particles only nucleate ice in their crystalline state, their ice nucleation potential depends on the ambient atmospheric conditions. Ammonium sulfate particles undergo phase transitions via a hysteresis process, i.e. the transition from aqueous solution droplets to the solid crystalline phase (efflorescence) happens at a different characteristic relative humidity, the efflorescence relative humidity (ERH), than the converse process. The dissociation of solid crystals to solution droplets is called deliquescence, and the deliquescence relative humidity (DRH) is typically higher than ERH (Martin, 2000; Martin et al., 2003). For humidities between ERH and DRH, particles are either liquid or solid, depending on their RH history.

2.3.2 Cirrus clouds

According to the Glossary of Meteorology[2], cirrus clouds are "a principal cloud type [...] in the form of white, delicate filaments, of white (or mostly white) patches, or of narrow bands", that are composed of ice crystals. Cirrus clouds are typically defined according to the ambient temperature. While warm clouds ($T > 0\,°C$) consist of liquid droplets and occur in the lower troposphere, cirrus clouds ($T < -38\,°C$) consist of ice crystals and are observed frequently above $\sim 7\,km$ height in the midlatitudes and above $\sim 12\,km$ in the tropics (Sassen et al., 2008; Heymsfield et al., 2017). Clouds at temperatures between $-38\,°C$ and $0\,°C$ can contain both ice crystals and supercooled solution droplets and are called mixed-phase clouds (Heymsfield et al., 2017). Krämer et al. (2016, 2020) classified cirrus types as "liquid origin cirrus", i.e. mixed-phase or liquid clouds lifted by strong convective updrafts to altitudes with temperatures below $-38\,°C$, and as "in situ cirrus" that are formed by homogeneous or heterogeneous nucleation of insoluble of solution aerosols at $T < -38\,°C$.

Due to the large spatial extent of cirrus clouds and their strong interactions with both solar and terrestrial radiation, cirrus clouds play an important role for the Earth's energy budget. Cirrus clouds reflect solar radiation back to space, resulting in a cooling effect at the top of the atmosphere and at the surface. Additionally, cirrus clouds absorb outgoing longwave radiation emitted by the Earth's surface, which eventually leads to a warming of the climate system. If the total effect leads to a global warming or cooling depends on the prevalence of shortwave cooling versus longwave warming. Estimates of the global annual mean cirrus cloud radiative effect from model simulations (the difference between net top of the atmosphere radiation with and without cirrus) show a warming amounting to $5.7\,Wm^{-2}$ (Gasparini and Lohmann, 2016). Estimates from satellite-based studies show smaller effects, e.g. $1.3\,Wm^{-2}$ (Chen et al., 2000).

Importantly, the radiative impact of cirrus clouds depends on their microphysical properties, such as number concentration, size and shape of ice crystals or ice water content (i.e. cloud ice mass per unit volume of air), which in turn are related to environmental conditions and the formation mechanisms of the cloud (Zhang et al., 1999; Kärcher and

[2] American Meteorological Society, 2021: "Cirrus". Glossary of Meteorology, `http://glossary.ametsoc.org/wiki/cirrus`

Lohmann, 2003; DeMott et al., 2010). It is believed that the presence of a sufficiently large quantity of INPs leads to cirrus clouds consisting of fewer but larger ice crystals, compared to the homogeneous freezing pathway (DeMott et al., 2010). This reduces the optical thickness of the cloud. Additionally, larger ice crystals sediment faster, further decreasing optical thickness. Results from global modelling studies suggest that heterogeneous ice nucleation may lead to a net negative radiative effect (e.g., Penner et al., 2009; Liu et al., 2012; Kuebbeler et al., 2014; Wang et al., 2014). However, this cooling effect is still unclear as other studies report non-significant (Hendricks et al., 2011; Gettelman et al., 2012) or even small positive radiative effects (Liu et al., 2009; Gettelman et al., 2012), see also Sect. 2.2.2. The potential cooling effect of INPs led to the proposal to engineer climate and reduce global warming by seeding cirrus clouds with highly efficient INPs, thus converting homogeneously to heterogeneously formed cirrus clouds (Mitchell and Finnegan, 2009). But such measures are controversially debated and their effects are still highly uncertain (Storelvmo et al., 2013; Penner et al., 2015; Gasparini and Lohmann, 2016).

2.3.3 Climatic impacts of ice nucleating particles in the cirrus regime

In this section, a brief overview on INPs in the cirrus regime ($T < -38\,°C$) is presented, including a summary of resulting climate effects from recent studies. Mineral dust particles are widely considered as one of the most important types of cirrus INPs, due to their strong ice nucleation potential (e.g., Möhler et al., 2006, 2008; Koehler et al., 2010; Paramonov et al., 2018). Additionally, BC or soot particles, were observed to nucleate ice at cirrus temperatures (e.g., Koehler et al., 2009; Chou et al., 2013; Kulkarni et al., 2016; Mahrt et al., 2018). However, the ice nucleation potential of BC is highly uncertain, as it strongly depends on its source, composition, mixing-state, and possible atmospheric processing. While DU INPs are largely related to natural sources, BC has a strong anthropogenic influence (e.g. soot particles from fossil fuel combustion). Typically, only mineral dust and soot particles were considered in many previous global modelling studies analysing INP-effects on cirrus clouds and resulting climate modifications (e.g., Hendricks et al., 2011; Gettelman et al., 2012; Zhou and Penner, 2014).

Recently, additional types of cirrus INPs have been identified from laboratory studies. Organic particles that undergo a glass transition at low temperatures and are transformed into a high-viscosity, amorphous state, were observed to nucleate ice under cirrus conditions (Murray et al., 2010; Ignatius et al., 2016; Wagner et al., 2017). Additionally, several studies show that crystalline ammonium sulfate particles can serve as efficient INPs in the cirrus regime (e.g., Abbatt et al., 2006; Wise et al., 2009; Baustian et al., 2010; Ladino et al., 2014). Glassy organics are produced naturally from SOA precursors in regions with strong biogenic activity (e.g. tropical rainforests). Ammonium sulfate is produced from NH_4 and SO_4, generated in part naturally but mainly from anthropogenic sources. The global effects of glassy organics and crystalline ammonium sulfate INPs on cirrus clouds are still unclear, as up to date only few studies have included these particles in global models (e.g., Abbatt et al., 2006; Penner et al., 2018; Zhu and Penner, 2020).

Generally, the simulation of aerosol-cirrus interactions and resulting climate perturbations in global models is a challenging task. In the cirrus regime several different ice nucleation processes and pathways exist, which occur on a much smaller spatial scale than a global climate model can resolve. Therefore, models have to rely on assumptions and parametrizations to represent these processes at the large-scale global model resolution. Thus, the importance of INP-effects on cirrus clouds and the resulting climate modifications are still poorly constrained and subject of ongoing research. There is e.g. conflicting evidence about the importance of the radiative effect due to cirrus cloud modifications ranging from statistically insignificant effects (Hendricks et al., 2011; Gettelman et al., 2012) to small or sometimes very large negative forcings (Zhou and Penner, 2014; Penner et al., 2018; Zhu and Penner, 2020; McGraw et al., 2020), or even small positive forcings (Liu et al., 2009). Table 2.2 lists results from different global model studies on the climate impacts of aerosol-cirrus interactions, showing the wide range of possible results. The comparison of different studies is further complicated, as they use different models and techniques, consider different types of INPs, and analyse different sensitivities and effects.

This thesis particularly focuses on the modifications of cirrus clouds induced by ice nucleating aerosol particles and contributes to assessing resulting climate effects and corresponding uncertainties. Here, also glassy organics and crystalline ammonium sulfate are considered as INPs in addition to mineral dust and soot, to further constrain their importance for cirrus cloud and climate modifications on a global scale.

Table 2.2: Comparison of different studies on the climate impacts and radiative effects of ice nucleating particles influencing cirrus clouds. The global RE represents the net radiative effect at the top of the atmosphere unless stated otherwise.

Reference	Model	INP-types	Analysed effect	Global radiative effect [Wm^{-2}]
Liu et al. (2009)	CAM3[a]	BC	Anthropogenic BC effect	$[0.1, 0.6]$
Penner et al. (2009)	Offline calculations	BC	Total BC effect	$[-0.4, -0.3]$
Hendricks et al. (2011)	ECHAM4[b]	DU, BC	Total DU + BC effect	< 0.1 (noise level)
Gettelman et al. (2012)	CAM5[c], ECHAM5-HAM[d]	DU, BC	Anthropogenic BC effect	not significant
Liu et al. (2012)	CAM5	DU	Total DU effect	$[-0.6, -0.2]$[e]
Kuebbeler et al. (2014)	ECHAM5-HAM	DU	Total DU effect + preexisting ice crystals	-0.94
Wang et al. (2014)	CAM5	DU	Total DU effect	$[-1.59, -0.24]$[f], $[-0.2, -0.9]$[e]
Zhou and Penner (2014)	CAM5-IMPACT[g]	DU, BC	Aircraft BC effect	$[-0.35, 0.09]$
Penner et al. (2018)	CAM5-IMPACT	DU, BC, ammonium sulfate, glassy organics	Aircraft BC effect Fossil/biofuel BC effect	$[-0.26, -0.14]$ $[-0.126, -0.06]$
Zhu and Penner (2020)	CESM-IMPACT[h]	DU, BC, glassy organics	Aircraft BC effect	$[-0.21, -0.07]$
McGraw et al. (2020)	CESM-MAM4[i]	DU, BC	Total BC effect	$[-0.20, -0.06]$

[a] National Center for Atmospheric Research (NCAR) Community Atmosphere Model, version 3 (Collins et al., 2006) coupled to the Massively Parallel Atmospheric Chemical Transport (IMPACT) aerosol model (Rotman et al., 2004)
[b] Fourth version of the European Center Hamburg general circulation model (Roeckner et al., 1996)
[c] National Center for Atmospheric Research (NCAR) Community Atmosphere Model, version 5 (Neale et al., 2010)
[d] The global model ECHAM5 (Roeckner et al., 2003) coupled to the HAM aerosol model (Stier et al., 2005)
[e] Total cloud RE
[f] Net top of the atmosphere RE
[g] University of Michigan IMPACT (Integrated Massively Parallel Atmospheric Chemical Transport) aerosol model (Rotman et al., 2004) coupled to CAM5 (Community Atmosphere Model, version 5; Neale et al., 2010)
[h] University of Michigan IMPACT (Integrated Massively Parallel Atmospheric Chemical Transport) aerosol model (Rotman et al., 2004) coupled to the Community Earth System Model (CESM; `www.cesm.ucar.edu/models/cesm1.2/`, last access: 2 February, 2021)
[i] Modal Aerosol Module (four-mode version; Liu et al., 2016) within the Community Earth System Model (CESM)

Chapter 3

Methods

This chapter describes methods, techniques, and schemes applied in this work, focusing on the numerical modelling of the global aerosol and aerosol-induced climate modifications. In Sect. 3.1, the aerosol microphysics model MADE3 is described, which is employed as part of the general circulation model EMAC (ECHAM/MESSy Atmospheric Chemistry (EMAC) general circulation model, Sect. 3.2). Section 3.3 focuses on the representation of mineral dust emissions in EMAC-MADE3. The implementation of additional aerosol tracers for tagging BC from aircraft emissions (BCair), glassy organics (glPOM), and crystalline ammonium sulfate (AmSu) is described in Sect. 3.4. The coupling of these new ice-nucleating tracers to clouds, especially cirrus, is highlighted in Sect. 3.5. The chapter concludes with a summary of observational data used for the model evaluation, as well as evaluation methods (Sect. 3.6).

Parts of this chapter appeared similarly in my recent publication (C. G. Beer, J. Hendricks, M. Righi, B. Heinold, I. Tegen, S. Groß, D. Sauer, A. Walser, and B. Weinzierl. Modelling mineral dust emissions and atmospheric dispersion with MADE3 in EMAC v2.54. *Geosci. Model Dev.*, 13(9):4287–4303, 2020. doi:10.5194/gmd-13-4287-2020). Corresponding sections are marked in the text.

3.1 The aerosol microphysics submodel MADE3

The aerosol microphysics model MADE3 (Modal Aerosol Dynamics Model for Europe, adapted for global applications, third generation) is employed to simulate the global atmospheric aerosol. Originally, the first generation of MADE was developed for application in a regional model (Ackermann et al., 1998) but was subsequently adapted for global applications in the general circulation model ECHAM4 (fourth version of the European Center HAMburg general circulation model; Roeckner et al., 1996) by Lauer et al. (2005). It was later transformed into a MESSy submodel in the framework of EMAC (Lauer et al., 2007), and subsequently extended to the second generation submodel MADE-in (Aquila et al., 2011). Further developments by Kaiser et al. (2014) resulted in the current third version submodel MADE3 and were described in detail by Kaiser et al. (2014) and Kaiser et al. (2019). The main aspects are reviewed in the following.

3.1.1 Aerosol species and modes

MADE3 simulates 9 different aerosol species (see Fig. 3.1), which in some cases represent more than one chemical component. These species are represented as tracers in the 3D-model: sulfate (SO_4), ammonium (NH_4), nitrate (NO_3), sea-spray components other than chloride (mainly sodium; Na), chloride (Cl), particulate organic matter (POM), black carbon (BC), mineral dust (DU), and aerosol water (H_2O). These aerosol components are distributed over 9 lognormal modes (see also Sect. 2.1.3.1) that represent different particle size ranges, covering the Aitken, accumulation, and coarse mode and different mixing states (Fig. 3.1). Each of the MADE3 Aitken-, accumulation- and coarse-mode size ranges incorporates three modes for different particle mixing states: particles fully composed of water-soluble components, particles mainly composed of insoluble material (i.e. insoluble particles with only very thin coatings of soluble material), and mixed particles (i.e. soluble material with inclusions of insoluble particles). MADE3 solves equations for the number concentration and for the mass concentrations of the J different aerosol species in each mode. MADE3 uses fixed mode widths σ_g, expressed in terms of geometric standard deviations of the lognormal modes, of 1.7, 2.0, and 2.2 for the Aitken, accumulation, and coarse modes, respectively. The median diameter $\tilde{D}_{g,k}$ of mode k is calculated from the mass concentrations $m_{a,k}$ of the species in that mode, assuming spherical particles:

$$\tilde{D}_{g,k} = \left[\frac{6V_k}{\pi N_k} \exp\left(-\frac{9}{2} \ln^2 \sigma_{g,k} \right) \right]^{\frac{1}{3}} \quad , \tag{3.1}$$

where

$$V_k = \sum_{j=0}^{J} \frac{m_{j,k}}{\rho_j} \quad , \tag{3.2}$$

is the particle volume concentration in mode k, and ρ_j is the density of species j (e.g. $2500\,\mathrm{kg\,m^{-3}}$ for mineral dust).

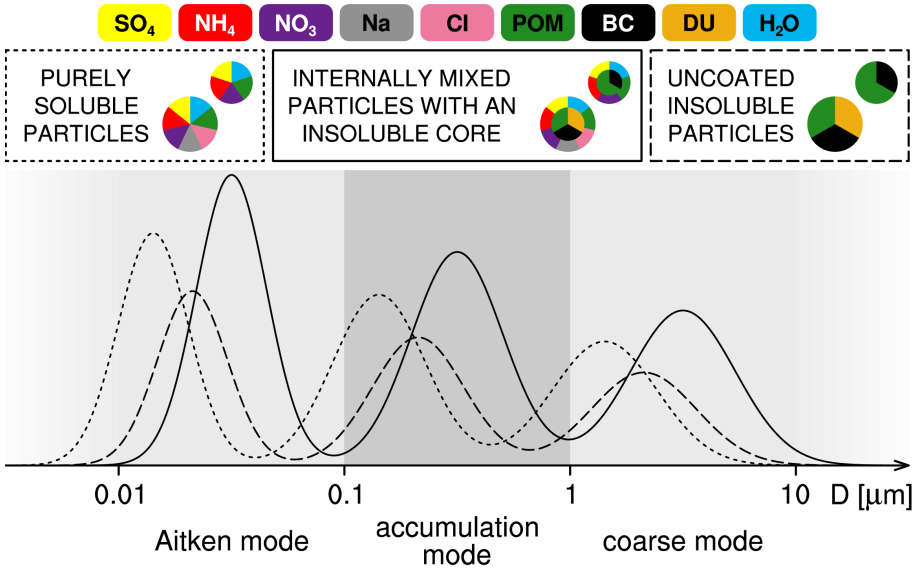

Figure 3.1: Schematic representation of the MADE3 submodel, as shown in Kaiser et al. (2019). The colours represent the different chemical components. The dotted, solid, and dashed lines correspond to the different mixing states (soluble, mixed, and insoluble, respectively). Grey shadings are to visually separate typical Aitken, accumulation and coarse mode sizes.

3.1.2 Aerosol processes

MADE3 simulates aerosol microphysical processes, calculates changes of particle number concentration, size distribution, and particle composition induced by these processes and solves the aerosol dynamics equations by applying analytical approximations and process-specific numerical solvers. A detailed description of this approach can be found in Kaiser et al. (2014) and Kaiser (2016). The following aerosol processes are simulated by MADE3:

- Gas-particle partitioning of semi-volatile species includes ammonia (NH_3/NH_4), nitric acid (HNO_3/NO_3), hydrochloric acid (HCl/Cl), and water (H_2O), and is simulated by the thermodynamic equilibrium model EQSAM (EQuilibrium Simplified Aerosol Model; Metzger et al., 2002), extended by flux limitations accounting for the large equilibrium timescales of coarse mode particles.
- Condensation of sulfuric acid (H_2SO_4) and low-volatile secondary organic aerosol species is treated by calculating the corresponding condensation fluxes.
- Coagulation of particles and resulting number and mass concentration changes are calculated for each mode, utilizing Brownian coagulation theory.
- New particle formation includes the nucleation of H_2SO_4-H_2O droplets and their subsequent growth.
- The ageing of insoluble particles, i.e. the development of a coating of soluble components, is explicitly represented in MADE3 as the transfer from insoluble to mixed modes, if the soluble mass fraction is larger than 10 %.

Other processes influencing the modelled aerosol include emission, transport, scavenging, deposition and sedimentation. However, these are not calculated by the submodel MADE3, but are treated by other submodels within the framework of the global EMAC model (see Sect. 3.2).

3.2 The atmospheric chemistry general circulation model EMAC

The aerosol submodel MADE3 is employed as part of the global numerical chemistry and climate simulation system EMAC (ECHAM/MESSy Atmospheric Chemistry (EMAC) general circulation model, Jöckel et al., 2010). EMAC uses the 2nd version of the Modular Earth Submodel System (MESSy) to link multi-institutional computer codes. The MESSy submodels (e.g. MADE3) describe various tropospheric and middle atmosphere processes. The core atmospheric model is the ECHAM5 (5th generation European Centre Hamburg) general circulation model (Roeckner et al., 2006). In the following, the basic settings of EMAC and the submodels relevant for this thesis are briefly described.

3.2.1 Basic settings

In this work EMAC is applied in three different model resolutions, namely T42L19, T42L31, and T63L31 with spherical truncations of T42 (corresponding to a quadratic Gaussian grid of approx. 2.8 by 2.8 degrees in latitude and longitude) or T63 (approx. 1.9 by 1.9 degrees), respectively, and with 19 or 31 vertical hybrid pressure levels up to 10 hPa. Model time steps for these resolutions are 30 minutes, 20 minutes, and 12 minutes, respectively, and the temporal resolution for most simulation output is chosen as 11 or 12 hours. Some simulation output is generated every hour for comparisons with observational data at higher temporal resolution. Most simulations were performed in nudged mode, i.e. wind divergence and vorticity, temperature, as well as the logarithm of the surface pressure were relaxed towards ECMWF reanalyses (ERA-Interim; Dee et al., 2011) for the corresponding years. This is important for episodic comparisons with observational campaigns but also reduces the simulated time necessary to detect significant effects between model simulations. Free-running model simulations would create much more internal noise and therefore require more computation time for these comparisons. An Overview of the MESSy submodels applied in this work is presented in Table 3.1.

3.2.2 Emissions

The emission setup is based in large parts on the setup described in Kaiser et al. (2019). Emissions are grouped into prescribed offline emissions and online emissions. The latter are calculated from model variables such as wind speed, according to parametrizations. Prescribed offline emissions include volcanic sulfur (Dentener et al., 2006), terrestrial DMS (Spiro et al., 1992), natural SOA precursors (Guenther et al., 1995), as well as anthropogenic and biomass burning emissions. In contrast to Kaiser et al. (2019), where prescribed monthly anthropogenic and biomass burning emissions were representative of the year 2000 (Lamarque et al., 2010), here, transient prescribed emissions matching the simulated time period are used. This is important for direct comparability of the model results with observation campaigns. For the transient monthly anthropogenic emissions, a combination of ACCMIP[1], for years prior 2000, and RCP8.5[2] data, for years after 2000, are

[1] Atmospheric Chemistry and Climate - Model Intercomparison Project (Lamarque et al., 2010)
[2] Representative Concentration Pathway leading to a RF of 8.5 Wm^{-2} (Riahi et al., 2007, 2011)

Table 3.1: Overview of the MESSy submodels applied in this work as part of the EMAC model. Additional details and information can be found on the MESSY webpage under `www.messy-interface.org`, last access: 2 February, 2021.

Submodel	Function	Reference
AEROPT	Calculation of aerosol optical properties, such as optical thickness or single scattering albedo	Dietmüller et al. (2016)
CLOUD	Formation of clouds and precipitation	Roeckner et al. (2006)
CONVECT	Calculation of convective transport of air parcels	Tost et al. (2006b)
CVTRANS	Convective gas-phase and aerosol tracer transport	Tost (2006)
DDEP	Dry deposition of trace gases and aerosols	Kerkweg et al. (2006a)
H2O	Initialization of water vapour and control of feedbacks with humidity	Jöckel et al. (2006)
JVAL	Calculation of photolysis rates, i.e. the rates of dissociation of atmospheric molecules in the sunlight	Sander et al. (2014)
LNOX	Parametrization of NO_x produced by lightning	Tost et al. (2007)
MADE3	Aerosol microphysical processes	Kaiser et al. (2014)
MECCA	Calculation of tropospheric and stratospheric chemical reactions	Sander et al. (2011)
OFFEMIS	Reading gas and particle emission fluxes from prescribed fields	Kerkweg et al. (2006b)
ONEMIS	Online calculation of gas and particle emissions (e.g. wind-driven DU emissions)	Kerkweg et al. (2006b)
OROGW	Parametrization of subgrid scale orographic gravity waves)	Joos et al. (2008)
PTRAC	Initialization of user-defined prognostic tracers	Jöckel et al. (2008)
RAD	Treatment of radiative processes	Dietmüller et al. (2016)
S4D	Interpolation of model output along the track of a moving platform (e.g. aircraft, ship)	Jöckel et al. (2010)
SCAV	Cloud and precipitation processing of aerosols and trace gases	Tost et al. (2006a)
SEDI	Sedimentation of aerosol particles	Kerkweg et al. (2006a)
SURFACE	Calculation of surface properties (e.g. surface temperature)	Jöckel et al. (2016)
TNUDGE	Nudging tracers according to user-defined fields	Kerkweg et al. (2006b)
TROPOP	Calculation of the heights of the tropopause and the planetary boundary layer	Jöckel et al. (2006)

applied. Biomass burning emissions are taken from the Global Fire Emissions Database version 4 (GFED4s, van der Werf et al., 2017). Oceanic DMS emissions are calculated online according to the formulation by Liss and Merlivat (1986), depending on wind speed and sea surface temperature. Kaiser et al. (2019) used prescribed monthly-mean dust emissions from the AeroCom[3] offline climatology, described in Dentener et al. (2006). In contrast, here the dust parametrization developed by Tegen et al. (2002) is applied that calculates dust emissions online for every model time step, according to the wind speed. This dust emission parametrization is described in Sect. 3.3, where also a detailed comparison between these two different dust emission representations is presented. An overview of the emission setup applied in this thesis is shown in Table 3.2.

Table 3.2: Summary of the emission setup used for the EMAC/MADE3 simulations. The MADE3 species and modes for each Emission sector are shown. The mode naming convention follows Kaiser et al. (2014) and Kaiser et al. (2019): the indices "k", "a", and "c" specify the Aitken, accumulation, and coarse mode, respectively, and "s", "m", and "i" as the second index specifies the soluble, mixed, and insoluble mode, respectively. The emission sectors are abbreviated as follows: AIR (aviation), ANT (anthropogenic non-traffic), AWB (agricultural waste burning), LAND (land transport), SHIP (shipping), and BB (biomass burning).

Emission sector	MADE3 species and modes	Reference
Natural emissions		
Sea spray (online)	Na, Cl: as, cs	Guelle et al. (2001)
Mineral dust (online)	DU: ai, ci	Tegen et al. (2002)
Volcanic	SO_4: ks, as	Dentener et al. (2006)
Anthropogenic and biomass burning emissions		
AIR	BC: ki, km, ai, am	years prior 2000: ACCMIP, Lamarque et al. (2010)
ANT	BC, POM: ai, am	
AWB	BC, POM: ai, am SO_4: am	
LAND	BC, POM: ki, km, ai, am SO_4: ks	years after 2000: RCP8.5, Riahi et al., (2007; 2011)
SHIP	BC, POM: ki, km, ai, am SO_4: km, am	
BB	BC, POM: ai, am SO_4: am	GFED4s (van der Werf et al., 2017)

[3] Aerosol Comparison between Observations and Models, `https://aerocom.met.no/`, last access: 12 March, 2021.

3.2.3 Transport

Particle transport due to advection and vertical diffusion is calculated by the base model ECHAM5 and convective transport by the submodel CVTRANS. Horizontal diffusion has only neglectable influences for the scales of model grid boxes and is not considered. The advection scheme relies on the approach by Lin and Rood (1996). During convective events, the submodel CONVECT assumes that tracers travel with the convected air masses. Tracer fluxes are coupled to convective air mass fluxes via the submodel CVTRANS.

3.2.4 Gas phase chemistry

The submodel MECCA (Module Efficiently Calculating the Chemistry of the Atmosphere) is used to simulate atmospheric gas-phase chemistry. As described in Kaiser et al. (2019), a simplified tropospheric chemistry scheme created by Lauer et al. (2007) is employed to improve computational efficiency. This scheme includes 34 gas species and 60 chemical reactions to describe the chemistry of NO_x-HOx-CH_4-CO-O_3 and the tropospheric sulfur cycle. Additionally, only VOC species with one carbon atom are included. While reactions of trace gases with or on aerosol particle surfaces are not considered, reactions on cloud droplet surfaces are taken into account (see Sect. 3.2.6).

3.2.5 Cloud formation

Stratiform clouds

The CLOUD submodel provides the platform for selecting different schemes and representations for stratiform, large-scale clouds. These schemes vary in complexity and are typically differentiated as one-moment and two-moment schemes. One-moment schemes predict only total cloud water or ice, while in two-moment schemes also cloud droplet and ice crystal numbers are calculated, enabling the quantification of climatic impacts of aerosol-induced cloud modifications. The standard ECHAM5 single-moment cloud scheme (Roeckner et al., 2003) is applied in this work. Additionally, for analyses concerning INPs and related cloud modifications a two-moment scheme is applied here. This two-moment cloud scheme was originally developed by Kuebbeler et al. (2014) and coupled to the Hamburg Aerosol Model (HAM, Stier et al. 2005) within the framework of the ECHAM5 model. Here, the version of this scheme coupled to MADE3 as part of the EMAC model is applied, as described and evaluated in Righi et al. (2020). The scheme describes aerosol-driven formation of cloud droplets and ice crystals, as well as rain and snow formation, condensational and depositional growth of cloud particles, evaporation of cloud water and rain, sublimation and melting of cloud ice and snow, freezing of cloud water, and sedimentation of cloud ice (Lohmann et al., 2007, 2008). It solves prognostic equations for cloud liquid water content, ice water content, cloud droplet and ice crystal number concentrations. The cloud cover is calculated according to the Sundqvist scheme (Sundqvist et al., 1989), assuming partial covered model grid boxes above a critical threshold for relative humidity and full cloud coverage at saturation. Sub-grid scale variability of vertical updraft velocities that cannot be resolved with the coarse model resolution, are accounted for by adding a turbulent component ω_t to the large-scale vertical velocity

ω_{ls}. ω_{t} is assumed to be proportional to the square root of the turbulent kinetic energy (TKE):

$$\omega = \omega_{\mathrm{ls}} + \omega_{\mathrm{t}} + \omega_{\mathrm{gw}} = \omega_{\mathrm{ls}} + c\sqrt{\mathrm{TKE}} + \omega_{\mathrm{gw}} \quad . \tag{3.3}$$

Here, c is a constant and chosen as $c = 1.33$ for the case of liquid and mixed phase clouds, and $c = 0.7$ for cirrus clouds, as described in Lohmann et al. (2007) and in Righi et al. (2020). The effect of gravity waves is treated by adding the additional term ω_{gw} to the total vertical velocity in Eq. 3.3. This component is calculated by the orographic gravity wave submodel (OROGW) in EMAC, based on (Joos et al., 2008).

The cloud scheme treats liquid, mixed-phase and cirrus clouds using dedicated microphysical parametrizations. Aerosol-driven formation of cloud droplets is calculated following the parametrization by Abdul-Razzak and Ghan (2000). The formation of ice crystals is described by two different parametrizations for mixed phase and cirrus clouds. Ice nucleation in the mixed phase regime considers deposition nucleation of dust particles and immersion freezing of BC and dust particles following the description of Lohmann and Diehl (2006) and Hoose et al. (2008). Deposition nucleation of BC is considered less important and neglected in the mixed phase regime.

In the cirrus regime, the parametrization of Kärcher et al. (2006) describes the formation of ice crystals considering the competition between various ice formation mechanisms for the available supersaturated water vapour, i.e. homogeneous freezing of solution droplets, deposition and immersion nucleation induced by INPs, and the growth of pre-existing ice crystals. As stated previously in Sect. 2.3, deposition nucleation may in fact be the mechanism of pore condensation and freezing (e.g., Marcolli, 2014; Wagner et al., 2016; Marcolli, 2017). In each of the heterogeneous freezing modes the ice-nucleation properties of the INPs are represented by two parameters, namely the activated fraction (f_{act}) of ice nucleating particles and the critical supersaturation (S_c), at which the freezing process is initiated.

Here, ice nucleation induced by DU, BC (all sources except aviation), BC from aviation (BCair), glassy organic particles, and crystalline ammonium sulfate is considered. A summary of the freezing properties of these INPs is presented in Table 3.3. For ammonium sulfate and organic INPs only few studies exist that consider specific phase states of these INPs, i.e. particles in a crystalline or glassy state. In this work, the corresponding freezing properties for crystalline ammonium sulfate and glassy organics are assumed according to Ladino et al. (2014) and Ignatius et al. (2016), respectively. Dust immersion freezing was also only rarely investigated in laboratory experiments. In the original Kuebbeler et al. scheme, dust immersion freezing with $S_c = 1.3$ was assumed according to Möhler et al. (2008). Here a slightly higher value of $S_c = 1.35$ is assumed according to Kulkarni et al. (2014), where the mixed-phase regime at $T = -35$°C is considered, with sulfuric acid coatings around dust particles. Despite the mixed-phase temperature, this value is used as a more conservative assumption in the cirrus regime, as Möhler et al. (2008) only considers dust particles with organic coatings at very low temperatures (-68°C $< T < -63$°C). For DU deposition freezing, f_{act} is calculated according to the parametrization developed by Kuebbeler et al. (2014), depending on the supersaturation with respect to ice (S_i) and the temperature. For BC freezing there exist a large number of different studies considering soot particles from a variety of different sources. For example, Koehler et al. (2009) analysed different soot types, including soot resulting from burning aviation kerosene, and observed ice nucleation below the homogeneous freezing threshold. Kanji et al. (2011) reported ice nucleation on graphite soot at supersaturations S_c between 1.3 and 1.5, while

Table 3.3: Freezing properties of ice nucleating particles in the cirrus regime assumed in this study, i.e. critical supersaturation S_c and activated fraction f_{act} at the freezing onset. Additionally, a larger value for f_{act} in the centre of the spectrum is assumed (as an alternative to the onset value for sensitivity studies), representing roughly the middle point between the onset and the homogeneous freezing threshold. S_i is the supersaturation with respect to ice. In addition to onset and central f_{act}, values for f_{act} at about $S_i = 1.4$ are used for the comparison of different INPs in some experiments.

Freezing mode		S_c	f_{act} onset	f_{act} central	f_{act} at $S_i = 1.4$	Reference
DU deposition	$T \leq 220\,\text{K}$	1.10	$\exp[2\,(S_i - S_c)] - 1$		0.822	Kuebbeler et al. (2014)
	$T > 220\,\text{K}$	1.20	$\exp[0.5\,(S_i - S_c)] - 1$		0.105	
AmSu		1.25	0.001	0.05	0.02	Ladino et al. (2014)
glPOM		1.30	0.001	0.06	0.08	Ignatius et al. (2016)
DU immersion		1.35	0.01	0.065	0.1	Kulkarni et al. (2014)
BC aviation		1.40 [a]	0.001	0.006	0.003	e.g. Kulkarni et al. (2016)
BC other sources		1.40 [a]	0.001	0.006	0.003	e.g. Kulkarni et al. (2016)

[a] For technical reasons the S_c values of BC and BCair are slightly below $S_c = 1.4$ and slightly different compared to each other (i.e. 1.39 and 1.391, for BC and BCair, respectively) to realize their freezing at about $S_c = 1.4$ in the parametrization.

Chou et al. (2013) and Kulkarni et al. (2016) measured S_c around 1.4 for fresh and aged diesel soot particles. Recent studies observed BC ice nucleation at cirrus temperatures and attributed this to the pore condensation and freezing mechanism rather than deposition freezing (e.g., Marcolli, 2017; Mahrt et al., 2018; David et al., 2019; Mahrt et al., 2020; Nichman et al., 2019). This was shown to be related to the cloud processing of soot particles and the resulting enhancement of their freezing potential by lowering S_c. In this thesis a value of $S_c = 1.4$ for BC (and aviation BC) ice nucleation is assumed in accordance with the wide range of results from measurements.

The Kärcher et al. (2006) parametrization treats the different freezing modes in the order of their freezing threshold relative humidity expressed as critical supersaturation S_c, i.e. starting with the heterogeneous freezing of INPs with the lowest S_c and ending with homogeneous freezing. During the vertical updraft and the resulting cooling of an air parcel the supersaturation with respect to ice (S_i) increases. This increase is compensated by the consumption of water vapour via depositional growth of newly formed or pre-existing ice crystals. The reduction of supersaturated water vapour by depositional growth of pre-existing ice crystals is accounted for by introducing a fictitious downdraft that reduces the vertical velocity in Eq. 3.3. If the cooling rate is still large enough after this reduction, heterogeneous and homogeneous freezing, and competition processes can take place. Ice crystals larger than 200 µm are transferred to snow crystals that are subsequently removed by precipitation, melting, or sublimation (Levkov et al., 1992). The output of the parametrization includes the number concentration of ice crystals (N_{ice}) per freezing mode and their size (R_{ice}).

Convective clouds

Convective clouds need to be parametrized in large-scale global models, as convection processes occur on scales much smaller than the size of model grid boxes (a few tens of kilometres compared to a few hundred kilometres, for the grid resolutions T42 and T63, applied in this work). These parametrizations account for liquid and ice water content,

fractional cloud cover, precipitation, and vertical air transport in convective clouds. Different convection schemes can be selected in EMAC via the submodel CONVECT. Here, the original ECHAM5 scheme, based on the studies of Tiedtke (1989) and Nordeng (1994), with modifications by Brinkop and Sausen (1997), is used. Convective tracer transport is treated by the EMAC submodel CVTRANS.

3.2.6 Precipitation processing of aerosols

Wet deposition of aerosols via scavenging by clouds and precipitation, as well as cloud and precipitation chemistry, are treated by the EMAC submodel SCAV. Scavenging is the process of aerosol uptake via cloud droplets, ice crystals and precipitation. If the aerosol particles are removed from the atmosphere via precipitation interactions, this process is called wet deposition. SCAV considers nucleation and impaction scavenging for both cloud droplets and ice crystals. Nucleation scavenging, in this context, refers to the actual nucleation of cloud droplets and ice crystals but also includes scavenging due to Brownian motion. Impaction scavenging in SCAV includes the processes of aerosol uptake by precipitation, i.e. Brownian motion of aerosol particles towards falling hydrometeors, as well as impaction and interception of aerosol particles by hydrometeors. SCAV also includes an explicit treatment of aqueous phase chemistry, involving 35 chemical species and 45 reactions. For instance, a major fraction of aerosol SO_4 is produced via the aqueous phase. Also, heterogeneous processes like the formation of aqueous HNO_3 from gaseous N_2O_5 on the surface of cloud droplets are considered. More details on the chemical reactions of SCAV can be found in the supplement of Kaiser et al. (2019). The original description of SCAV is presented in Tost et al. (2006a). For the application with MADE3 the SCAV submodel was extensively modified as described in detail in Kaiser (2016) and Kaiser et al. (2019).

3.2.7 Dry deposition and sedimentation

Dry deposition of trace gases and aerosols is calculated by the submodel DDEP, described in detail by Kerkweg et al. (2006a). Dry deposition includes the processes of diffusive transport towards the surface and the uptake by the surface, resulting, in addition to precipitation scavenging, in a removal of aerosol particles and trace gases from the atmosphere. Dry deposition velocities depend on the near-surface turbulence and the physical and chemical properties of the surface cover. DDEP considers the different soil types of water, ice, snow, bare soil, vegetation, and wet surfaces (wet soil and vegetation).

Sedimentation, or gravitational settling, is an additional removal process of atmospheric aerosol and is most efficient for coarse mode particles. Sedimentation velocities are calculated in the MESSy submodel SEDI, as described in Kerkweg et al. (2006a).

3.3 Mineral dust emission schemes

Parts of this section appeared similarly in my recent publication (C. G. Beer, J. Hendricks, M. Righi, B. Heinold, I. Tegen, S. Gro, D. Sauer, A. Walser, and B. Weinzierl. Modelling mineral dust emissions and atmospheric dispersion with MADE3 in EMAC v2.54. *Geosci. Model Dev.*, 13(9):4287–4303, 2020. doi:10.5194/gmd-13-4287-2020).

To correctly simulate mineral dust in global models, a reliable representation of the particle numbers, the size distribution and the global distribution of dust particles is necessary (e.g., Shao et al., 2011). As mineral dust is a primary aerosol, dust abundance and distribution in the atmosphere are strongly related to its emissions. In the following, the two different emission schemes for mineral dust, which are applied in this study, are described: a prescribed (offline) climatology of monthly-mean emissions and an online calculation of wind driven emissions.

3.3.1 Offline dust emission climatology

A simple and straightforward way of representing dust emissions in AC-GCMs is the use of climatologies, i.e. prescribed monthly-mean dust emissions for a specific year (e.g., de Meij et al., 2006; Liu et al., 2007). The AeroCom project[4] led to the development of a global dust emission climatology (Ginoux et al., 2001, 2004; Dentener et al., 2006), that has been widely used in global modelling studies (e.g., Huneeus et al., 2011). To simplify the description of dust emissions in global models, the climatology prescribes monthly-mean emission rates for the year 2000, neglecting the variation of emission fluxes on shorter time scales. The offline AeroCom climatology was used in previous model studies with MADE3 (or its predecessors) in EMAC, to represent mineral dust emissions (Aquila et al., 2011; Righi et al., 2013, 2015, 2016; Kaiser et al., 2019).

3.3.2 Online dust emission parametrization

Dust emissions are strongly influenced by meteorology resulting in high temporal variability from day to day, caused, for instance, by dust storms (e.g., Prakash et al., 2015) and also show large long-term (e.g. year-to-year) variations (Mahowald et al., 2010; Banks et al., 2017). The AeroCom dust climatology, however, is representative of the year 2000, which was characterized by relatively low dust emissions (Weinzierl et al., 2017). It has been argued that using monthly-mean dust climatologies in AC-GCMs could lead to a misrepresentation of strong dust outbreaks, resulting in a negative bias of model dust concentrations during these episodes compared to observations (Aquila et al., 2011; Huneeus et al., 2011; Kaiser et al., 2019). Additionally, several studies report a strong dependence of the number concentrations of emitted dust particles and their size distribution on the wind friction velocity (Alfaro et al., 1997; Ishizuka et al., 2008; Shao et al., 2020), influencing the intensity of saltation processes at dust emission (see Sect. 2.1.1.2).

[4] Aerosol Comparison between Observations and Models; see also `https://aerocom.met.no/`, last access: 12 March, 2021

As an alternative to offline dust emission climatologies, online parametrizations have been developed that account for temporal variability by calculating dust emissions from local surface wind velocities in each model time step (e.g., Tegen et al., 2002; Balkanski et al., 2004). Several online dust emission schemes have been successfully implemented in AC-GCMs and have been shown to adequately simulate global dust distribution patterns on daily, seasonal and multi-annual timescales (Stier et al., 2005; Astitha et al., 2012; Gläser et al., 2012). However, online dust parametrizations also suffer from drawbacks. For example, they need to be tuned for every model setup according to a reference emission climatology by setting specific tuning parameters employed in the calculation of dust emission fluxes (e.g., Tegen et al., 2004). This is necessary to keep the total dust emissions comparable between different model simulations. In this work, the online dust emission scheme developed by Tegen et al. (2002) has been applied to account for highly variable wind-driven dust emissions and strong emission episodes.

3.3.2.1 The Tegen et al. (2002) emission scheme

The Tegen et al. (2002) dust parametrization calculates dust emissions online for every model time step. Dust emissions are calculated for 192 internal dust size classes ranging from 0.2 µm to 1300 µm diameter according to the simulated 10-meter wind velocity and prescribed external input fields of dust source areas, soil types and vegetation cover (for details see Tegen et al., 2002; Stier et al., 2005; Cheng et al., 2008; Gläser et al., 2012). The horizontal soil particle flux (HF) is calculated for each dust size class i as:

$$\mathrm{HF}(i) = \frac{\rho_{\mathrm{air}}}{g} \cdot u^3 \cdot \left(1 + \frac{u_{\mathrm{thr}}(i)}{u}\right) \cdot \left(1 - \frac{u_{\mathrm{thr}}^2(i)}{u^2}\right) \cdot s_i \ , \ \text{ if } u > u_{\mathrm{thr}}(i) \ , \ (\text{otherwise } \mathrm{HF}(i) = 0) \ , \tag{3.4}$$

with the density of air ρ_{air}, the gravitational constant g, the relative surface area coverage for each size class s_i, the wind friction velocity u, which is calculated from the prognostic 10-meter wind speed, and the threshold friction velocity $u_{\mathrm{thr}}(i)$. Only for velocities exceeding this threshold, dust emissions can occur. The vertical emission fluxes $\mathrm{VF}(i)$ are calculated from the horizontal particle fluxes according to:

$$\mathrm{VF}(i) = \alpha \cdot I_\Theta \cdot f(\mathrm{LAI}) \cdot \mathrm{HF}(i) \ , \tag{3.5}$$

where α accounts for the soil texture characteristics, I_Θ is zero if the upper layer soil moisture is at field capacity and 0.99 otherwise, and f is a function of the Leaf Area Index (LAI) describing the vegetation cover.

To account for the lognormal representation of the aerosol size distribution in modal aerosol models like MADE3, the vertical emission fluxes of the single size classes are summed according to accumulation and coarse size ranges in the Tegen et al. (2002) scheme and assigned to the MADE3 insoluble accumulation and coarse mode, respectively. As MADE3 also requires the corresponding number emissions, these are derived from mass emissions assuming a lognormal size distribution with count median diameter $D = 0.42$ µm and geometric standard deviation $\sigma_{\mathrm{g}} = 1.59$ for the accumulation mode, and $D = 1.3$ µm, $\sigma_{\mathrm{g}} = 2.0$ for the coarse mode, respectively, following the AeroCom recommendations (Dentener et al., 2006). The corresponding conversion function (M2N) for lognormal distributions is given as (e.g., Seinfeld and Pandis, 2016):

$$\mathrm{M2N}_i(D_i, \sigma_{\mathrm{g},i}) = \frac{6}{\pi} \frac{1}{D_i^3 \ \exp(4.5 \ln^2 \sigma_{\mathrm{g},i}) \ \rho} \ , \tag{3.6}$$

with the median diameter D_i and geometric standard deviation $\sigma_{g,i}$ of the lognormal size distribution for mode i, and the density $\rho = 2500\,\mathrm{kg/m^3}$ of mineral dust.

In a sensitivity experiment (T42L31TegenS), the effect of using a different assumption for the dust size distribution upon emission was tested (results in Sect. 4.1.3), i.e. by varying the parameters for converting dust mass to number emissions. This leads to changes in the number concentration of emitted particles (while the mass emission remains the same) and can subsequently influence dust concentrations in the atmosphere. To this purpose, the dust size distribution measured during the SAMUM-1 dust campaign (Weinzierl et al., 2009, 2011) was used. This campaign took place in 2006, in southern Morocco, close to the Sahara desert. It is therefore especially suited for this sensitivity study, as it focuses on dust near the source regions in the Sahara. In Weinzierl et al. (2011) the dust size distribution is represented by four modes with D_i, $\sigma_{g,i}$, and the number concentration N_i, $i = 1, \ldots, 4$. The mass concentration m_i of each of these four modes can be calculated using the factor $\mathrm{M2N}_i^{-1}$. For the online dust emission scheme a bimodal distribution is required. Therefore, the two smaller sized modes and the two larger ones are combined, in order to calculate the conversion factors for the accumulation ($\mathrm{M2N_{acc}}$) and the coarse mode ($\mathrm{M2N_{coa}}$) of the required bimodal distribution,

$$\mathrm{M2N_{acc}} = \frac{N_1 + N_2}{m_1 + m_2}, \qquad \mathrm{M2N_{coa}} = \frac{N_3 + N_4}{m_3 + m_4}\ . \tag{3.7}$$

An overview of the mass-to-number conversion factors (M2N) for the different online dust model setups is shown in Table 3.4. Additionally, Fig. 3.2 compares the two number size distributions of the reference and the sensitivity study. Wind-driven online dust emissions need to be tuned for each model setup, to keep emissions comparable and within reasonable ranges. The tuning procedure is described in the following section.

Table 3.4: Summary of wind stress threshold tuning parameter (t_{wind}), orographic threshold for dust emission tuning (t_{orogr}), mass-to-number conversion factors for accumulation and coarse mode ($\mathrm{M2N_{acc}}$, $\mathrm{M2N_{coa}}$), and resulting global and northern Africa (0°– 40° N and 20° W – 50° E) dust emissions of the year 2000, for the different online dust model setups, after the tuning procedure. T42L31TegenS differs from T42L31Tegen only in assuming a different size distribution for emitted dust (according to measurements from the SAMUM-1 dust campaign; Weinzierl et al., 2009, 2011).

Model setup	t_{wind}	t_{orogr} (m)	$\mathrm{M2N_{acc}}$ ($\mathrm{kg^{-1}}$)	$\mathrm{M2N_{coa}}$ ($\mathrm{kg^{-1}}$)	Global emissions ($\mathrm{Tg\,a^{-1}}$)	Northern Africa emissions [a] ($\mathrm{Tg\,a^{-1}}$)
T42L19Tegen	0.72	2500	3.92×10^{15}	4.0×10^{13}	2900	1210
T42L31Tegen	0.69	4000	3.92×10^{15}	4.0×10^{13}	1990	1230
T42L31TegenS	0.69	4000	5.79×10^{16}	1.16×10^{13}	2000	1240
T63L31Tegen	0.775	1770	3.92×10^{15}	4.0×10^{13}	1770	1270

[a] As the Tegen dust emissions were tuned to match AeroCom emissions over northern Africa ($1230\,\mathrm{Tg\,a^{-1}}$), these values are almost identical.

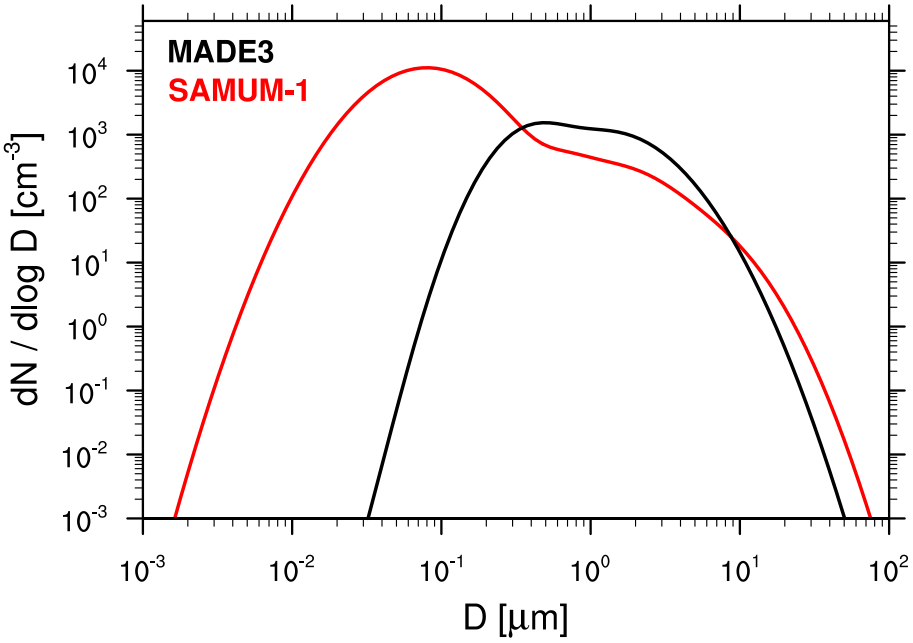

Figure 3.2: Number size distributions of emitted mineral dust assumed in MADE3, for the reference case (MADE3, black) and the sensitivity study (SAMUM-1, red). The size distributions were calculated for the year 2006 and the region of 0°– 40° N and 20° W – 0° E, which includes the Western Sahara where the SAMUM observations took place. For the SAMUM-1 distribution, median diameters and geometric standard deviations were taken from Weinzierl et al., 2011 (their Table 5). As shown in Beer et al. (2020, Fig. S2).

3.3.2.2 Dust emission tuning

In order to keep total wind-driven dust emissions comparable between different model simulations, dust emissions were tuned in the following way. As a reference for dust emissions we use the AeroCom climatology (Dentener et al., 2006), as this dataset is well evaluated and widely used in global modelling studies. We apply a global correction for online dust emissions by adjusting the wind friction velocity threshold for dust emissions by multiplication with the scaling factor t_{wind}, as described in Tegen et al. (2004). Only for velocities exceeding this scaled threshold, dust emissions can occur. A higher (lower) threshold therefore results in lower (higher) dust emissions. The emissions were tuned for the year 2000 in every model simulation, aiming to reproduce AeroCom total yearly emissions in the Saharan and Arabian desert region of 0°– 40° N and 20° W – 50° E, which amount to an annual dust emission of roughly 1200 Tg. This region was selected because it is the largest dust source on the globe and because the SALTRACE dust campaign focuses on dust transport from northern Africa to the Caribbean, which is a central point for model evaluation in this study. The resulting values for the wind stress threshold tuning parameter (t_{wind}) are shown in Table 3.4.

Furthermore, an additional correction to dust emissions was necessary in the model, since it simulates unrealistically high emissions in a few model grid boxes close to the Himalaya region. These artefacts dominate global dust emissions and are – e.g. for the T42L19 resolution – up to 100 times higher than emission peaks in the Sahara. In this critical region, dust sources, namely the Taklamakan desert, and areas of high surface winds (resulting from pronounced orographic gradients at the northern slope of the Himalayas) are located within the same model grid box. Hence, due to the relatively low spatial resolution, these areas overlap in the model, although they are spatially disjunct

in reality. This conflict results in unrealistically high dust emissions in the corresponding grid boxes and was also reported by Gläser et al. (2012) in a model study with EMAC using the Tegen et al. (2002) dust scheme. They further showed that these artefacts vanish for horizontal grid resolutions of and above T85 (approx. 1.4 by 1.4 degrees in latitude and longitude). As such a high resolution would be computationally too expensive and time consuming for the simulations in this study and the planned applications of this model setup, a different solution is chosen here.

In order to remove the high emission artefacts in the Himalaya region prior to the tuning procedure described above, the corresponding grid boxes are excluded from the calculation of dust emissions by setting an upper threshold for orography. Above this threshold-height, emission fluxes are set to zero. The threshold value was adjusted for every model setup depending on the resolution, in order to target mostly the problematic grid boxes in the Himalaya region. Threshold values (t_{orogr}) for the three different model resolutions are shown in Table 3.4. This procedure affects also some other grid boxes that

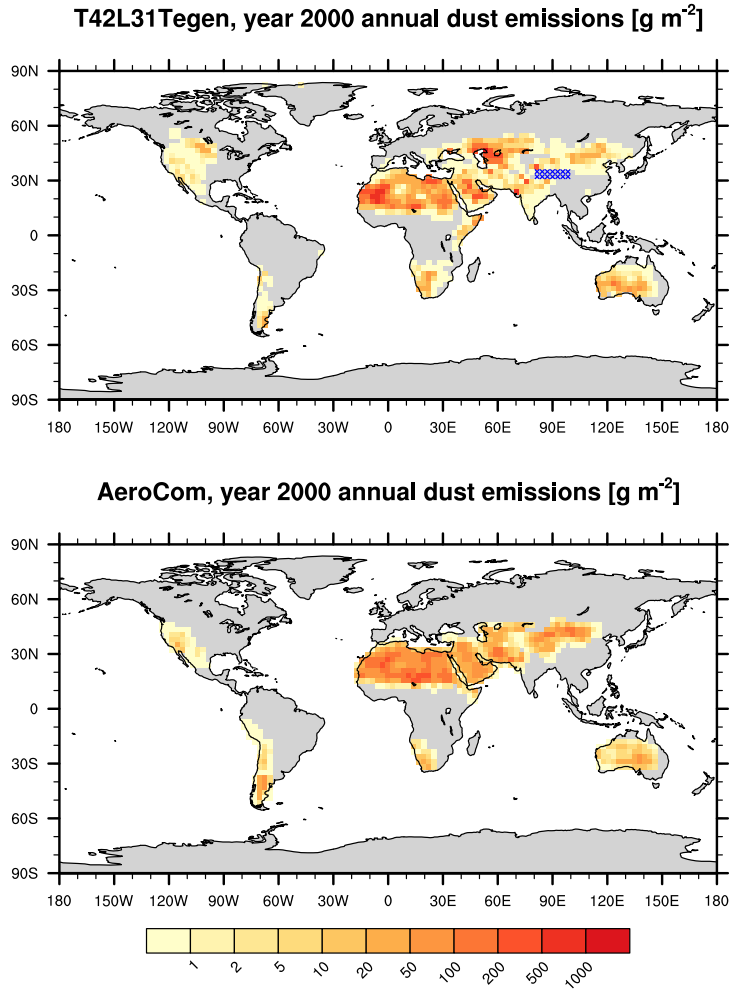

Figure 3.3: Global annual dust emissions in the T42L31Tegen (top) and T42L31AeroCom (bottom) setup. (Top) Emissions were corrected for artefacts in the Himalaya region and tuned according to AeroCom (for the region of 0° – 40° N and 20° W – 50° E). Blue crosses correspond to excluded grid boxes due to setting t_{orogr} to 4000 m (12 of these 14 boxes would otherwise have emitted dust). The tuning results in a total dust emission of 1230 Tg a^{-1} in the Sahara region and a total global dust emission of 1990 Tg a^{-1} for the year 2000. (Bottom) Aerocom dust emissions were used for the T42L31AeroCom setup and as a reference for tuning online calculated Tegen et al. (2002) dust emissions. The total global AeroCom dust emission is 1700 Tg a^{-1}. As shown in Beer et al. (2020, Fig. 2).

show no high emission artefacts, mainly in the T42L19 and T63L31 setups, due to the somewhat lower t_{orogr} compared with T42L31. However, these boxes are few and they correspond only to minor dust sources, mostly in the Tibetan Plateau. The numbers of dust emitting grid boxes that are excluded by setting t_{orogr} are 35, 12, 80, for the T42L19, T42L31, and T63L31 model setups, respectively. This procedure for tuning online dust emissions was also described and applied in Righi et al. (2020) and Beer et al. (2020).

The resulting tuned dust emissions of the year 2000 are shown in Fig. 3.3 for the T42L31Tegen setup. Total emissions over northern Africa were tuned to match total emissions in the AeroCom climatology (about $1200\,\mathrm{Tg\,a^{-1}}$). Total global dust emissions of $2000\,\mathrm{Tg\,a^{-1}}$ are also comparable to the AeroCom value ($1700\,\mathrm{Tg\,a^{-1}}$) and lie in the range of other model studies, which simulate dust emissions between $514\,\mathrm{Tg\,a^{-1}}$ and $4313\,\mathrm{Tg\,a^{-1}}$ (Huneeus et al., 2011).

The seasonal online dust emissions also compare reasonably well with the AeroCom climatology. However, the online emissions are strongest in the spring and summer months, while the AeroCom climatology shows the maximum in the winter season (see Fig. A.1 in the Appendix). This deviation may be a result of the calculation of wind-driven dust emissions, but could also be due to a possible atypical seasonal cycle for the year 2000. A summary of tuned dust emissions for all online dust model setups is shown in Table 3.4.

3.4 Implementation of additional ice nucleating particle tracers

In order to analyse the ice nucleation potential of additional INPs, which were previously not considered in EMAC-MADE3 (Righi et al., 2020), new aerosol tracers for these particles have been implemented. Here, tracers for BC from aircraft emissions (BCair), for glassy organic particles (glPOM), and for crystalline ammonium sulfate (AmSu) are considered.

3.4.1 Implementation of aircraft soot

An existing BC tracer for tagging BC emissions from different emission sectors was adapted to simulate BC from aviation emissions. This tracer (BCair) is implemented as additional MADE3 tracer similar to the standard BC tracer Kaiser et al. (2014, 2019). BCair is distributed in the same six modes as BC, namely insoluble and mixed Aitken, accumulation, and coarse mode. It has the same microphysical properties (density, molecular weight) and is subject to the same processes in the model as the standard BC tracer. Number and mass emissions of BC from aircraft are used to calculate BCair, while BC emissions from other sources are assigned to the standard BC tracer. Alternatively, BC from other emission sectors (e.g. land transport, shipping) can be traced with this approach, which could be a possible subject for future applications.

3.4.2 Implementation of glassy organics

Similar to BCair, a MADE3 tracer for glassy organic particles (glPOM) was included in addition to the standard POM tracer, considering emissions of natural SOA precursors taken from Guenther et al. (1995). The precursor gases include isoprene, monoterpenes and other VOCs, which are mainly emitted from tropical woodlands, especially rainforests. In analogy to Kaiser et al. (2019), following Dentener et al. (2006), it is assumed that natural terpenes are transformed to SOA with a constant yield of 15 %. The resulting SOA species are assumed to irreversibly condense as particulate organic matter on preexisting aerosol particles. To track SOA from natural terpenes the condensed mass is assigned to the glPOM tracer.

As only glassy organics with extremely high viscosities $\eta > 10^{12}\,\mathrm{Pa\,s}$ (Koop et al., 2011), were observed to be efficient INPs, a glass transition is considered for glPOM, depending on the ambient temperature T and the glass transition temperature T_g. For temperatures $T < T_g$ the particles are in a glassy state. T_g depends on the relative humidity and the chemical composition of the organic compound and can be determined experimentally.

Here, T_g is assumed according to citric acid, which is a common SOA proxy (Baustian et al., 2013). T_g in units of Kelvin is given in Baustian et al. (2013) for relative humidities RH between 0 % and 100 %:

$$T_g(\mathrm{RH}) = 277.14 - 0.33\,\mathrm{RH} - 0.01\,\mathrm{RH}^2 \tag{3.8}$$

3.4.3 Implementation of crystalline ammonium sulfate

In contrast to glPOM, crystalline ammonium sulfate (AmSu) requires the representation of a dedicated phase transition, including a hysteresis process depending on the history of the relative humidity (e.g., Koop et al., 2011). Crystallization of ammonium sulfate occurs at a lower relative humidity (efflorescence, ERH) than the transition from crystals to aqueous particles (deliquescence, DRH).

3.4.3.1 Ammonium sulfate tracers

As no phase state characterization is possible for MADE3 aerosol tracers, a different approach is applied here. Ammonium sulfate tracers are realized as passive aerosol number density tracers using the EMAC submodel PTRAC for prognostic or passive tracers, i.e. particle radius, density and mode width are fixed at predefined values. As the number concentration of INPs is the central quantity for ice nucleation processes, AmSu is implemented here as a number density tracer. In order to realize different assumptions for the representation of ammonium sulfate and to assess related uncertainties, three different PTRAC tracers are defined:

$\mathbf{AmSu_{mixS}}$: Crystalline ammonium sulfate particles with 100 nm particle radius and possible inclusions of other components. This represents typical MADE3 accumulation mode sizes for polluted air (i.e. mainly soot particles). The formulation of phase transitions, with efflorescence and deliquescence, is described below. For this tracer only grid boxes where the fraction of NH_4 and SO_4 dominates the total grid box mass, are considered.

$\mathbf{AmSu_{mixL}}$: Similar to $AmSu_{mixS}$ but for crystalline ammonium sulfate particles with 250 nm particle radius and inclusions of other components and . This represents larger accumulation mode particles consisting mainly of sea salt and coated mineral dust. Again, only grid boxes dominated by NH_4 and SO_4 are considered.

$\mathbf{AmSu_{ext}}$: Externally mixed crystalline ammonium sulfate (without inclusions) and 100 nm particle radius. This represents a control estimate for the crystalline ammonium sulfate particle number concentration, independent from the MADE3 representation of mixing state. Here, all available ammonium and sulfate mass in the accumulation mode is used, without the restriction to NH_4 and SO_4 dominated grid boxes.

These AmSu tracers are calculated according to NH_4 and SO_4 input masses from the MADE3 soluble and mixed accumulation modes. As $AmSu_{mixS}$ and $AmSu_{mixL}$ have different particle diameters, the total soluble and mixed accumulation mode masses are separated in two fractions according to the intersection diameter $D_{inter} = 350\,nm$, in analogy to the MADE3 mode renaming operation described in Kaiser et al. (2014). The soluble and mixed accumulation modes are most relevant for ice nucleation induced by crystalline ammonium sulfate (insoluble modes carry too less NH_4, SO_4). Aitken mode particles are too small to be efficient ice nuclei (e.g., Kanji et al., 2017), while coarse modes have only few particles. However, as large coarse mode particles can be highly efficient ice nuclei, two additional tracers for internally and externally mixed coarse ammonium sulfate ($AmSu_{mix,coa}$ and $AmSu_{ext,coa}$) are defined similarly to the AmSu tracers described above, but with 1.75 µm and 1.0 µm particle radii, respectively. These sizes are chosen

similar to the AmSu accumulation mode tracers but are one order of magnitude larger[5], representing typical coarse mode sizes. The density of AmSu tracers is set to $1770\,\mathrm{kg\,m^{-3}}$ (Rumble, 2004). The geometric standard deviations or mode widths σ_g are defined in analogy to the MADE3 accumulation and coarse modes as $\sigma_g = 2.0$ for the accumulation mode, and $\sigma_g = 2.2$ for the coarse mode, respectively. The calculations of AmSu tracers consider phase transitions according to the relative humidity, as well as changes of tracer concentrations due to removal processes in clouds and precipitation. The subroutines concerning these calculations are part of the MADE3 submodel.

3.4.3.2 Phase transition formulation

Crystalline ammonium sulfate numbers are calculated according to the NH_4 and SO_4 input masses from MADE3, the local relative humidity, as well as efflorescence (ERH) and deliquescence (DRH) relative humidities.

In order to exclude grid boxes with no or only little NH_4 and SO_4 particulate matter contribution (only relevant for $\mathrm{AmSu_{mixS}}$, $\mathrm{AmSu_{mixL}}$ tracers), only those grid boxes are taken into account, where the non-dust fraction is dominated by NH_4 and SO_4, i.e. where $(m_{\mathrm{NH_4}} + m_{\mathrm{SO_4}})/(m_{\mathrm{tot}} - m_{\mathrm{DU}}) \geq 0.5$. This fraction is calculated from the corresponding input masses taken from MADE3. Dust plays a special role as it facilitates crystallization (e.g., Ushijima et al., 2018). Therefore, if the non-NH_4-SO_4-mass is dominated by dust, i.e. $m_{\mathrm{DU}}/(m_{\mathrm{tot}} - m_{\mathrm{NH_4}} - m_{\mathrm{SO_4}}) \geq 0.5$, this effect is taken into account (by an increase of the ERH, as described below).

Additionally, the ammonium input mass is limited, if there is too much ammonium compared to the available sulfate, i.e. NH_4 is scaled by 1/ASR (for ASR > 1), where ASR is the ammonium-to-sulfate molar ratio defined as

$$\mathrm{ASR} = \frac{[\mathrm{NH_4}]}{2\,[\mathrm{SO_4}]}\ . \tag{3.9}$$

For stoichiometric reasons, this reduction represents the maximum amount of ammonium which can be transformed to the solid phase. For the case of $\mathrm{AmSu_{mixS}}$ and $\mathrm{AmSu_{mixL}}$, the mass of non-NH_4-SO_4 inclusions is calculated as

$$\mathrm{m_{incl}} = \mathrm{m_{tot}} - \mathrm{m_{SO4}} - \mathrm{m_{NH4}}\ . \tag{3.10}$$

In addition to NH_4, the inclusion mass has to be scaled (if ASR > 1) by $\frac{\mathrm{SO_4+NH_4/ASR}}{\mathrm{SO_4+NH_4}}$, which represents the reduction of the (SO_4 + NH_4) mass. ASR is subsequently limited to $0 \leq \mathrm{ASR} \leq 1$.

The deliquescence relative humidity is set to DRH = 80 % (Martin, 2000). Temperature dependency of DRH can be neglected, as it has only minor influence (Onasch et al., 1999; Tang and Munkelwitz, 1993). Efflorescence relative humidity is calculated as a function of ASR according to Martin et al. (2003) and Wang et al. (2008).

$$\mathrm{ERH(ASR)} = \begin{cases} -71925 + 1690\ \mathrm{ASR} - 139\ \mathrm{ASR}^2 + \frac{1770760}{25.0+0.5(\mathrm{ASR}-0.7)}\ , & \text{if } 0.5 \leq \mathrm{ASR} \leq 1.0 \\ 0\ , & \text{if } \mathrm{ASR} < 0.5 \end{cases} \tag{3.11}$$

[5] For simplicity, only one mixed coarse mode AmSu tracer is considered, with a size in the middle between 1.0 µm and 2.5 µm, similar to the mixed accumulation mode tracers but one order of magnitude larger.

Setting ERH to zero if ASR < 0.5 considers the cases where there is too much SO_4 for the available NH_4. This implies that no crystallization is possible for ASR < 0.5, as reported in Martin et al. (2003); Wang et al. (2008). Similar to DRH the temperature dependency of ERH is small and can be neglected (Onasch et al., 1999).

Equation (3.11) provides a minimum ERH for the case of pure ammonium sulfate particles (without inclusions). As stated in various studies (e.g., Martin, 2000; Martin et al., 2001; Han et al., 2002; Martin et al., 2003; Pant et al., 2006; Ushijima et al., 2018), inclusions of e.g. mineral dust can increase the ERH significantly, leading to more favourable conditions for the crystalline phase. This effect of mineral dust is enhanced for larger inclusion diameters. According to Martin et al. (2003) this inclusion effect (heterogeneous nucleation) can be added to Eq. (3.11) by:

$$\mathrm{ERH}_{\mathrm{het}}(\mathrm{ASR}, D) = \mathrm{ERH}_{\mathrm{hom}}(\mathrm{ASR}) + f(D) \ , \tag{3.12}$$

with $f(D)$ being a function of the inclusion diameter D. Here, the effect of mineral dust inclusions is implemented in the following way. For $\mathrm{AmSu}_{\mathrm{mixS}}$ and $\mathrm{AmSu}_{\mathrm{mixL}}$ tracers, ERH is increased by 10 %, if dust inclusions are present in a significant amount (dust fraction with respect to non-SO_4-NH_4 components > 0.5). This is in accordance with measurements from Ushijima et al. (2018) and Pant et al. (2006), where ERH is increased by approximately 10 % compared to homogeneous efflorescence for dust inclusions with diameters of about 400 nm (corresponding to typical MADE3 accumulation mode dust particle sizes). For simplicity, this ERH increase is assumed to be the same for $\mathrm{AmSu}_{\mathrm{mixS}}$ and $\mathrm{AmSu}_{\mathrm{mixL}}$ tracers.

The actual ammonium sulfate phase transition is calculated in the following way, depending on the local RH. If RH $<$ ERH, the total ammonium and sulfate mass (with possible inclusions of other components for the case of $\mathrm{AmSu}_{\mathrm{mixS}}$ and $\mathrm{AmSu}_{\mathrm{mixL}}$) is used to update the AmSu mass. Subsequently, this is converted to a number concentration by using a component-mass-weighted mean particle density according to the mean particle density calculated in MADE3, and mode width (σ_g) and diameter (D) input values of the corresponding AmSu tracer, via Eq. 3.6. If RH $>$ DRH, AmSu is set to zero.

As AmSu tracers are removed in clouds (see Sect. 3.4.3.3 below), the relative humidity in the cloud-free area of the grid box (RH_0) is used for RH. RH_0 can be calculated from the grid box mean RH (RH_m) according to the following equations. With the grid box mean specific humidity (Q_m), the cloud-free specific humidity (Q_0), the in-cloud specific humidity (Q_s) assumed to be equal to the saturation specific humidity, and the cloud covered fraction of the grid box (C_{cl}), it follows:

$$Q_m = (1 - C_{\mathrm{cl}})\ Q_0 + C_{\mathrm{cl}}\ Q_s \Rightarrow Q_0 = (Q_m - C_{\mathrm{cl}}\ Q_s)/(1 - C_{\mathrm{cl}}) \tag{3.13a}$$

$$\mathrm{RH}_0 = \frac{Q_0}{Q_s} = (\mathrm{RH}_m - C_{\mathrm{cl}})/(1 - C_{\mathrm{cl}}) \tag{3.13b}$$

3.4.3.3 Removal by clouds and precipitation

The use of the scavenging submodel SCAV is deactivated for the AmSu tracers, since a very detailed representation of different scavenging processes is probably not required, due to a high probability of deliquescence of crystalline ammonium sulfate in the presence of clouds and precipitation. Instead, concentration changes of AmSu tracers due to interactions with clouds and precipitation are dealt with in the following way.

The idea is to set AmSu to zero in the presence of clouds or precipitation as this would imply a high probability for deliquescence due to the high relative humidity. This applies for liquid clouds, but also for the mixed phase regime as there ice originates from freezing of liquid water. In the cirrus regime a different removal process is performed (as described below). Since the presence of clouds and precipitation is an indicator for enhanced relative humidity within the corresponding grid box and the simulation of clouds and precipitation is highly uncertain in global climate models, it is assumed that deliquescence occurs in the whole grid box as soon as the fraction of the grid box covered by cloud or precipitation exceeds a critical value. Here, we assume a comparatively conservative threshold value of 10 %. This assumption represents a conservative approach (in contrast to scaling ammonium sulfate tracer changes with the cloud and precipitation free area fraction of the grid box) to avoid overestimations of crystalline ammonium sulfate numbers.

In addition to stratiform clouds, convective clouds are considered by setting an additional threshold (0.1 %) for convective cloud cover (C_{cv}) and the corresponding removal of AmSu[6]. The information about cloud-covered and precipitation-covered fraction of the grid box is taken from the CLOUD submodel. A random overlap of cloud cover and precipitation cover within a grid box is assumed, i.e. the area covered by clouds or precipitation ($C_{\mathrm{cl,pr}}$) is given by:

$$C_{\mathrm{cl,pr}} = C_{\mathrm{cl}} + C_{\mathrm{pr}} - C_{\mathrm{cl}} \cdot C_{\mathrm{pr}} \ , \tag{3.14}$$

with the area of the grid box covered with clouds (C_{cl}) and precipitation (C_{pr}), respectively.

A caveat of this procedure is that the cloud cover does not differentiate between liquid and ice clouds. For ice clouds there may possibly be no deliquescence. Hence, an alternative concept for handling ammonium sulfate in the cirrus regime has been implemented and is described below. The same issue applies to precipitation cover. Deliquescence will happen for the case of rain, but possibly not for snow. Subsequent evaporation of snow could lead to a release of AmSu. However, this process is probably not very relevant for ice nucleation processes as, in many cases, those particles would be released well below the cirrus level.

In cirrus clouds the relative humidity with respect to ice could be lower than the deliquescence humidity of ammonium sulfate, so that AmSu crystals can persist. Therefore, AmSu should be removed in the cirrus regime ($T < T_{\mathrm{hom}} = -35\,°\mathrm{C}$) for non-deliquescence conditions only if snow formation takes place. In addition, cloud ice could possibly release crystalline ammonium sulfate after evaporation. Here, AmSu removal in cirrus clouds is implemented in the following way: The AmSu fraction that is removed by snow is calculated from the snow formation rate (R_{snow}) and the cloud ice water content (i.e. cloud ice mass per unit mass of air; IWC) taken from the CLOUD submodel, cloudcover (C_{cl}), and ice active fraction of AmSu (f_{act}):

$$f_{\mathrm{snow}} = \frac{R_{\mathrm{snow}}}{\mathrm{IWC}} \cdot C_{\mathrm{cl}} \cdot f_{\mathrm{act}} \tag{3.15}$$

f_{act} is set to 0.01, according to typical literature values (e.g., Ladino et al., 2014). Subsequently, AmSu concentrations are scaled with $(1 - f_{\mathrm{snow}})$. In this approach, the effect of snow impaction scavenging of AmSu particles is neglected.

[6] A low sensitivity to variations of this threshold is observed, i.e. changes in AmSu concentrations of mostly a few percent when increasing the threshold by a factor of ten.

A schematic overview of the representation of AmSu in the EMAC-MADE3 model is presented in Fig. 3.4. Calculations concerning ammonium sulfate are performed by the subroutines `update_amsu` and `amsu_phasetrans`, which are part of the MADE3 submodel and require input from the MESSy submodels PTRAC, MADE3, and CLOUD.

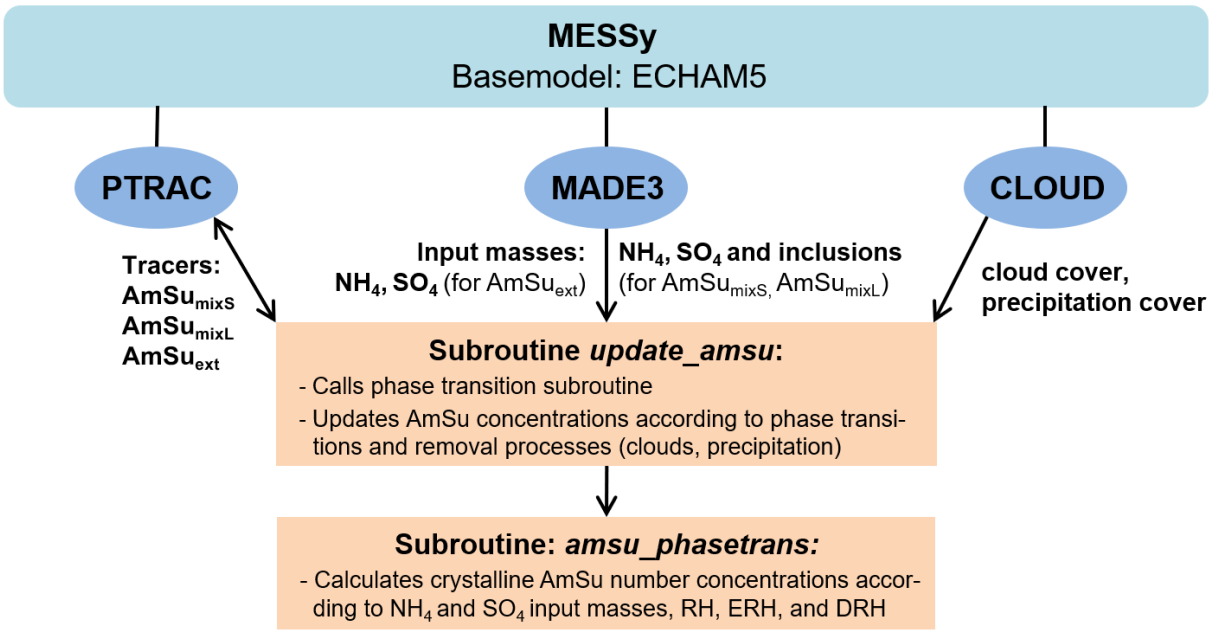

Figure 3.4: Schematic overview of the representation of AmSu tracers in EMAC-MADE3. The subroutines `update_amsu` and `amsu_phasetrans` are part of the MADE3 submodel and interact with the MESSy submodels PTRAC, MADE3, and CLOUD (see also Table 3.1). The additional AmSu tracers for the coarse mode, i.e. AmSu$_{mix,coa}$ and AmSu$_{ext,coa}$, are not shown for the sake of simplicity.

3.5 Coupling additional aerosol tracers to the cloud module

In order to realize ice nucleation induced by aerosol particles in the model, the corresponding aerosol tracers need to be coupled to the cloud parametrizations in the EMAC CLOUD module (see also Sect. 3.2.5). There, the number concentrations of potential INPs are calculated for the different ice formation modes in the mixed-phase and the cirrus regime according to the procedure described in Righi et al. (2020). Potential INP numbers are multiplied with the respective ice-active fractions f_{act} to be used as input for the cirrus cloud parametrization. Here, the calculations described in Righi et al. (2020) are expanded to include also the additional INPs, i.e. glPOM, AmSu and BCair. The calculation of INP concentrations available for freezing events is performed for every MADE3 mode as described below in Sect. 3.5.1. Following the same notation as in Righi et al. (2020), MADE3 Aitken, accumulation, and coarse modes are indicated with the indices k, a, and c, respectively. Mixing states are depicted by s, i, and m for soluble, insoluble, and mixed, respectively. All the calculated number concentrations undergo consistency checks in the code, to make sure that the estimated number concentrations in each mode are positive and do not exceed the total number concentration in the mode itself.

For the freezing of crystalline ammonium sulfate, the sum of $\text{AmSu}_{\text{mixS}}$ and $\text{AmSu}_{\text{mixL}}$ tracers is considered, as they provide a more detailed and realistic representation in contrast to AmSu_{ext}. Additionally, AmSu freezing is only considered if $S_c < DRH$, as the particles would otherwise undergo deliquescence and not be in the crystalline phase. For this condition the supersaturation with respect to ice was converted to the value with respect to liquid water using the formulations described by Murphy and Koop (2005), depending on the ratio of the vapour pressures of liquid water and ice, respectively. As the information about AmSu concentrations is needed per MADE3 mode, AmSu numbers are separated according to NH_4 and SO_4 masses in MADE3 soluble and mixed modes. Additionally, possible inclusions in AmSu particles (e.g. DU) have to be subtracted from the corresponding concentration in other freezing modes.

Generally, in every mode where glPOM is present, the number of glPOM INPs is calculated first and subtracted from the number in the other freezing modes, as glassy organics are assumed to form a shell around other particles (e.g., Smith et al., 2012, 2013; Schill et al., 2014; Saukko et al., 2015). This shell is then the relevant part of the particle for ice nucleation mechanisms. An alternative formulation for glPOM freezing, considering glPOM INPs only for grid boxes where the glPOM mass-fraction (with respect to the total mass in the mode) exceeds certain thresholds (e.g. 0.3 or 0.5), resulted in negligible number concentrations of potential glPOM INPs.

3.5.1 Calculation of numbers of ice nucleating aerosol particles

In Righi et al. (2020) the calculations for different freezing mechanisms in the mixed-phase and cirrus regime considering mineral dust and soot INPs are described in detail. Here, the focus is on the addition of glPOM and AmSu freezing in the cirrus regime. The existing formulation for tagged BC particles is used and adapted for BC emissions from aviation. The number of particles available for immersion freezing in mixed-phase clouds is estimated as a fraction of the number of aerosol particles activated to form

cloud droplets (N_{act}), as described in Righi et al. (2020). The number concentrations of potential INPs available for deposition nucleation and immersion freezing in cirrus clouds are indicated by $N^{\mathrm{dep(c)}}$ and $N^{\mathrm{imm(c)}}$, respectively. For AmSu and glPOM the freezing mode (deposition or immersion freezing) is uncertain and the number concentrations are defined more generally as $N^{(\mathrm{c})}$. The number concentrations of actual INPs are then calculated according to their freezing spectra depending on S_c and f_{act} applying the Kärcher et al. (2006) parametrization.

The mixed and insoluble Aitken modes, where no dust is present, are dominated by BC particles. The freezing efficiency of AmSu and glPOM in the Aitken modes is assumed to be low, due to the small particle size, and these INPs are neglected for the Aitken modes. In the cirrus regime, first the numbers of BCair INPs are calculated from their masses in the two different Aitken modes using the M2N factors from Eq. 3.6 and assuming size distribution parameters typical for aircraft soot, i.e. $D = 0.025\,\mu\mathrm{m}, \sigma_g = 1.55$ for the Aitken mode and $\rho = 1500\,\mathrm{kg/m^3}$ (Petzold et al., 1999). Since no dust is present in this mode, the remaining number of particles in the mode is then assigned to BC (from non-aircraft sources).

$$N^{\mathrm{imm(c)}}_{\mathrm{BCair,k}} = M_{\mathrm{BCair,km}}\,\mathrm{M2N}_{\mathrm{BCair,k}} \tag{3.16a}$$

$$N^{\mathrm{dep(c)}}_{\mathrm{BCair,k}} = M_{\mathrm{BCair,ki}}\,\mathrm{M2N}_{\mathrm{BCair,k}} \tag{3.16b}$$

$$N^{\mathrm{imm(c)}}_{\mathrm{BC,k}} = \max(0, N_{\mathrm{km}} - N^{\mathrm{imm(c)}}_{\mathrm{BCair,k}}) \tag{3.16c}$$

$$N^{\mathrm{dep(c)}}_{\mathrm{BC,k}} = \max(0, N_{\mathrm{ki}} - N^{\mathrm{dep(c)}}_{\mathrm{BCair,k}}) \tag{3.16d}$$

In the soluble accumulation mode, no DU or BC are present. The number concentration of glPOM potential INPs is calculated from the glPOM mass according to Eq. 3.6, assuming $D = 0.2\,\mu\mathrm{m}, \sigma_g = 2.0$ (this represents typical accumulation mode sizes and is chosen to be comparable with the assumptions for AmSu) and $\rho = 1000\,\mathrm{kg/m^3}$ (as for the MADE3 POM tracer).

$$N^{(\mathrm{c})}_{\mathrm{glPOM,as}} = M_{\mathrm{glPOM,as}}\,\mathrm{M2N}_{\mathrm{glPOM,as}} \tag{3.17}$$

For ammonium sulfate freezing, the number concentration of the AmSu tracers in the mode is used. The contribution of the $\mathrm{AmSu_{mixS}}$ and $\mathrm{AmSu_{mixL}}$ tracers for this mode is calculated according to the MADE3 NH_4 and SO_4 mass concentrations.

$$N^{\mathrm{as}}_{\mathrm{AmSu_{mix}}} = f_{\mathrm{as}} \cdot (N_{\mathrm{AmSu_{mixS}}} + N_{\mathrm{AmSu_{mixL}}}) \quad , \tag{3.18}$$

where f_{as} is the soluble fraction in the mode, calculated from NH_4 and SO_4 masses in the MADE3 soluble accumulation mode as

$$f_{\mathrm{as}} = \frac{m^{\mathrm{as}}_{\mathrm{NH_4}} + m^{\mathrm{as}}_{\mathrm{SO_4}}}{m^{\mathrm{as}}_{\mathrm{NH_4}} + m^{\mathrm{as}}_{\mathrm{SO_4}} + m^{\mathrm{am}}_{\mathrm{NH_4}} + m^{\mathrm{am}}_{\mathrm{SO_4}}} \quad . \tag{3.19}$$

Subsequently, this number is reduced by the number of glPOM INPs in the mode (assuming an organic shell around the ammonium sulfate particles) to obtain the number of potential AmSu INPs in the mode.

$$N^{(\mathrm{c})}_{\mathrm{AmSu,as}} = \max(0, N^{\mathrm{as}}_{\mathrm{AmSu_{mix}}} - N^{(\mathrm{c})}_{\mathrm{glPOM,as}}) \tag{3.20}$$

Additionally, the number concentration of soluble aerosols available for homogeneous freezing in the mode ($N_{\mathrm{hom,as}}$) is reduced by AmSu and glPOM numbers. For AmSu, this

reduction is dependent on the relation between the ice supersaturation for homogeneous freezing (S_{hom}; Koop et al., 2000) and the deliquescence relative humidity (DRH). If $S_{\mathrm{hom}} \geq \mathrm{DRH}$ only the ice active fraction of AmSu (f_{act}) is subtracted, as the remaining particles would be liquid and available for homogeneous freezing.

$$N_{\mathrm{hom,as}} = \begin{cases} \max(0, N_{\mathrm{as}} - N^{(\mathrm{c})}_{\mathrm{glPOM,as}} - N^{\mathrm{as}}_{\mathrm{AmSu_{mix}}}) \ , & \text{if } S_{\mathrm{hom}} < \mathrm{DRH} \\ \max(0, N_{\mathrm{as}} - N^{(\mathrm{c})}_{\mathrm{glPOM,as}} - f_{\mathrm{act}} \cdot N^{\mathrm{as}}_{\mathrm{AmSu_{mix}}}) \ , & \text{if } S_{\mathrm{hom}} \geq \mathrm{DRH} \end{cases} \tag{3.21}$$

In the mixed accumulation mode all possible INPs can be present, i.e. DU, BC, BCair, AmSu, and glPOM. First, the number of glassy organics is calculated from their mass, assuming a 50 nm thick spherical glPOM shell around a 100 nm core. This size corresponds to the assumption used for AmSu particle sizes, to keep these potential INPs comparable. Following a simple geometric calculation, such a shell has an equivalent volume as a sphere with $D = 190\,\mathrm{nm}$. Together with $\sigma_g = 2.0$ and $\rho = 1000\,\mathrm{kg/m^3}$ this diameter is used to convert glPOM mass to number concentration using Eq. 3.6:

$$N^{(\mathrm{c})}_{\mathrm{glPOM,am}} = M_{\mathrm{glPOM,am}}\,\mathrm{M2N_{glPOM,am}} \tag{3.22}$$

The number concentration of potential AmSu INPs is again calculated as the fraction of AmSu tracers in this mode:

$$N^{(\mathrm{c})}_{\mathrm{AmSu,am}} = (1 - f_{\mathrm{as}}) \cdot (N_{\mathrm{AmSu_{mixS}}} + N_{\mathrm{AmSu_{mixL}}}) \tag{3.23}$$

The numbers of potential BCair and DU INPs are calculated similarly, with the assumption of $D = 0.15\,\mu\mathrm{m}, \sigma_g = 1.65$ and $\rho = 1500\,\mathrm{kg/m^3}$ for BCair (Petzold et al., 1999) and $D = 0.42\,\mu\mathrm{m}, \sigma_g = 1.59$ and $\rho = 2500\,\mathrm{kg/m^3}$ for DU following the AeroCom assumptions (Dentener et al., 2006). These parameters for DU are the same that are also used to calculate the number of emitted dust particles in the model (see Sect 3.3), i.e. the ageing of dust particles due to coagulation is neglected. Additionally, the numbers of DU and BCair immersion freezing INPs have to be reduced according to the respective inclusions inside AmSu particles ($N^{\mathrm{DU}}_{\mathrm{incl}}, N^{\mathrm{BCair}}_{\mathrm{incl}}$). Therefore, DU and BCair numbers are calculated as:

$$N^{\mathrm{imm(c)}}_{\mathrm{DU,am}} = \max(0, M_{\mathrm{DU,am}}\,\mathrm{M2N_{DU,a}} - N^{\mathrm{DU}}_{\mathrm{incl}}) \tag{3.24a}$$

$$N^{\mathrm{imm(c)}}_{\mathrm{BCair,am}} = \max(0, M_{\mathrm{BCair,am}}\,\mathrm{M2N_{BCair,a}} - N^{\mathrm{BCair}}_{\mathrm{incl}}) \ , \tag{3.24b}$$

with

$$N^{\mathrm{DU}}_{\mathrm{incl}} = \frac{N_{\mathrm{DU,am}}}{N_{\mathrm{am}}} \cdot N^{\mathrm{imm(c)}}_{\mathrm{AmSu,am}} \tag{3.25a}$$

$$N^{\mathrm{BCair}}_{\mathrm{incl}} = \frac{N_{\mathrm{BCair,am}}}{N_{\mathrm{am}}} \cdot N^{\mathrm{imm(c)}}_{\mathrm{AmSu,am}} \ . \tag{3.25b}$$

Subsequently, the numbers of potential DU, BCair, and AmSu INPs have to be reduced according to glPOM numbers following the assumption of glPOM forming a shell around other particles (e.g., Smith et al., 2012, 2013; Schill et al., 2014; Saukko et al., 2015). The number of BC particles available for immersion freezing is finally calculated as the remaining number in the mode:

$$N^{\mathrm{imm(c)}}_{\mathrm{BC,am}} = \max(0, N_{\mathrm{am}} - N^{\mathrm{imm(c)}}_{\mathrm{DU,am}} - N^{\mathrm{imm(c)}}_{\mathrm{BCair,am}} - N^{(\mathrm{c})}_{\mathrm{glPOM,am}} - N^{(\mathrm{c})}_{\mathrm{AmSu,am}}) \tag{3.26}$$

Here, BC particles are assumed to have accumulation mode sizes. The mixed accumulation mode may consist of a mixture of particles from the soluble accumulation and insoluble or mixed Aitken mode BC or BCair particles. However, such mixures are not considered here, as soluble accumulation mode particles are only rarely present at cirrus altitudes.

In the insoluble accumulation mode only DU, BCair and BC are present. The numbers of DU and BCair deposition freezing INPs are again calculated from their masses, and the remaining particles in the mode are ascribed to BC deposition freezing.

$$N_{\mathrm{DU,a}}^{\mathrm{dep(c)}} = M_{\mathrm{DU,ai}}\,\mathrm{M2N}_{\mathrm{DU,a}} \tag{3.27a}$$

$$N_{\mathrm{BCair,a}}^{\mathrm{dep(c)}} = M_{\mathrm{BCair,ai}}\,\mathrm{M2N}_{\mathrm{BCair,a}} \tag{3.27b}$$

$$N_{\mathrm{BC,a}}^{\mathrm{dep(c)}} = \max(0, N_{\mathrm{ai}} - N_{\mathrm{DU,a}}^{\mathrm{dep(c)}} - N_{\mathrm{BCair,a}}^{\mathrm{dep(c)}}) \tag{3.27c}$$

The above formulations and representations assumed for potential INPs in the accumulation modes are also depicted schematically in Fig. 3.5.

Calculations for the soluble coarse mode, concerning immersion freezing of glPOM and AmSu, and homogeneous freezing of solution droplets, are performed similar to those in the soluble accumulation mode, but with different assumptions for the parameters used for mass-to-number conversion for glPOM particles. These are, $D = 1.75\,\mu\mathrm{m}$ (as for the coarse mode AmSu tracer), $\sigma_g = 2.2$ and $\rho = 1000\,\mathrm{kg/m^3}$.

$$N_{\mathrm{glPOM,cs}}^{(\mathrm{c})} = M_{\mathrm{glPOM,cs}}\,\mathrm{M2N}_{\mathrm{glPOM,cs}} \tag{3.28}$$

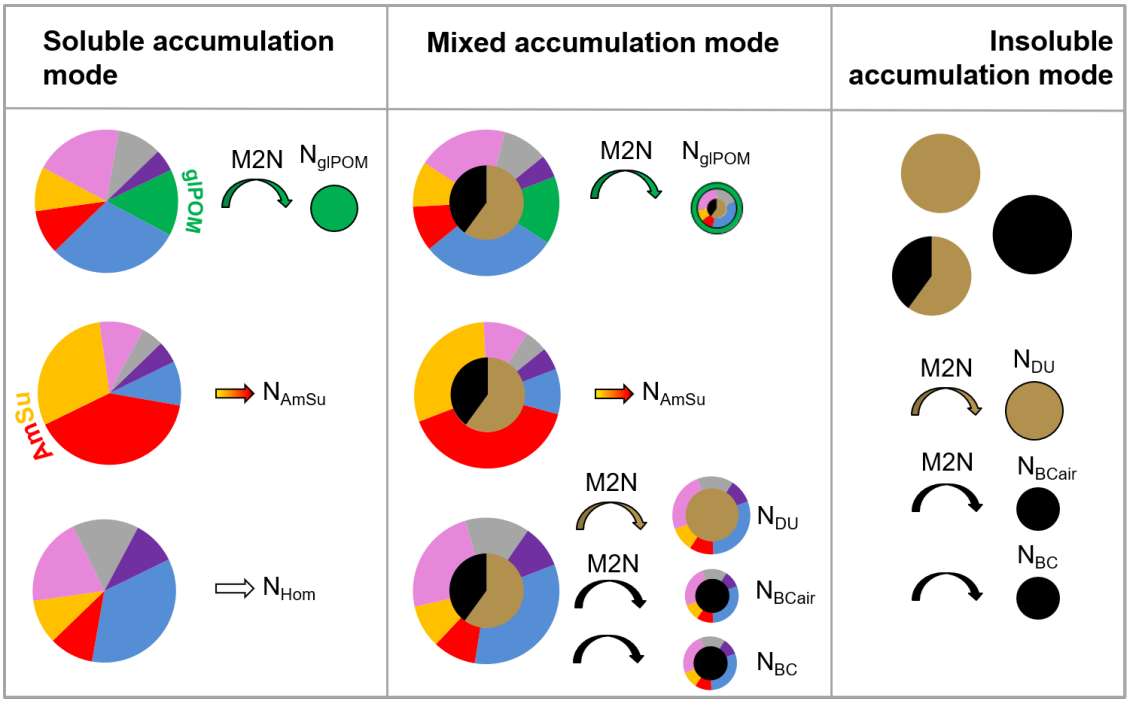

Figure 3.5: Schematic representation of assumed potential INPs concerning the calculation of number concentrations available for freezing processes in the accumulation modes. In the Aitken and coarse modes other sets of possible INP-types are participating, e.g. no AmSu and glPOM freezing in the Aitken modes, and no BCair freezing in the coarse mode is assumed. M2N represents the conversion of aerosol mass to number concentrations using Eq. 3.6. The colors of the different aerosol species are the same as in Fig. 3.1. Ammonium sulfate is represented in red and yellow, BC (and BCair) and DU in black and brown, respectively. In addition to glPOM (green), other POM may also be present but is omitted here, for the sake of simplicity.

For ammonium sulfate freezing the fraction of the $\mathrm{AmSu_{mix,coa}}$ tracer in the mode is used considering the reduction according to glPOM numbers in the mode (assuming a glPOM shell around the particles).

$$N^{\mathrm{cs}}_{\mathrm{AmSu_{mix,coa}}} = f_{\mathrm{cs}} \cdot N_{\mathrm{AmSu_{mix,coa}}} \tag{3.29a}$$

$$N^{(\mathrm{c})}_{\mathrm{AmSu,cs}} = \max(0, N^{\mathrm{cs}}_{\mathrm{AmSu_{mix,coa}}} - N^{(\mathrm{c})}_{\mathrm{glPOM,cs}}) \quad , \tag{3.29b}$$

where f_{cs} is the soluble fraction of NH_4 and SO_4 in the coarse modes, in analogy to f_{as} in the accumulation modes.

Additionally, the number concentration of soluble aerosols available for homogeneous freezing in the mode ($N_{\mathrm{hom,cs}}$) is reduced by AmSu and glPOM numbers depending on S_{hom}, DRH, and the ice active fraction of AmSu (f_{act}) as for the soluble accumulation mode.

$$N_{\mathrm{hom,cs}} = \begin{cases} \max(0, N_{\mathrm{cs}} - N^{(\mathrm{c})}_{\mathrm{glPOM,cs}} - N^{\mathrm{cs}}_{\mathrm{AmSu_{mix,coa}}}) \, , & \text{if } S_{\mathrm{hom}} < \mathrm{DRH} \\ \max(0, N_{\mathrm{cs}} - N^{(\mathrm{c})}_{\mathrm{glPOM,cs}} - f_{\mathrm{act}} \cdot N^{\mathrm{cs}}_{\mathrm{AmSu_{mix,coa}}}) \, , & \text{if } S_{\mathrm{hom}} \geq \mathrm{DRH} \end{cases} \tag{3.30}$$

In the mixed coarse mode DU, BC, glPOM, and AmSu INPs may be present. In this mode it is assumed that there is no contribution of BCair particles to the number concentrations. A similar calculation as in the mixed accumulation mode is performed. Here, glPOM is assumed to form a 0.5 µm thick spherical shell around a 1 µm core, which has an equivalent volume (or mass) as a sphere with $D = 1.9\,\mu\mathrm{m}$, $\sigma_g = 2.2$ and $\rho = 1000\,\mathrm{kg/m^3}$. For DU, $D = 1.3\,\mu\mathrm{m}, \sigma_g = 2.0$ and $\rho = 2500\,\mathrm{kg/m^3}$ are used, according to the AeroCom assumptions (Dentener et al., 2006). However, as in this mode particles can be composed of dust from both the accumulation and coarse size ranges, whose relative contribution is unknown, two cases are distinguished, in analogy to Righi et al. (2020), according to the relative abundance of mineral dust. Defining the dust number fraction as

$$f_{\mathrm{DU}} = \frac{M_{\mathrm{DU,cm}}\,\mathrm{M2N_{DU,c}}}{N_{\mathrm{cm}}} \quad , \tag{3.31}$$

it is assumed that for large f_{DU} the mode is dominated by mineral dust. Here, coarse dust particles are assumed to calculate the number fraction, as these particles dominate the dust mass (possible mass contributions of accumulation-mode dust are small, according to Dentener et al., 2006). For large f_{DU} it can be expected that other INPs have a relatively small contribution, and all particles in the mode can be regarded as possible DU INPs. Here, a dominance threshold for DU is assumed if $f_{\mathrm{DU}} \geq 0.7$. For this case, this results in

$$N^{\mathrm{imm(c)}}_{\mathrm{DU,c}} = N_{\mathrm{cm}} \tag{3.32a}$$

$$N^{\mathrm{imm(c)}}_{\mathrm{BC,c}} = N^{\mathrm{imm(c)}}_{\mathrm{glPOM,c}} = N^{\mathrm{imm(c)}}_{\mathrm{AmSu,c}} = 0 \tag{3.32b}$$

If $f_{\mathrm{DU}} < 0.7$, other INPs can play a major role and similar calculations as in the mixed accumulation mode are performed.

$$N^{\mathrm{imm(c)}}_{\mathrm{glPOM,cm}} = M_{\mathrm{glPOM,cm}}\,\mathrm{M2N_{glPOM,cm}} \tag{3.33}$$

The number concentration of possible AmSu INPs in this mode is calculated from the fraction of the $\mathrm{AmSu_{mix,coa}}$ tracer in the mode.

$$N^{(\mathrm{c})}_{\mathrm{AmSu,cm}} = (1 - f_{\mathrm{cs}}) \cdot N_{\mathrm{AmSu_{mix,coa}}} \tag{3.34}$$

Potential DU INP numbers are calculated from the DU mass in the mode and subsequently reduced by respective inclusions inside AmSu particles.

$$N_{\mathrm{DU,cm}}^{\mathrm{imm(c)}} = M_{\mathrm{DU,cm}}\,\mathrm{M2N}_{\mathrm{DU,c}} - N_{\mathrm{incl}}^{\mathrm{DU}} \quad , \tag{3.35}$$

where

$$N_{\mathrm{incl}}^{\mathrm{DU}} = \frac{N_{\mathrm{DU,cm}}}{N_{\mathrm{cm}}} \cdot N_{\mathrm{AmSu,cm}}^{(\mathrm{c})} \quad . \tag{3.36}$$

This represents a minimum estimate of the number of DU particles in the mode, as also accumulation-mode dust may be present due to coagulation. Additionally the potential DU and AmSu INP number concentrations have to be reduced according to glPOM numbers following the assumption of an organic shell around other particles (e.g., Smith et al., 2012, 2013; Schill et al., 2014; Saukko et al., 2015).

The remaining particles in the mode are available for immersion freezing of BC, as the possible contribution of accumulation-mode dust is probably small in this non-dust-dominated regime

$$N_{\mathrm{BC,cm}}^{\mathrm{imm(c)}} = \max(0, N_{\mathrm{cm}} - N_{\mathrm{DU,cm}}^{\mathrm{imm(c)}} - N_{\mathrm{glPOM,cm}}^{\mathrm{imm(c)}} - N_{\mathrm{AmSu,cm}}^{\mathrm{imm(c)}}) \quad . \tag{3.37}$$

The insoluble coarse mode is dominated by mineral dust, since coagulational growth of BC particles from the insoluble accumulation mode can be neglected (limited BC mass and low self-coagulation efficiency). Therefore, the number of available deposition freezing dust INPs is given by:

$$N_{\mathrm{DU,c}}^{\mathrm{dep(c)}} = N_{\mathrm{ci}} \tag{3.38}$$

3.6 Observational data used for model evaluation

This section provides an overview of the various observational data sets used for model evaluation in this study and appeared similarly in my recent publication (Beer et al., 2020)[7].

Aircraft measurements provide valuable insights on the vertical distribution of aerosol particles by measurements of particle concentrations along the aircraft flight trajectory. Here, observational data from the SALTRACE campaign is used (Weinzierl et al., 2017). During this campaign (June–July 2013), aircraft measurements of various parameters, including size-resolved particle number and black carbon mass concentrations, were performed mainly in the regions around Cabo Verde, Puerto Rico, and Barbados. From this data set the integral particle number concentrations in the size ranges 0.3 µm - 1.0 µm and 0.7 µm - 50 µm and the total black carbon mass mixing ratios are used for the model evaluation.

The particle number concentrations in the size range from about 0.3 µm to 1.0 µm were measured by a Grimm model 1.129 optical particle counter (SkyOPC). The SkyOPC was operated onboard the Falcon research aircraft of the German Aerospace Center (DLR) behind an isokinetic aerosol inlet with an upper particle cutoff diameter of about 2.5 µm near ground level, decreasing to about 1.5 µm at an altitude of 10 km. depending on altitude. Detailed specifications and performance analyses for this instrument can be found in Bundke et al. (2015) and in Walser et al. (2017).

Detection of particles larger than the inlet cutoff was done using a wing-mounted aerosol size spectrometer CAS-DPOL (cloud and aerosol spectrometer probe with depolarization detection by Droplet Measurement Technologies Inc., Longmont, CO, U.S.A.; Baumgardner et al., 2001) with a nominal size detection range between 0.7 µm and 50 µm. The aircraft measurements are compared to model output extracted along the aircraft flight-tracks by spatial and temporal interpolation using the EMAC submodel S4D, to ensure direct comparability between observation and model data.

Additionally, ground-based lidar observations also collected during the SALTRACE campaign were employed. In particular dust extinction coefficients at 532 nm, measured with a stationary lidar system located on Barbados, provide valuable information directly related to mineral dust (Groß et al., 2015, 2016). In addition to the observational data sets mentioned above, further aircraft data was used for the model evaluation, as described in detail in Kaiser et al. (2019).

In addition to SALTRACE observations, sun photometer measurements of aerosol optical depth (AOD) at 440 nm from the ground-based AErosol RObotic NETwork (AERONET; Holben et al., 1998, 2001) are used. AOD provides an integral measure of radiation extinction by the vertical aerosol column. In the EMAC model, AOD is computed from simulated aerosol properties in the submodel AEROPT. AEROPT considers aerosol optical properties calculated according to the OPAC (Optical Properties for Aerosols and Clouds, Hess et al., 1998) software package, which follows the basic optical properties from Koepke et al. (1997).

[7] C. G. Beer, J. Hendricks, M. Righi, B. Heinold, I. Tegen, S. Groß, D. Sauer, A. Walser, and B. Weinzierl. Modelling mineral dust emissions and atmospheric dispersion with MADE3 in EMAC v2.54. *Geosci. Model Dev.*, 13(9):4287–4303, 2020. doi:10.5194/gmd-13-4287-2020

The AOD model output is compared with daily mean AOD values from AERONET radiometers (at 440 nm). To compare with the model data, a nearest-neighbour approach is applied by selecting the model grid box covering the station coordinates. The observational data used in this study are summarized in Table 3.5.

Table 3.5: Summary of relevant details and references of the observational datasets used for the evaluation of model results simulated with EMAC-MADE3. Numbers in brackets in the column "time" indicate the number of flights for aircraft measurements and the number of observation days for SALTRACE lidar measurements.

Name	Location	Time	Parameter	Reference
SALTRACE aircraft (East)	Cabo Verde	June 2013 (5)	Particle number BC mass	Weinzierl et al. (2017) Schwarz et al. (2017)
SALTRACE aircraft (West)	Eastern Caribbean	June/July 2013 (13)	Particle number BC mass	Weinzierl et al. (2017) Schwarz et al. (2017)
SALTRACE lidar	Barbados	June/July 2013 (24)	Dust extinction	Groß et al. (2015)
AERONET stations	17 stations [a]	2009–2013 [a]	AOD (440 nm)	Holben et al. (1998)

[a] AERONET data from various dust-dominated stations located in a region of 5° N – 40° N and 20° W – 50° E covering the time period 2009–2013 were used. A detailed description of the selection criterion is given in Sect. 4.1.1.

Chapter 4

Results and discussion

In this chapter, the results of this thesis are presented and discussed in detail, focusing on the representation of ice-nucleating aerosol species in the global model EMAC using the aerosol dynamics submodel MADE3. Section 4.1 deals with the improved representation of mineral dust in the model, with a special focus on dust emissions and long-range transport. Results on the atmospheric dispersion of soot particles are presented in Sect. 4.2. Section 4.3 focuses on glassy organic particles, while results on crystalline ammonium sulfate are presented in Sect. 4.4. Section 4.5 shows the global distribution of different INPs, number concentrations of nucleated ice crystals and ice water content resulting from heterogeneous freezing. Finally, Sect. 4.6 focuses on cirrus cloud modifications due to ice nucleating particles, including the effects on cirrus cloud properties and radiation.

4.1 Mineral dust in EMAC-MADE3

In this section results on modelled mineral dust emissions and atmospheric dispersion are presented. First, the effects of employing an online parametrization for mineral dust emissions in contrast to a prescribed offline climatology are shown. Second, the effects of increasing the horizontal and vertical model resolution is presented. Additionally, the sensitivity of the model results to size distribution assumptions for emitted dust is analysed. This section appeared similarly in my recent publication (Beer et al., 2020)[1].

4.1.1 Effects of dust emission scheme

Model results from simulations employing the two different dust emission representations are compared, i.e. simulations with the model setup including prescribed (offline) dust emissions (AeroCom climatology; Ginoux et al., 2001; 2004; Dentener et al., 2006; see Sect. 3.3.1) and the setup using the Tegen et al. (2002) online dust parametrization[2]. In particular, simulated AOD values are compared with data from ground-based AERONET stations (Holben et al., 1998), in order to evaluate the capability of the different model versions to represent the temporal variability of airborne mineral dust.

Figure 4.1 shows AOD time series of model results and observations, comparing the model setups with prescribed offline and parametrized online dust emissions, respectively. Apart from the representation of dust emissions, the two model setups are identical. As an example, time series of daily averages for the AERONET station Dakar (Senegal) are shown for a period of 36 months (Jan 2011 – Dec 2013). The model results obtained for this station benefit most from applying the online dust emission scheme, compared to other stations analysed below in this section. Compared to the AeroCom setup, AOD peaks from observations are expectedly in most cases much better represented in the online dust setup, e.g. the correlation coefficient is increased from 0.37 to 0.55 and the root mean square error is reduced from 0.31 to 0.29. This can also be seen in Fig. 4.1b,d, where scatterplots of model versus observational data for the two model setups are shown. Although total AOD is shown here (i.e. incorporating all types of aerosol particles), AOD peaks are probably related to strong dust events as the station is located in a dust-dominated region. This implies an improved representation of dust outbreaks when using the Tegen et al. (2002) online dust scheme. In addition, AOD time series of other AERONET stations in northern Africa and the Arabian Peninsula (see station locations in Fig. 4.2a) are shown in Fig. A.2 in the Appendix. There, an improved representation of AOD peaks in the T42L31Tegen model setup is also visible for these additional stations.

[1] C. G. Beer, J. Hendricks, M. Righi, B. Heinold, I. Tegen, S. Groß, D. Sauer, A. Walser, and B. Weinzierl. Modelling mineral dust emissions and atmospheric dispersion with MADE3 in EMAC v2.54. *Geosci. Model Dev.*, 13(9):4287–4303, 2020. doi:10.5194/gmd-13-4287-2020

[2] These are simulations T42L31AeroCom and T42L31Tegen, respectively, see Sect. 3.3.1.

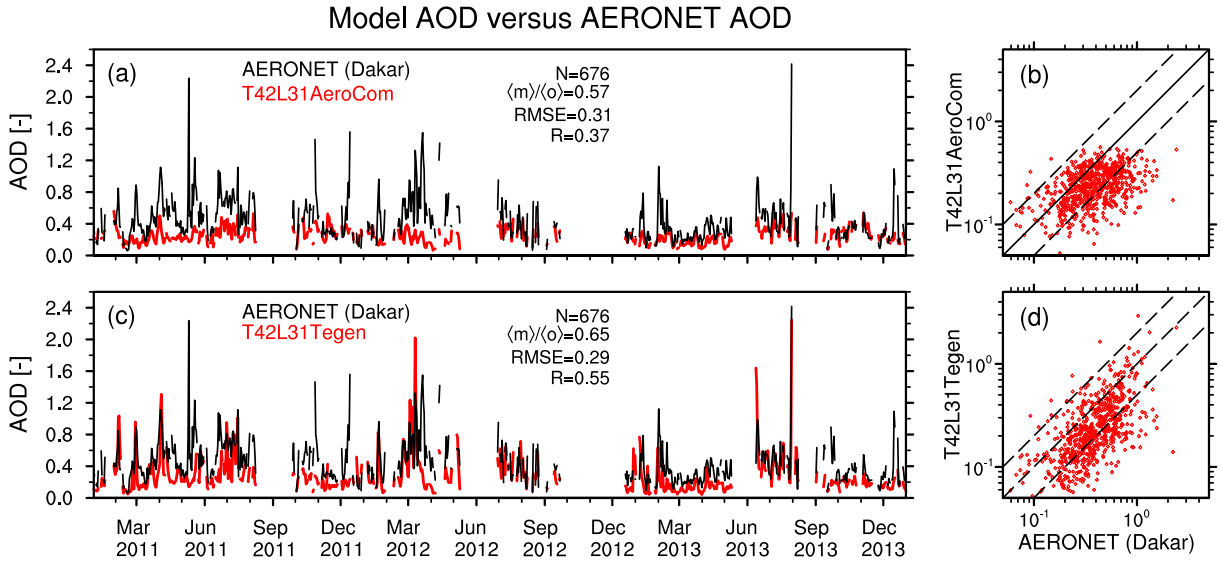

Figure 4.1: Model AOD versus AERONET station observations. Timeseries of AOD (at 440 nm) for the AERONET station located in Dakar (Senegal) are compared with model AOD on a daily mean basis for the time period 2011/01–2013/12. For clarity only a part of the full time period (starting in 2009/01) is shown here. Subfigure (a) compares observation AOD (black line) with the offline dust model setup (T42L31AeroCom, red line). Gaps in the time series are due to missing observations on those days. Number of data points, ratio of averages of model and observational data, root mean square error (RMSE), and Pearson correlation coefficient (R) are shown. Subfigure (b) shows the data as scatterplot of model versus observation AOD data for the T42L31AeroCom model setup. Subfigure (c) and (d) are the same as (a) and (b) but show results from the online dust model setup (T42L31Tegen). As shown in Beer et al. (2020, Fig. 3).

For a statistical comparison, simulated AOD is compared with observations from all dust-dominated AERONET stations in a region of 5° N – 40° N and 20° W – 50° E, for the time period 2009 – 2013, on a daily average basis. We use the Ångstrom exponent (AE, wavelength range of 870–440 nm) from AERONET measurements to select dust-dominated stations. The Ångstrom exponent (Ångström, 1929) is related to the AOD via:

$$\frac{\tau_\lambda}{\tau_{\lambda_0}} = \left(\frac{\lambda}{\lambda_0}\right)^\alpha \quad , \tag{4.1}$$

where τ_λ is the optical thickness at wavelength λ, τ_{λ_0} is the optical thickness at the reference wavelength λ_0, and α is the AE. An AE criterion is commonly used to extract the coarse-mode component from AOD data, which represents soil dust as the dominant coarse aerosol in desert regions (Ginoux et al., 2012; Eck et al., 1999; Parajuli et al., 2019). Stations with AE less than 0.75 (multi-annual mean) and with more than 50 observation days are selected. Their locations are shown in Fig. 4.2a.

To quantitatively compare model simulations with observational data, the skill score (S), defined by Taylor (2001), is used:

$$S = \frac{4(1+R)^4}{(\frac{\sigma_\mathrm{m}}{\sigma_\mathrm{o}} + \frac{\sigma_\mathrm{o}}{\sigma_\mathrm{m}})^2(1+R_0)^4} \quad , \tag{4.2}$$

where R is the correlation coefficient, σ_m and σ_o are the standard deviations of model and observational data, respectively, and R_0 is the maximum attainable correlation. This skill score is commonly used for model comparisons with observations (e.g., Klingmüller et al., 2018; Parajuli et al., 2019). For simplicity, $R_0 = 1$ is assumed, as the main interest is in

the relative changes of the skill score for different model simulations. Skill score values range from 0 to 1, with higher values indicating a better agreement between model and observations.

Fig. 4.2b shows the comparison of skill scores for the two model setups T42L31AeroCom and T42L31Tegen, respectively. In general, nearly all selected AERONET stations show an improved agreement with model results for the online dust setup (Tegen et al., 2002) compared to the offline dust setup. The average skill score over all stations is distinctively higher for the T42L31Tegen setup (0.22) as for the T42L31Aerocom setup (0.14). Especially the Dakar station shows a nearly five times higher skill score for the T42L31Tegen setup compared to T42L31AeroCom (0.38 versus 0.08, respectively). Additionally, a comparison with stations in other regions on the globe also shows improvements for most of these stations when using the online dust emission setup (Fig. 4.3). Especially stations affected by transported Saharan dust over the Atlantic profit most from applying the online emission setup (e.g. stations in the Cabo Verde or Caribbean region). Remaining uncertainties and deviations from observed values can be attributed to spatial sampling issues when comparing grid-box averages to localized observations (Schutgens et al., 2016). Ad-

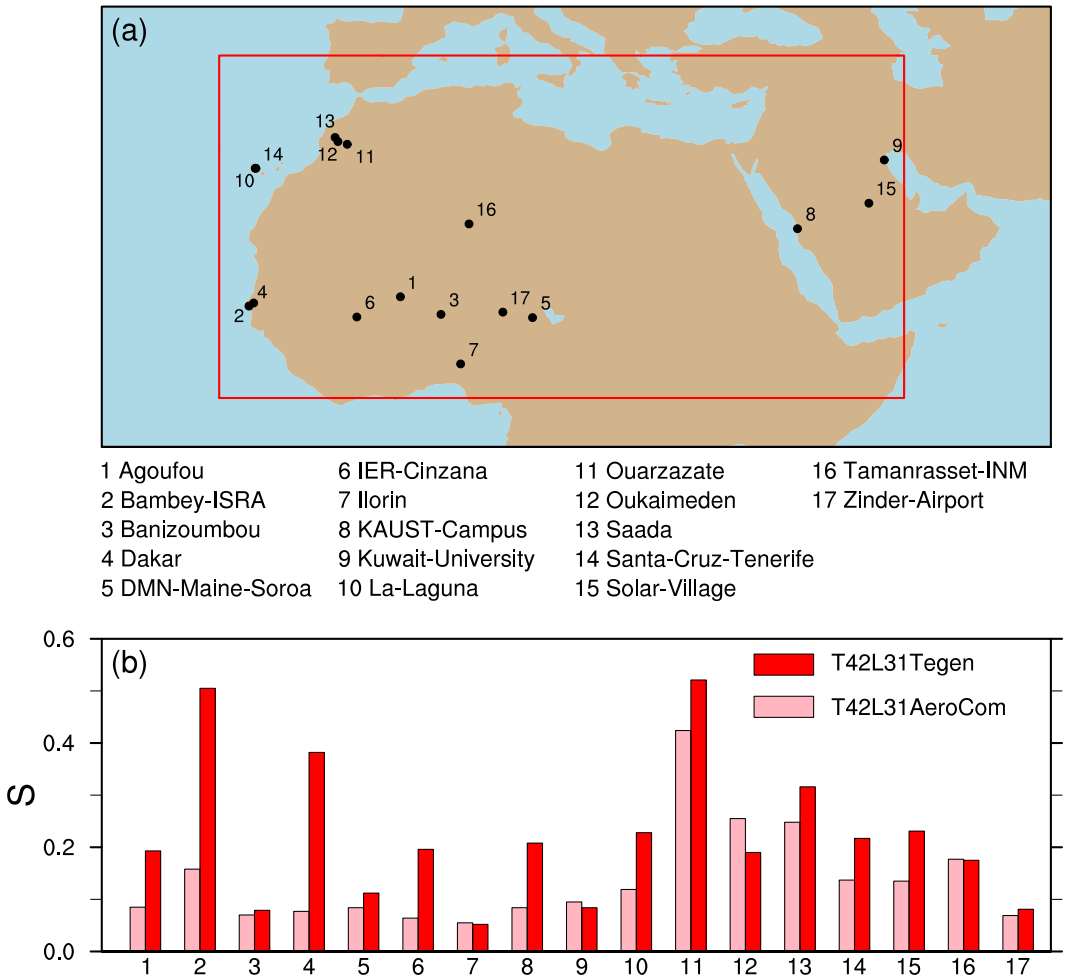

Figure 4.2: Locations of selected AERONET stations and skill scores for the T42L31AeroCom and T42L31Tegen setups. (a) AERONET stations in the region of 5° N–40° N and 20° W–50° E (red box), for the time period 2009–2013, with Ångstrom exponents of AE < 0.75 (AE averaged over the time period 2009–2013) and a minimum of 50 observation days were selected. (b) Skill scores (S) for these stations are calculated from AOD observations and model output for the T42L31AeroCom (pink bars) and T42L31Tegen setup (red bars), respectively. As shown in Beer et al. (2020, Fig. 4).

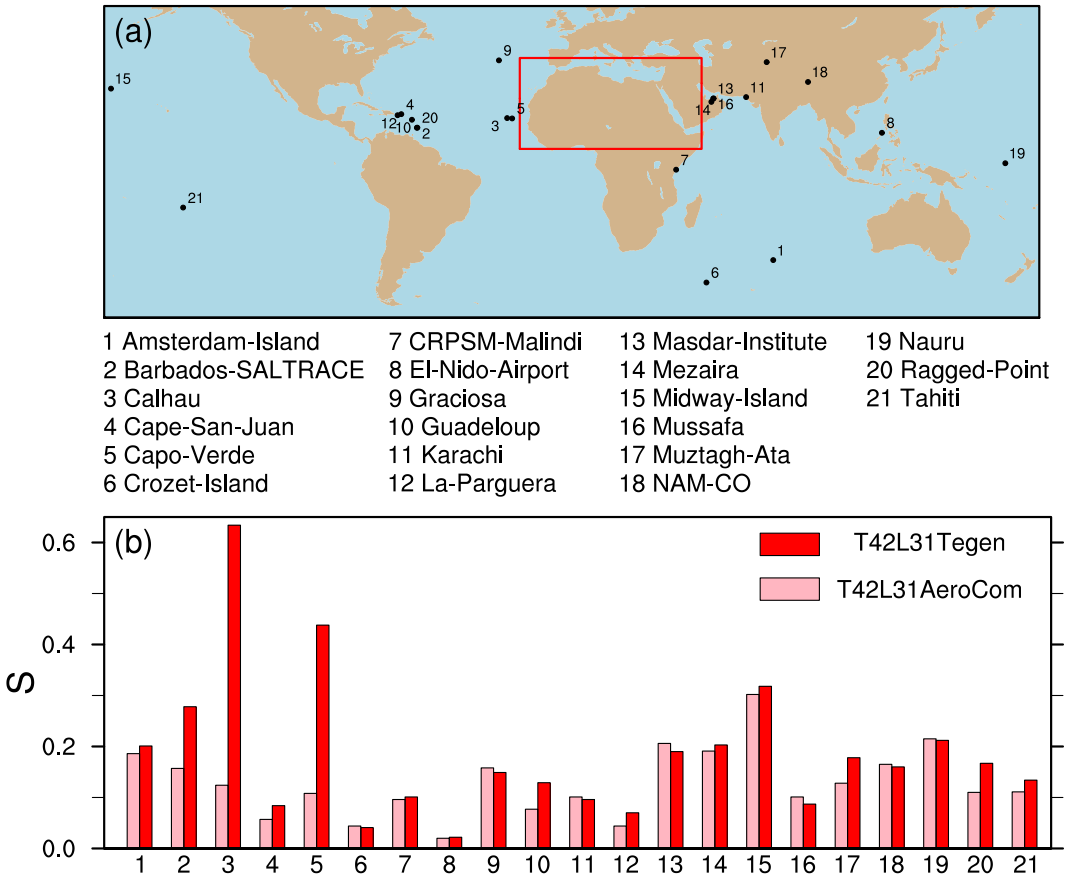

Figure 4.3: As in Fig. 4.2, but showing results for AERONET stations outside the region of 5° N–40° N and 20° W–50° E, for the time period 2009–2013. Stations with Ångstrom exponents of AE < 0.75 (AE averaged over the time period 2009–2013) and a minimum of 50 observation days were selected. As shown in Beer et al. (2020, Fig. S4).

ditional deviations may result from uncertainties in prescribed soil surface properties and modelled winds, as well as from assumptions on the specific optical properties of the single aerosol types in the AEROPT submodel in EMAC, which are used to calculate AOD. Furthermore, the assumption on the dust size distribution upon emission may lead to differences; this is analysed in Sect. 4.1.3 with a sensitivity experiment (T42L31TegenS).

4.1.2 Effects of model resolution

Previous EMAC studies employing the aerosol submodel MADE3 or its predecessors (Aquila et al., 2011; Righi et al., 2013, 2015, 2016; Kaiser et al., 2019) were mainly based on a relatively coarse model resolution of T42L19 (i.e. approx. 2.8 by 2.8 degrees in latitude and longitude with 19 vertical levels up to 10 hPa). In order to investigate the effect of the model resolution on dust emissions and transport with the Tegen et al. (2002) parametrization, simulations with enhanced vertical (T42L31Tegen) and horizontal (T63L31Tegen) model resolution are compared with the T42L19Tegen setup.

The simulated vertical aerosol distribution is compared with vertical aerosol concentration profiles measured during the SALTRACE campaign (Weinzierl et al., 2017). In general, comparing climatological 3-D model output with aircraft measurements is difficult and prone to large uncertainties due to the limited spatial and temporal data coverage of aircraft observations. In order to improve the climatological comparison method

used in Kaiser et al. (2019), the model is constrained here as described in Sect. 3.2.1 to reproduce the large-scale meteorological conditions during the episode of the field campaign. Furthermore, the S4D submodel is employed to extract model output along aircraft flight tracks online, i.e. during the model simulation, providing a more direct comparison of model output and aircraft observations, rather than by interpolating corresponding model values from the standard output. The aircraft observations have a time resolution of typically 1 to 10 seconds. For the evaluation, both the simulation and the measurement data are vertically binned into 1.6 km intervals. This enables a direct in situ-to-model comparison.

An additional analysis involves the comparison of the model results with ground-based lidar observations also collected during the SALTRACE campaign. In particular, vertical profiles of dust extinction coefficients at 532 nm, measured with a stationary lidar system located on Barbados (Groß et al., 2015, 2016), are considered. Simulation and lidar measurement data were binned into 500 m vertical intervals for this comparison.

In Fig. 4.4 vertical aerosol profiles of total particle number concentrations in two different size ranges, as well as vertical profiles of the lidar dust extinction coefficient are shown for the observations and the three different model setups, respectively. Only data from the SALTRACE-West regions (around Puerto Rico and Barbados) are presented here because of better data coverage due to a larger number of measurement flights compared to SALTRACE-East (around Cabo Verde). Number concentrations are shown for aerosol particles with diameters in the size range of $0.3\,\mu m < D < 1.0\,\mu m$ and $0.7\,\mu m < D < 50\,\mu m$, respectively. These size ranges represent the detection size limits of the particle counters used in the aircraft measurements and serve as rough estimates for aerosol numbers in the accumulation and coarse mode, respectively. The size cutoff values of the particle counters are also subject to uncertainties and may change slightly during a flight.

In general, the low resolution T42L19 setup shows a reasonably good agreement with both aircraft and lidar observations in the lower troposphere (up to around 600 hPa) but overestimates number concentrations and extinction coefficients at higher altitudes significantly, up to a factor of 10 for the number concentration above 400 hPa. This large positive bias is slightly reduced for the T42L31 setup with higher vertical resolution. When increasing both the horizontal and the vertical model resolution (T63L31 setup) the bias at higher altitudes vanishes almost completely in the comparisons with number concentration measurements (Fig. 4.4a, b). Number concentrations are reduced by up to a factor of 10 compared to the T42L19 setup above 400 hPa, so that they now correspond to observed values within the uncertainty ranges. Also, the steep gradient in the lidar observations around 600 hPa (Fig. 4.4c) is reproduced better by the T63L31 setup, with again up to 10 times lower values compared to the T42L19 setup. This steep decrease in the lidar observations is representative of the vertical extent of the Saharan Air Layer (SAL), a warm, dry, elevated air layer (reaching up to approx. 4 km in the Caribbean) in which the main dust transport from the Sahara to the Caribbean takes place (e.g., Weinzierl et al., 2017; Haarig et al., 2019; Gutleben et al., 2020).

The comparison with lidar observations is of special importance, as here the dust extinction coefficient provides a measure directly related to mineral dust, whereas in the total particle number concentrations also non-dust particles are included. Nevertheless, these size ranges comprising relatively large particles are probably dominated by mineral dust (Kaiser et al., 2019). The high bias of the T42L19 setup in the upper troposphere

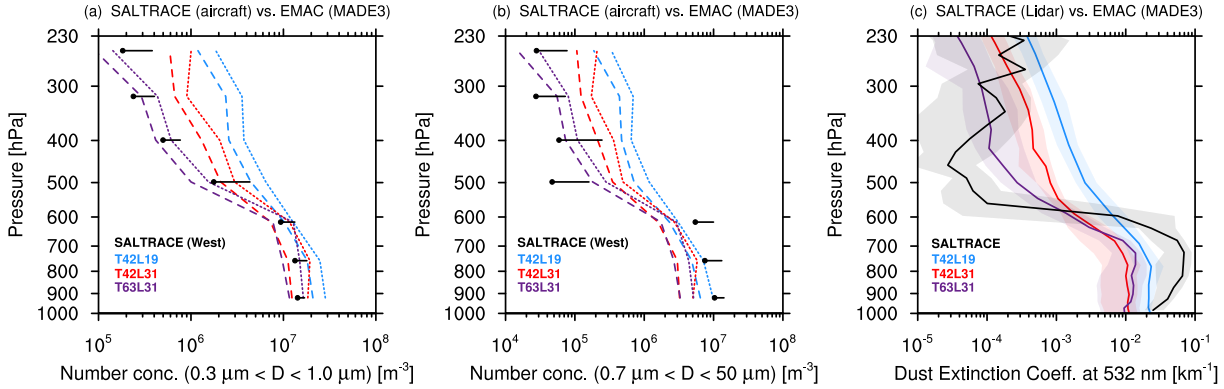

Figure 4.4: Comparisons between model results and different observational data from the SALTRACE mineral dust campaign (June, July 2013). (a) Data from aircraft measurements of total aerosol number concentration for particles with diameters in the range 0.3 µm < D < 1.0 µm are shown. Observational data from all SALTRACE-West flights (around Puerto Rico and Barbados) were binned into 1.6 km height bins in order to create the vertical profiles. Dots represent mean values, whiskers represent standard deviations of observations (only positive direction shown). Mean values (dashed lines) and standard deviations (dotted lines) of the model results are shown for the three different resolutions: T42L19 (blue), T42L31 (red), T63L31 (purple). (b) Similar to (a), but for total aerosol number concentrations in the size range 0.7 µm < D < 50 µm. (c) Simulated dust extinction coefficients compared with ground-based lidar measurements at Barbados. Simulation and lidar measurement data were binned into 500 m intervals. Lines represent median values, shadings represent 25th-75th percentiles for the observations (black) and the three model setups (blue, red, and purple), respectively. As shown in Beer et al. (2020, Fig. 5).

could be related to overestimated upward transport, possibly in convective plumes. This assumption is motivated by the fact that the convective top heights in the model (i.e. the uppermost model levels for convective transport) are on average approximately 15 percent higher in the T42L19 setup compared to T63L31 (890 hPa versus 780 hPa, also compared along the SALTRACE flight tracks). Another explanation for this strong positive bias could be an underestimation of aerosol scavenging through too-low an efficiency of the wet deposition processes in the model, as was also argued by Kaiser et al. (2019). A recent model study by Monerie et al. (2020) also described effects of increasing horizontal model resolution on simulated precipitation over South America. In that study the authors found that spatial and temporal features of precipitation are improved at higher model resolutions, probably as a result of a better representation of mesoscale convective systems.

A similar evaluation of the vertical aerosol total particle number distribution as presented in Fig. 4.4a, b (SALTRACE-West region) was performed for the SALTRACE-East region (around Cabo Verde; see Fig. 4.5). Those results show a similar behaviour as seen in Fig. 4.4a, b (SALTRACE-West), i.e. a large positive bias for the T42L19Tegen setup in the upper troposphere, which is reduced in the model configurations with higher spatial resolution (T42L31Tegen, T63L31Tegen). However, as only a few measurement flights were performed in that region, the data set is limited, which complicates the analysis and results in larger uncertainties. Additionally, the effect of increased model resolution on the AOD comparisons (as seen in Fig. 4.2) is analysed. However, no clear improvement of the model comparison with AERONET AOD data is visible from this analysis (see Fig. A.3 in the Appendix), as the increase of model resolution mainly influences the representation of long-range transport and dust properties larger distances away from the source regions. Also, as the AOD is an integral quantity, it is not strongly influenced by changes of the vertical model structure.

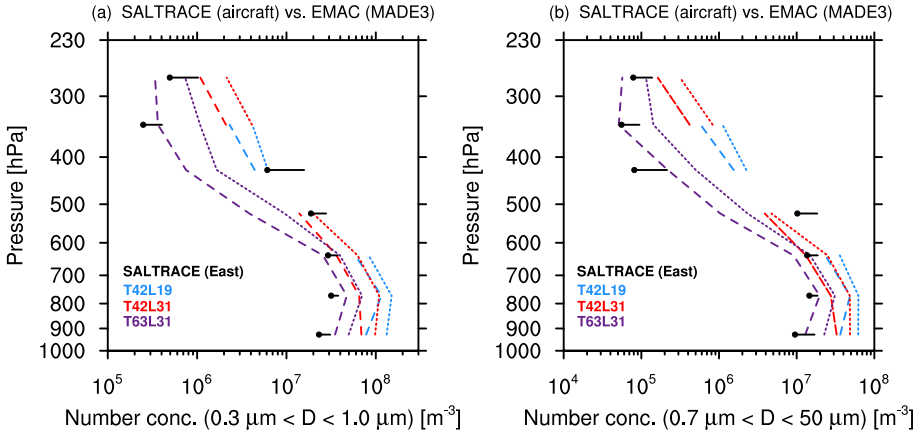

Figure 4.5: As in Fig. 4.4, but comparing model results with observational data from SALTRACE-East (region around Cabo Verde). A vertical binning of 1.5 km was employed. Missing values for the model curves result from too few data points available for a meaningful calculation of average and standard deviation in that bin. See Sect. 3.2 in the paper for details. As shown in Beer et al. (2020, Fig. S5).

4.1.3 Effects of size distribution assumptions

As described in Sect. 3.3.2, a typical mineral dust size distribution has to be assumed in the model in order to assign the emitted dust particles to the respective lognormal size modes of the MADE3 aerosol submodel and also to convert mass emissions to number emissions. This assumption controls key properties of the freshly emitted particles, such as the dust particle number concentration in the specific modes or the ratio of fine to coarse mode dust particle number concentration. Hence, it also has a large importance for modelling subsequent interactions of the particles with clouds and radiation. In order to analyse the sensitivity of the modelled atmospheric distribution and properties of mineral dust aerosols to an alternative size distribution assumption, an additional sensitivity simulation was performed (T42L31TegenS). In this experiment the dust size distribution calculated from aircraft-based in situ measurements during the SAMUM campaign (Saharan Mineral Dust Experiment) is applied instead of the AeroCom size distribution (Dentener et al., 2006) used in the T42L31Tegen simulation. Within the SAMUM project, two field experiments were performed, which focused on the properties of airborne Sahara dust particles near the source regions (SAMUM-1, conducted in May/June 2006 in Morocco) and the properties of transported dust (SAMUM-2, conducted in January/February 2008 in the Cabo Verde area). For this sensitivity experiment the median dust size distribution from SAMUM-1 given in Weinzierl et al. (2011) is used, which is based on numerous observations in elevated dust layers over the source region between 19 May 2006 and 7 June 2006 (Weinzierl et al., 2009). There, the particle number size distribution of mineral dust aerosol measured during that field campaign is represented by a lognormal distribution with four modes. As a bimodal size distribution is required as input for the dust emission scheme in EMAC-MADE3, the two smaller sized modes of the measured distribution are combined, as well as the two modes with larger particles, to match the accumulation and coarse mode of MADE3, respectively (as described in Sect. 3.3.2; resulting size distributions shown in Fig. 3.2).

The simulation output from the T42L31Tegen and T42L31TegenS experiments are compared with measurements from the SALTRACE campaign, similar to the evaluation in Sect. 4.1.2. Fig. 4.6 shows again aerosol number concentration profiles as well as vertical profiles of the lidar extinction coefficient (as seen in Fig. 4.4), but compar-

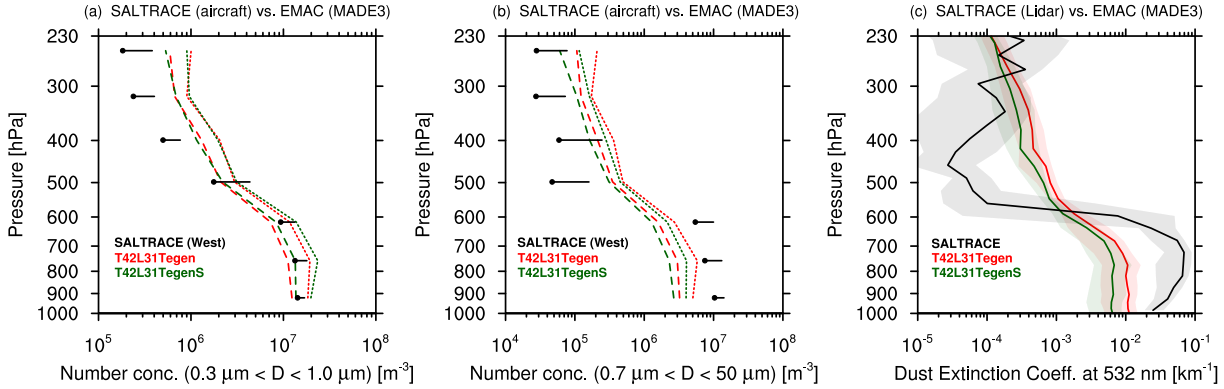

Figure 4.6: Similar to Fig. 4.4, but comparing the T42L31Tegen (red) and the T42L31TegenS (green) model setups with SALTRACE observations (black), i.e. the reference model setup and a setup with different assumptions for the size distribution of emitted dust. For the T42L31TegenS setup the dust size distribution calculated from measurements during the SAMUM-1 campaign is applied. As shown in Beer et al. (2020, Fig. 6).

ing the T42L31Tegen and T42L31TegenS model setups. For the sensitivity simulation (T42L31TegenS), number concentrations of smaller sized particles are slightly shifted to larger values (Fig. 4.6a), whereas concentrations of larger particles are slightly decreased (Fig. 4.6b). This is in line with the SAMUM-1 size distribution showing a larger (smaller) fraction of particles in the accumulation (coarse) mode, compared with the reference distribution (see also M2N values in Table 3.4). However, comparison of observed and simulated particle numbers is difficult, as the measured particle size ranges do not correspond directly to model accumulation and coarse mode. In the comparisons of dust extinction coefficients in Fig. 4.6c, the T42L31TegenS simulation shows smaller values. This is due to lower simulated dust mass concentrations compared with the reference simulation, resulting from stronger removal processes. The lower coarse mode numbers of the SAMUM-1 distribution lead to larger simulated particle diameters, as the emitted dust mass remains constant. These larger particles are more efficiently removed by sedimentation and dry deposition processes in the model, with approximately 10 percent larger sedimentation and dry deposition fluxes in northern Africa and the Caribbean. However, sedimentation of coarse particles is generally problematic for modal schemes, as size distributions may develop and deviate from the assumption of lognormal modes. Additionally, recent observations, in particular also during SALTRACE, found coarse and giant particles large distances downwind of their sources (Weinzierl et al., 2017; Ryder et al., 2019). This could also hint to possibly missing processes in the model that keep large dust particles airborne over that long distances (Gasteiger et al., 2017). Additionally, a recent study by O'Sullivan et al. (2020) shows that models often transport Saharan dust at too low altitudes in the atmosphere and underestimate coarse dust numbers.

In general, the differences between the two setups in Fig. 4.6 are small, with no notable improvement for the comparison with observations. Johnson et al. (2012) and Nabat et al. (2012) found improved agreement of simulated AOD with observations when using a dust representation with a larger fraction of the dust mass emitted in the coarse mode. However, the SAMUM-1 dust size distribution shows a larger fraction of emitted dust in the accumulation mode, compared with the reference size distribution. A comparison with AOD measurements from AERONET stations is shown in Fig. A.4 in the Appendix and shows worse agreement for the T42L31TegenS simulation. Testing a size distribution with a larger fraction of dust particles in the coarse mode could be a subject for future

studies. Additionally, a slight bias towards smaller particles in the SAMUM-1 data could be due to effects of dust transport from emission to observation regions. However, as the flights took place near the source regions, this effect is probably small.

4.1.4 Summary and conclusions: mineral dust

In this section, two different representations of modelled mineral dust are applied and compared. On the one hand, a climatology of prescribed monthly-mean dust emissions from the AeroCom climatology is used, as was also the case in the Kaiser et al. (2019) reference setup. On the other hand, the Tegen et al. (2002) dust emission parametrization is employed, where mineral dust emissions are calculated online for each model time step. The simulated aerosol optical depth at dust dominated locations is compared with observations from the AERONET station network. Results show that employing the Tegen et al. (2002) dust parametrization leads to improved agreement with observations compared with the offline dust model setup. Modelled AOD values show distinctively higher skill scores when evaluated against several dust-dominated AERONET stations in northern Africa (average skill score value of 0.22 for the online calculated dust setup versus 0.14 for the offline dust setup). This improvement is most likely due to a better representation of the highly variable wind-driven dust emissions and strong dust burst events.

Furthermore, the effect of increasing the horizontal and vertical model resolution on the dispersion of dust in the Tegen et al. (2002) dust emission model setup is analysed, by comparing the model results with ground-based lidar remote sensing and aircraft measurements performed during the SALTRACE mineral dust campaign. Increasing the vertical (setup T42L31) and both the vertical and horizontal (setup T63L31) model resolution from a setup with a spherical truncation of T42 and 19 vertical hybrid pressure levels (setup T42L19) results in an improved agreement between model and observations, especially in the upper troposphere (above 400 hPa). The main improvement is achieved by increasing the horizontal model resolution from T42 to T63. Modelled particle number concentrations and dust extinction coefficients above 400 hPa decrease by up to a factor of 10, for the T63L31 setup versus T42L19. Overall, the long-range transport of mineral dust from northern Africa to the Caribbean, as well as the vertical transport into the upper troposphere is well represented in this improved model setup.

Finally, the effect of varying the assumptions for the size distribution of emitted dust is tested when employing the Tegen et al. (2002) dust parametrization, by adopting the size distribution measured during the SAMUM-1 dust campaign (setup T42L31TegenS). However, no clear improvement with respect to the reference setup (T42L31-Tegen) is achieved. Applying a size distribution with a larger fraction of dust particles in the coarse mode may improve the model results and could be a subject for future studies.

In general, an improved representation of atmospheric mineral dust in EMAC(MADE3) is achieved, especially due to an enhanced representation of dust emissions, compared with previous model setups. Figure 4.7 shows the resulting simulated dust mass concentrations for the high resolution online dust emission setup (T63L31Tegen) near the surface (i.e. in the lowermost model layer), at 300 hPa, and the zonal-mean vertical distribution. As mineral dust is a primary aerosol, dust concentrations in the atmosphere are strongly connected to its emission regions (see Fig. 4.7). Concentrations of up to 100 $\mu g\,m^{-3}$ are

reached at the surface over the main desert regions (e.g. the Sahara and Arabian Desert). The model improvements described above provide an important foundation for follow-up model studies on the role of dust particles in the climate system including, for instance, simulations of the climatic impact of dust-induced modifications of cirrus clouds (see also Sect. 4.6).

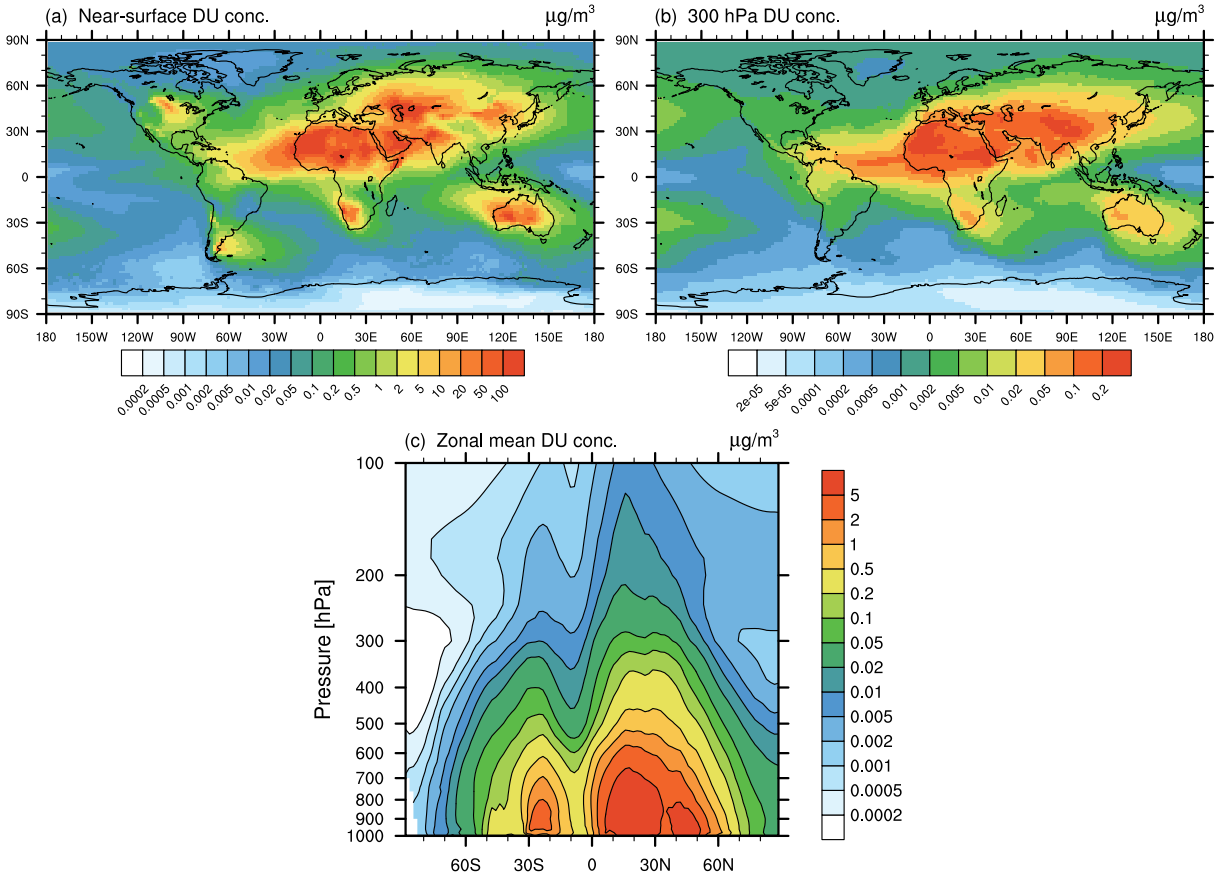

Figure 4.7: Simulated mineral dust mass concentrations in units of $\mu g\,m^{-3}$ for the T63L31Tegen setup (multi-annual mean, years 2000–2004). Dust concentrations are shown (a) near the surface, (b) at the 300 hPa level, and (c) as zonal-mean vertical distribution (pressure vs. latitude). Note the different scales in each plot.

4.2 Black carbon in EMAC-MADE3

In this section the simulated global distribution of atmospheric black carbon (BC) is presented. An improved representation of BC in the EMAC-MADE3 model is achieved by increasing the horizontal and vertical model resolution, as also described in the previous section for the case of mineral dust.

In addition to measurements focusing on mineral dust, black carbon mass mixing ratios were measured during the SALTRACE campaign, likely representing aerosol particles originating from biomass burning events in Central Africa (Weinzierl et al., 2017). Hence, a similar comparison as for aerosol particle numbers (as seen in Fig. 4.4) can be performed for BC mass mixing ratios (in units of $\mathrm{ng\,kg^{-1}}$) for the three different model setups (Fig. 4.8). Again, the high bias in the upper troposphere is significantly reduced for the T63L31Tegen setup relative to T42L19Tegen. This corroborates the findings described in the previous section concerning mineral dust aerosols.

Additionally, modelled BC mass mixing ratios, as well as number concentrations of particles in different size regimes were evaluated against several aircraft measurements from several campaigns, as done in Kaiser et al. (2019). The results are shown in Fig. A.6 and Fig. A.7 in the Appendix. This evaluation is performed on a climatological basis, i.e. comparing long-term simulations with the observation campaign data, as described in detail by Kaiser et al. (2019). Results from the T63L31Tegen model setup (enhanced horizontal and vertical resolution with online calculated dust) are compared with the model results from Kaiser et al. (2019), i.e. T42L19 resolution with prescribed monthly-mean AeroCom dust emissions. For most comparisons, the T63L31Tegen setup shows only slight changes and often a better agreement with observations compared with the Kaiser et al. (2019) simulation. This clearly shows that, beyond the representation of mineral dust, the enhanced model resolution generally improves the representation of the global aerosol.

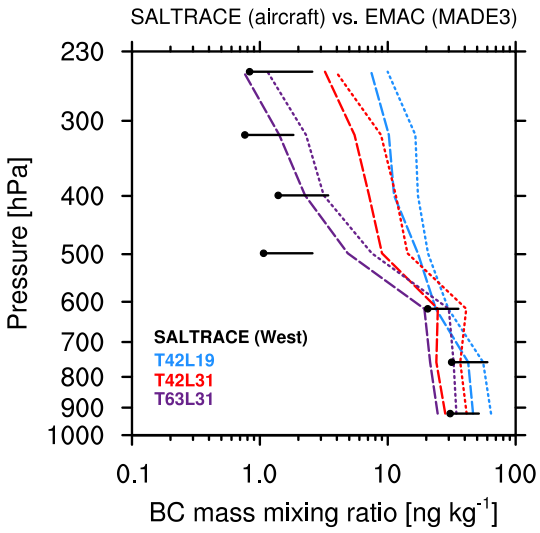

Figure 4.8: Similar to Fig. 4.4a and b, but comparing black carbon mass mixing ratio profiles for SALTRACE observations and model results for the three different model resolutions. As shown in Beer et al. (2020, Fig. S7).

The resulting BC mass concentrations simulated with EMAC-MADE3 using the T63L31 resolution setup is shown in Fig. 4.9 near the surface, at 300 hPa, and as zonal-mean vertical distribution. The highest BC concentrations occur on the Northern Hemisphere, where main sources of anthropogenic soot particles, produced from incomplete combustion of fossil fuels, are situated. Additionally, biomass burning is a possible source of atmospheric BC in remote regions on the Southern Hemisphere (e.g. in Africa and South America). Compared to the dust mass concentrations in Fig. 4.7, BC mass concentrations are much lower with peak values of up to 1 µg m^{-3} at the surface.

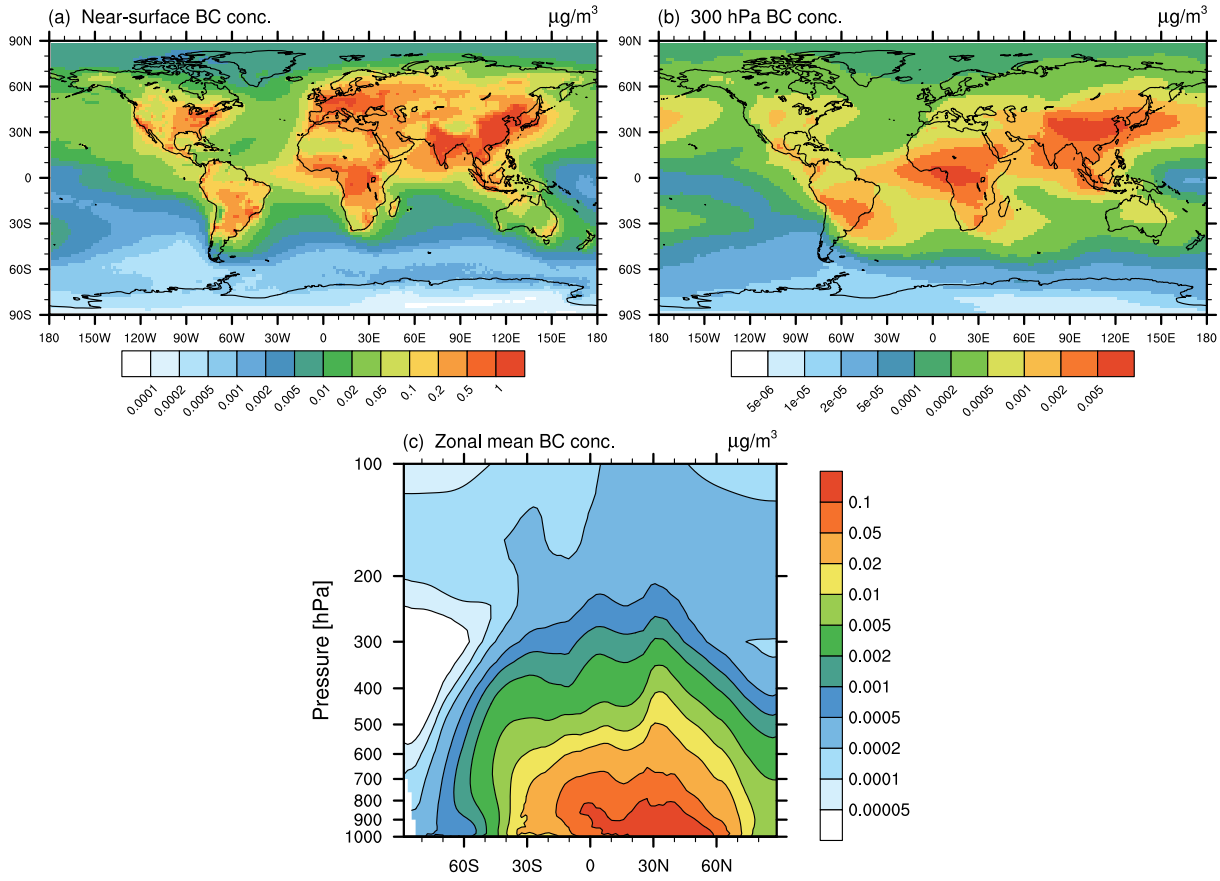

Figure 4.9: Simulated black carbon mass concentrations (BC emissions from all sources) in units of µg m^{-3} for a simulation with T63L31 model resolution (multi-annual mean, years 2000–2004). BC concentrations are shown (a) near the surface, (b) at the 300 hPa level, and (c) as zonal-mean vertical distribution.

4.3 Glassy organic particles in EMAC-MADE3

In this section, model results concerning the atmospheric dispersion of newly implemented glassy organic particles are presented. The additional MADE3 tracer glPOM represents organic particles formed from the condensation of natural precursors of organic aerosols, e.g. terpenes (see Sect. 3.4.2). Emissions occur mainly in regions with strong biogenic activity, e.g. tropical rainforests. Only high-viscosity, glassy particles are considered according to the phase separation depending on the ambient temperature and the glass transition temperature T_g.

The glass transition temperature is strongly influenced by the relative humidity according to Eq. 3.8, with T_g increasing with decreasing RH. Only for $T < T_g$ glassy particles can occur. This condition is only rarely fulfilled near the surface, where glPOM is only present in low concentrations in northern and southern polar regions (Fig. 4.10a). The highest mass concentrations (larger than 0.01 µg m^{-3}) are reached at pressure levels (or altitudes) above the 600 hPa niveau (Fig. 4.10b, c). There, the low ambient temperatures favour the occurrence of the glassy phase. Additionally, dry environments with low RH and therefore high T_g (e.g. the northern and southern midlatitudes around 600 hPa in addition to midlatitudes and polar regions in the upper troposphere above 200 hPa) lead

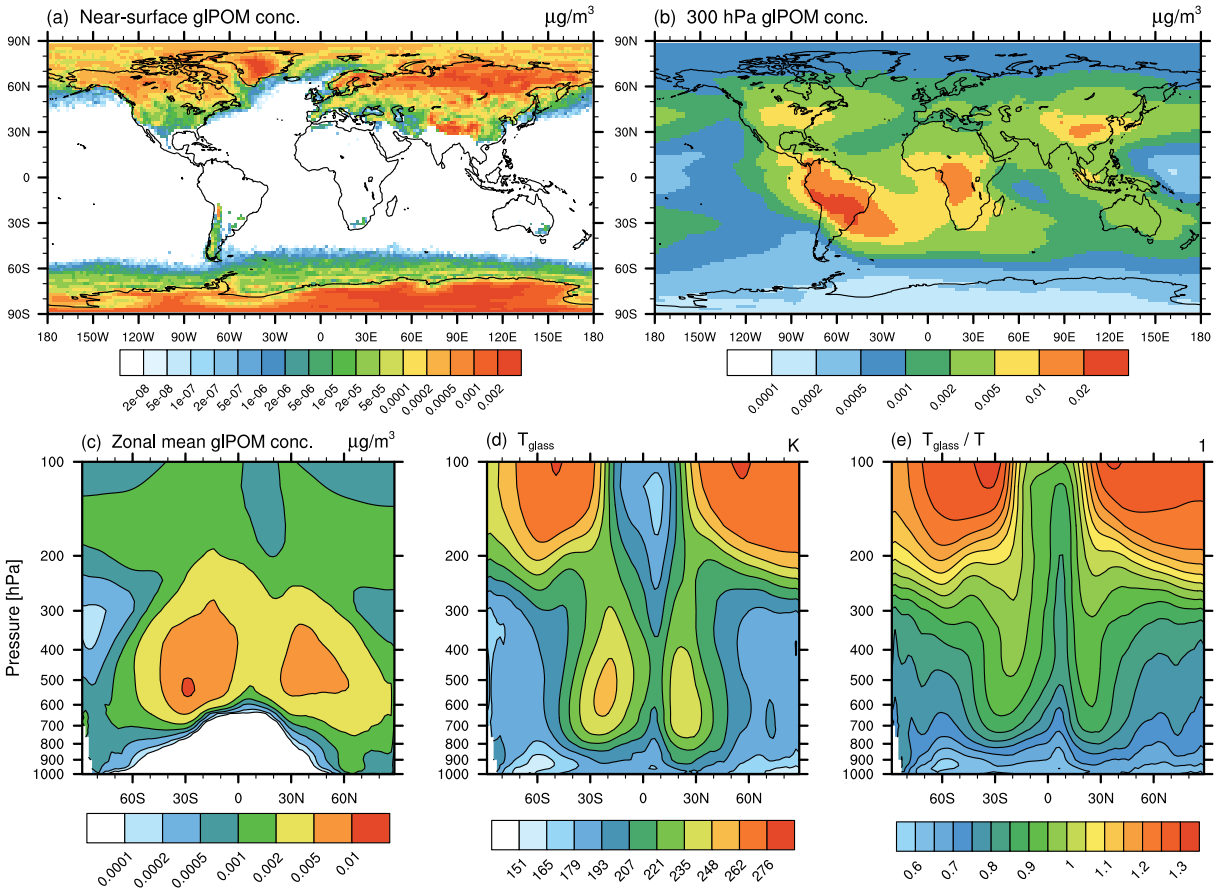

Figure 4.10: Simulated mass concentrations of glassy organics in EMAC-MADE3 from a simulation with T63L31 model resolution (multi-annual mean, years 2000–2004). glPOM mass concentrations in units of µg m^{-3} are shown (a) near the surface, (b) at the 300 hPa level, and (c) as zonal-mean vertical distribution. Additionally, the zonal-mean glass transition temperature T_g, and the ratio T_g/T indicating the particle phase state, are shown in (d) and (e), respectively.

to favourable conditions for glassy particles. This is in agreement with measurements of glassy SOA particles, which were found to exist in an amorphous solid state at cirrus temperatures (e.g., Järvinen et al., 2016), while mostly liquid SOA particles were observed in humid tropical regions (e.g., Bateman et al., 2015).

The ratio T_g/T can be used as an indicator of the particle phase state (Fig. 4.10e). For $T_g/T \geq 1$ the particle behaves like a solid, while $T_g/T < 1$ indicates a semi-solid or liquid state (Shiraiwa et al., 2017). A comparison of the ratio T_g/T with model results from Shiraiwa et al. (2017), also employing the global EMAC model, shows in general a good agreement of the global patterns. However, their results indicate that already above around 500 hPa almost all SOA particles are transformed into a glassy solid state, while this is here the case only above 250 hPa. Deviations could be due to the different model representation of SOA particles and the parametrization of glass transition temperatures. Instead of the simple calculation depending on the relative humidity adopted here, Shiraiwa et al. (2017) employ the organic aerosol submodule ORACLE to simulate the phase state of atmospheric SOA. A simplified approach is chosen here, as this is the first attempt to include glassy organic INPs in EMAC-MADE3, their effect on cirrus clouds is highly uncertain, and this approach reduces computational cost while facilitating the interpretation of results.

4.4 Crystalline ammonium sulfate in EMAC-MADE3

In this section, model results concerning the newly implemented ammonium sulfate tracer (AmSu) are presented. A detailed description of related calculations and parametrizations of the life cycle of atmospheric ammonium sulfate particles in EMAC-MADE3 is given in Sect. 3.4.3. AmSu is implemented as a number density tracer and includes a formulation of phase transitions depending on the ambient relative humidity, i.e. only the crystalline form is represented by this tracer. To analyse the sensitivity of modelled AmSu to different assumptions for its size and composition, different representations of AmSu tracers are used (see Sect. 3.4.3). $\mathrm{AmSu_{mixS}}$ and $\mathrm{AmSu_{mixL}}$ consider crystalline ammonium sulfate with smaller and larger particle diameters internally mixed with other components, while $\mathrm{AmSu_{ext}}$ assumes externally mixed pure ammonium sulfate crystals. Number concentrations of these three AmSu tracers near the surface, at the 300 hPa level, and as zonal-mean vertical distribution are shown in Fig. 4.11. These results represent averages over the whole simulated time period, which includes cases where ammonium sulfate occurs in its crystalline form but also cases where the environmental conditions exclude the formation of AmSu crystals.

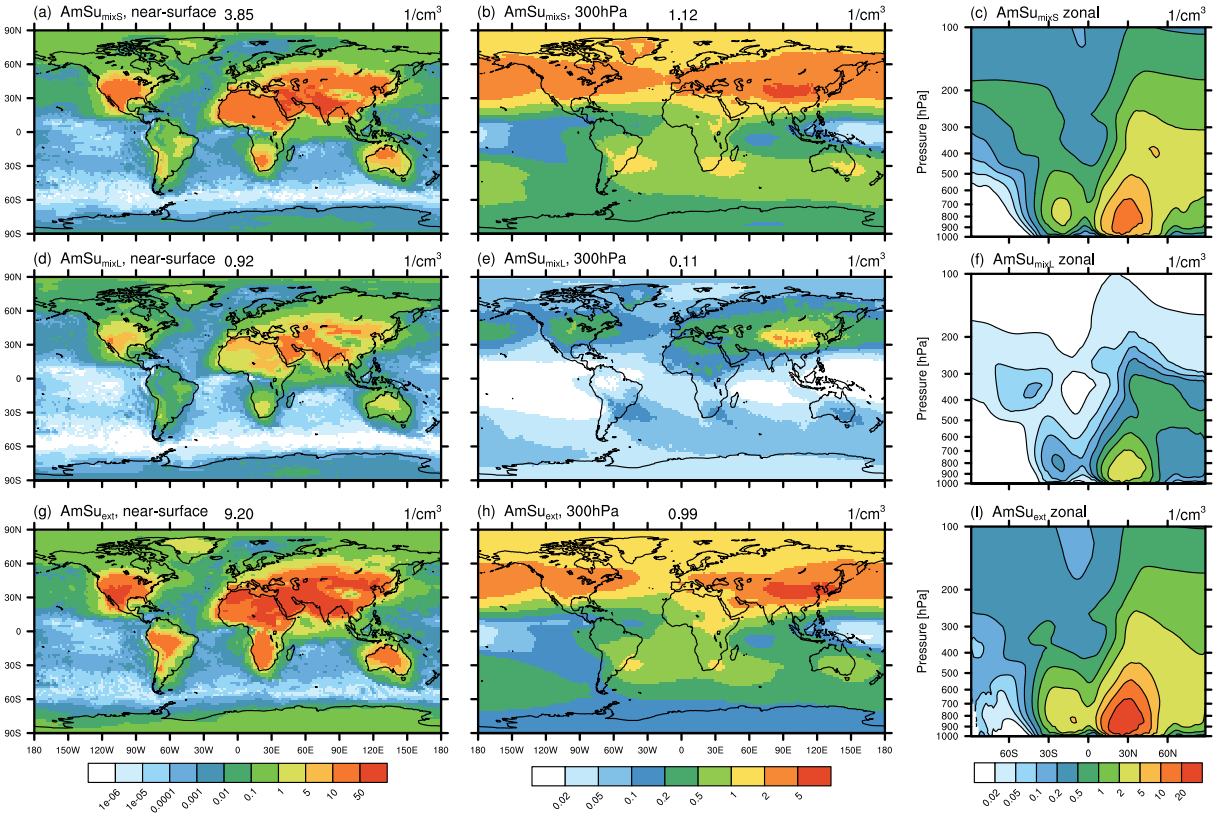

Figure 4.11: Simulated crystalline ammonium sulfate number concentrations in EMAC-MADE3 from a simulation with T63L31 model resolution (multi-annual mean, years 2000–2004). Number concentrations in units of $\mathrm{cm^{-3}}$ are shown for different AmSu tracers, i.e $\mathrm{AmSu_{mixS}}$ (a, b, c), $\mathrm{AmSu_{mixL}}$ (d, e, f), $\mathrm{AmSu_{ext}}$ (g, h, i). AmSu concentrations are shown near the surface (a, d, g), at the 300 hPa level (b, e, h), and as zonal-mean (c, f, i). Numbers above the map plots represent global averages at that respective pressure level. Note the different scales in each column.

The global patterns are similar for all three AmSu tracers. High number concentrations are simulated at ground level over the continents and in large parts of the middle and upper troposphere. $AmSu_{mixL}$ shows the lowest concentration values, as these particles have a larger diameter, which leads to fewer numbers in the mass-to-number conversion of the aerosol mass (Sect. 3.4.3 and Eq. 3.6). Highest number concentrations are found for $AmSu_{ext}$ (above $50\,cm^{-3}$ near the surface). The sum of $AmSu_{mixS}$ and $AmSu_{mixL}$ concentrations is similar to that of $AmSu_{ext}$ indicating a low sensitivity to the assumption of internally or externally mixed particles.

The global dispersion of crystalline ammonium sulfate is strongly related to concentrations of NH_4 and SO_4 from which it is formed (see Fig. A.10 in the Appendix). Sources of aerosol sulfate and ammonium are predominantly of anthropogenic origin, e.g. the combustion of sulfur-containing fossil fuels or the use of ammoniacal fertilizers, and are mostly situated on the Northern Hemisphere (see Sect. 2.1.1.2). Furthermore, the ambient environmental conditions have to fulfil the requirements for ammonium sulfate to reside in the solid phase. Only if the ambient RH is below the efflorescence relative humidity (ERH) crystallization can occur. Zonal-mean profiles of RH and ERH are shown in Fig. 4.12d, e. These quantities are variable in time, i.e. the analysis of multi-year means gives only an approximate overview about the AmSu phase state.

ERH is calculated depending on the ammonium-to-sulfate ratio according to Eq. 3.11. Upon re-hydration ammonium sulfate crystals remain solid until the deliquescence relative humidity (DRH) is reached, which is 80 % for ammonium sulfate (Martin, 2000). Figures 4.12a-c depict the solid fraction of ammonium sulfate, which increases with in-

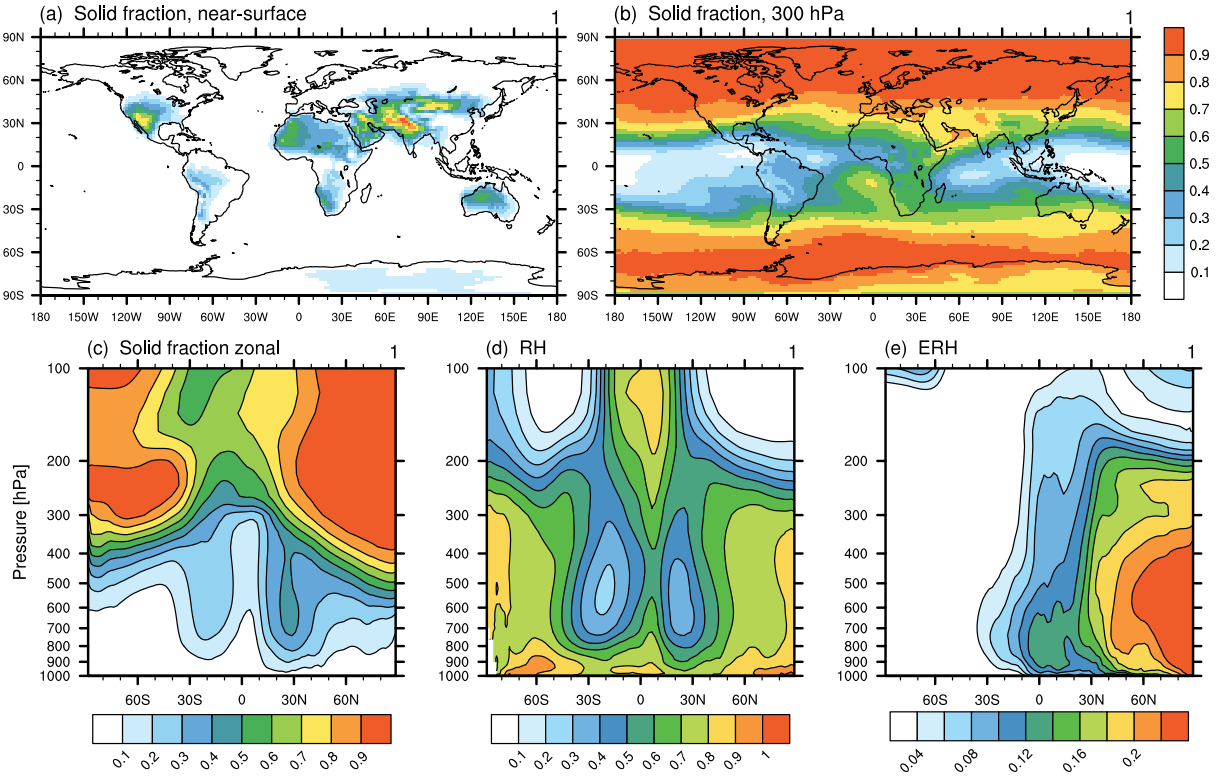

Figure 4.12: Modelled AmSu solid fractions in EMAC-MADE3 from a simulation with T63L31 model resolution (multi-annual mean, years 2000–2004). (a-c) Fraction of solid ammonium sulfate particles near the surface, at 300 hPa, and as zonal-mean vertical distribution, (d) zonal-mean relative humidity, (e) zonal-mean efflorescence relative humidity. All quantities are dimensionless.

creasing altitude and shows the largest values (close to 1) in the upper troposphere of the Northern Hemisphere. High solid fractions are closely related to dry regions with low RH, which favours the formation of the crystalline phase.

The global distribution of simulated AmSu concentrations is in good agreement with results from other model studies. Wang et al. (2008) analysed the distribution of solid and aqueous sulfate aerosols employing the GEOS-Chem chemical transport model (Martin et al., 2004; Park et al., 2004) and simulated a similar global distribution pattern of solid ammonium sulfate particles as shown in Fig.4.11. Penner et al. (2018) used the CAM/IMPACT atmospheric model to simulate the aerosol effect on cirrus clouds, including a representation for solid ammonium sulfate in their model and found also similar global distributions of ammonium sulfate particles compared with the ones presented here.

Figure 4.12 shows the simulated solid fractions of ammonium sulfate. As crystallization depends on the ambient relative humidity (RH) and the efflorescence relative humidity (ERH; see also Sect. 3.4.3), large solid fractions occur in regions with low RH and high ERH (see Fig. 4.12d, e). The simulated solid fractions shown in Fig. 4.12 are in good quantitative agreement with results from Wang et al. (2008) and also Colberg et al. (2003), where a Lagrangian model is employed that calculates trajectories from ECMWF analyses and takes the deliquescence/efflorescence hysteresis of ammonium sulfate into account. Similar to glPOM, the implementation of AmSu in the EMAC-MADE3 model represents a simplified approach (see Sect. 3.4.3) to present a first order estimate of the highly uncertain climate effects regarding cirrus cloud modifications due to AmSu INPs.

4.5 Climatology of ice nucleating particles

In this section the global distribution of the different INPs simulated with EMAC-MADE3 is presented. Additionally, results concerning pristine, i.e. newly formed ice crystal numbers from heterogeneous freezing, as well as ice water content (i.e. ice mass per unit mass of air) per heterogeneous freezing mode are shown.

Simulations presented here, were performed with a lower horizontal model resolution, i.e. the T42L31 setup. This has the advantage of requiring lower computational resources, which is essential for performing a large number of sensitivity experiments to analyse aerosol induced cirrus modifications (as shown in Sect. 4.6). In addition to the results on DU, BC, glPOM, and AmSu applying the higher resolution model setup (T63L31) presented in the previous sections, aerosol mass concentrations (of DU, BC, and glPOM), and number concentrations (of AmSu) simulated with the T42L31 setup are shown in Fig. A.5, Fig. A.8, Fig. A.9, and Fig. A.11, respectively, in the Appendix.

4.5.1 Global distributions of INPs and nucleated ice crystals

Global distributions of number concentrations of different INPs (DU, BC, AmSu, glPOM, BCair) in units of L^{-1} are shown in Fig. 4.13, calculated from a simulation with T42L31 resolution using instantaneous (11 hour) model output (three-year annual mean over the years 2009–2011, averaged over all pressure levels). For this comparison the number concentrations of potential INPs (calculations described in Sect. 3.5.1) are multiplied by the ice-active fraction f_{act} provided by measurements (see Table 3.3), to obtain the actual concentrations of INPs. Here, values of f_{act} at a supersaturation ratio with respect to ice of $S_i = 1.4$ are chosen. At such a high S_i value near the homogeneous freezing threshold, all different INP-types are able to nucleate ice. This facilitates a direct comparison of INP number concentrations, as possible biases due to different freezing efficiencies are excluded. For this analysis only grid boxes inside cirrus clouds are considered, selected according to simulated ambient temperature ($T < -35\,°\mathrm{C}$) and ice water content ($\mathrm{IWC} > 0.5\,\mathrm{mg/kg}$). The global distribution of average cirrus cloud occurrence frequency calculated according to these threshold values for T and IWC is shown in Fig. 4.14.

Peak INP number concentrations per species in Fig. 4.13 reach values of up to $50\,L^{-1}$ for most INP types, while total INP number concentrations show values of up to $100\,L^{-1}$. Mineral dust INPs are mostly concentrated near strong dust emission regions (e.g. the Sahara or Arabian Desert), but also in regions of enhanced dust-transport (e.g. over the Atlantic Ocean). The INP-types BC, BCair and AmSu show a strong hemispheric gradient with high concentrations on the Northern Hemisphere, as these INPs are strongly related to anthropogenic activities (e.g. combustion of fossil fuels, industrial processes). For the case of BCair the main flight corridors are clearly visible, which are dominated by air traffic over the Northern Atlantic Ocean. BCair number concentrations of up to $2\,L^{-1}$ are generally smaller compared to other INP-types. However, BCair numbers could be larger, as the activated fraction of BCair ($f_{\mathrm{act}} = 0.003$) is chosen according to the value for BC. This represents a rather conservative assumption, as aircraft soot could possibly be preactivated via cloud processing (e.g., Mahrt et al., 2018; David et al., 2019; Nichman et al., 2019) (see Sect. 2.3.1.1). Glassy organic INPs are more homogeneously distributed over Northern and Southern Hemisphere with highest concentrations over regions of strong

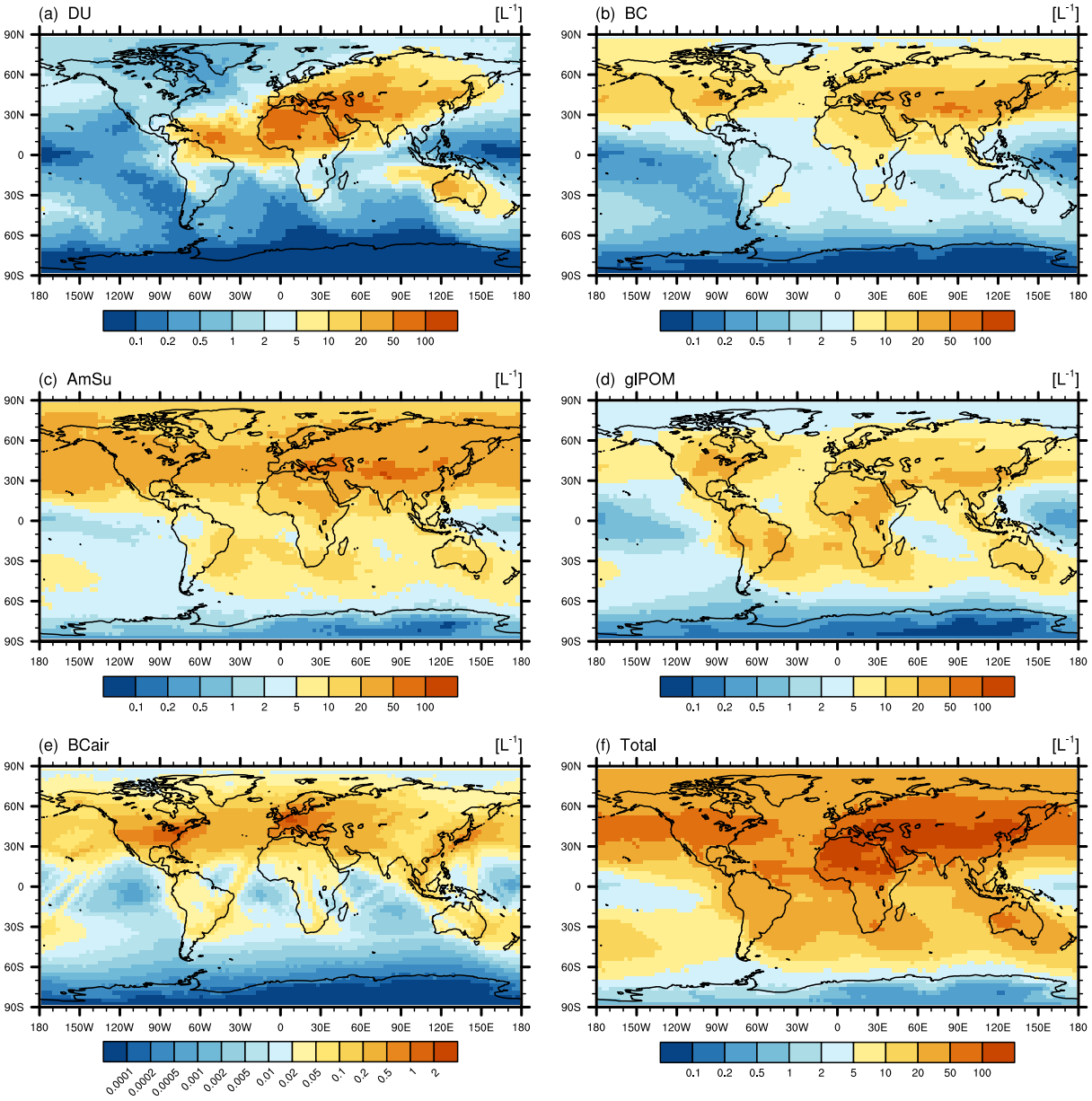

Figure 4.13: Global distribution of simulated number concentrations of different INPs (in units of L^{-1}) inside cirrus clouds (selecting only grid boxes with cirrus occurrence) calculated from a simulation with T43L31 model resolution, multi-annual mean (years 2009–2011) and average over all vertical levels. Shown are (a) DU, (b) BC, (c) AmSu, (d) glPOM, (e) BCair, and (f) total INP concentrations. Cirrus conditions are selected according to modelled ambient temperature ($T < -35\,°C$) and ice water content (IWC $> 0.5\,mg/kg$) in every grid box. Number concentrations of potential INPs (see calculations in Sect. 3.5.1) are weighted with ice-active fractions, f_{act} at ice supersaturations of S_i= 1.4, from laboratory measurements (see Table 3.3). Note the different scale in panel (e).

biogenic activity (e.g. tropical rainforests) with number concentrations mostly around $10\,\mathrm{L}^{-1}$, slightly smaller compared to most other INP-types. As stated earlier, glassy organics as well as crystalline ammonium sulfate INPs occur not invariably, as their phase state depends on the ambient temperature and humidity. Differences of the global distribution of INPs as seen in Fig. 4.13 compared to the respective aerosol concentrations shown in the previous sections are a result of the selection of cirrus conditions, but can also be related to the assumptions and calculations of INP numbers as described in Sect. 3.5.1.

A direct comparison of model results with in situ observations of INP numbers in cirrus clouds is challenging, as most measurements took place at lower altitudes and focused on mixed-phase temperatures. Also, in situ measurements of collected particle samples were often performed using diffusion chambers (e.g., Rogers et al., 2001b), where temperatures and supersaturations can be directly controlled but may not correspond to the actual ambient conditions at sample collection, e.g. temperatures below the homogeneous freezing threshold are often difficult to realize. Several studies describe in situ observations of number concentrations of atmospheric INPs, mostly collected at low altitudes and analysed at temperatures above $-35\,°\mathrm{C}$, ranging from concentrations below $0.1\,\mathrm{L}^{-1}$ to several $100\,\mathrm{L}^{-1}$ (e.g., Rogers et al., 1998, 2001a; DeMott et al., 2010; Schrod et al., 2017), in accordance with INP concentrations simulated here (Fig. 4.13). Additionally, the positive bias of aerosol concentrations due to the lower horizontal model resolution (T42) with respect to the T63 setup in the upper troposphere (see Sect. 4.1.2) can lead to about two times higher number concentrations of INPs and has to be considered when comparing model results with observations.

In addition to the global distributions in Fig. 4.13, a more condensed analysis is presented in Fig. 4.15a. INP number concentrations for five different latitude regions are shown as a frequency distribution. Frequencies are drawn as shaded colours for every INP-type and latitude region. Mean and median values for every INP-type and region are shown as filled dots and open diamonds, respectively. Number concentrations of potential INPs are again multiplied with f_{act} at $S_i = 1.4$, and cirrus conditions are selected according to temperature and ice water content.

All INP-types except glPOM show a marked difference between Northern and Southern Hemisphere with the highest concentrations at northern latitudes. BC, BCair and AmSu are mostly concentrated in the region of 30°–60° N as anthropogenic influences and emissions play a key role for these INP-types. Aircraft BC has notable concentrations al-

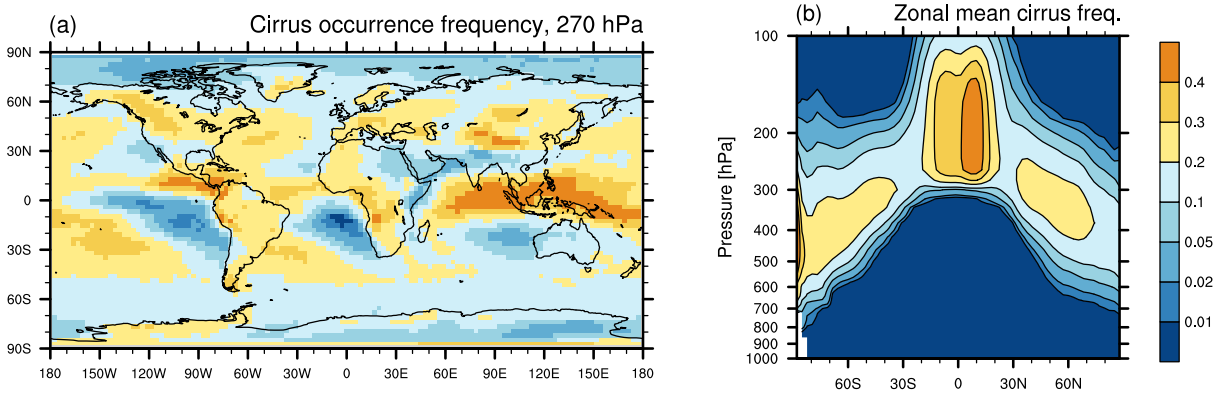

Figure 4.14: Global distribution of modelled cirrus cloud occurrence frequency (annual mean, years 2009–2011) calculated according to temperature ($T < -35\,°\mathrm{C}$) and ice water content ($\mathrm{IWC} > 0.5\,\mathrm{mg/kg}$). (a) Cirrus frequency at 270 hPa. (b) Zonal-mean cirrus frequency.

most only in this region with a concentration of around $1\,L^{-1}$ occurring with probabilities between 20 % and 50 %. In other regions BCair concentrations are generally much lower than those of other INPs. Non-aircraft BC INPs frequently reach concentrations of up to $10\,L^{-1}$ in those regions. AmSu INPs show high concentrations of up to $40\,L^{-1}$, exceeding in most cases other INP concentrations. However, in many other cases AmSu concentrations are very low or zero (bottom bins occurring with probabilities of up to 50 %). These are mainly related to ambient conditions where ammonium sulfate does not occur in its crystalline state. Mineral dust INPs occur most frequently in the latitude region around the equator and 30°–60° N, where dominant dust emission regions are situated (e.g. the Sahara, Arabian and Asian deserts). Glassy organic INPs are almost evenly distributed over all latitudes except the southern polar region, with concentrations between 1 and $10\,L^{-1}$. In contrast to AmSu, glPOM has only very low occurrence probabilities in the lowest concentration bin (below 2 %). This indicates that conditions favouring the glassy phase are nearly always fulfilled in the cirrus regime.

Figures 4.13 and 4.15a can help to identify regions on the globe where different INP-types are likely to compete with each other for the available supersaturated water vapour during the freezing process. On the Southern Hemisphere a competition between ammonium sulfate and glassy organics is possible, as these INPs are highly concentrated in southern regions while other INP-types show only low concentrations. The Northern Atlantic is a possible competition region between AmSu and BCair INPs. Over most regions in Central Asia several different INP-types (DU, BC, AmSu) are present in relatively similar concentrations indicating possible competition mechanisms between these INPs.

Similar to INP concentrations, the number concentrations of newly formed, pristine ice crystals formed via heterogeneous freezing induced by INPs, and the corresponding ice water content (i.e. cloud ice mass per unit mass of air) are shown in Fig. 4.15b, c for each heterogeneous freezing mode. Here, an additional selection criterion is employed to select only grid boxes with low concentrations of preexisting ice crystals ($N_{\mathrm{preex}} < 10^{-5}\,m^{-3}$). This represents conditions where pristine ice crystals form via heterogeneous and homogeneous nucleation. Additionally, those cases where the crystal size exceeds a certain threshold ($R_{\mathrm{ice}} > 1000\,\mu m$) are filtered out, as such large crystals readily sediment and are removed from the cirrus niveau. This threshold is chosen according to the analysis of crystal sizes of newly formed ice crystals (see Fig. A.13 in the Appendix) to include most of the distribution of simulated R_{ice} values, while excluding very large crystals.

Concentrations of newly formed ice crystals from the different freezing modes (Fig. 4.15b) are generally lower than INP number concentrations (on average about 1–2 orders of magnitude). Additionally, very small values (bottom bins in Fig. 4.15b) occur much more frequently. This clearly shows that only a fraction of the number of INPs actually nucleates and forms ice crystals. In addition to N_{ice} from heterogeneous freezing modes, the number concentrations of homogeneously formed ice crystals are shown in Fig. 4.16. These are for all latitude regions much higher than concentrations of heterogeneously formed ice crystals (up to 3–4 orders of magnitude). This indicates that heterogeneous freezing is, in most cases, not able to suppress homogeneous freezing completely; it can, however, attenuate it. The extent of this effect is analysed in Sect. 4.6.

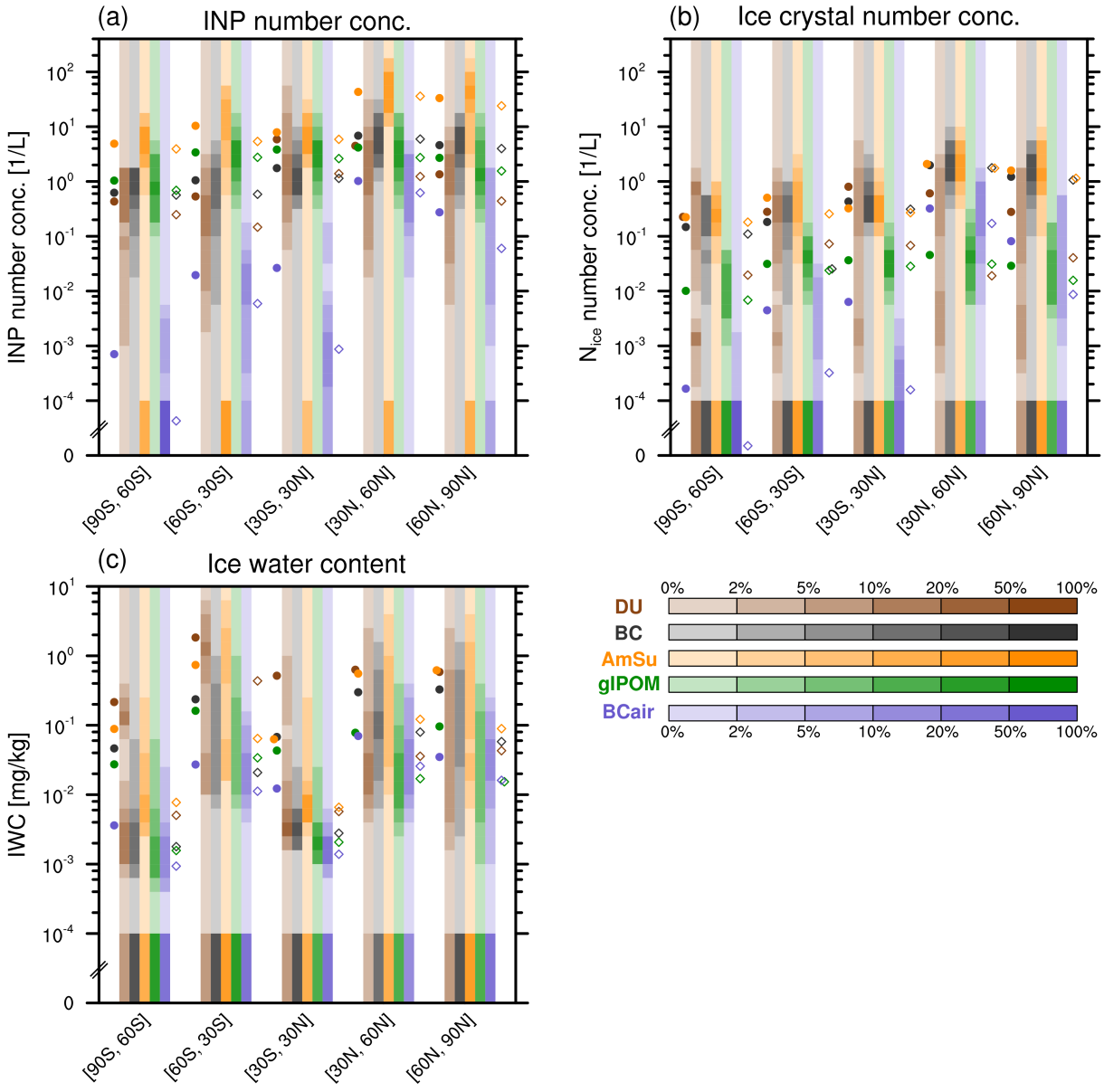

Figure 4.15: Frequency distributions of (a) modelled INP number concentrations (in units of L^{-1}), (b) number concentrations of pristine ice crystals (N_{ice}; in units of L^{-1}), and (c) ice water content (IWC; in units of $mg\,kg^{-1}$) inside cirrus clouds per freezing mode for five different latitude regions (in steps of 30 degrees), considering the simulated period 2009–2011. Shaded colours represent the frequency of occurrence for the respective variable considering four (a, b) and five (c) logarithmic bins per order of magnitude; DU (brown), BC (black), AmSu (orange), glPOM (green), BCair (purple). The bottom bin includes all values down to zero. Cirrus conditions are selected according to temperature ($T < -35\,°C$) and ice water content (IWC $> 0.5\,mg\,kg^{-1}$) in every grid box. Additionally, only grid boxes with a low contribution of ice-formation on preexisting ice crystals are selected ($N_{preex} < 10^{-5} m^{-3}$). Number concentrations of potential INPs are weighted with ice-active fractions from laboratory measurements (f_{act} at $S_i = 1.4$, see Table 3.3). Filled dots to the left of every latitude region denote mean values for the different INPs. Open diamonds to the right represent median values.

Figure 4.15c shows the ice water content (i.e. cloud ice mass per unit mass of air) for each heterogeneous freezing mode, calculated from N_{ice} and R_{ice} assuming spherical ice crystals. The IWC measures how much ice mass accumulates on INPs during the freezing process, which in turn results in the growth of ice crystals. INPs with a high freezing-efficiency, initiate nucleation already at relatively low ice-supersaturations, resulting in ice crystals growing to larger sizes during the freezing process. Here, the highly efficient mineral dust INPs, often dominate the IWC in several regions with average values up to $2\,\text{mg}\,\text{kg}^{-1}$. The high frequencies of large dust-IWC values result in larger average values compared to other INP-types.

Simulated INP numbers can be compared with in situ observations that were, however, mostly performed at altitudes below the cirrus level and focused on the mixed-phase temperature regime. Rogers et al. (1998) describe aircraft measurements performed in North America at high altitudes around 10 km but analysed samples at temperatures mostly above −30 °C in a flow diffusion chamber. They reported INP concentrations between $\sim$ 0.1 and $500\,\text{L}^{-1}$, with larger concentrations at lower temperatures and higher supersaturations. This agrees well with simulated results in that region (Fig. 4.13f). Additionally, Rogers et al. (2001a) analysed aircraft measurements conducted in the Arctic for temperatures between −10 °C and −30 °C and humidities ranging from ice saturation to water supersaturation. They observed an average INP-concentration of $16\,\text{L}^{-1}$ with rare very high values (hundreds per litre). This is in good accordance with modelled INP concentrations in the region of 60°–90° N of around $10\,\text{L}^{-1}$. DeMott et al. (2010) present a parametrization of INP data using a combination of data from several different aircraft campaigns. Measurements were mostly performed for temperatures above −34 °C and INP concentrations ranging from 0.1–$100\,\text{L}^{-1}$ were observed, which corresponds to the range of modelled values (Fig. 4.15a). Jensen et al. (2010, 2013) focus on cirrus clouds in the TTL, and predict that measured ice crystal numbers and cloud optical properties are in accordance with INP concentrations below $20\,\text{L}^{-1}$. This is in agreement with model results in the equatorial region presented here (Figs. 4.13, 4.15a).

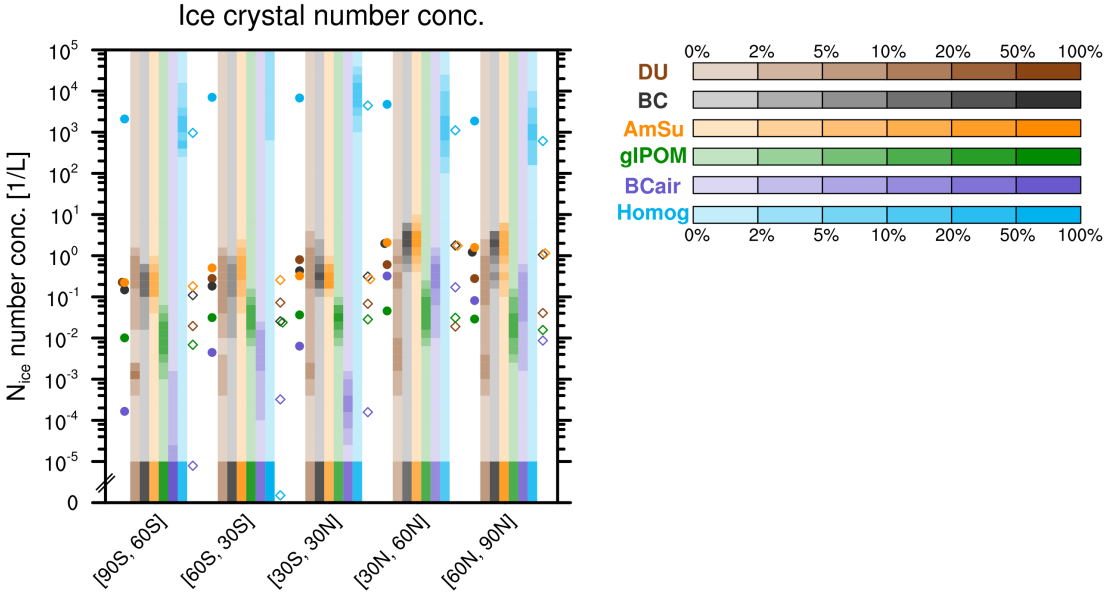

Figure 4.16: As in Fig. 4.15, but additionally showing the frequency distribution of ice crystals formed by homogeneous freezing (light blue).

Additionally, Schrod et al. (2017) presented measurements performed with unmanned aircraft systems over the Eastern Mediterranean at altitudes below 2.5 km and reported INP peak concentrations of above $100\,\mathrm{L}^{-1}$ at $-30\,^{\circ}\mathrm{C}$, also confirming the model results presented in Fig. 4.13f.

In addition to observations, other global model studies have been performed to analyse the distribution of ice nucleating particles on the globe. Barahona et al. (2010) carried out simulations with the NASA Global Modeling Initiative chemical and transport model (Rotman et al., 2001; Liu et al., 2007), coupled to an analytical ice microphysics parametrization, considering DU, BC, and glassy organics as heterogeneous freezing nuclei. Their results show INP concentrations mostly around $5\,\mathrm{L}^{-1}$ in the equatorial region, which is in accordance with the results presented here (Fig. 4.15a). Hendricks et al. (2011) performed a similar study to analyse the effect of INPs on cirrus clouds employing the ECHAM4 general circulation model (Roeckner et al., 1996), considering heterogeneous freezing on DU and BC in addition to homogeneous freezing. They report modelled ice crystal number concentrations formed via heterogeneous freezing between 0.01 and $0.1\,\mathrm{L}^{-1}$ in agreement with the range of N_{ice} values described in this section (Fig. 4.15b). However, N_{ice} from BC freezing in Hendricks et al. (2011) is about 10 times lower compared to the dust freezing mode. This difference between DU and BC is not visible in the results presented here. Disparities with respect to Hendricks et al. (2011) could be due to differences in the representation of the atmospheric aerosol and the parametrizations of the freezing process.

4.5.2 Summary and conclusions: INP climatology

In this section, a global climatology of simulated INP number concentrations inside cirrus clouds was presented in addition to the global distribution of pristine ice crystal numbers and ice water content per freezing mode, enabling a direct comparison between the different INP-types. In general, INP number concentrations are largest on the Northern Hemisphere (about $10\,\mathrm{L}^{-1}$, and occasionally reaching concentrations of up to $100\,\mathrm{L}^{-1}$). Aircraft BC shows relevant contributions (concentrations of about $1\,\mathrm{L}^{-1}$) between 30° and 60° N, where the majority of flight trajectories are located. The newly implemented glassy organic INPs show concentrations comparable to mineral dust and black carbon, with a larger contribution on the Southern Hemisphere, due to strong biogenic activity. Crystalline ammonium sulfate INPs occasionally reach very high concentrations (up to $100\,\mathrm{L}^{-1}$ on the Northern Hemisphere) but also often show low concentrations where ammonium sulfate is not in its crystalline state. Number concentrations of pristine, heterogeneously formed ice crystals are typically lower than INP number concentrations by one to two orders of magnitude, and are much lower than those of homogeneously formed crystals (up to 3–4 orders of magnitude). The analysis of ice water content per freezing mode indicates a high importance of very efficient INPs, like mineral dust, as ice crystals nucleate earlier and grow to larger sizes. In general, a comparison with observations is difficult due to limited in situ measurements in the cirrus regime. However, the results presented here agree well with in situ observations, mostly performed at $T > -35\,^{\circ}\mathrm{C}$ and also other model studies.

4.6 Cirrus cloud modifications and radiative effects

In this section, the modifications of cirrus clouds and radiation induced by the different INPs are described in detail. Simulations were performed with the T42L31 model resolution (simulation setup described in Sect. 3.2). This lower model resolution (compared to the T63L31 setup) is necessary to reduce the computation cost for the large number of sensitivity experiments conducted here. Additionally, the setup includes the coupling of the MADE3 aerosol to (cirrus) clouds as described in Righi et al. (2020) (two-moment cloud scheme, Sect. 3.2.5). There, a detailed evaluation and tuning of this cloud scheme was performed. The main difference here is the lower vertical model resolution: 31 vertical levels compared to 41 levels in Righi et al. (2020). This was chosen to limit the required computation cost for the large number of sensitivity experiments to be performed, but also to be consistent with the model version used in the previous sections evaluating simulated concentrations of DU, BC, glPOM, and AmSu. A comparison of simulated global cloud and radiation variables between these two model versions is presented below in this section (see Table 4.1), showing, in general, only slight deviations, thus supporting the results presented here. Additionally, model simulations employing this explicitly tuned model setup at higher vertical resolution (as in Righi et al., 2020) will be the subject of planned future studies.

The results presented here describe the effect of INPs on cirrus clouds and radiation, calculated as the difference between simulations with heterogeneous freezing (INPs) in addition to homogeneous freezing and simulations with purely homogeneous freezing (no INPs). Often these differences are small, occur infrequently, and spatio-temporal distributions are often difficult to quantify, due to the low signal-to-noise ratio when analysing effects at specific locations. Therefore, a condensed analysis, considering global and regional differences (tropical, southern-, and northern extra-tropical latitude regions) above the 400 hPa level (to set a focus on cirrus modifications) facilitates the interpretation of the results.

In the following, the effects of different INPs, as well as the total INP-effect with respect to homogeneous freezing are presented in Sect. 4.6.1. Additional sensitivity experiments concerning the role of the dynamic forcing (i.e. the updraft velocity influencing the cooling rate during the freezing process) are analysed in Sect. 4.6.2. Differences between Simulations performed in nudged and free-running mode are evaluated in Sect. 4.6.3. Furthermore, the effects of cloud-seeding using highly-efficient INPs are presented in Sect. 4.6.4. Finally, potential influences of anthropogenic INPs are analysed in Sect. 4.6.5.

4.6.1 Effects of different INPs

In Fig. 4.17 the effect of all INPs (i.e. DU, BC, BCair, AmSu, and glPOM) on different cloud and radiation variables is shown. This effect is calculated as the difference between two simulations: one simulation including heterogeneous freezing on these INPs (in addition to homogeneous freezing) – a simulation including only homogeneous freezing. Results for the top-of-the-atmosphere (TOA) radiative effects (all-sky and cloudy-sky) are represented as absolute differences in units of $\mathrm{W\,m^{-2}}$ (Fig. 4.17a, b), while relative differences (in %) are shown for the other variables (Fig. 4.17c–f), i.e. ice crystal number concentrations (ICNC), ice water content (IWC), cloud occurrence frequency (CLFREQ), and the total water mass concentration (H2Otot, water vapour plus ice mass).

For each quantity the global and regional, latitude-specific (Southern Hemisphere extra-tropics, tropics, Northern Hemisphere extra-tropics) differences are shown. The statistical confidence of the calculated anomalies is assessed employing a paired-sample Student's t-test, with the null hypothesis that the annual mean values of a given quantity (e.g. the radiative effect) are identical in the two simulations (with and without heterogeneous freezing). The response of the t-test is represented in terms of confidence levels (in %), i.e. $100\,(1-p)$, where p is the p-value. The results are regarded as statistically significant for confidence levels larger than 90 % ($p < 0.1$). Calculations of the confidence levels with respect to the model interannual variability include corrections for possible auto-correlations (lag-1) between different years (Zwiers and von Storch, 1995).

The freezing parametrization requires freezing properties to be specified for each INP-type, i.e. representative values for S_c and f_{act} (see Sect. 3.2.5). However, in reality the activated fraction of INPs increases with increasing ice-supersaturations during the freezing process (e.g., Ladino et al., 2014; Ignatius et al., 2016). These complete freezing spectra are, however, for reasons of computational efficiency not included in the parametrization. To quantify uncertainties related to prescribing specific freezing properties, two cases are analysed (see also Table 3.3): (i) freezing properties representative of freezing onset conditions, i.e. low freezing efficiencies and f_{act} values (red bars in Fig. 4.17), and (ii) freezing properties in the centre of the freezing spectrum, i.e. larger f_{act} values (middle point between freezing onset and homogeneous freezing threshold; blue bars in Fig. 4.17).

Model results, assuming onset freezing conditions (red bars), show a negative radiative effect due to heterogeneous freezing on INPs, i.e. a cooling of the climate system. This cooling effect is largest on the Northern Hemisphere, with TOA radiative forcings of about -50 $\mathrm{mW\,m^{-2}}$ and -70 $\mathrm{mW\,m^{-2}}$ for the cloud and total radiative effects, respectively, considering the freezing onset assumption for f_{act} (Fig. 4.17a, b). Global values are, however, below the significance-level of 90 %. Ice crystal numbers and total water mass are reduced with respect to the pure homogeneous freezing case (Fig. 4.17c, f). The occurrence frequency of clouds is mostly enhanced with relative changes of up to 4 %, while the IWC signal shows enhanced values on the Southern Hemisphere and a reduction on the Northern Hemisphere. Additionally, to show more details of these effects, zonal-mean vertical distributions of simulated cloud variables, as well as absolute differences with respect to homogeneous freezing are presented in Fig. A.12 and Fig. A.14 in the Appendix.

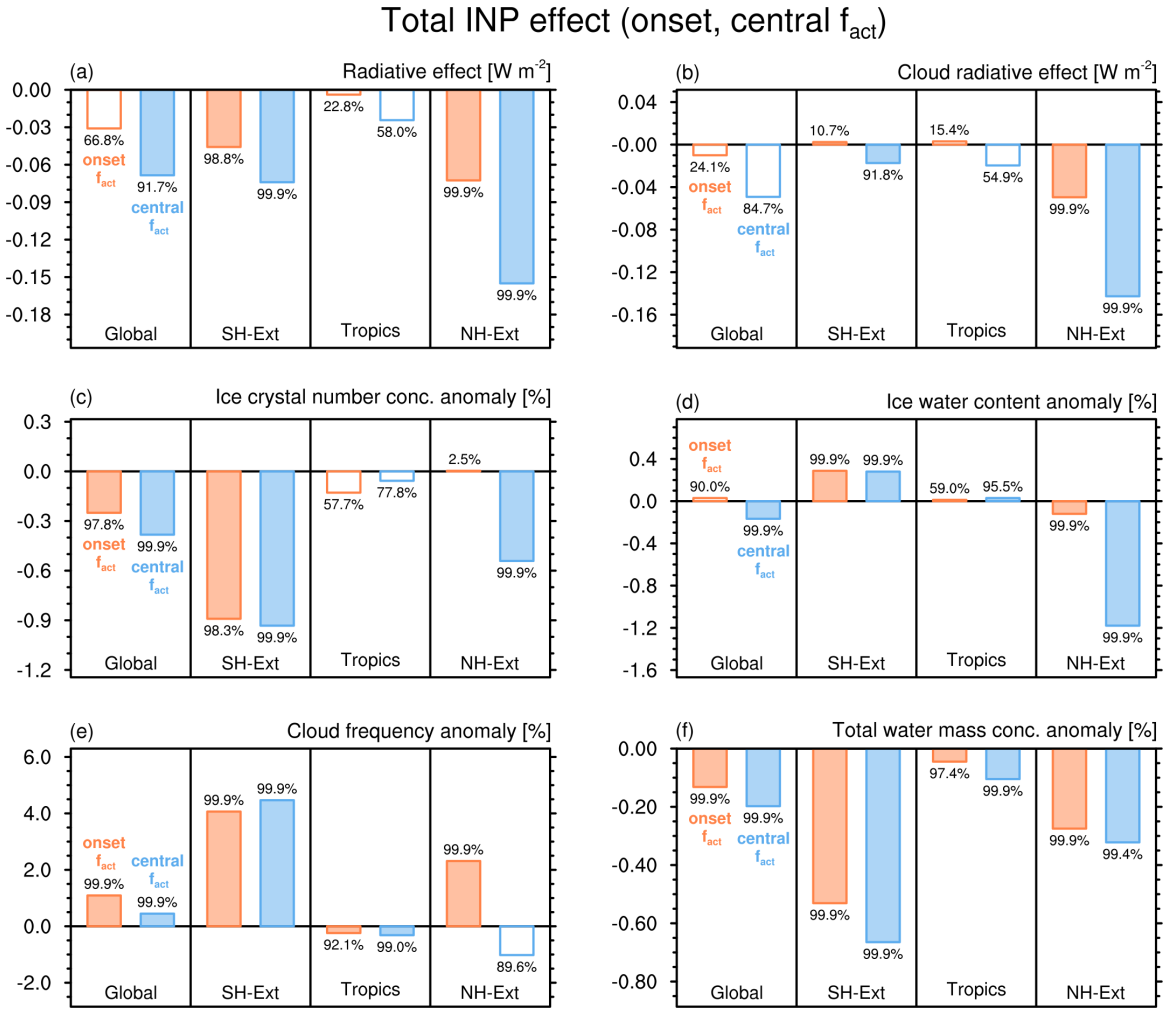

Figure 4.17: Effect of all INPs (DU, BC, BCair, AmSu, glPOM) calculated from the difference between a simulation including these INPs and a simulation with only homogeneous freezing (multi-annual mean, years 2000–2004, average above the 400 hPa pressure level for panels (c-f) and top-of-the-atmosphere value, i.e. the uppermost model level, for panels (a, b)). Two different freezing conditions are chosen for the activated fractions f_{act}, i.e. freezing onset values (red bars), and larger f_{act} values in the centre of the freezing spectrum (blue bars, middle point between freezing onset and homogeneous freezing threshold, see Table 3.3). Global and latitude-specific, regional differences are shown for (a) the radiative effect at the top-of-the-atmosphere (TOA), (b) the cloud radiative effect (difference of all-sky – clear-sky values), (c) the ice crystal number concentration, (d) the ice water content, (e) the cloud occurrence frequency, (f) the total water mass concentration (water vapour plus ice mass). Absolute differences (simulation with heterogeneous freezing – simulation with purely homogeneous freezing) are shown for the radiative effects in units of $\mathrm{W\,m^{-2}}$ (a, b), relative differences (in %) with respect to purely homogeneous freezing for the other variables (c–f). Latitude regions are Southern Hemisphere extra-tropics (90°–30° S), tropics (30° S–30° N), and Northern Hemisphere extra-tropics (30°–90° N). Confidence levels (in %) with respect to the model interannual variability are calculated according to the two-tailed Student's t-test and are shown at the top of each bar. Differences below the 90 % significance-level are drawn as open bars, differences above 90 % as filled bars. Note the different y-axis scales in each plot.

An enhancement of the freezing properties, using larger values of f_{act} in the centre of the freezing spectrum (middle point between freezing onset and homogeneous freezing threshold, see Table 3.3) results in similar features as for freezing-onset conditions, albeit with larger effects (and higher statistical confidence; blue bars in Fig. 4.17). The global radiative effect due to the presence of INPs is significant with about $-68 \pm 28\,\mathrm{mW\,m^{-2}}$ ($\pm$ 1 standard deviation range). The Northern Hemisphere shows the largest cooling effect of $-155 \pm 36\,\mathrm{mW\,m^{-2}}$. In reality the activated fraction of INPs increases with increasing ice-supersaturations during the freezing process (e.g., Ladino et al., 2014; Ignatius et al., 2016), while the freezing parametrization considers a single f_{act} value for each INP-type. Using freezing-onset conditions (with lower f_{act} values) therefore represents a more conservative assumption, while a larger f_{act} (in the centre of the freezing spectrum) could be more realistic.

As described in Sect. 2.3.1, the presence of INPs results in a competition between heterogeneous freezing (at relatively low ice-supersaturation) and homogeneous freezing (at higher supersaturation). This typically leads to a reduction in ice crystal numbers, and the formation of larger ice crystals compared to homogeneous freezing, as shown e.g. in a process-model study by Kärcher et al. (2006). This reduction of ice crystal numbers is also visible in the global simulations (Fig. 4.17c), and is in agreement with previous global modelling studies (e.g. Hendricks et al., 2011; Gasparini and Lohmann, 2016; Zhu and Penner, 2020). The decrease of total water (water vapour and ice) mass indicates an increased sedimentation loss of the larger crystals resulting in a thinning of cirrus clouds. In addition to this process, the presence of INPs can also increase the occurrence frequency of cirrus clouds, as heterogeneous freezing occurs earlier than homogeneous freezing (at lower critical supersaturations S_c with respect to ice), resulting in an increased cloud lifetime (Fig. 4.17e).

In general cirrus clouds have a pronounced longwave warming effect (absorption of terrestrial radiation), which together with the smaller shortwave cooling (reflection of solar radiation) results in a net warming of the atmosphere (e.g., Chen et al., 2000; Gasparini and Lohmann, 2016). This global warming is strongly enhanced during night times due to the missing shortwave cooling effect. The results presented here indicate a thinning of cirrus clouds in the presence of INPs due to fewer ice crystals and stronger sedimentation. Together with a tendency of reduced cloud frequency on the Northern Hemisphere this leads to a strong cooling effect, i.e. a reduced cirrus cloud warming in that region. On the Southern Hemisphere this cooling is weakened by an increase in cloud frequency, possibly due to increased cloud lifetimes in the presence of INPs. On the global scale, these effects result in a net negative RE due to heterogeneous freezing (Fig. 4.17a). Regional differences are possibly a result of variations in INP concentrations or because of the different dynamic forcings and cooling rates (e.g. comparatively small updraft velocities on the Southern Hemisphere, due to less orographic gravity wave activity compared to the Northern Hemisphere).

However, one has to bear in mind that these simulated effects are subject to various uncertainties, which are described in the following. The diagnostic cloud cover scheme by Sundqvist et al. (1989), adopted in the present model configuration, assumes that a grid box is partly covered by clouds if the grid-mean relative humidity exceeds a critical value, and totally covered if saturation is reached. For the representation of cirrus clouds, supersaturation with respect to ice is allowed, which leads to a cloud cover $C_{\mathrm{cl}} = 1$, if ice nucleation occurs and consequently newly formed cirrus clouds always covering the whole

grid box (Kuebbeler et al., 2014). An alternative prognostic treatment of fractional cirrus cloud cover, as proposed by Kärcher and Burkhardt (2008) could reduce this uncertainty and should be a focus of future studies.

Further uncertainties of the simulated modifications of clouds and radiation are related to the assumed ice nucleation efficiencies of different INPs, which are not clearly resolved from measurements. These usually focus on specific types of particles (e.g. soot particles from a variety of different sources), but information on all possible forms of atmospheric particles is necessarily limited. Moreover, different particle types of the same aerosol species often show a large spread of measured freezing properties (e.g., Mahrt et al., 2018). Additionally, the assumption of a single f_{act} value for the parametrization of heterogeneous freezing in the model is a simplification. Furthermore, a correct representation of the vertical velocity and cooling rate is important in the context of ice-nucleation (Kärcher and Lohmann, 2003; Kärcher et al., 2006). Here, sub-grid variations of the vertical velocity are represented by the turbulent component of the kinetic energy extended by an orographic gravity wave term (see Eq. 3.3). However, this representation is also subject to uncertainties as certain components of small-scale fluctuations, e.g. non-orographic subgrid-scale gravity waves, are not taken into account. In general, parametrizations of sub-grid cooling rate variations suffer from the lack of related observations (e.g., Podglajen et al., 2016). Hence, the sensitivity of simulated INP-effects to the representation of the vertical velocity is analysed in this thesis in Sect. 4.6.2.

In addition to the uncertainties mentioned above, performing simulations in the nudged mode, i.e. relaxing model winds, temperature and surface pressure towards ECMWF reanalyses (see Sect. 3.2.1), may affect the cirrus cloud and radiation modifications described above. Nudging could possibly suppress important feedback mechanisms that would occur in the free-running mode where the meteorology is not influenced by predefined values. However, simulating in nudged mode results in a more realistic representation of atmospheric dynamics, e.g. by influencing the vertical velocities in the model. Furthermore, nudged model simulations create much less internal noise (compared to the free-running case), and therefore often require fewer simulated years to achieve statistical significance for the effects investigated here. To investigate the impact of model nudging a comparison of results from simulations performed in nudged and free-running mode is presented in Sect. 4.6.3.

The effects of a subset of INP-types considering only DU and BC (including BCair) for heterogeneous freezing is shown in Fig. 4.18, assuming a larger f_{act} value. The results are similar to the case where all INP-types can initiate freezing. However, the radiative effect with respect to homogeneous freezing is roughly reduced by a factor of two, e.g. a global RE of about -37 $\mathrm{mW\,m^{-2}}$, compared to -68 $\mathrm{mW\,m^{-2}}$ for the effect of all INPs. This result is corroborated by the analysis of INP-effects due to AmSu and glPOM freezing (Fig. 4.19), showing a global RE of about -32 $\mathrm{mW\,m^{-2}}$. Importantly, the radiative effects due to DU and BC, and due to AmSu and glPOM add up almost linearly to the total INP-effect. This indicates that possible interactions between these INP-types are less important on the global scale. Furthermore, AmSu and glPOM INP-effects result in a reduced cloud frequency on the Northern Hemisphere (compared to an increase for the case of DU and BC). This indicates that the effect of low S_c values of INPs (compared to homogeneous freezing), and consequently earlier ice formation and increased cirrus lifetimes, is already exhausted by DU and BC. The addition of AmSu and glPOM INPs further suppresses homogeneous freezing and results in increased sedimentation of ice crystals and lower cirrus occurrence frequencies.

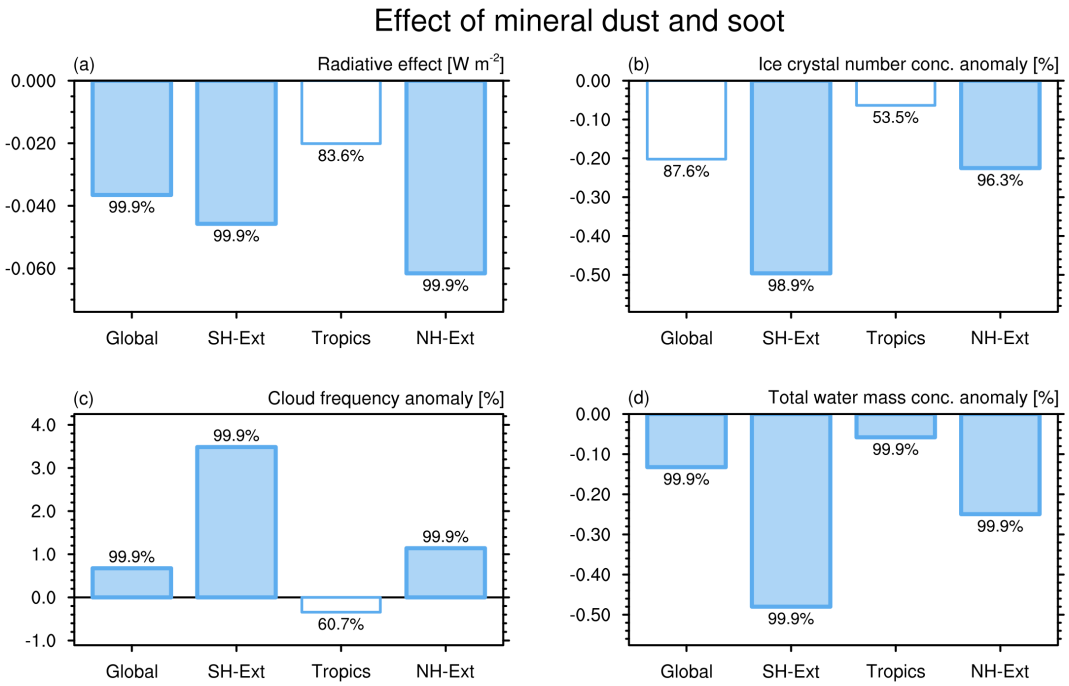

Figure 4.18: As in Fig. 4.17, but showing the effects of DU and BC (including BCair) INPs (central f_{act} value), calculated from the difference between a simulation including these INPs and a simulation with only homogeneous freezing. Shown are (a) the radiative effect, in addition to relative differences of (b) ice crystal number concentration, (c) cloud frequency, and (d) of total water mass concentration (water vapour plus ice mass). Note the different y-axis scales in each plot.

Figure 4.20 presents the effect of adding only AmSu freezing to the DU and BC INPs. Here, the radiative effects are mostly non-significant with the exception of the Northern Hemisphere, where a cooling of -90 mW m^{-2} is simulated (Fig. 4.20a). This value is nearly as large as the RE due to the combined effect of AmSu and glPOM in that region, and also larger than the regional effect due to DU and BC INPs (-62 mW m^{-2}, Fig. 4.18a). On the Southern Hemisphere, AmSu freezing results in an increased cloud frequency (Fig. 4.20c) and a decreased water concentration (due to stronger sedimentation of ice crystals, Fig. 4.20d). However, these effects tend to compensate each other, leading to a small, not-significant, radiative effect on the Southern Hemisphere.

In general, these results indicate that heterogeneous freezing on AmSu has a major influence on the Northern Hemisphere (compared to homogeneous freezing) with respect to the radiative effects, while glPOM is mainly important on the Southern Hemisphere. This is in line with the global distributions of AmSu and glPOM INPs presented in Sect. 4.5, i.e. high AmSu INP concentrations in the Northern Hemisphere, high glPOM concentrations in the tropics and the southern regions. Importantly, the addition of heterogeneous freezing on AmSu and glPOM INPs contributes a considerable fraction to the global and regional radiative effects of INPs, which is comparable to the effects of DU and BC ice nucleation.

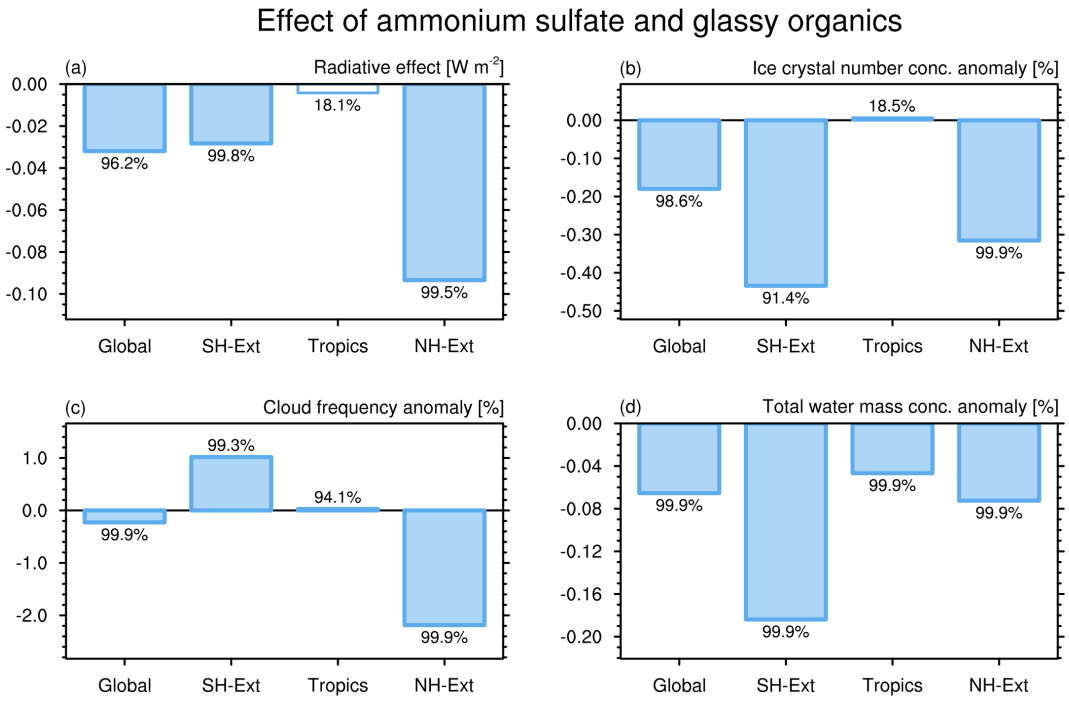

Figure 4.19: As in Fig. 4.18, but showing the effects of AmSu and glPOM INPs (central f_{act} value), calculated from the difference between a simulation including AmSu, glPOM, DU and BC INPs and a simulation including only heterogeneous freezing on DU and BC. Note the different y-axis scales in each plot.

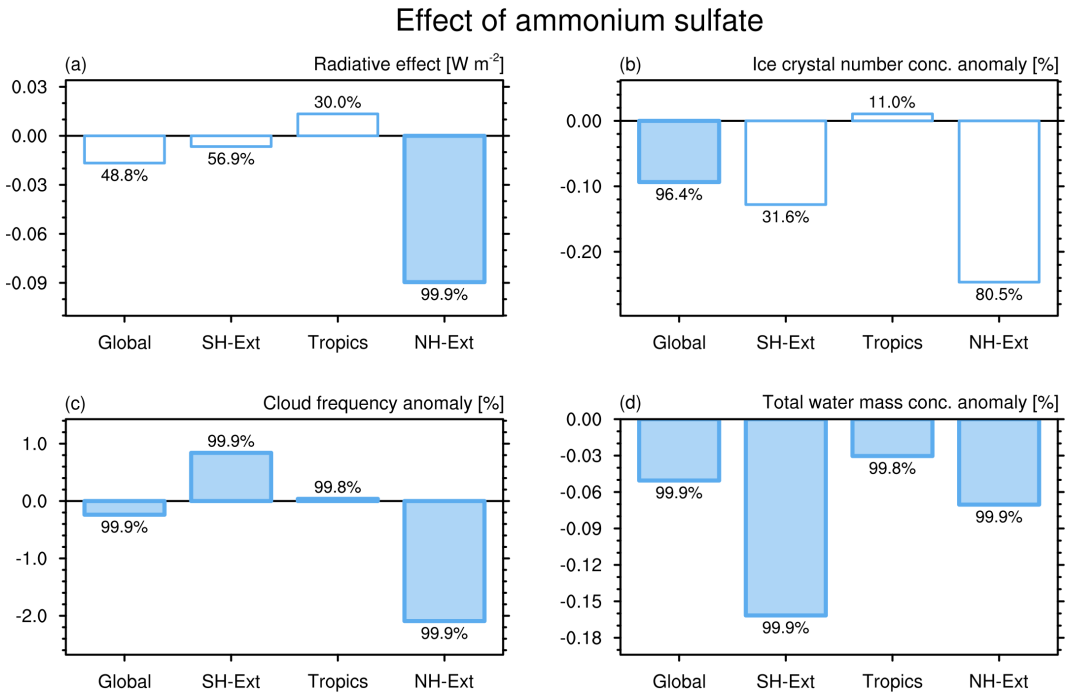

Figure 4.20: As in Fig. 4.18, but showing the effects of AmSu INPs (central f_{act} value), calculated from the difference between a simulation including AmSu, DU and BC INPs and a simulation including only heterogeneous freezing on DU and BC. Note the different y-axis scales in each plot.

4.6.2 Sensitivity to the vertical velocity

This section deals with the impact of the vertical velocity on cloud formation in the model. The particular role of the updraft speed of air parcels is discussed, which controls their adiabatic cooling rate, as the temperature decreases during the lifting process. Various studies show that this dynamic forcing is crucial for the interplay between heterogeneous and homogeneous freezing (e.g., Kärcher and Lohmann, 2002, 2003; Kärcher et al., 2006).

To analyse the sensitivity of INP-induced cirrus modifications to the vertical velocities in the model, a simplified representation for the updraft speed in the freezing parametrization is employed here, i.e. using a prescribed constant vertical velocity across the whole globe in the range of 1 to 50 $\mathrm{cm\,s^{-1}}$. In comparison, the simulations analysed in the previous section employed a parametrization of the modelled updraft speeds, including large-scale and sub-grid variability (see Sect. 3.2.5 and Eq. 3.3). Treating the vertical velocity in such a simplified way (i.e. prescribing a global value) has the advantage that also regions on the globe are taken into account, where no effects would occur in the standard case (parametrized vertical velocity). This is essential, as the standard representation of modelled updrafts is highly uncertain and only poorly constrained by observations. Additionally, some processes influencing the sub-grid variations of updraft speeds may be missing in the parametrization (e.g. possible fluctuations due to small-scale, non-orographic gravity waves). An overview of the global distribution of modelled vertical velocities (including also the single components in Eq. 3.3) is represented in the Appendix (Fig. A.15). Furthermore, the correct representation of gravity wave influences on vertical velocity fluctuations is highly important, as recent studies observe a strong impact of gravity wave temperature perturbations on cirrus cloud occurrence and properties in the TTL (Kim et al., 2016; Podglajen et al., 2018; Chang and L'Ecuyer, 2020).

Figure 4.21 shows the sensitivity of the effect of all INPs (compared to pure homogeneous freezing, assuming a central f_{act} value) to the variation of the prescribed global vertical velocity. Different values of 1 $\mathrm{cm\,s^{-1}}$, 5 $\mathrm{cm\,s^{-1}}$, 10 $\mathrm{cm\,s^{-1}}$, 20 $\mathrm{cm\,s^{-1}}$, and 50 $\mathrm{cm\,s^{-1}}$ are analysed with respect to changes in the global RE (Fig. 4.21a, b), and global and latitude-specific regional cloud variables (Fig. 4.21c–f). For small vertical velocities (1 and 5 $\mathrm{cm\,s^{-1}}$) the INP-effect on the radiation is small (values around zero), which is in line with only small relative changes in e.g. ice crystal numbers, total water, and cloud occurrence frequency. When increasing the vertical velocity up to 20 $\mathrm{cm\,s^{-1}}$, the RE (with respect to homogeneous freezing) increases, i.e. becomes more negative, to around $-210 \pm 50\,\mathrm{mW\,m^{-2}}$ (Fig. 4.21a). In addition, the increasing global reduction in ICNC, IWC, total water, and cloud frequency (Fig. 4.21c–f) indicate a pronounced cirrus cloud thinning for higher updraft speeds up to 20 $\mathrm{cm\,s^{-1}}$. Increasing the vertical velocity even further to 50 $\mathrm{cm\,s^{-1}}$ results in a weakened INP-effect on radiation and clouds compared to the 20 $\mathrm{cm\,s^{-1}}$ case.

This increase of the INP-effect with increasing vertical velocity is in line with results from a process-model study by Kärcher et al. (2006). The authors also showed that for updraft speeds exceeding a certain threshold, homogeneous freezing is gaining increasing importance, leading to a reduction of the effect of heterogeneous INPs, which is in line with simulated global effects presented here. Regional differences in Fig. 4.21 (e.g. smaller effects on IWC and cloud frequency in the tropics) are possibly related to the regional variation in INP number concentrations. At very low vertical velocities Kärcher et al. (2006) predict an increase in ice crystal numbers compared to pure homogeneous freezing.

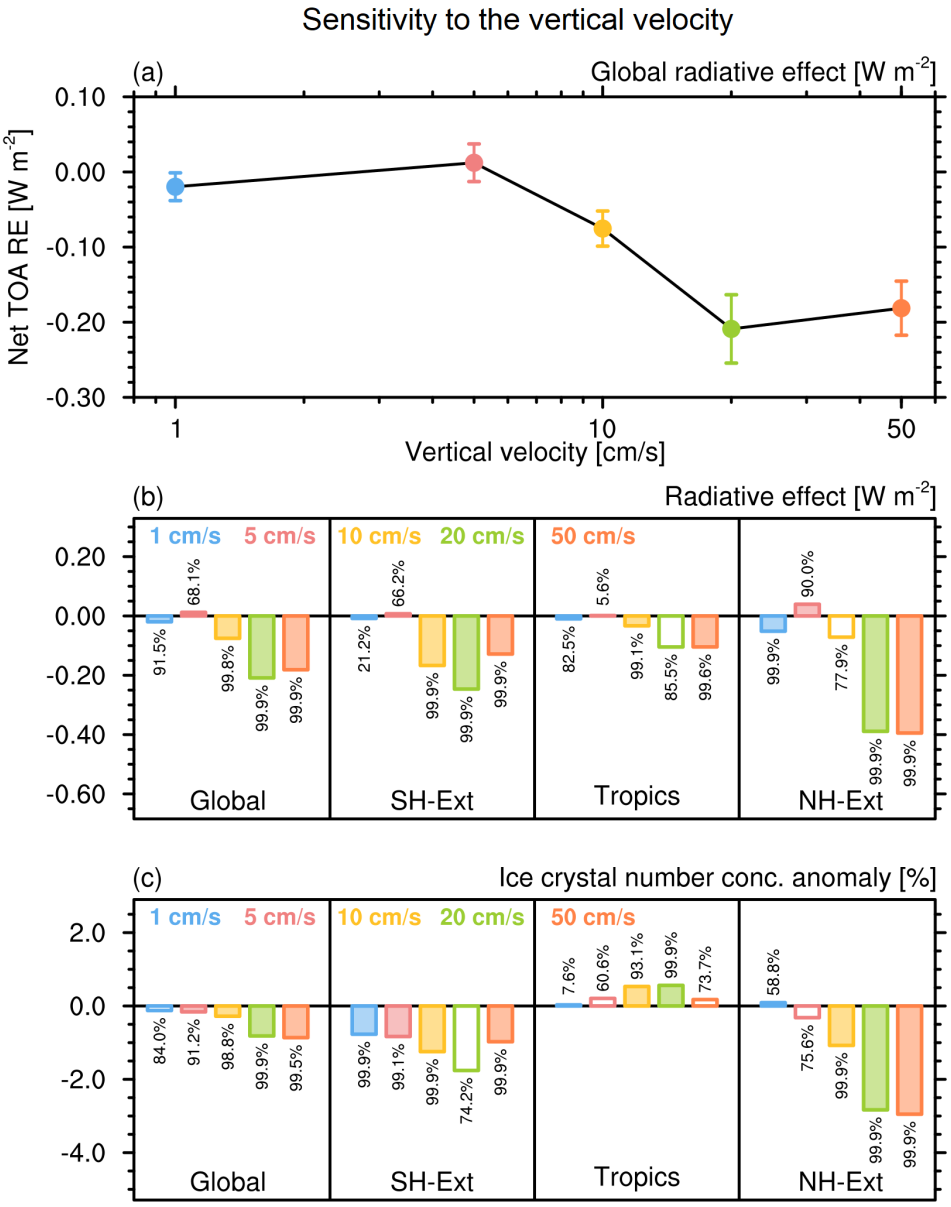

Figure 4.21: Sensitivity of simulated INP-effects to the vertical velocity in the model, using a prescribed, globally homogeneous updraft speed. Global vertical velocity values of $1\,\mathrm{cm\,s^{-1}}$ (blue), $5\,\mathrm{cm\,s^{-1}}$ (red), $10\,\mathrm{cm\,s^{-1}}$ (yellow), $20\,\mathrm{cm\,s^{-1}}$ (green), $50\,\mathrm{cm\,s^{-1}}$ (orange) are analysed with respect to the differences in the (a) global radiative effect (top-of-the-atmosphere), global and latitude-specific, regional (b) radiative effect, (c) ice crystal number concentration. Shown on the next page are (d) ice water content, (e) cloud occurrence frequency, (f) total water mass concentration (water vapour plus ice mass). Absolute differences (a, b) and relative differences (c–f) are shown (averages above the 400 hPa pressure level, latitude regions as in Fig.4.17). Dots in (a) represent mean values, bars represent the ± 1 standard deviation range, derived from the inter-annual variability. Numbers above the bars in (b–f) represent statistical confidence levels. Note the different y-axis scales in each plot.

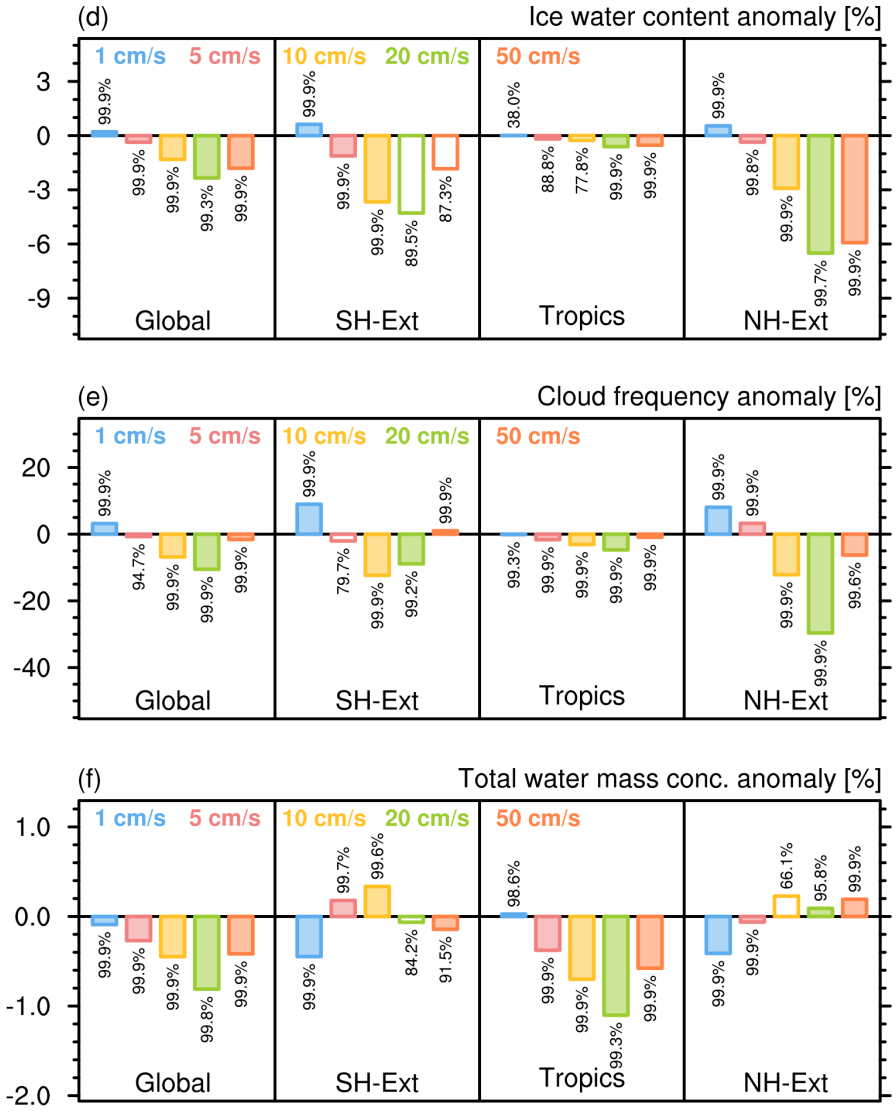

Figure 4.21: Continued.

This is a result of the critical freezing threshold S_c of heterogeneous INPs being much smaller than the homogeneous value. Therefore INP-induced ice crystals experience less supersaturation and grow more slowly than homogeneously formed crystals, resulting in a lower efficiency to reduce S_i and allowing more ice crystals to be formed. However, the effect of enhanced ice crystal numbers for small updraft speeds is not visible in the results presented here (Fig. 4.21b). This could be a result of S_c being not small enough compared to S_{hom}. Additionally, such low vertical velocities probably hinder cirrus cloud formation, resulting in only small simulated INP-effects in the model.

Importantly, the simulated radiative effect due to INPs for a vertical velocity of $10\,\mathrm{cm\,s^{-1}}$ ($-75 \pm 23\,\mathrm{mW\,m^{-2}}$; Fig. 4.21a) is comparable to the value from the standard setup (parametrized updraft speed) of $-68 \pm 28\,\mathrm{mW\,m^{-2}}$ (Fig. 4.17a). Additionally, simulated vertical velocities around $10\,\mathrm{cm\,s^{-1}}$ are typical values and occur often in the model (see Fig. A.15 in the Appendix) and are frequently observed in the global atmosphere (e.g., Uma and Rao, 2009; Tonttila et al., 2011). This indicates that uncertainties due to a misrepresentation of modelled vertical velocities are possibly small in the reference case. However, the steep gradient between 5 and $20\,\mathrm{cm\,s^{-1}}$ in Fig. 4.21a shows that already

slight variations in the updraft speed can lead to large changes in the RE. Additionally, a global model study by West et al. (2014) shows a strong influence of vertical velocity variability on simulated indirect aerosol effects on warm clouds. In general, these results show that further improvements of the dynamic forcings in the model should be aimed at in future studies.

In addition to varying the prescribed global vertical velocity, additional simulations were performed, where updraft speeds are parametrized (according to Eq. 3.3) and the total vertical velocity ω is scaled by factors of 0.2, 2, and 5 (see Fig. A.16 in the Appendix). Results show decreased ICNC and IWC global values (compared to homogeneous freezing) for scaling factors of 1 (i.e. the reference case), 2, and 5, with the strongest reductions for the largest vertical velocity scaling (Fig. A.16c, d in the Appendix). Decreasing ω by a factor of 0.2 results in a slight positive change in ICNC and IWC, which is in line with the results described above and in Kärcher et al. (2006). The largest global RE is simulated for the reference case (no scaling), while smaller and larger vertical velocities lead to less negative values. This behaviour is different compared to the results using a simple prescribed updraft speed (Fig. 4.21a). However, a comparison of the different radiative effects is complicated due to the large uncertainties, probably as a result of the different representation of vertical velocities in the model.

4.6.3 Impact of model nudging

As described previously, performing simulations in nudged mode (see Sect. 3.2.1) reduces the internal noise, therefore facilitating the analysis of statistically significant differences between model simulations. However, nudging possibly suppresses important feedback mechanisms (as meteorological variables, e.g. temperature, winds, and surface pressure, are relaxed towards predefined values) compared to free-running simulations, i.e. simulations without nudging (Zhang et al., 2014). Here, this effect is analysed by comparing the INP-effect from a nudged simulation with results from a simulation performed in free-running mode (Fig. 4.22), with prescribed climatological (2000–2009) sea surface temperature and sea ice concentration from the Met Office Hadley Centre dataset (HadISST, Rayner et al., 2003). This comparison is performed for the simulation setup applying a prescribed global vertical velocity of $20\,\mathrm{cm\,s^{-1}}$, as this setup shows the largest effects (see Fig. 4.21). This is important to achieve higher statistical confidence in the free-running case, which suffers from increased statistical noise. Additionally, the simulated time period is expanded to ten years (time period 2000–2009). For the free-running simulations statistical confidence levels are calculated using the Welch's t-test, instead of the paired-sample t-test for the nudged experiments (Welch, 1947).

In general, Fig. 4.22 shows that the free-running simulation often results in larger effects, albeit with lower statistical significance. However, the difference with respect to the nudged case is mostly small (about 20 % averaging over all significant values) with effects showing nearly always the same sign. However, regionally larger differences can occur, e.g. the radiative effects on the Southern Hemisphere are increased by a factor of 1.6 in the free-running case. Overall, this comparison shows that nudging can result in reduced effects due to suppressed feedback mechanisms. However, differences compared to free-running simulations are mainly small and nudging is necessary to achieve statistical significance.

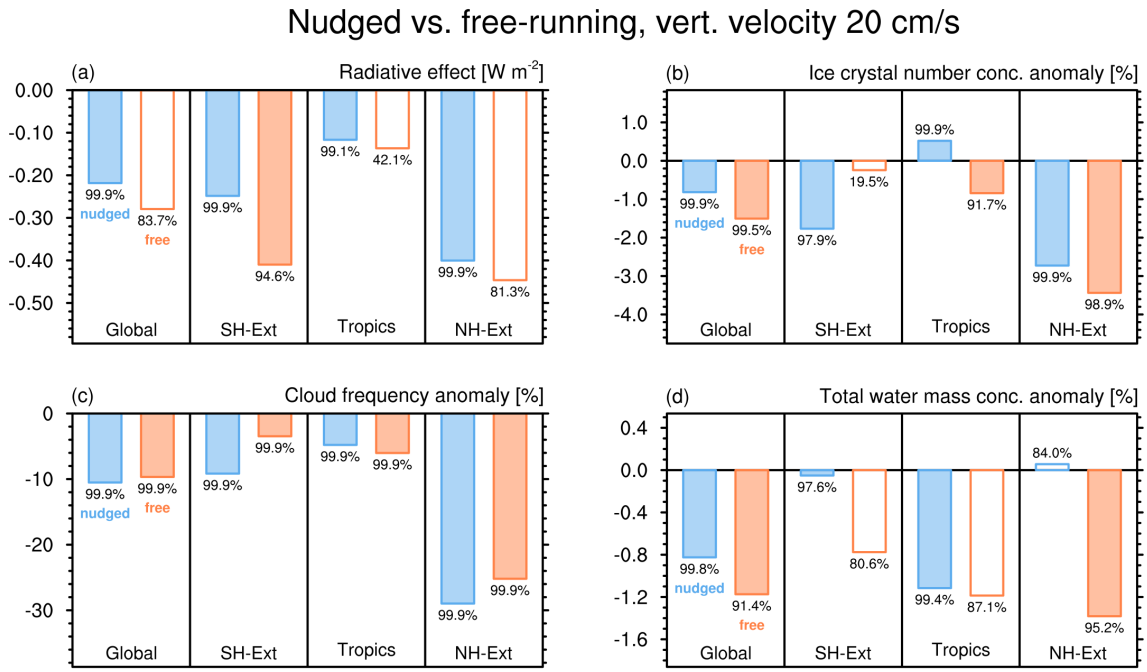

Figure 4.22: As in Fig. 4.21, but comparing the global and regional INP-effect on radiation and cloud variables from simulations performed in nudged (blue) and free-running (red) mode (multi-annual means, years 2000–2009). The simple representation of vertical velocities using a global value of 20 cm s^{-1} is employed. Values of f_{act} are assumed to correspond to the center of the freezing spectrum.

Additionally, Table 4.1 presents a comparison of modelled global cloud and radiation variables from this study with results from Righi et al. (2020) and observations presented therein. Three different simulation setups from this thesis are used for the comparison, each considering heterogeneous freezing of all possible INP-types at an f_{act} value in the centre of the freezing spectrum: the default setup in nudged mode with the vertical velocity parametrized according to Eq. 3.3 (HetRef), as well as the setup with a prescribed global vertical velocity of 20 cm s^{-1} in nudged (HetVervel) and free-running (HetVervel-Free) mode. In general simulated cloud variables (e.g. cloud cover, CDNC, precipitation) show only small variations with respect to the tuned model version of Righi et al. (2020) and agree well with observations. For the simulated radiation variables (i.e. short-wave and long-wave CRE, and the radiative balance) differences are larger; especially the radiative balance (i.e. the net radiative flux at the top of the atmosphere, which would be 0 W m^{-2} in an ideally balanced simulation) is higher (cases HetRef, HetVervel) and on the upper end of the range of radiative imbalances achieved in similar model studies (e.g., Bacer et al., 2018; Schultz et al., 2018; Neubauer et al., 2019).

In addition to the comparison in Table 4.1, an evaluation of simulated ice crystal numbers, crystal size, and ice water content was performed in analogy to Righi et al. (2020), showing a generally good agreement with in situ observations (see Fig. A.17 in the Appendix) and only small deviations with respect to the model results of Righi et al. (2020). For this comparison, a collection of in situ measurements from 18 aircraft-based field campaigns was used, which were compiled into a climatology by Krämer et al. (2009, 2016) and further complemented with more recent data (Krämer et al., 2020).

Table 4.1: Summary of globally averaged cloud and radiation variables in the model (multi-annual mean, years 2000–2004). Different model setups from this study (HetRef, HetVervel, HetVervelFree; information in the text, see page 95) are compared with Righi et al. (2020) and with observations. Righi et al. (2020) describe and evaluate the coupling of aerosols and clouds in EMAC-MADE3 but apply a different model setup, mainly a higher vertical model resolution with 41 vertical levels (compared to 31 levels, used here). The observational data presented here are described in Righi et al. (2020), their Tables 2 and 3. LWP and IWP represent the liquid and ice water path, i.e. vertically integrated liquid and ice water content.

	This study, HetRef	This study, HetVervel	This study, HetVervelFree	Righi et al. (2020)	Observations
Cloud cover (%)	65.0	67.9	71.0	66.1	64.5 ± 17.4
LWP oceans ($g\,m^{-2}$)	84.7	85.3	97.9	91.1	81.8 ± 10.2
CDNC oceans (cm^{-3})	68.3	67.8	67.7	73.6	77.4 ± 41.1
IWP ($g\,m^{-2}$)	5.7	5.7	5.8	6.1	–
Precipitation ($mm\,d^{-1}$)	3.0	3.0	3.1	3.1	2.7 ± 0.2
SWCRE ($W\,m^{-2}$)	-52.7	-54.5	-61.5	-53.0	-45.9 ± 5.5
LWCRE ($W\,m^{-2}$)	29.5	30.9	31.4	27.4	28.1 ± 4.4
Radiative Balance ($W\,m^{-2}$)	5.9	5.2	-0.5	3.4	–

Importantly, employing the free-running model setup results in a radiative balance close to zero (HetVervelFree in Table 4.1). Generally, models that are well balanced in free-running mode tend to introduce a positive imbalance of a few $W\,m^{-2}$ in nudged mode (e.g., Schultz et al., 2018). Together with the mostly small differences concerning the INP-effect between nudged and free-running simulations (see Fig. 4.22), these findings corroborate the reliability of results presented in this section.

4.6.4 Effects of highly-efficient INPs

As heterogeneous INPs have the potential to reduce the occurrence frequency and optical thickness of cirrus clouds consequently lowering their warming effect on the global climate, several studies proposed a climate engineering approach to reduce global warming by seeding cirrus clouds with highly efficient INPs (e.g., Mitchell and Finnegan, 2009; Storelvmo et al., 2013; Muri et al., 2014). Here, the effects of seeding cirrus clouds with different concentrations of very efficient INPs is analysed to estimate INP-effects in extreme cases. Additionally, this analysis is performed similarly to the study of Gasparini and Lohmann (2016) to facilitate a direct comparison of simulated effects. Different INP concentrations (ranging from 0.5 to $100\,L^{-1}$) are prescribed for every model grid box, with a critical freezing supersaturation with respect to ice of $S_c = 1.05$ (the activated fraction is set to $f_{act} = 1$), and differences compared to the purely homogeneous freezing case are analysed. In this section, vertical velocities are parametrized according to Eq. 3.3. By following the approach of Gasparini and Lohmann (2016), who employ the global model ECHAM6-HAM2 (Stevens et al., 2013; Zhang et al., 2012) together with a similar cloud scheme as used here with EMAC-MADE3, a consistent comparison of INP-effects between these two model systems is possible.

The INP-effects on radiation and clouds for four different number concentrations of highly efficient INPs are presented in Fig. 4.23. Low INP concentrations of 0.5 and $1.0\,L^{-1}$ result in only small effects with respect to homogeneous freezing, i.e. slight reductions in e.g. ICNC, IWC and cloud frequency (Fig. 4.23c, d, and e). At higher INP concentrations,

the cloud-effects increase notably in magnitude but show a positive change, e.g. a large increase (relative to homogeneous freezing) of regionally up to 20 % in cloud occurrence. The global radiative effect is positive for the whole range of analysed INP concentrations, with the strongest global warming of $248 \pm 53\,\mathrm{mW\,m^{-2}}$ for an INP concentration of $100\,\mathrm{L^{-1}}$.

This strong warming for high INP concentrations was also described by Gasparini and Lohmann (2016), who simulate even larger forcings of $490 \pm 240\,\mathrm{mW\,m^{-2}}$ at an INP concentration of $100\,\mathrm{L^{-1}}$. At lower INP concentrations Gasparini and Lohmann (2016) show small net negative forcings, albeit with uncertainty ranges reaching positive values. The large uncertainties of the results presented in Gasparini and Lohmann (2016) are

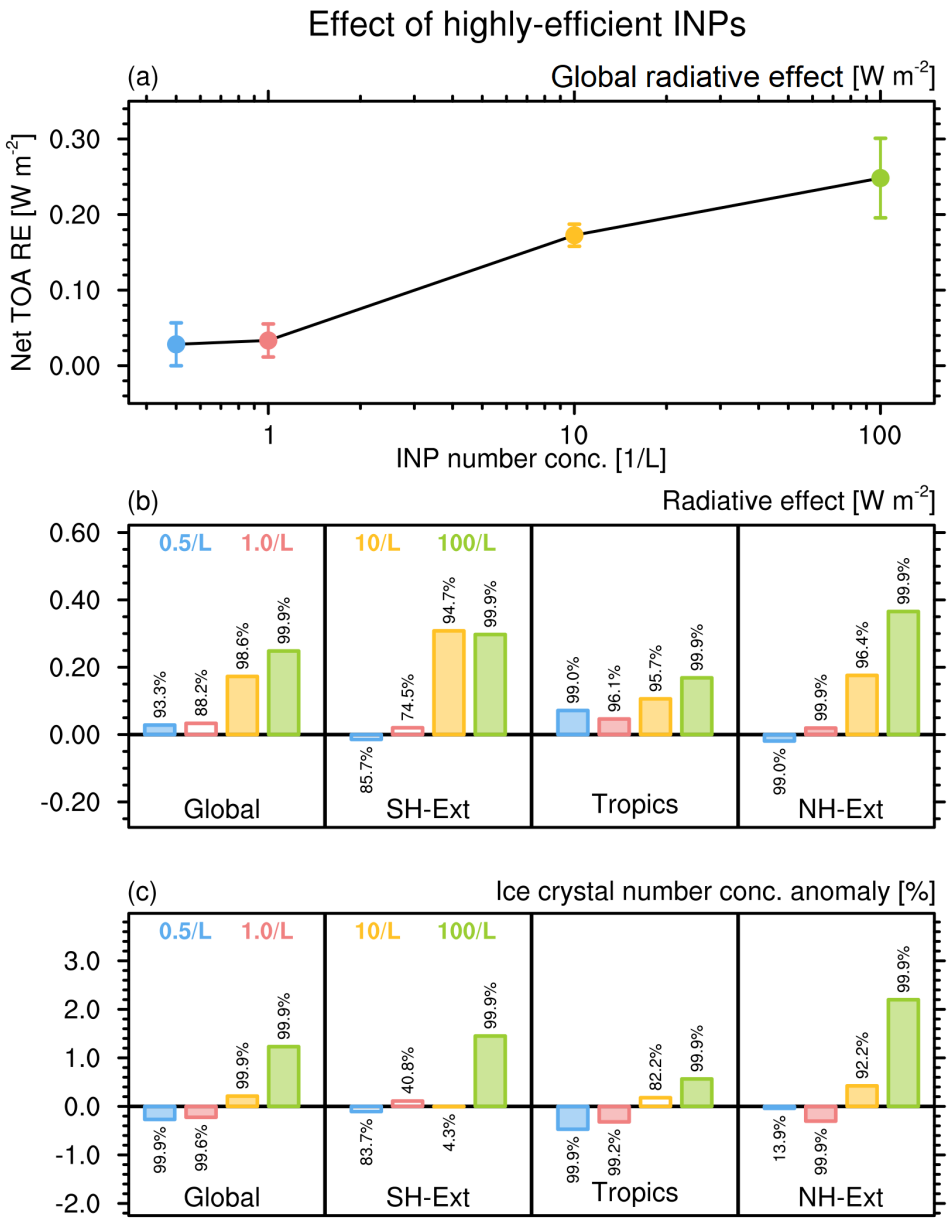

Figure 4.23: As in Fig. 4.21, but for the effect of highly efficient INPs proposed for cirrus cloud seeding. Different INP concentrations are prescribed, which freeze at a critical supersaturation ratio with respect to ice of $S_c = 1.05$ ($f_{\mathrm{act}} = 1$). Seed INP concentrations are $0.5\,\mathrm{L^{-1}}$ (blue), $1\,\mathrm{L^{-1}}$ (red), $10\,\mathrm{L^{-1}}$ (yellow), $100\,\mathrm{L^{-1}}$ (green). Note the different y-axis scales in each plot.

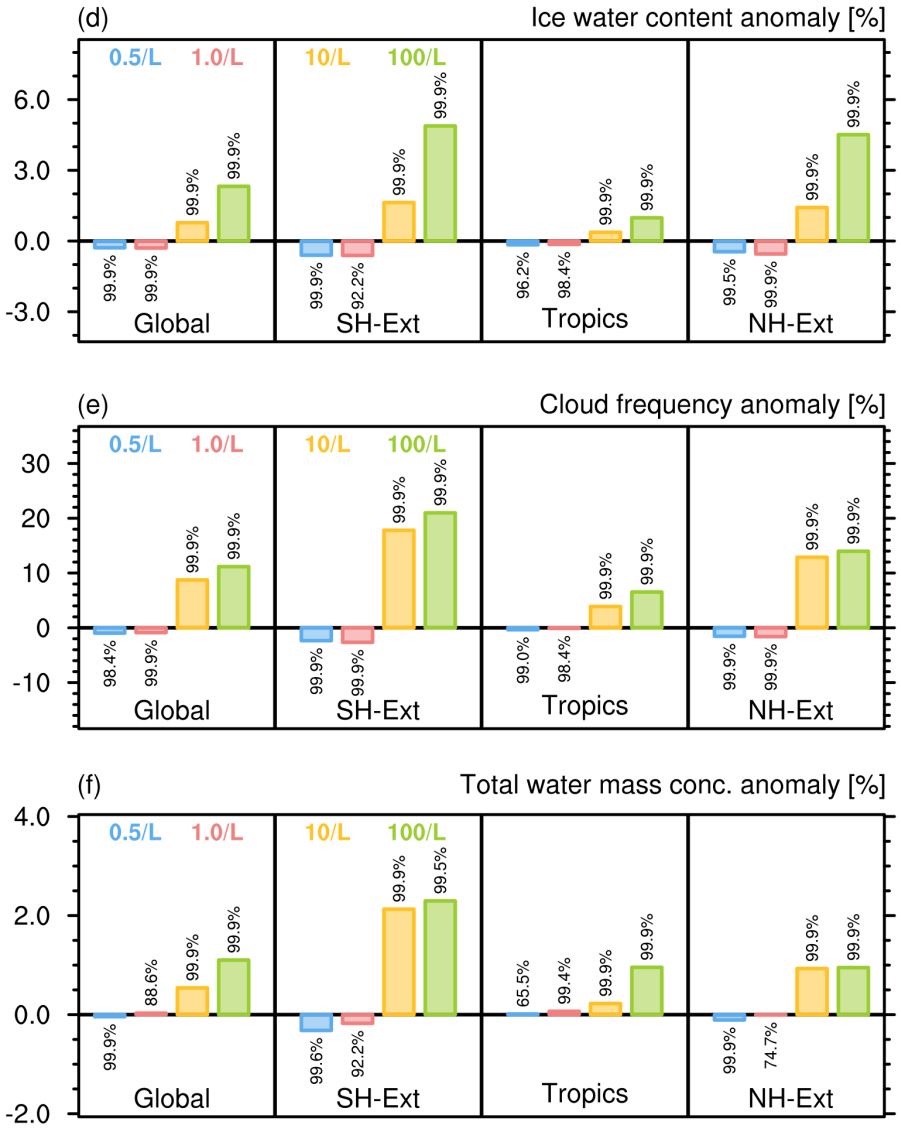

Figure 4.23: Continued.

a result of performing simulations in free-running mode. To improve the comparability to the results presented here, the seed INP-effect (for a concentration of $100\,\mathrm{L}^{-1}$) is also simulated in free-running mode (see Fig. A.18 in the Appendix). This results in slightly larger effects on clouds and radiation, albeit with lower statistical confidence.

The heterogeneous freezing effects presented here are probably a result of the very high freezing efficiency assumed for seed INPs. Heterogeneous freezing is initiated at very low supersaturations with respect to ice and occurs already for low dynamic forcings or updraft speeds. For high INP concentrations, ice crystal numbers increase with respect to homogeneous freezing, as a result of the low freezing threshold (i.e. lower S_c) compared to homogeneous freezing. This leads to reduced sedimentation (due to smaller crystals) and increased cirrus cloud coverage, consequently increasing the global warming due to cirrus clouds.

These results indicate that climate engineering via cirrus cloud seeding risks an over-seeding of clouds subsequently increasing their warming effect. Importantly, none of the analysed INP concentrations results in a negative radiative effect. Previous studies

showed that only optimal seed INP concentrations and freezing efficiencies could achieve a negative climate forcing (Storelvmo et al., 2013; Penner et al., 2015), and described the potential deleterious effects due to over-seeding, making this approach an unfeasible climate engineering technique.

4.6.5 Effects of anthropogenic INPs

In this section, potential influences of anthropogenic INPs are analysed. As a first indicator of anthropogenic effects, Fig. 4.24 shows the INP-effect due to black carbon, calculated by adding heterogeneous freezing of BC (and BCair) to the population of mineral dust INPs. BC acts as a proxy for anthropogenic activity, as sources of atmospheric soot particles are to a large extent the incomplete combustion of fossil fuels (with additional contributions of natural emissions, e.g. biomass burning during forest fires; Dentener et al., 2006).

The global radiative effect due to BC INPs results in a negative forcing of $-15\,\mathrm{mW\,m^{-2}}$, which corresponds to about 20 % of the total INP-effect with respect to purely homogeneous freezing ($-68\,\mathrm{mW\,m^{-2}}$, see Fig. 4.17). This cooling is a result of the reduced ice crystal concentrations, stronger sedimentation of larger crystals and subsequently a reduced cirrus cloud coverage (Fig. 4.24b–d).

However, the BC-effect can only be regarded as a first estimate of anthropogenic impacts, as it includes also BC from natural sources, and effects of other anthropogenic INPs (e.g. AmSu) are not considered. Therefore, the effects of anthropogenic emissions (mainly fossil fuel combustion) are analysed by comparing simulations with and without

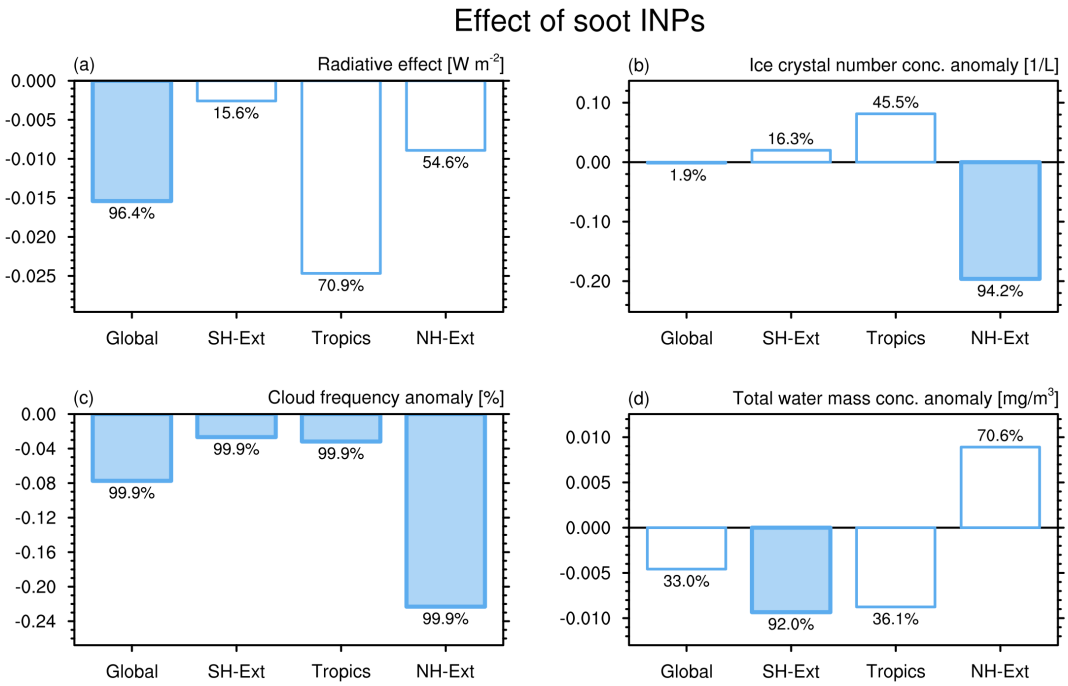

Figure 4.24: As in Fig. 4.18, but showing the effect of BC (including BCair) INPs (central f_{act} value), calculated from the difference between a simulation including DU and BC INPs and a simulation including only heterogeneous freezing on DU. Absolute differences of the (a) radiative balance (in $\mathrm{W\,m^{-2}}$), (b) ice crystal number concentration (in $\mathrm{L^{-1}}$), (c) cloud occurrence frequency (in %), and (d) total water (i.e. water vapour plus ice) mass concentration (in $\mathrm{mg\,m^{-3}}$), are shown.

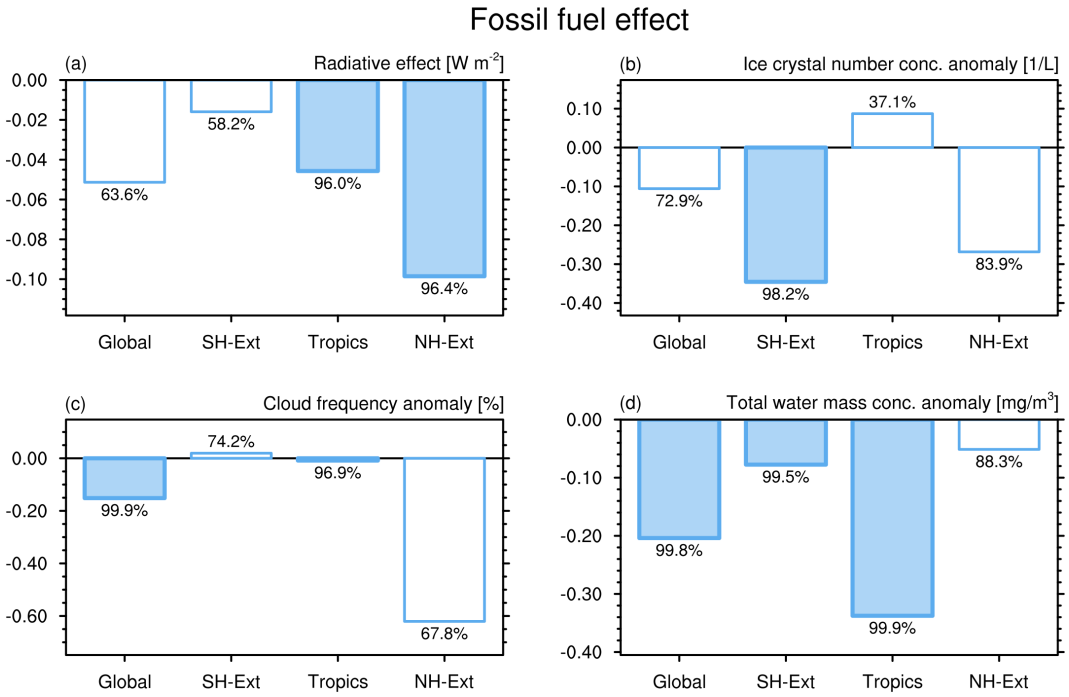

Figure 4.25: As in Fig. 4.18, but showing the effect of anthropogenic emissions (fossil fuels and anthropogenic waste burning), calculated from the difference in the INP-effect between simulations with and without fossil fuel emissions. Absolute differences of the (a) radiative balance (in $\mathrm{W\,m^{-2}}$), (b) ice crystal number concentration (in $\mathrm{L^{-1}}$), (c) cloud occurrence frequency (in %), and (d) total water (i.e. water vapour plus ice) mass concentration (in $\mathrm{mg\,m^{-3}}$), are shown.

fossil fuel burning emissions (including agricultural waste burning), regarding the differences with respect to homogeneous freezing. Here, also effects on AmSu are included (e.g. anthropogenic sulfur emissions). Resulting cloud and radiation modifications are shown in Fig. 4.25. Anthropogenic emissions include fossil fuel burning emissions from the three traffic sectors (road traffic, shipping, aviation) as well as other non-traffic emissions (e.g. energy production and industry) in addition to agricultural waste burning. Anthropogenic contributions to other biomass burning emissions (e.g. vegetation burning for land clearing and land-use change) are not included in this approach. However, their contribution to the total anthropogenic emissions is small (about a few percent, regarding emissions of BC, SO_4, and SO_2), considering present-day (year 2000) and pre-industrial (year 1850) emission inventories from the Coupled Model Intercomparison Project phase 5 (CMIP5; Lamarque et al., 2010). Anthropogenic emissions mainly affect atmospheric concentrations of BC, SO_4, and SO_2, consequently influencing the number concentrations of BC and AmSu INPs. In general, the INP-effect due to anthropogenic emissions results in lower ice crystal numbers and cloud occurrence (in line with increased sedimentation of larger ice crystals), which reduces the warming effect due to cirrus clouds and consequently leads to a negative radiative effect. This cooling is strongly pronounced on the Northern Hemisphere with an RE of $-99\,\mathrm{mW\,m^{-2}}$ (Fig. 4.25a), which corresponds to roughly 60 % of the total INP-effect in that region (see Fig. 4.17a).

In general, anthropogenic fossil fuel and waste burning emissions have a notable influence on the INP-effects simulated here, most pronounced on the Northern Hemisphere. However, often low statistical confidence levels probably due to smaller simulated effects compared to the reference setup complicate the interpretation of results. A direct comparison of INP-effects for present-day and pre-industrial emission scenarios, consistent with

recent studies (e.g., Penner et al., 2018; Zhu and Penner, 2020), should be considered for future work to provide a more complete view on the anthropogenic effects compared to conditions dominated by natural emissions.

4.6.6 Summary and conclusions: INP-effects

In this section, a detailed analysis of cirrus cloud and radiation modifications due to heterogeneous freezing on ice nucleating particles was presented. INPs influence important cirrus cloud properties like ice crystal number, crystal size, and cloud coverage, consequently affecting the radiative effect of cirrus clouds. Important mechanisms of INPs, as simulated in this thesis, include the reduction of ICNC, increased sedimentation of larger ice crystals, resulting in a thinning of cirrus clouds and regionally also in a possible reduction of cirrus cloud occurrence. However, cirrus cloud coverage can also be increased, as INPs freeze at lower supersaturations compared to homogeneous freezing, resulting in earlier cirrus cloud formation during adiabatic cooling in updrafts and consequently increased cloud lifetimes.

On the global scale, reduced cirrus optical thickness and possible decreases in cloud occurrence frequencies reduce the global warming effect of cirrus clouds and result in a net negative radiative effect. The simulated globally averaged annual-mean radiative effect due to heterogeneous freezing is $-68 \pm 28\,\mathrm{mW\,m^{-2}}$ (± 1 standard deviation range) and represents a cooling of the climate system. The largest effects occur in the Northern Hemisphere extratropics (where INP concentrations are larger) with an RE of $-155 \pm 36\,\mathrm{mW\,m^{-2}}$ (average in that latitude-region). These cooling effects are strongly dependent on the freezing efficiency of INPs, as model results show a reduced RE (e.g. by a factor of 2 on the Northern Hemisphere) for lower assumed activated fractions of INPs (see Fig. 4.17, Table 3.3).

The newly implemented INPs, i.e. crystalline ammonium sulfate and glassy organics, show notable effects compared with mineral dust and soot INPs, e.g. about half of the total global INP radiative effect. Impacts of AmSu INPs are largest on the Northern Hemisphere, while glPOM effects occur mainly in southern regions. Additionally, anthropogenic INPs (e.g. BC and AmSu from fossil fuel emissions) show a notable impact on simulated cloud and radiation properties, and result in a global cooling effect, which is strongest in the Northern Hemisphere extratropics with about $-100\,\mathrm{mW\,m^{-2}}$. This corresponds to about 10 % of the total anthropogenic aerosol forcing and to about 20 % of the total anthropogenic aerosol-cloud effect (Boucher et al., 2013; Bellouin et al., 2020).

In general, the global cooling as a result of cloud modifications due to heterogeneous freezing is in line with previous model studies (e.g. Liu et al. (2012); Kuebbeler et al. (2014); Wang et al. (2014); Penner et al. (2018), see also Table 2.2). The range of simulated global radiative effects of $(-100, -40)\,\mathrm{mW\,m^{-2}}$ shows, however, smaller values compared to other studies (e.g., Penner et al., 2009; Liu et al., 2012; Wang et al., 2014; McGraw et al., 2020). On the other hand, some studies also simulate small, mostly not significant INP-effects (Hendricks et al., 2011; Gettelman et al., 2012). However, a direct comparison of different model results is difficult due to model differences in the representation of cirrus clouds and freezing mechanisms, e.g. often different types of INPs (with different freezing properties) are assumed and different effects are analysed (see Table 2.2).

INP-effects are strongly dependent on the dynamic forcing, i.e. the vertical velocities in the model. To analyse this sensitivity, a prescribed global updraft speed was used (compared to the parametrization of vertical velocities in the reference case, see Eq. 3.3). Model results show increased INP-effects for vertical velocities around $20\,\mathrm{cm\,s^{-1}}$, e.g. a global RE of $-210 \pm 50\,\mathrm{mW\,m^{-2}}$. Further increasing the updraft speed results in reduced INP-effects due to a gaining importance of homogeneous freezing at very high vertical velocities. The strong gradient of simulated radiative effects for typical vertical velocities of about $10\,\mathrm{cm\,s^{-1}}$ indicates that further improving the representation of updraft speeds in the model (e.g. by refining the parametrization of sub-grid variabilities) should be the aim of future studies.

Additionally, the effect of nudging model meteorology (e.g. temperature, surface pressure) towards predefined fields according to meteorological analysis data was quantified by comparing the results with simulations performed in free-running mode. This analysis shows that results from nudged simulations are similar to the free-running case, albeit with slightly smaller effects due to suppressed feedback mechanisms. However, nudging is often important to achieve statistical significance for the analyses in this study.

Furthermore, climate effects of highly efficient INPs, e.g. proposed for cirrus cloud seeding in climate engineering, were evaluated in this work. Results show that such INPs with very high freezing efficiencies (S_c= 1.05) can lead to an increase in ice crystal numbers and reduced sedimentation due to smaller crystals. This results in increased cirrus cloud coverage and consequently in a positive radiative effect, i.e a warming of the climate system of up to $250 \pm 50\,\mathrm{mW\,m^{-2}}$ for an INP concentration of $100\,\mathrm{L^{-1}}$. These results are in accordance with previous studies (e.g., Storelvmo et al., 2013; Penner et al., 2015; Gasparini and Lohmann, 2016) and reveal the problem of over-seeding cirrus clouds, making this approach still unsuitable for climate engineering.

Chapter 5

Summary, conclusions and outlook

5.1 Summary and conclusions

In this thesis, cirrus cloud modifications induced by ice nucleating aerosol particles and resulting influences on the global climate were analysed, employing the aerosol microphysics submodel MADE3 as part of the general circulation model EMAC. A summary of important results and conclusions is presented in the following, with specific references to the scientific research questions (Q.1 to Q.5) posed in Sect. 1.2.

Q.1 *What is the global distribution of the different ice nucleating particles?*

By applying several model improvements and developments, a novel global INP-climatology has been compiled, which includes all major, currently discussed INP-types in the cirrus regime, i.e. mineral dust (DU), black carbon BC, crystalline ammonium sulfate (AmSu), and glassy organics (glPOM). The global distributions of these different INP-types were analysed in detail. Simulated INP number concentrations, in the range of about 1 to $100\,\mathrm{L}^{-1}$, agree well with in situ observations (e.g., Rogers et al., 1998, 2001a; DeMott et al., 2010; Schrod et al., 2017) and other global model studies (e.g., Barahona et al., 2010; Hendricks et al., 2011).

High dust INP concentrations (about $20\,\mathrm{L}^{-1}$) are simulated over dust-dominated regions (e.g. the Sahara, Arabian, and Asian deserts). BC and AmSu INPs show a distinct north-south gradient with largest concentrations of up to $50\,\mathrm{L}^{-1}$ on the Northern Hemisphere, probably dominated by anthropogenic influences. Concentrations of glPOM INPs often range between 2 and $20\,\mathrm{L}^{-1}$ in regions with strong biogenic activity mainly in the tropics and on the Southern Hemisphere. BCair INPs are highly concentrated along typical aircraft flight routes, mainly between Europe and North America (about $1\,\mathrm{L}^{-1}$).

To develop this global climatology of simulated INPs, considering the different INP-types, several model improvements and developments were applied. In a first step, the representation of mineral dust and black carbon particles in the model, typically considered as important types of INPs, was improved considerably. The online Tegen et al. (2002) dust emission scheme was adapted for application in the EMAC-MADE3 model framework to calculate wind-driven dust emissions. This resulted in a considerable improvement of the temporal variability of mineral dust in EMAC-MADE3, compared to the previously used offline emission climatology. When employing the online dust emission setup, dust emission peaks during dust burst events are much better represented in the model, evaluated against observed AOD at dust-dominated stations in northern Africa. Additionally, increasing the horizontal and vertical model resolution led to an improved representation of the spatial dispersion of mineral dust compared with ground-based lidar remote sensing and aircraft measurements of long-range transported Sahara dust. The strong positive bias of modelled particle number concentrations and dust extinction coefficients in the upper troposphere occurring in former model versions is strongly reduced (e.g. number concentrations decrease by up to a factor of 10, when employing the high resolution setup). Additionally, an increased model resolution also improves simulated black carbon mixing ratios compared with various aircraft-based observations.

In addition to mineral dust and black carbon, two more species of ice nucleating particles, i.e. glassy organics and crystalline ammonium sulfate, have been implemented in the model, including a representation of their phase state (glassy or crystalline, respectively), and have been coupled to the cirrus cloud freezing processes in EMAC. This represents a considerable improvement of the model system, as ammonium sulfate and glassy organics were observed to efficiently nucleate ice at cirrus temperatures, but were, however, only rarely considered in global models. Additionally, an existing BC tracer for tagging black carbon emissions was adapted to explicitly track BC from aviation.

By coupling the different INP-types to the microphysical cirrus cloud scheme, their ice nucleation potential at cirrus conditions has been analysed, including possible competition mechanisms between different INPs and considering regional, latitude-specific differences. Concentrations of freshly nucleated pristine ice crystals from heterogeneous freezing are typically one to two orders of magnitude lower than respective INP number concentrations. The most abundant INP-types, e.g. soot and ammonium sulfate show the largest impact on the ice crystal number concentration of freshly nucleated crystals, while highly efficient dust INPs generate the largest ice mass and show a marked effect on the ice water content.

Q.2 *To what extent do ice nucleating particles change the microphysical properties of cirrus clouds?*

The global effects of INPs on cirrus cloud properties and the Earth's radiation budget, compared to purely homogeneous freezing, were explicitly analysed in this thesis. Overall, the results presented here show that heterogeneous freezing induced by INPs has the potential to considerably alter global climate via cirrus cloud modifications. On the global scale, heterogeneous freezing results in reduced ice crystal number concentrations, enhanced sedimentation due to larger crystals, leading to a thinning of cirrus clouds and possible reductions in cloud occurrence, in agreement with previous studies (e.g., Kärcher et al., 2006; Hendricks et al., 2011; Gasparini and Lohmann, 2016; Zhu and Penner, 2020).

Additionally, the presence of INPs can also lead to increased cirrus cloud coverage compared to purely homogeneous freezing, as INPs freeze at lower supersaturations during the adiabatic cooling in updrafts, resulting in earlier cirrus cloud formation and consequently increased cloud lifetimes.

Q.3 *What are the magnitude and sign of the climatic effect of cirrus cloud modifications induced by ice nucleating particles compared with previous studies?*

INP-induced cloud modifications result in a net negative radiative effect, i.e. a global cooling, ranging between -100 and $-40\,\mathrm{mW\,m^{-2}}$, which is, compared to previous studies, mostly at the lower end of the range of simulated cooling effects (e.g., Liu et al., 2012; Wang et al., 2014; Penner et al., 2018; McGraw et al., 2020), putting these studies in a different perspective.

A large number of global model simulations were performed in this thesis to evaluate important sensitivities concerning the climatic impacts of INPs. Simulated radiative effects depend on the assumed freezing efficiency of INPs, e.g. radiative effects are reduced by a factor of 2 (i.e. are less negative) on the Northern Hemisphere, when a lower activated fraction of INPs is assumed.

INP-effects are strongly dependent on the cooling rates, i.e. the updraft velocities in the model. Using prescribed global updraft speeds ranging between 1 and $50\,\mathrm{cm\,s^{-1}}$, global radiative effects in the range of $(-260, +40)\,\mathrm{mW\,m^{-2}}$ are simulated. A strong gradient at updraft velocities of about $10\,\mathrm{cm\,s^{-1}}$ clearly indicates the crucial role of the dynamic forcing for the resulting climatic impact of INPs.

Q.4 *How large is the contribution of previously not considered particles, i.e. ammonium sulfate and organic particles to the climatic impact of aerosol-cirrus interactions?*

Newly implemented glassy organics and crystalline ammonium sulfate INPs show considerable effects (about 50 % of the total INP-effect), which are comparable to mineral dust and soot, i.e. $-32\,\mathrm{mW\,m^{-2}}$ and $-37\,\mathrm{mW\,m^{-2}}$ for the global mean radiative effect of ammonium sulfate and glassy organics, and of mineral dust and soot INPs, respectively. Impacts of ammonium sulfate are largest on the Northern Hemisphere, while glassy organic INPs mainly influence southern regions.

Importantly, the radiative effects of ammonium sulfate and glassy organics, and of mineral dust and soot add up almost linearly to the total INP-effect (about $-68\,\mathrm{mW\,m^{-2}}$ in the global mean), indicating that possible interactions and competition mechanisms between these INP-types are less important on the global scale.

Q.5 *What are possible contributions of anthropogenic aerosols with regard to the climate effects of ice nucleating particles?*

Anthropogenic INPs (e.g. black carbon and ammonium sulfate related to the combustion of fossil fuels) have the potential to considerably modify cloud and radiative properties, and show largest effects on the Northern Hemisphere of about $-100\,\mathrm{mW\,m^{-2}}$ (mean radiative effect at Northern Hemisphere extratropics).

Additionally, highly efficient INPs, e.g. proposed for cirrus cloud seeding in climate engineering, were shown to lead to increased ice crystal numbers and cloud coverage, as these INPs initiate freezing already at very low supersaturations with respect to ice. This results in large warming effects of up to $250 \pm 50\,\mathrm{mW\,m^{-2}}$, revealing the problem of overseeding cirrus clouds with this climate engineering approach, as also stated in previous studies (e.g., Storelvmo et al., 2013; Penner et al., 2015; Gasparini and Lohmann, 2016).

To conclude, the results of this thesis show that ice nucleating particles can lead to considerable cirrus cloud and climate modifications. A global climatology of INPs is presented, which for the first time considers all major INP-types in the cirrus regime, i.e. mineral dust, soot, crystalline ammonium sulfate, and glassy organics. A major improvement, compared to most previous studies which only consider mineral dust and soot, is the inclusion of ammonium sulfate and glassy organic INPs. These show considerable impacts on cirrus clouds and radiation, similar to mineral dust and soot, and need to be taken into account in future model applications. Anthropogenic INP-effects described in this work have the potential to influence climate change and contribute a notable part to the total anthropogenic aerosol forcing.

5.2 Outlook

The analysis of cirrus cloud and climate modifications induced by ice nucleating particles presented in this work needs to be further continued in future studies. An important application should be the quantification of anthropogenic effects, e.g. the indirect aerosol effect of aviation soot particles is strongly debated and the subject of ongoing research. Additionally, anthropogenic INP-effects related to other traffic and non-traffic sectors (shipping, land transport, energy production) should be evaluated in follow-up studies. Further constraining uncertainties in these indirect aerosol effects is a crucial aspect for developing effective climate change mitigation strategies.

Future work should in particular take important sensitivities into account, which have been described and analysed in this thesis, e.g. variations of freezing efficiencies of INPs, or the dependency on updraft velocities and cooling rates. In this context, additional measurements on the freezing properties of INPs at cirrus temperatures, and also on atmospheric updraft velocities, are necessary to further constrain the climatic impact of INPs.

To facilitate a detailed interpretation of the diversity of simulated indirect aerosol effects, inter-comparison studies between different model systems with commonly-designed experiments would be helpful. Notable examples of the benefits of such inter-comparison exercises are provided by the CMIP activities (e.g., Eyring et al., 2016; Collins et al., 2017; Wu et al., 2020) and the AeroCom project (e.g., Huneeus et al., 2011; Samset et al., 2014; Gliß et al., 2021). Moreover, the analysis of the simulated global distribution of different INPs could be further refined by applying machine learning clustering algorithms (e.g. k-means clustering; Hartigan and Wong, 1979) to identify regions dominated by specific INP-types or by possible competition mechanisms between different INPs.

Further model developments and improvements are conceivable and could be considered for future studies. A re-evaluation of the results presented here, employing a higher model resolution and the extensively tuned model setup of Righi et al. (2020) could corroborate the results of this thesis. Additionally, the heterogeneous freezing scheme applied in this work could be improved, e.g. by including a spectrum of possible activated fractions of INPs depending on the supersaturation with respect to ice, in contrast to using a single value for f_{act}. Possible further model developments could focus on the representation of the sub-grid vertical velocity fluctuations in the model, as this has a pronounced influence on the simulated INP-effects.

Appendix

This Appendix contains additional figures complementing the evaluation of the model results presented in Chapter 4 of this thesis. Details about each figure can be found in the corresponding sections of this thesis as mentioned in the respective appendix figure captions.

A.1 Supplementary evaluation of mineral dust

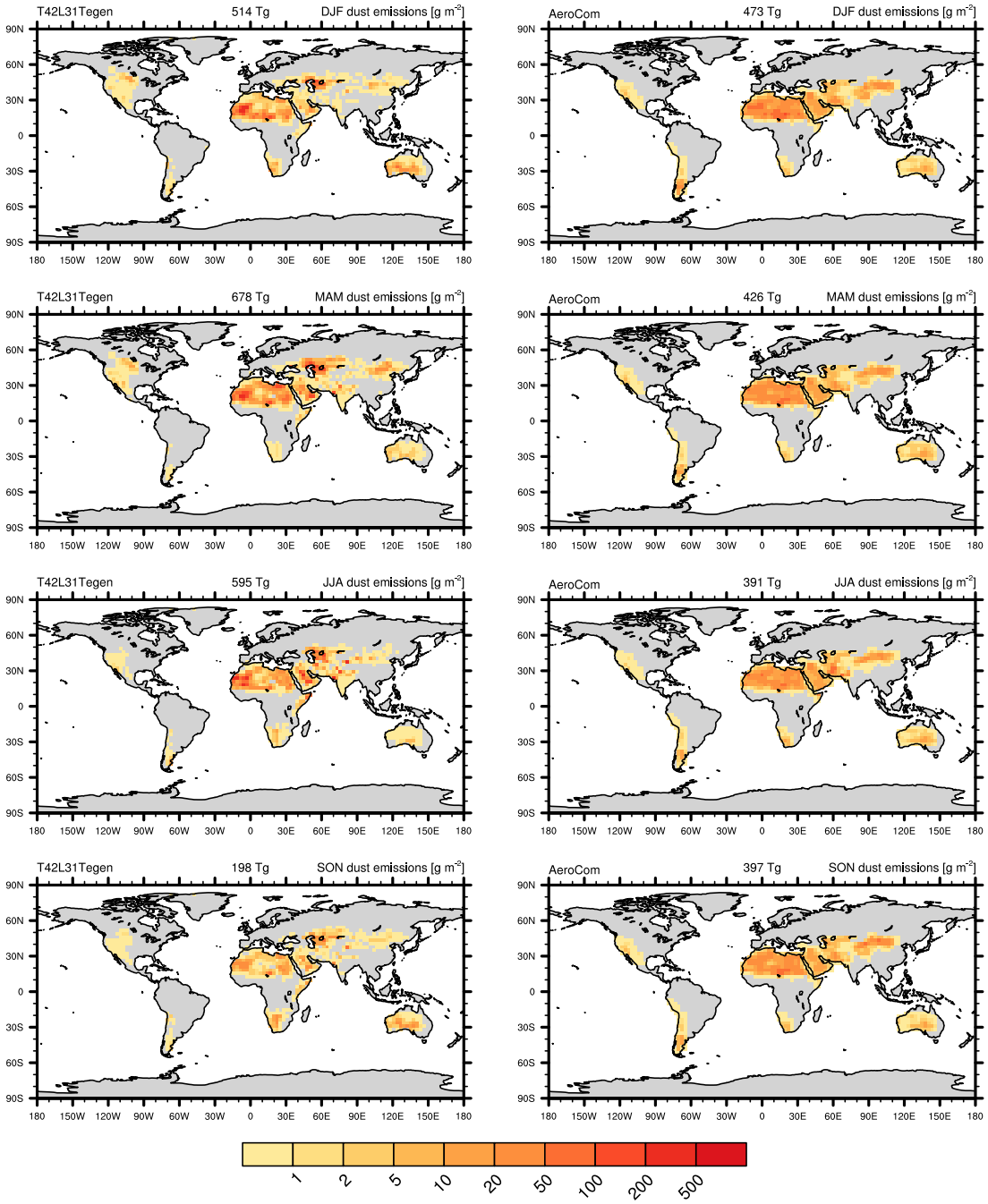

Figure A.1: Similar to Fig. 3.3, but showing the global seasonal (from top to bottom: DJF, MAM, JJA, SON) dust emissions in the T42L31Tegen (left column) and T42L31AeroCom (right column) setup. Emissions are given in units of $\mathrm{g\,m^{-2}}$. Total seasonal dust emissions are shown at the top of each plot in units of Tg. As shown in Beer et al. (2020, Fig. S1). See Sect. 3.3 for details.

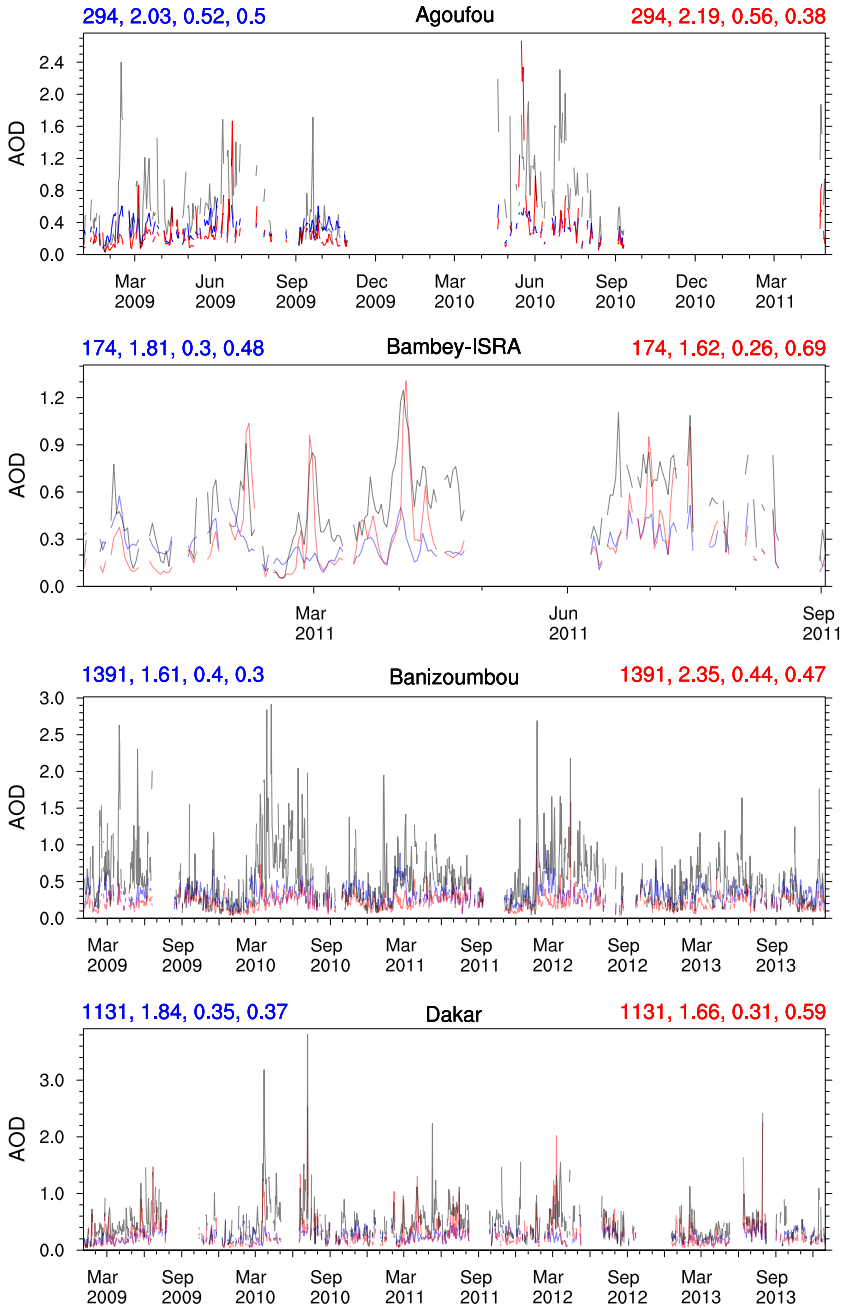

Figure A.2: Similar to Fig. 4.1, but comparing model (T42L31AeroCom in blue, T42L31Tegen in red) and AERONET (grey) AOD time series for all 17 stations depicted in Fig. 4.2, showing the full comparison period (2009/01–2013/12). Gaps in the time series correspond to missing observations. The numbers at the top left and right represent the number of data points, the ratio of averages of observation and model data, root mean square error, and Pearson correlation coefficient, for the two model setups, respectively. As shown in Beer et al. (2020, Fig. S3). See Sect. 4.1.1 for details.

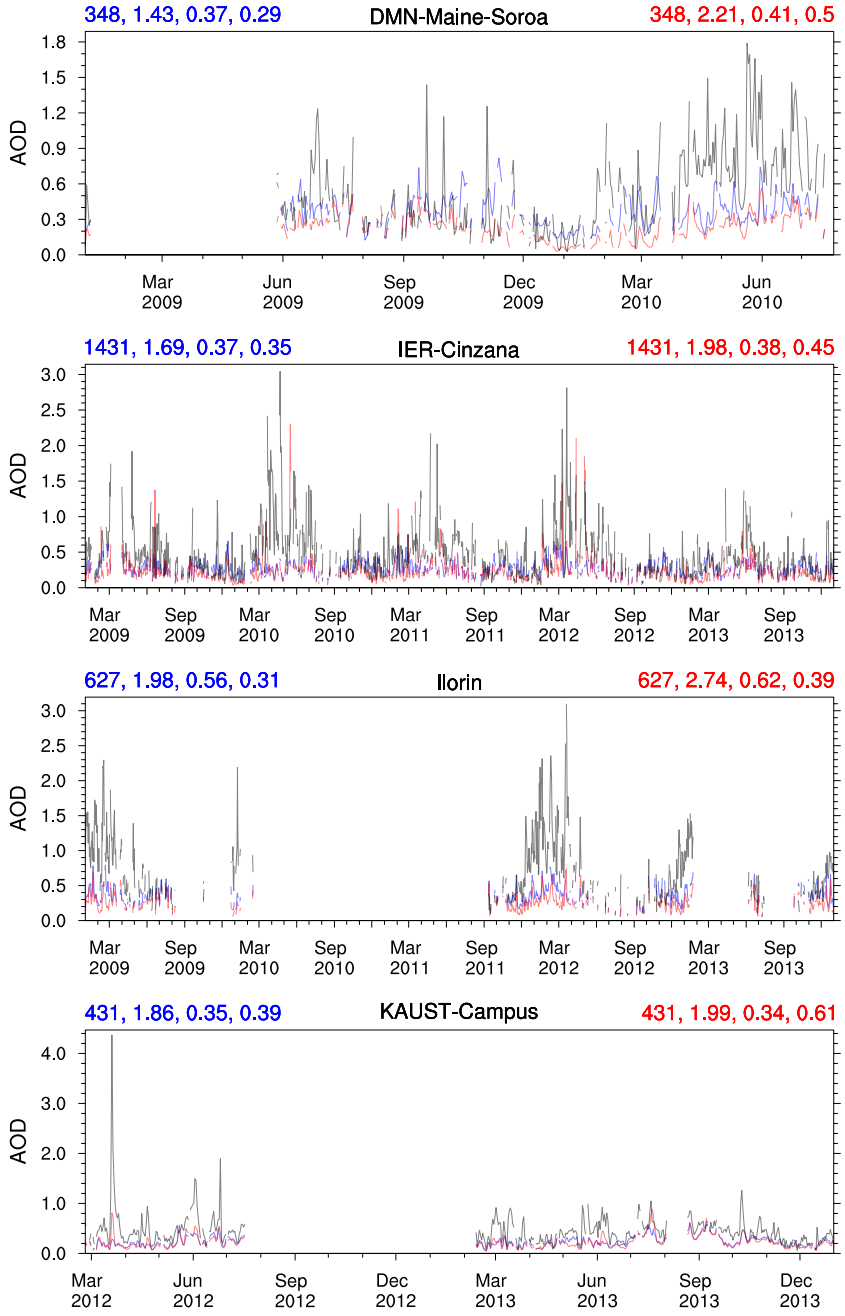

Figure A.2: Continued.

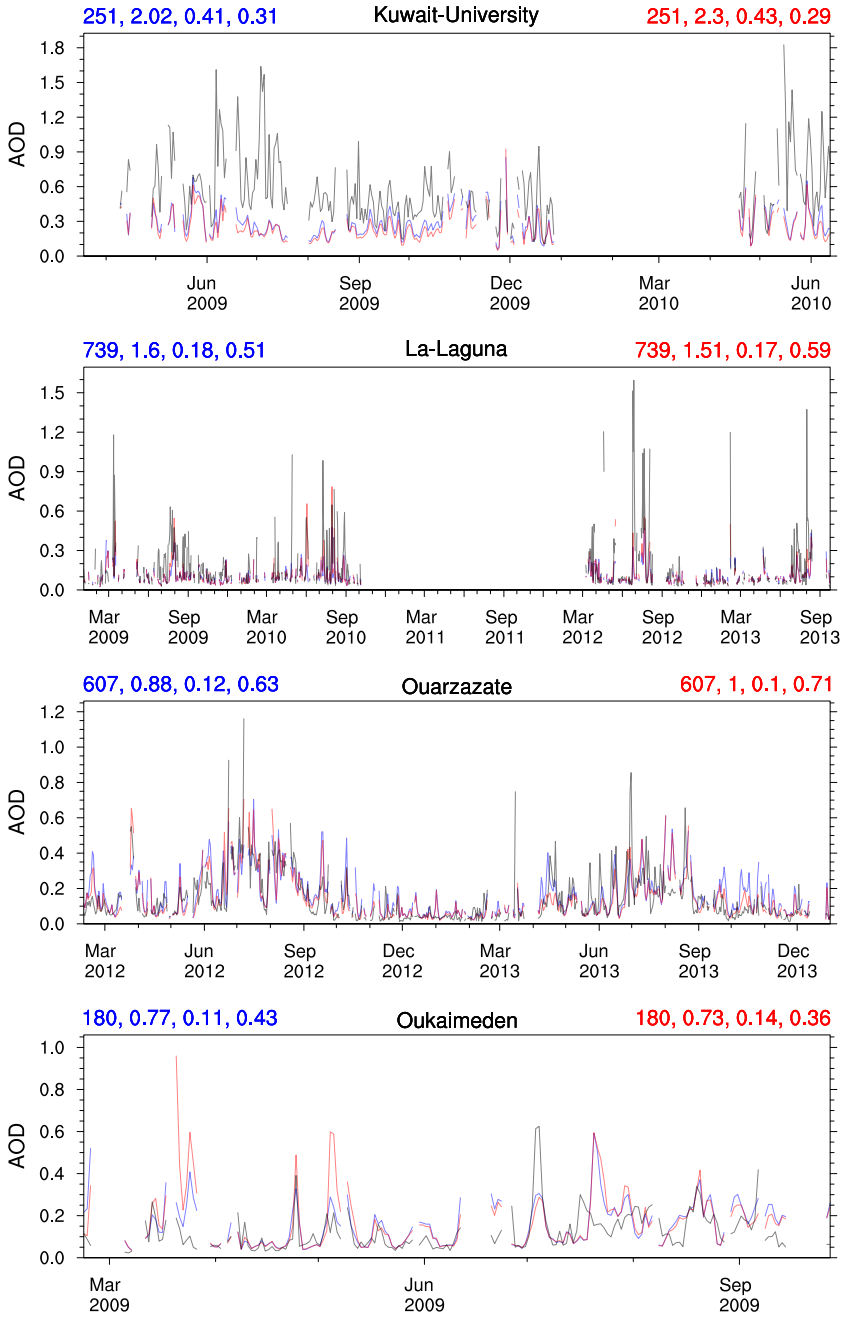

Figure A.2: Continued.

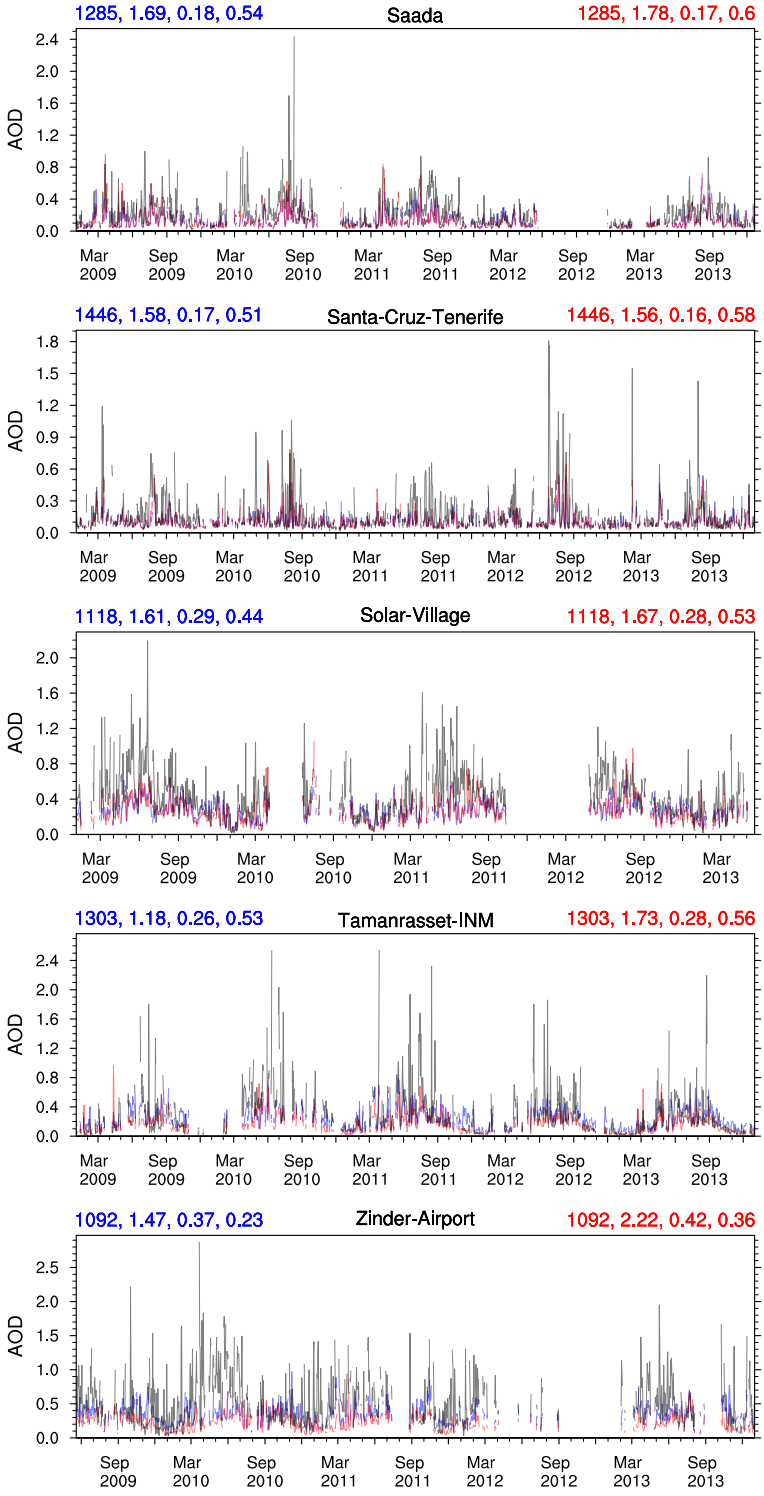

Figure A.2: Continued.

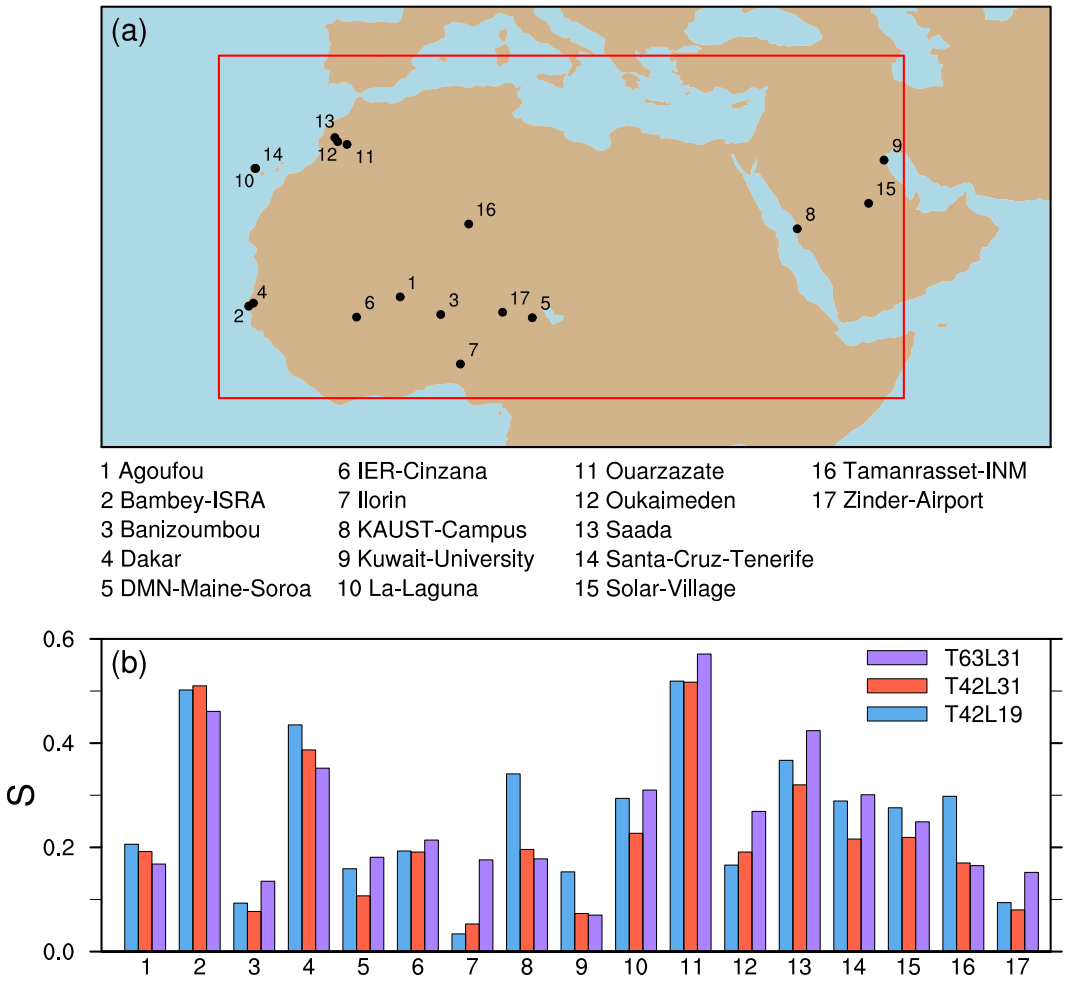

Figure A.3: As in Fig. 4.2, but comparing model results for the three different model resolutions (T42L19 in blue, T42L31 in red, T63L31 in purple). As shown in Beer et al. (2020, Fig. S6). See Sect. 4.1.2 for details.

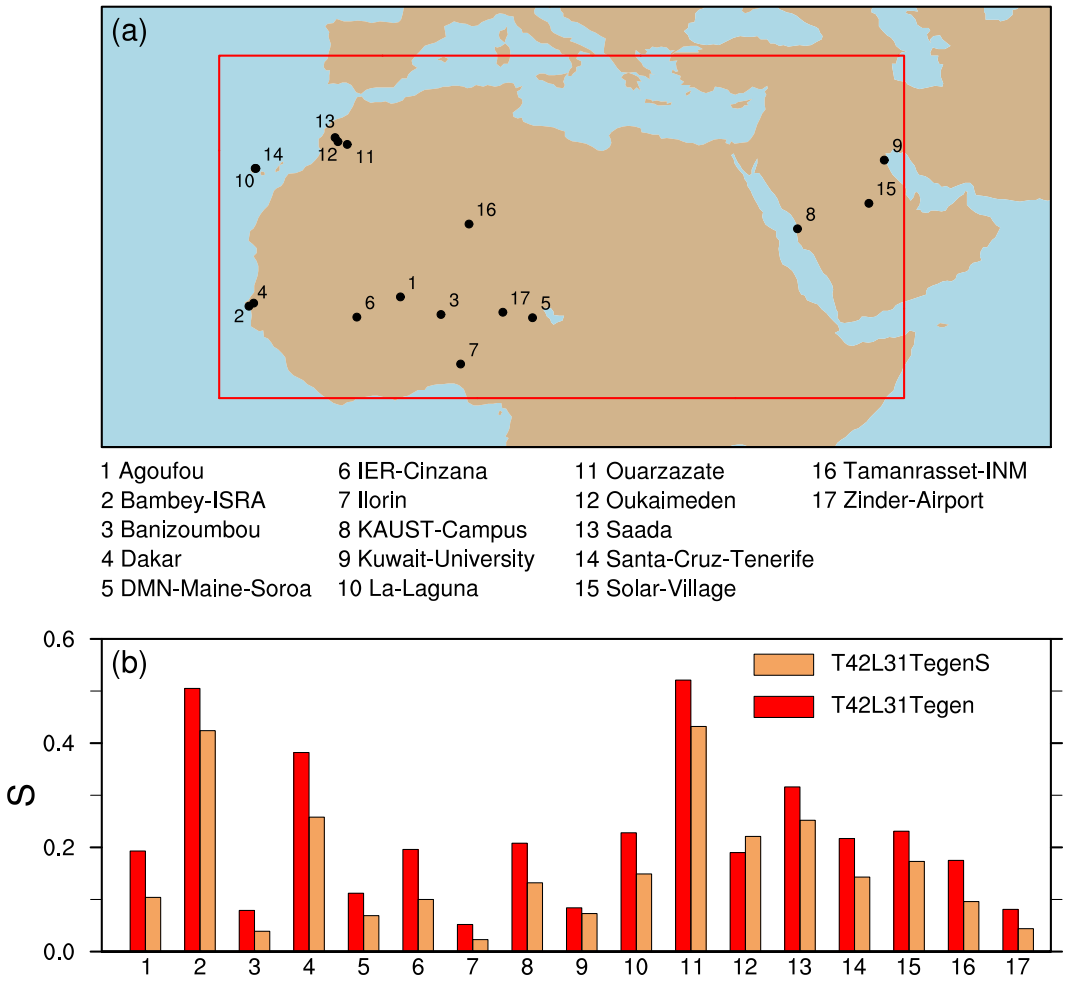

Figure A.4: As in Fig. 4.2, but comparing AOD station data with the T42L31Tegen (red) and T42L31TegenS (orange) model setups, i.e. varying the size distribution of emitted dust. As shown in Beer et al. (2020, Fig. S10). See Sect. 4.1.3 for details.

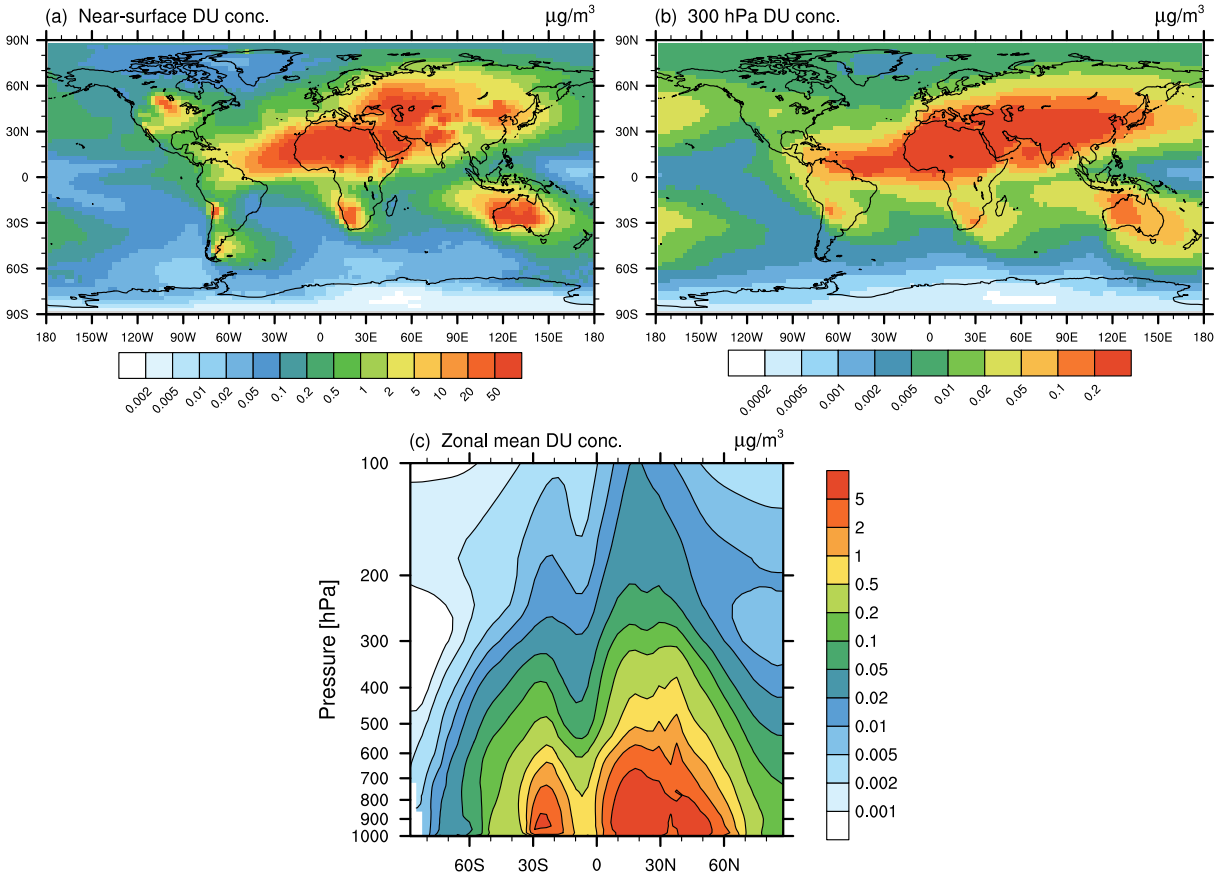

Figure A.5: As in Fig. 4.7, but showing simulated mineral dust (DU) mass concentrations for the T42L31 model resolution setup. See Sect. 4.1 for details.

A.2 Supplementary evaluation of black carbon

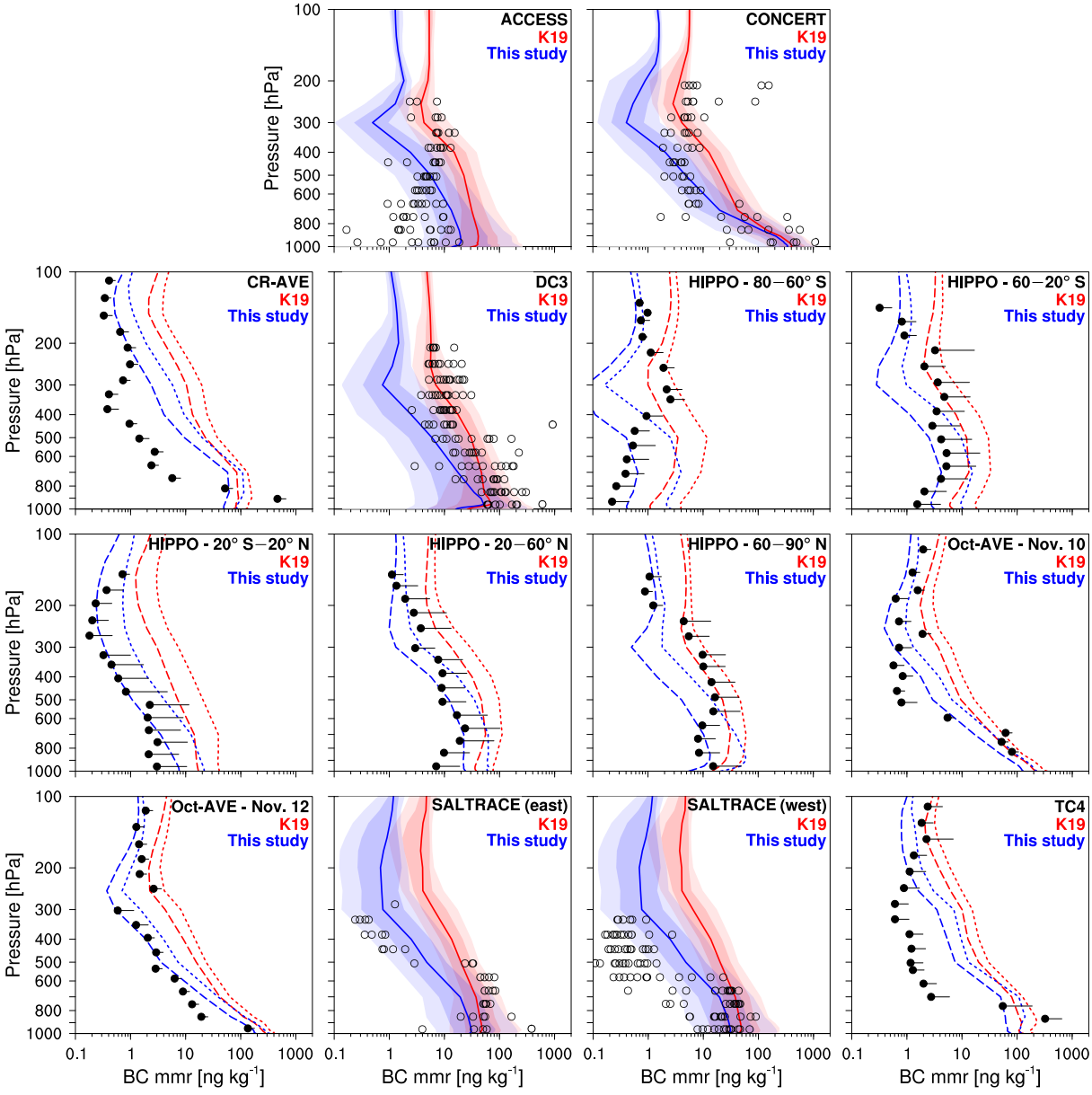

Figure A.6: As in Kaiser et al. (2019), their Fig. 5, comparing various aircraft measurements of BC (black) with their results (K19, red) and with results from the T63L31Tegen setup presented in this work (blue). Dashed lines and filled circles represent mean values; dotted lines and whiskers represent standard deviations, which are only shown in the direction of larger values for clarity. Solid lines stand for median values. Light and dark shadings indicate the 10th to 90th, and 25th to 75th percentiles, respectively. Hollow circles are the median values of individual flights. As shown in Beer et al. (2020, Fig. S8). See Sect. 4.2 for details.

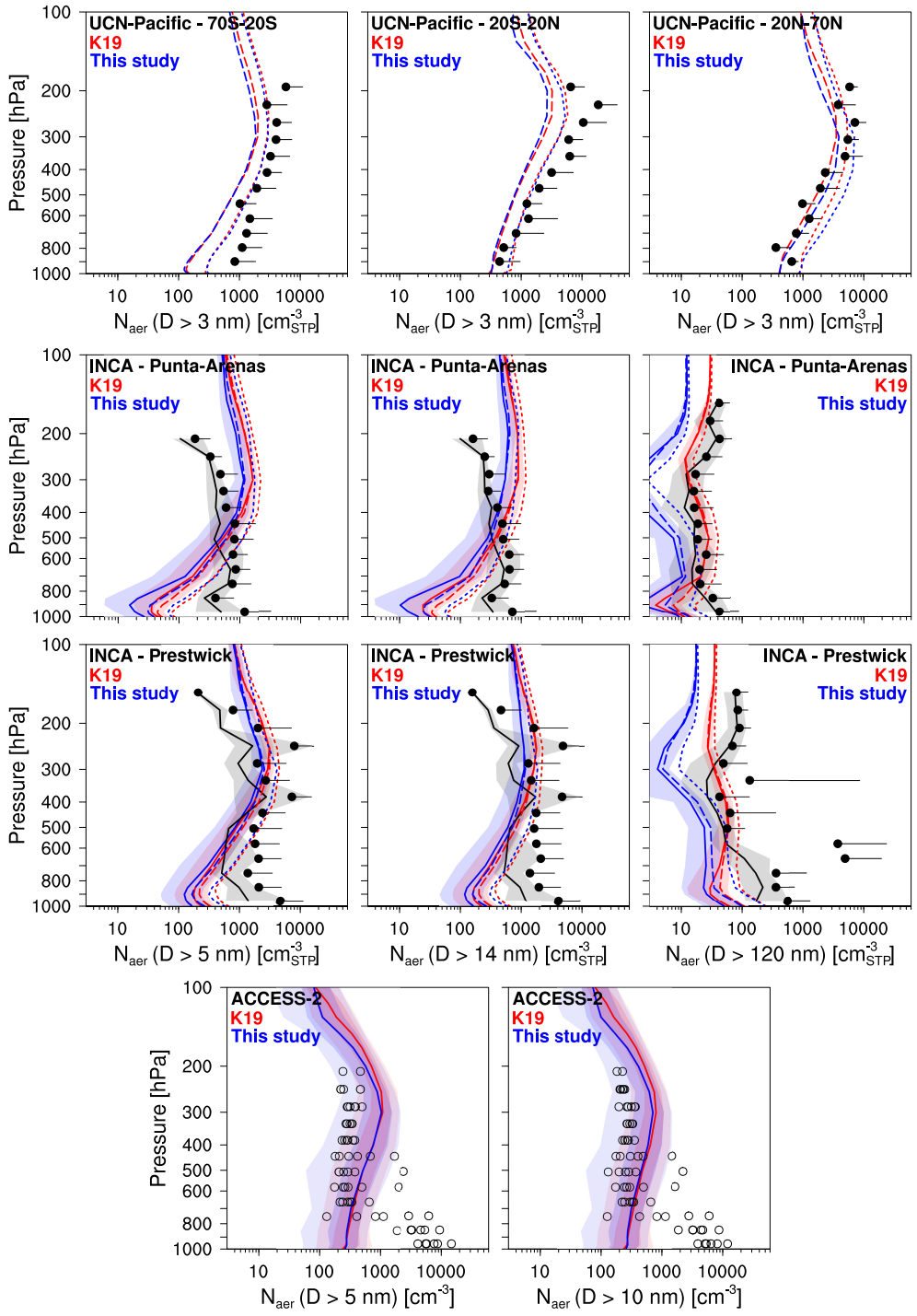

Figure A.7: Same as Fig. A.6, but for particle number concentrations with various cutoff diameters. As shown in Beer et al. (2020, Fig. S9). See Sect. 4.2 for details.

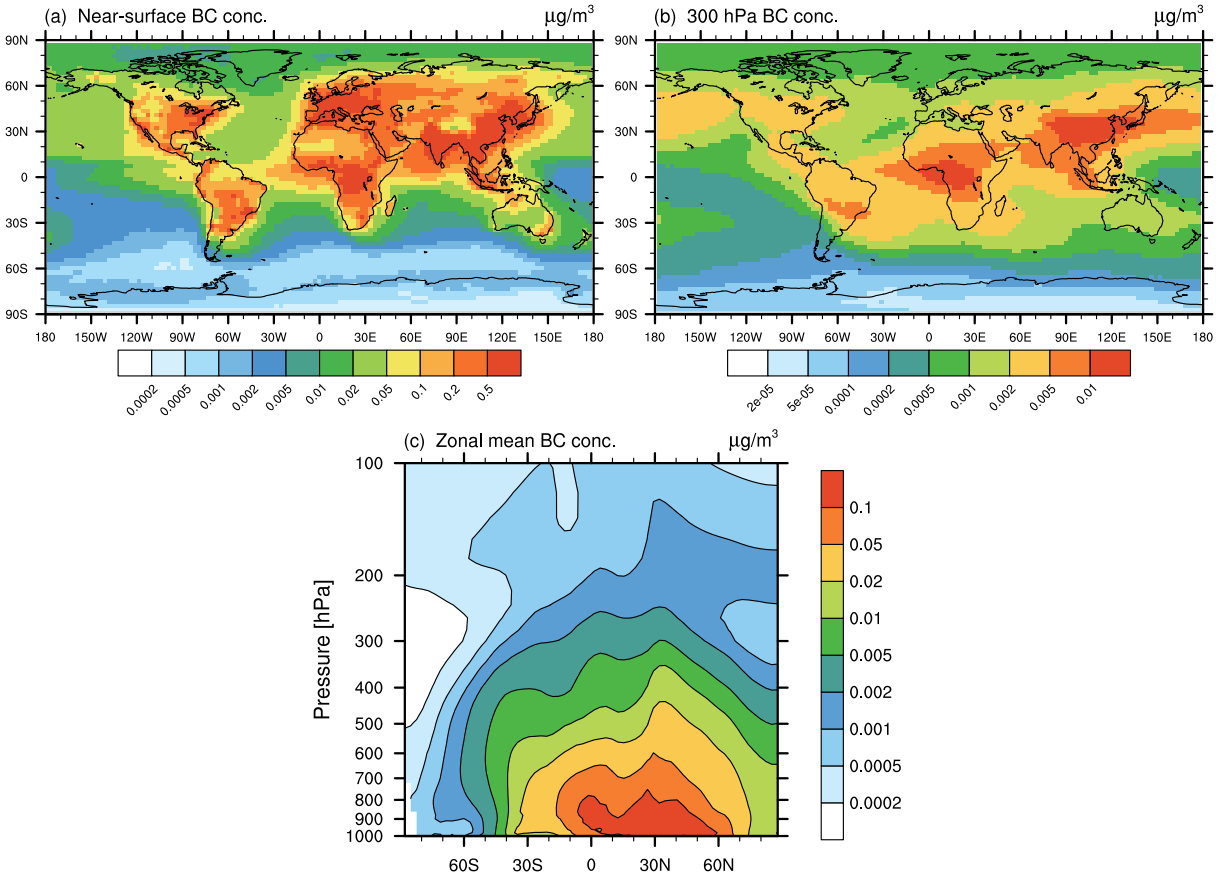

Figure A.8: As in Fig. 4.9, but showing simulated black carbon (BC) mass concentrations for the T42L31 model resolution setup. See Sect. 4.2 for details.

A.3 Supplementary evaluation of glassy organics

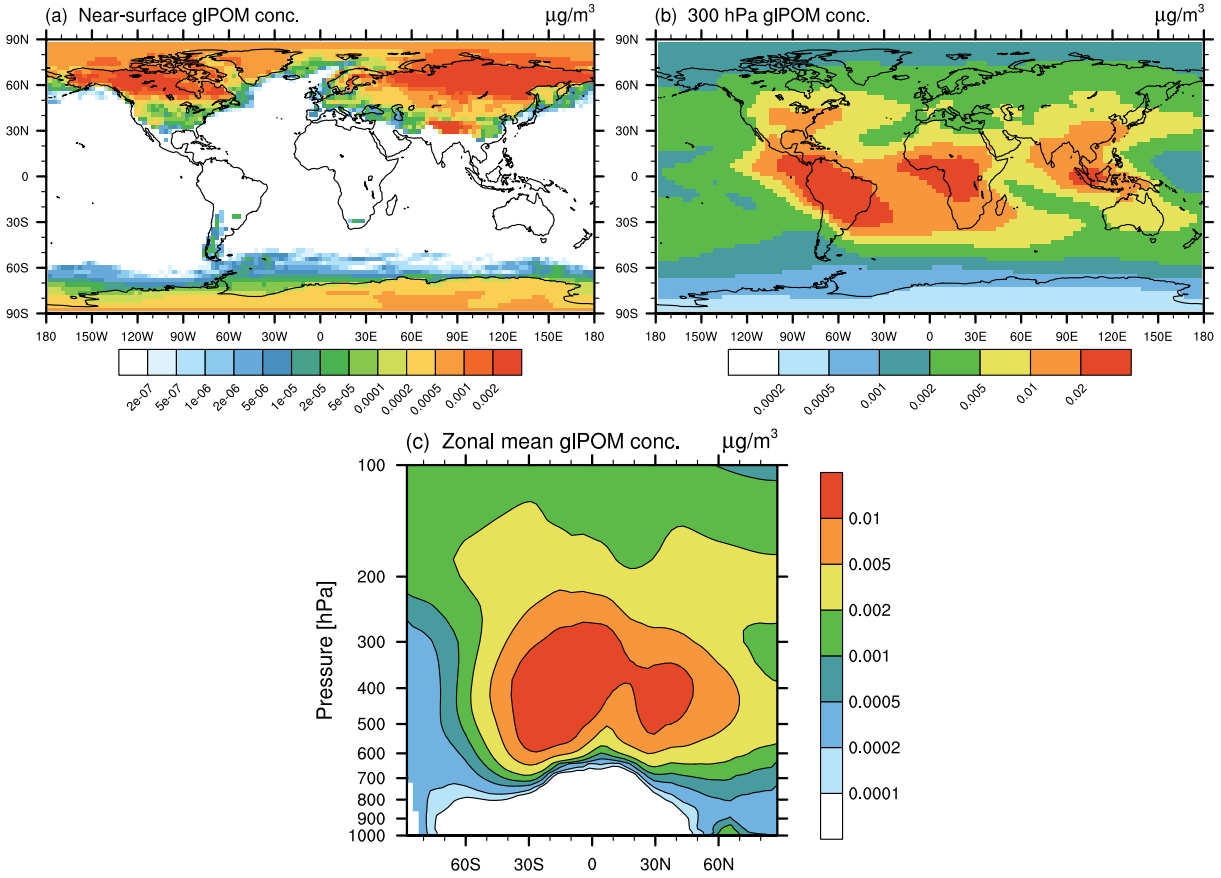

Figure A.9: As in Fig. 4.10, but showing simulated glassy organics (glPOM) mass concentrations for the T42L31 model resolution setup. See Sect. 4.3 for details.

A.4 Supplementary evaluation of ammonium sulfate

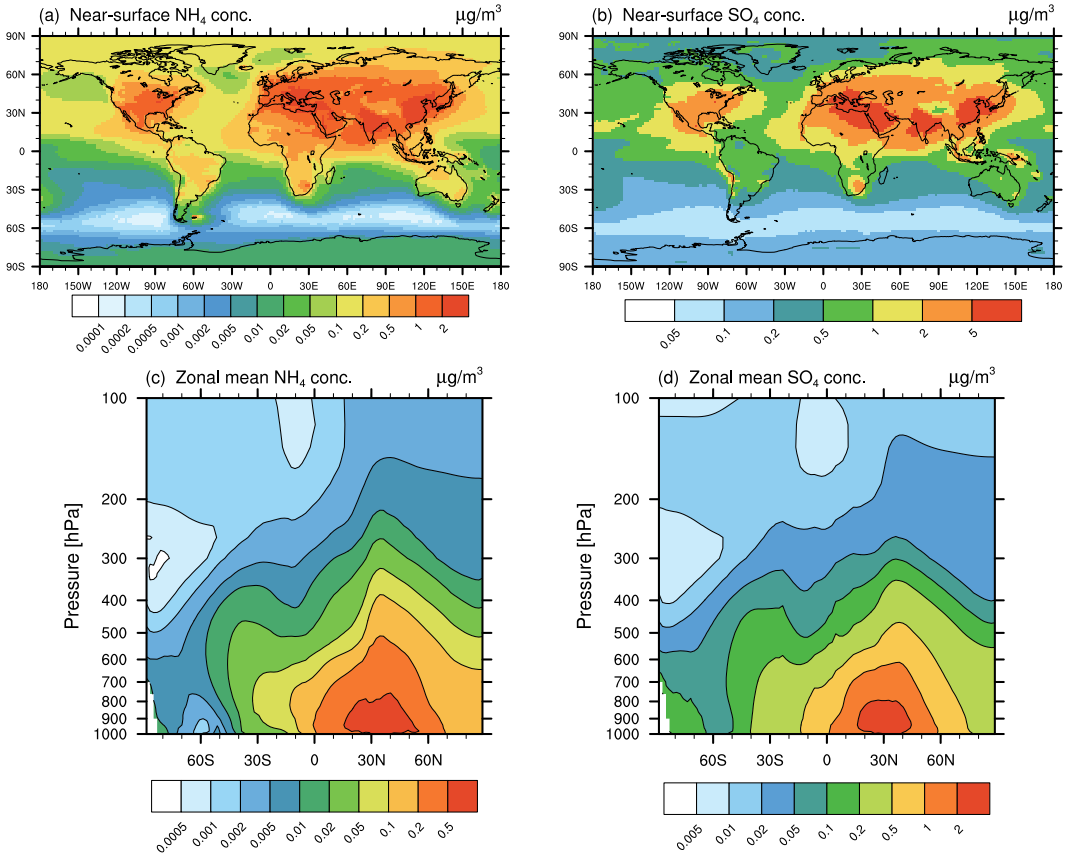

Figure A.10: Simulated mass concentrations of ammonium (NH_4) and sulfate (SO_4) from a simulation with T63L31 model resolution (multi-annual mean, years 2000–2004). Mass concentrations in units of $\mu g\, m^{-3}$ are shown near the surface (a, b) and as zonal mean vertical distribution (c, d) for NH_4 and SO_4, respectively. See Sect. 4.4 for details.

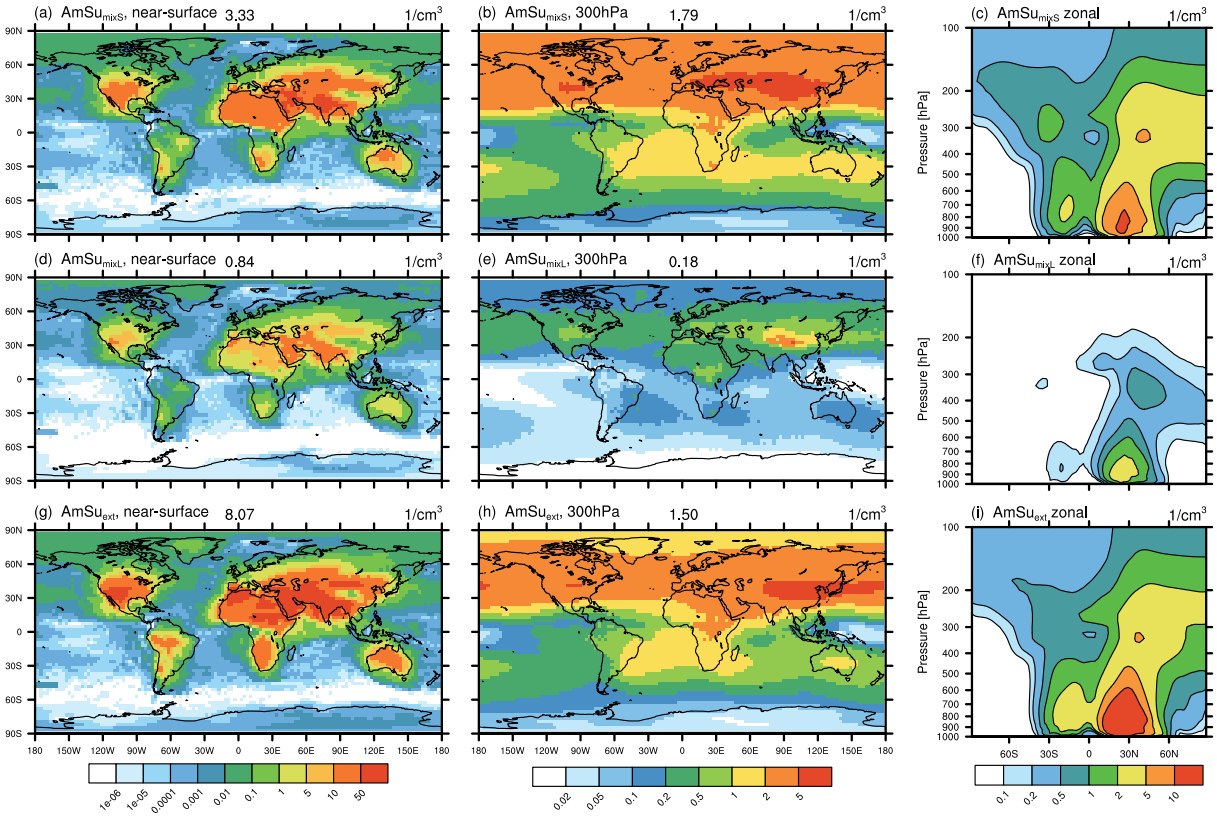

Figure A.11: As in Fig. 4.11, but showing simulated crystalline ammonium sulfate (AmSu) number concentrations in units of cm^{-3} for the T42L31 model resolution setup. See Sect. 4.4 for details.

A.5 Supplementary evaluation of INP-induced cirrus modifications

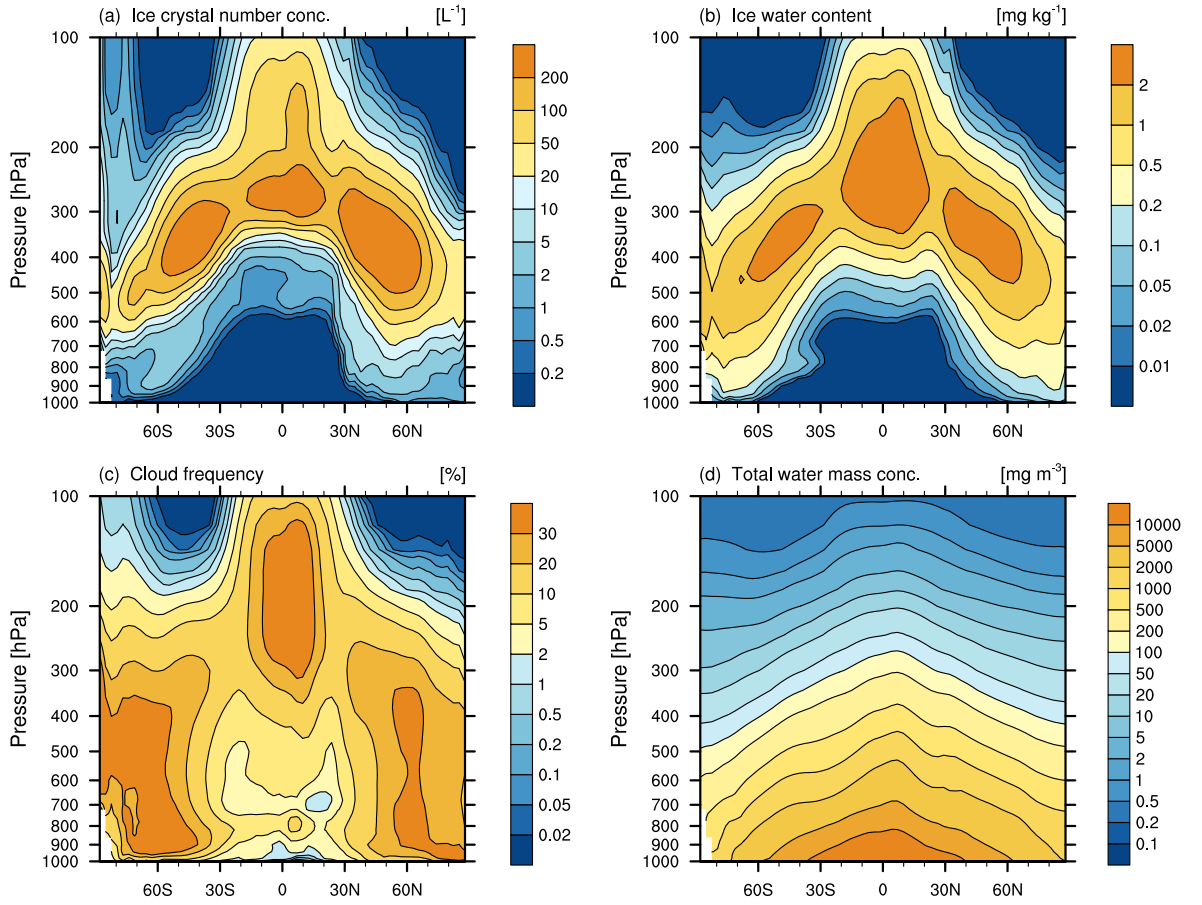

Figure A.12: Zonal mean vertical distributions of simulated cloud variables, for a simulation including all INPs (freezing properties corresponding to a value of f_{act} in the middle of the freezing spectrum, see Table 3.3), multi-annual mean (years 2000–2004). Shown are (a) ice crystal number concentration in units of L^{-1}, (b) ice water content in units of $\mathrm{mg\,kg}^{-1}$, (c) frequency of cloud occurrence in %, and (d) total water (water vapour plus ice) mass concentration in units of $\mathrm{mg\,m}^{-3}$. See Sect. 4.6.1 for details.

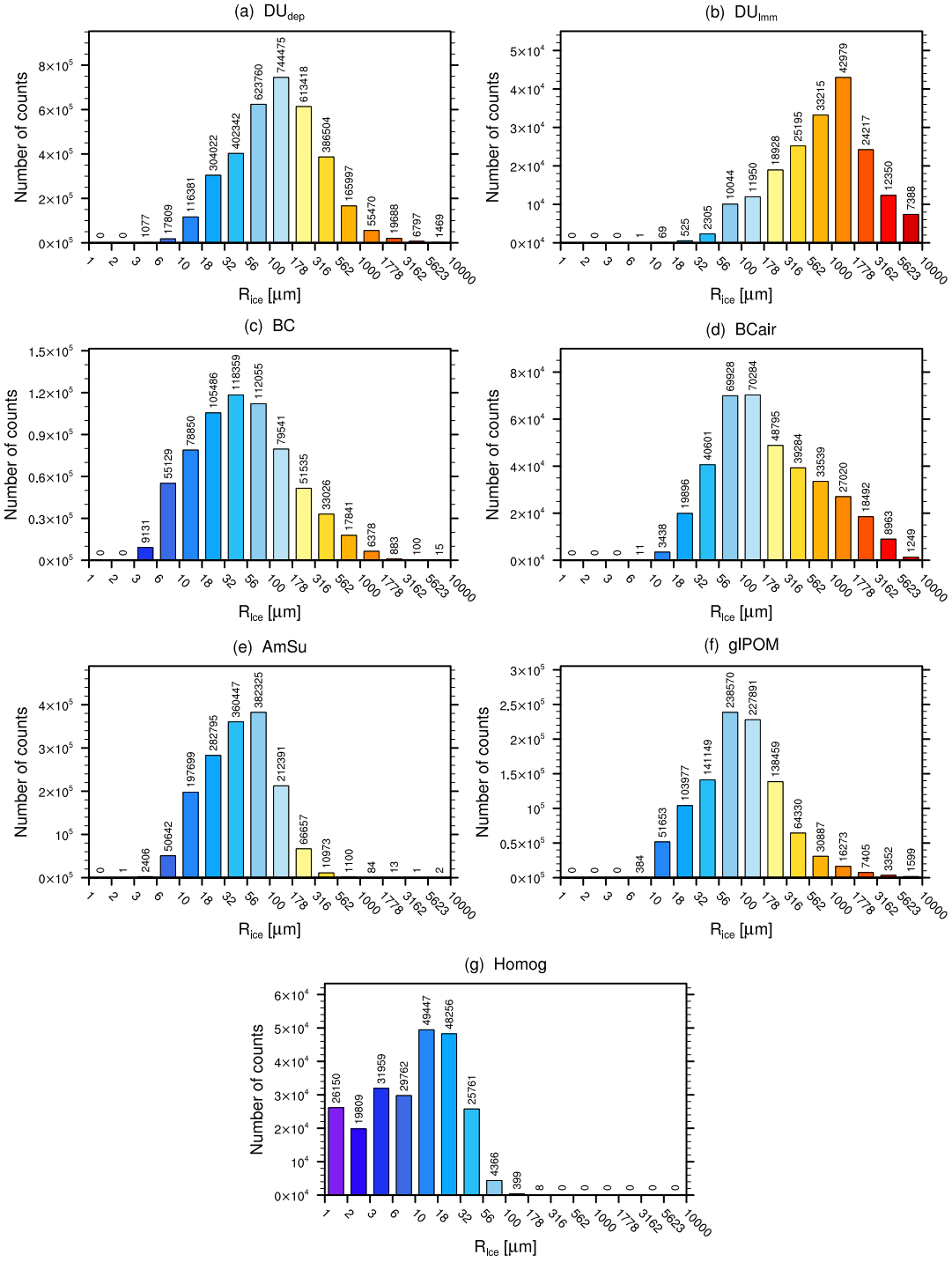

Figure A.13: Ice crystal radii (in units of µm) of newly formed crystals per freezing mode. The histograms are calculated from one simulated year (using instantaneous, i.e. 11 hour model output), with four logarithmic bins per order of magnitude. Shown are (a) DU immersion, (b) DU deposition, (c) BC, (d) BCair, (e) AmSu, (f) glPOM, and (g) homogeneous freezing. Numbers above each bar represent actual counts. Note the different y-axis scales in each plot. See Sect. 4.5 for details.

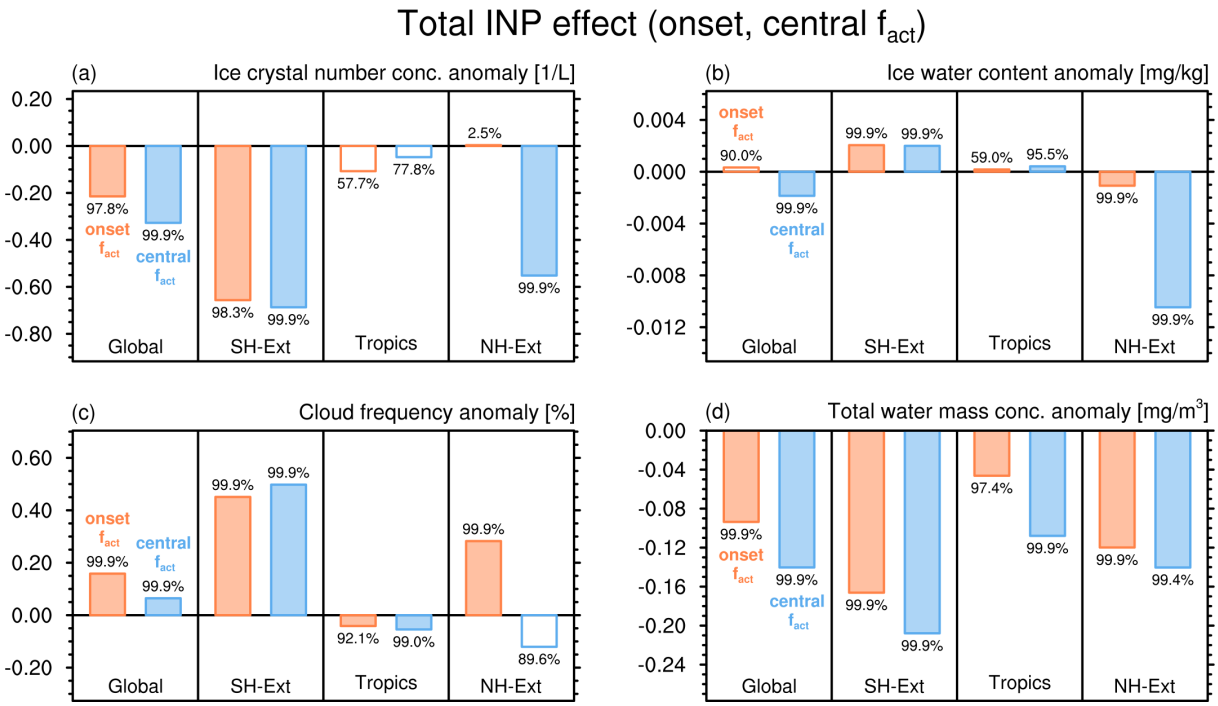

Figure A.14: As in Fig. 4.17, but showing absolute differences of (a) ice crystal number concentration in units of L^{-1}, (b) ice water content in units of $mg\,kg^{-1}$, (c) frequency of cloud occurrence in %, and (d) total water (water vapour plus ice) mass concentration in units of $mg\,m^{-3}$, with respect to pure homogeneous freezing. See Sect. 4.6.1 for details.

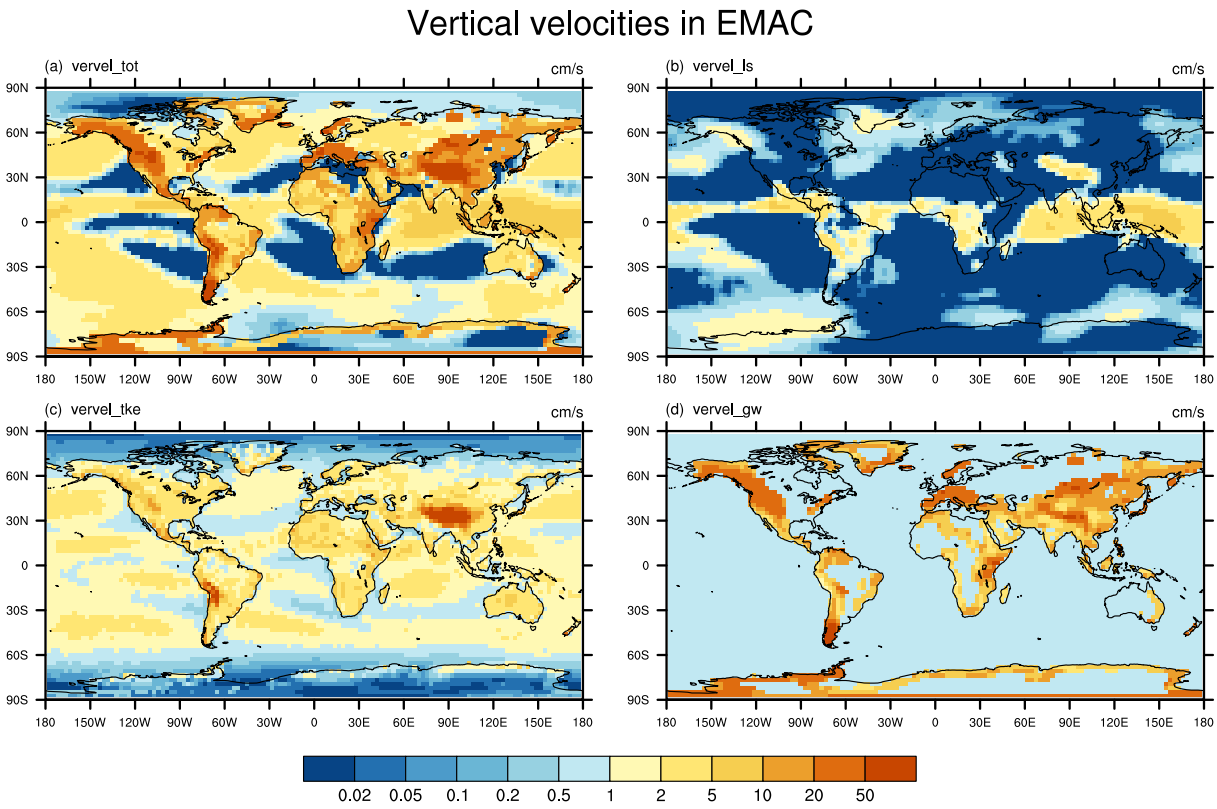

Figure A.15: Simulated vertical velocities in EMAC-MADE3 as parametrized according to Eq. 3.3, multi-annual mean (years 2000–2004) and averaged above 400 hPa. Shown are (a) the total vertical velocity in units of $\mathrm{cm\,s^{-1}}$, i.e. the sum of (b) the large-scale component, (c) the turbulent component, and (d) the gravity wave component due to small-scale orographic gravity waves. See Sect. 4.6.2 for details.

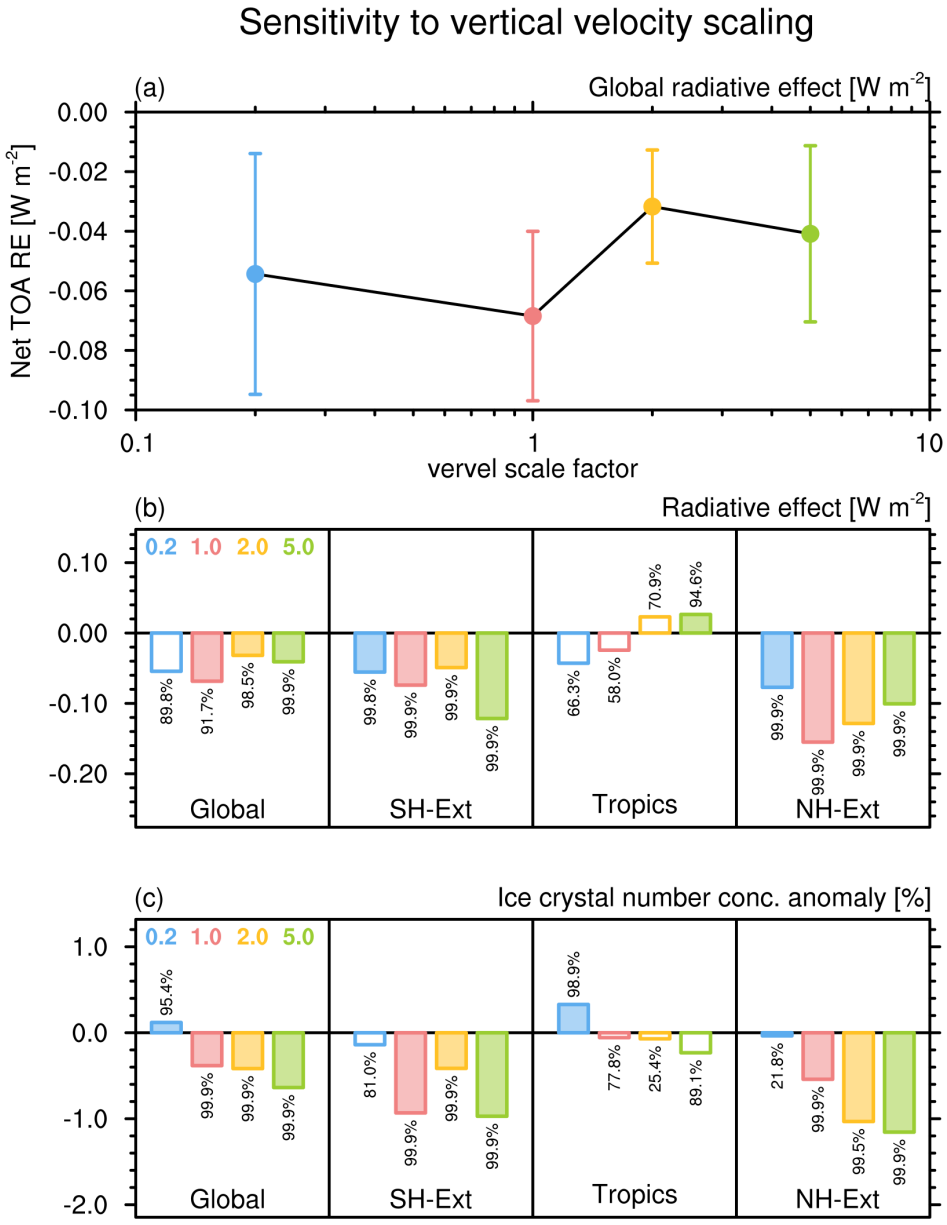

Figure A.16: As in Fig. 4.21, but showing the sensitivity of the total INP-effect to the scaling of the vertical velocity ω (see Eq. 3.3), with scaling factors of 0.2 (blue), 1.0 (red, i.e. the reference), 2.0 (yellow), and 5.0 (green). Note the different y-axis scales in each plot. See Sect. 4.6.2 for details.

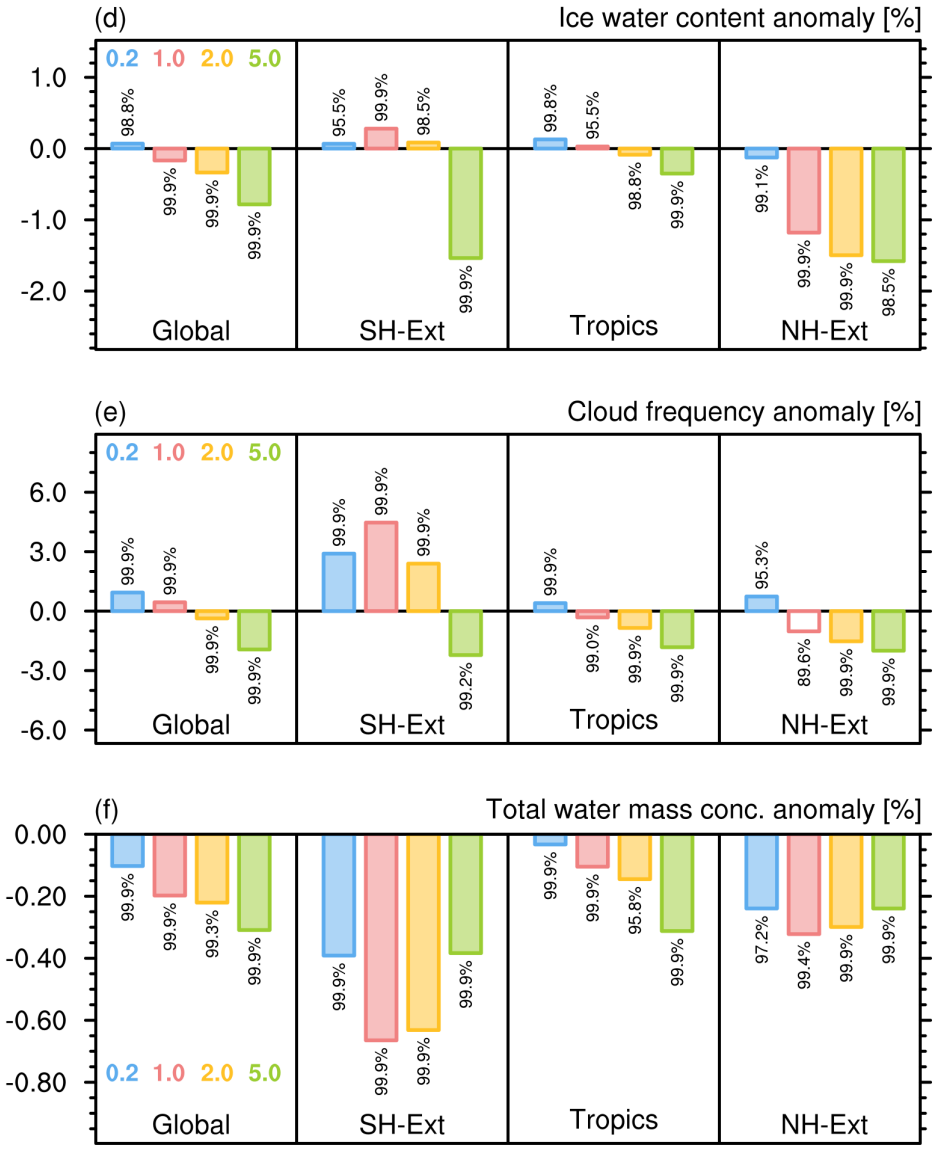

Figure A.16: Continued.

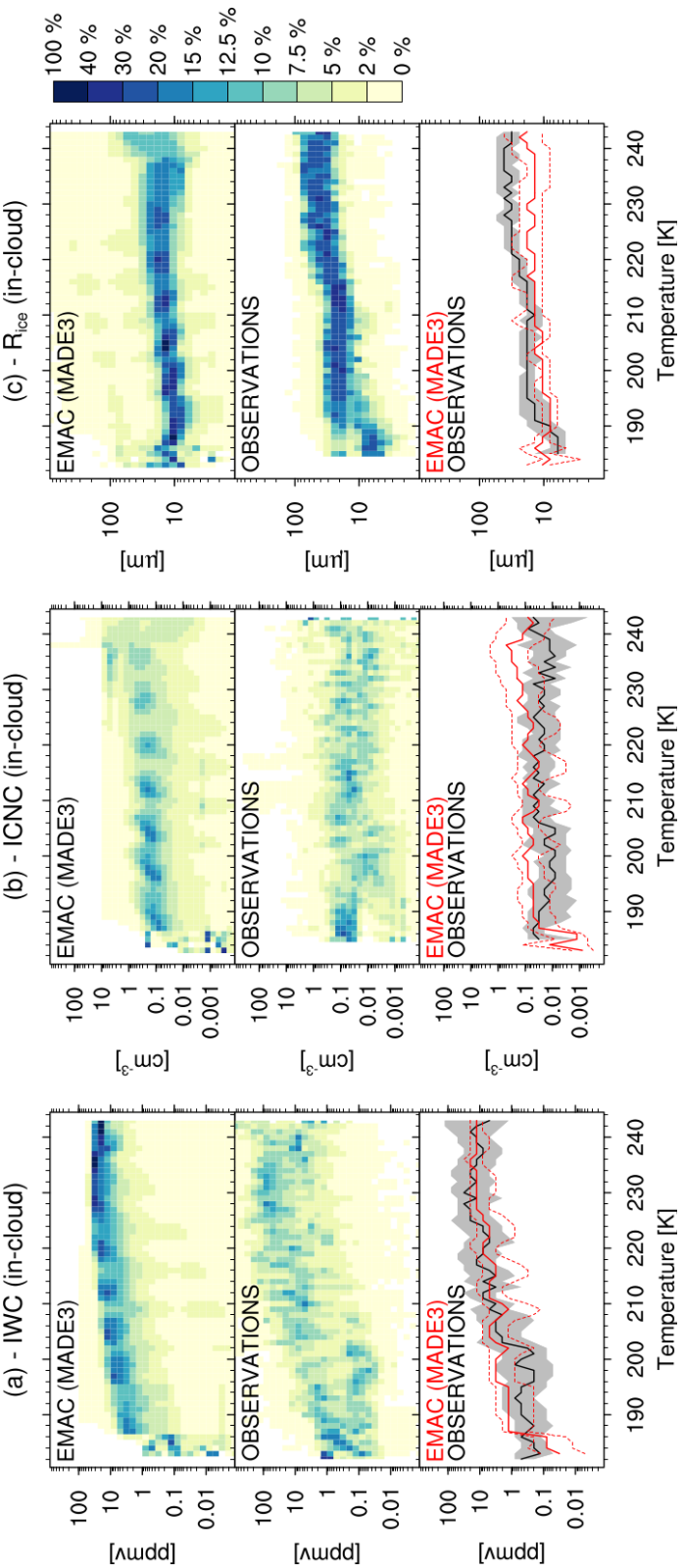

Figure A.17: Climatology of simulated cirrus cloud properties with EMAC-MADE3 compared with in-situ aircraft observations, as shown in Righi et al. (2020), but using the model setup presented in this work (setup HetRef, see Table 4.1; multi annual mean of years 2000–2003). Observational data represent a climatology calculated from 18 aircraft-based field campaigns (Krämer et al., 2009, 2016), further complemented with more recent data (Krämer et al., 2020). Shown are in-cloud values of (a) ice water content, (b) ice crystal number concentration, and (c) ice crystal mean-volume radius, plotted as probability distribution functions in 1 K temperature bins in the model (top plot in each panel) and in the observations (middle plot). The bottom panel in each plot shows the median (solid lines) and 25/75% quantiles (dashed lines) of model (red) and observational (black) data, respectively. See Sect. 4.6.3 for details.

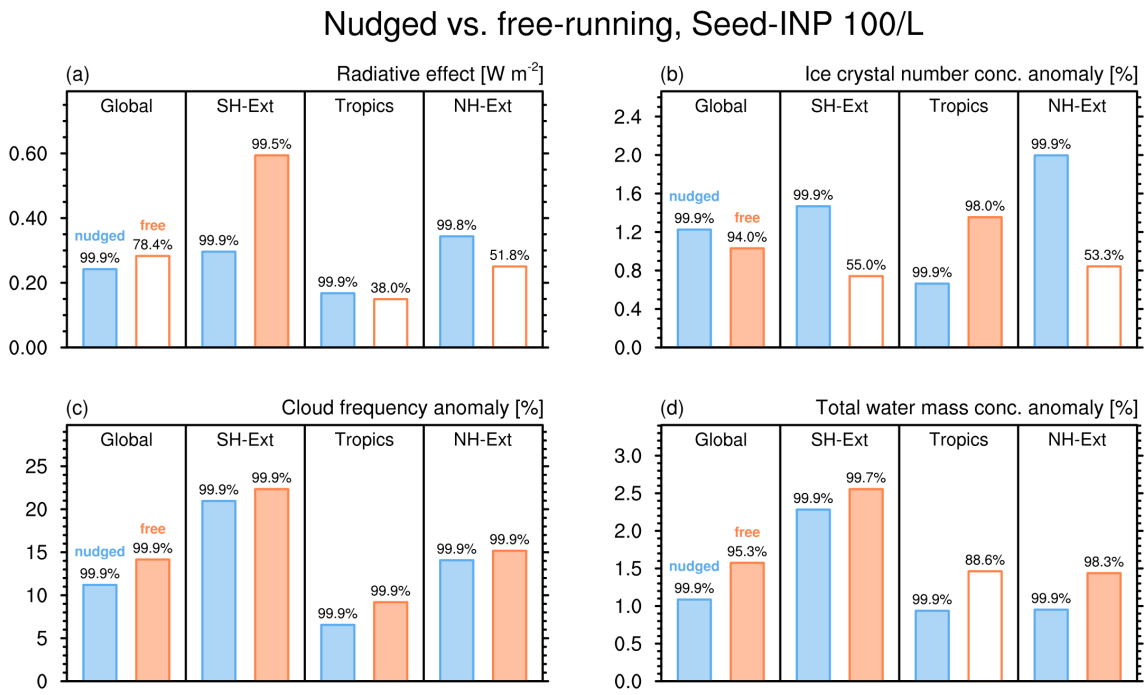

Figure A.18: As in Fig. 4.22, but comparing the global and regional INP-effect due to highly efficient INPs used for cirrus cloud seeding, for an INP concentration of $100\,\mathrm{L}^{-1}$ (multi-annual mean, years 2000–2009). Vertical velocities were parametrized according to Eq. 3.3. Note the different y-axis scales in each plot. See Sect. 4.6.4 for details.

References

Abbatt, J. P. D., Benz, S., Cziczo, D. J., Kanji, Z., Lohmann, U., and Möhler, O. Solid ammonium sulfate aerosols as ice nuclei: A pathway for cirrus cloud formation. *Science*, 313:1770–1773, 2006. ISSN 0036-8075. doi:10.1126/science.1129726.

Abdul-Razzak, H. and Ghan, S. J. A parameterization of aerosol activation: 2. Multiple aerosol types. *J. Geophys. Res. Atmos.*, 105(D5):6837–6844, 2000. doi:10.1029/1999jd901161.

Ackermann, I. J., Hass, H., Memmesheimer, M., Ebel, A., Binkowski, F. S., and Shankar, U. Modal aerosol dynamics model for europe: Development and first applications. *Atmos. Environ.*, 32(17):2981–2999, 1998. doi:10.1016/S1352-2310(98)00006-5.

Ahola, J., Korhonen, H., Tonttila, J., Romakkaniemi, S., Kokkola, H., and Raatikainen, T. Modelling mixed-phase clouds with the large-eddy model UCLALES–SALSA. *Atmos. Chem. Phys.*, 20(19):11639–11654, 2020. doi:10.5194/acp-20-11639-2020.

Albrecht, B. A. Aerosols, cloud microphysics, and fractional cloudiness. *Science*, 245 (4923):1227–1230, 1989. doi:10.1126/science.245.4923.1227.

Alfaro, S. C., Gaudichet, A., Gomes, L., and Maillé, M. Modeling the size distribution of a soil aerosol produced by sandblasting. *J. Geophys. Res. Atmos.*, 102(D10):11239–11249, 1997. doi:10.1029/97jd00403.

Ångström, A. On the atmospheric transmission of sun radiation and on dust in the air. *Geografiska Annaler*, 11(2):156–166, 1929. doi:10.1080/20014422.1929.11880498.

Aquila, V., Hendricks, J., Lauer, A., Riemer, N., Vogel, H., Baumgardner, D., Minikin, A., Petzold, A., Schwarz, J., Spackman, J., Weinzierl, B., Righi, M., and Dall'Amico, M. MADE-in: A new aerosol microphysics submodel for global simulation of insoluble particles and their mixing state. *Geosci. Model Dev.*, 4(2):325–355, 2011. doi:10.5194/gmd-4-325-2011.

Astitha, M., Lelieveld, J., Abdel Kader, M., Pozzer, A., and Meij, A. d. Parameterization of dust emissions in the global atmospheric chemistry-climate model EMAC: impact of nudging and soil properties. *Atmos. Chem. Phys.*, 12(22):11057–11083, 2012. doi:10.5194/acp-12-11057-2012.

Bacer, S., Sullivan, S. C., Karydis, V. A., Barahona, D., Krämer, M., Nenes, A., Tost, H., Tsimpidi, A. P., Lelieveld, J., and Pozzer, A. Implementation of a comprehensive ice crystal formation parameterization for cirrus and mixed-phase clouds in the EMAC model (based on MESSy 2.53). *Geosci. Model Dev.*, 11(10):4021–4041, 2018. doi:10.5194/gmd-11-4021-2018.

Balkanski, Y., Schulz, M., Claquin, T., Moulin, C., and Ginoux, P. Global emissions of mineral aerosol: formulation and validation using satellite imagery. In *Emissions of Atmospheric Trace Compounds*, volume 18, pages 239–267. Springer, 2004. doi:10.1007/978-1-4020-2167-1_6.

Banks, J. R., Brindley, H. E., Stenchikov, G., and Schepanski, K. Satellite retrievals of dust aerosol over the Red Sea and the Persian Gulf (2005–2015). *Atmos. Chem. Phys.*, 17(6):3987–4003, 2017. doi:10.5194/acp-17-3987-2017.

Barahona, D., Rodriguez, J., and Nenes, A. Sensitivity of the global distribution of cirrus ice crystal concentration to heterogeneous freezing. *J. Geophys. Res. Atmos.*, 115(D23): D23213, 2010. doi:10.1029/2010JD014273.

Bateman, A. P., Gong, Z., Liu, P., Sato, B., Cirino, G., Zhang, Y., Artaxo, P., Bertram, A. K., Manzi, A. O., Rizzo, L. V., Souza, R. A. F., Zaveri, R. A., and Martin, S. T. Sub-micrometre particulate matter is primarily in liquid form over Amazon rainforest. *Nat. Geosci.*, 9(1):34–37, 2015. doi:10.1038/ngeo2599.

Baumgardner, D., Jonsson, H., Dawson, W., O'Connor, D., and Newton, R. The cloud, aerosol and precipitation spectrometer: a new instrument for cloud investigations. *Atmos. Res.*, 59-60:251–264, 2001. doi:10.1016/s0169-8095(01)00119-3.

Baustian, K., Wise, M., Jensen, E., Schill, G., Freedman, M., and Tolbert, M. State transformations and ice nucleation in amorphous (semi-) solid organic aerosol. *Atmos. Chem. Phys.*, 13:5615–5628, 2013. doi:10.5194/acp-13-5615-2013.

Baustian, K. J., Wise, M. E., and Tolbert, M. A. Depositional ice nucleation on solid ammonium sulfate and glutaric acid particles. *Atmos. Chem. Phys.*, 10(5):2307–2317, 2010. doi:10.5194/acp-10-2307-2010.

Beer, C. G., Hendricks, J., Righi, M., Heinold, B., Tegen, I., Groß, S., Sauer, D., Walser, A., and Weinzierl, B. Modelling mineral dust emissions and atmospheric dispersion with MADE3 in EMAC v2.54. *Geosci. Model Dev.*, 13(9):4287–4303, 2020. doi:10.5194/gmd-13-4287-2020.

Behera, S. N., Sharma, M., Aneja, V. P., and Balasubramanian, R. Ammonia in the atmosphere: a review on emission sources, atmospheric chemistry and deposition on terrestrial bodies. *Environ. Sci. Pollut. Res.*, 20(11):8092–8131, 2013. doi:10.1007/s11356-013-2051-9.

Bellouin, N., Quaas, J., Morcrette, J.-J., and Boucher, O. Estimates of aerosol radiative forcing from the MACC re-analysis. *Atmos. Chem. Phys.*, 13(4):2045–2062, 2013. doi:10.5194/acp-13-2045-2013.

Bellouin, N., Quaas, J., Gryspeerdt, E., Kinne, S., Stier, P., Watson-Parris, D., Boucher, O., Carslaw, K. S., Christensen, M., Daniau, A.-L., Dufresne, J.-L., Feingold, G., Fiedler, S., Forster, P., Gettelman, A., Haywood, J. M., Lohmann, U., Malavelle, F., Mauritsen, T., McCoy, D. T., Myhre, G., Mülmenstädt, J., Neubauer, D., Possner, A., Rugenstein, M., Sato, Y., Schulz, M., Schwartz, S. E., Sourdeval, O., Storelvmo, T., Toll, V., Winker, D., and Stevens, B. Bounding global aerosol radiative forcing of climate change. *Rev. Geophys.*, 58(1), 2020. doi:10.1029/2019rg000660.

Berndt, T., Stratmann, F., Sipilä, M., Vanhanen, J., Petäjä, T., Mikkilä, J., Grüner, A., Spindler, G., Mauldin, R. L., Curtius, J., Kulmala, M., and Heintzenberg, J. Laboratory study on new particle formation from the reaction OH + SO2: influence of experimental conditions, H2O vapour, NH3 and the amine tert-butylamine on the overall process. *Atmos. Chem. Phys.*, 10(15):7101–7116, 2010. doi:10.5194/acp-10-7101-2010.

Bianchi, F., Trostl, J., Junninen, H., Frege, C., Henne, S., Hoyle, C. R., Molteni, U., Herrmann, E., Adamov, A., Bukowiecki, N., Chen, X., Duplissy, J., Gysel, M., Hutterli, M., Kangasluoma, J., Kontkanen, J., Kurten, A., Manninen, H. E., Munch, S., Perakyla, O., Petaja, T., Rondo, L., Williamson, C., Weingartner, E., Curtius, J., Worsnop, D. R., Kulmala, M., Dommen, J., and Baltensperger, U. New particle formation in the free troposphere: A question of chemistry and timing. *Science*, 352(6289):1109–1112, 2016. doi:10.1126/science.aad5456.

Bond, T. C., Doherty, S. J., Fahey, D. W., Forster, P. M., Berntsen, T., DeAngelo, B. J., Flanner, M. G., Ghan, S., Kärcher, B., Koch, D., Kinne, S., Kondo, Y., Quinn, P. K., Sarofim, M. C., Schultz, M. G., Schulz, M., Venkataraman, C., Zhang, H., Zhang, S., Bellouin, N., Guttikunda, S. K., Hopke, P. K., Jacobson, M. Z., Kaiser, J. W., Klimont, Z., Lohmann, U., Schwarz, J. P., Shindell, D., Storelvmo, T., Warren, S. G., and Zender, C. S. Bounding the role of black carbon in the climate system: A scientific assessment. *J. Geophys. Res. Atmos.*, 118(11):5380–5552, 2013. doi:10.1002/jgrd.50171.

Bones, D. L., Reid, J. P., Lienhard, D. M., and Krieger, U. K. Comparing the mechanism of water condensation and evaporation in glassy aerosol. *Proc. Natl. Acad. Sci.*, 109 (29):11613–11618, 2012. doi:10.1073/pnas.1200691109.

Boucher, O., Randall, D., Artaxo, P., Bretherton, C., Feingold, G., Forster, P., Kerminen, V.-M., Kondo, Y., Liao, H., Lohmann, U., Rasch, P., Satheesh, S., Sherwood, S., Stevens, B., and Zhang, X.-Y. Clouds and aerosols. In *Climate change 2013: the physical science basis. Contribution of Working Group I to the Fifth Assessment Report of the Intergovernmental Panel on Climate Change*, pages 571–657. Cambridge University Press, 2013. doi:10.1017/CBO9781107415324.016.

Brinkop, S. and Sausen, R. A finite difference approximation for convective transports which maintains positive tracer concentrations. *Beiträge zur Physik der Atmosphäre-Contributions to Atmospheric Physics*, 70(3):245, 1997.

Bundke, U., Berg, M., Houben, N., Ibrahim, A., Fiebig, M., Tettich, F., Klaus, C., Franke, H., and Petzold, A. The IAGOS-CORE aerosol package: instrument design, operation and performance for continuous measurement aboard in-service aircraft. *Tellus B: Chemical and Physical Meteorology*, 67(1):28339, 2015. doi:10.3402/tellusb.v67.28339.

Carlton, A. G., Wiedinmyer, C., and Kroll, J. H. A review of secondary organic aerosol (SOA) formation from isoprene. *Atmos. Chem. Phys.*, 9(14):4987–5005, 2009. doi:10.5194/acp-9-4987-2009.

Chadwick, O. A., Derry, L. A., Vitousek, P. M., Huebert, B. J., and Hedin, L. O. Changing sources of nutrients during four million years of ecosystem development. *Nature*, 397 (6719):491, 1999. URL `https://www.nature.com/articles/17276`.

Chameides, W. L. and Stelson, A. W. Aqueous-phase chemical processes in deliquescent sea-salt aerosols: A mechanism that couples the atmospheric cycles of S and sea salt. *J. Geophys. Res.*, 97(D18):20565, 1992. doi:10.1029/92jd01923.

Chang, K.-W. and L'Ecuyer, T. Influence of gravity wave temperature anomalies and their vertical gradients on cirrus clouds in the tropical tropopause layer – a satellite-based view. *Atmos. Chem. Phys.*, 20(21):12499–12514, 2020. doi:10.5194/acp-20-12499-2020.

Chen, J., Wu, Z., Augustin-Bauditz, S., Grawe, S., Hartmann, M., Pei, X., Liu, Z., Ji, D., and Wex, H. Ice-nucleating particle concentrations unaffected by urban air pollution in Beijing, China. *Atmos. Chem. Phys.*, 18(5):3523–3539, 2018. doi:10.5194/acp-18-3523-2018.

Chen, Y., DeMott, P. J., Kreidenweis, S. M., Rogers, D. C., and Sherman, D. E. Ice formation by sulfate and sulfuric acid aerosol particles under upper-tropospheric conditions. *J. Atmos. Sci.*, 57(22):3752–3766, 2000. doi:10.1175/1520-0469(2000)057<3752:IFBSAS>2.0.CO;2.

Cheng, T., Peng, Y., Feichter, J., and Tegen, I. An improvement on the dust emission scheme in the global aerosol-climate model ECHAM5-HAM. *Atmos. Chem. Phys.*, 8 (4):1105–1117, 2008. doi:10.5194/acp-8-1105-2008.

Chou, C., Kanji, Z. A., Stetzer, O., Tritscher, T., Chirico, R., Heringa, M. F., Weingartner, E., Prévôt, A. S. H., Baltensperger, U., and Lohmann, U. Effect of photochemical ageing on the ice nucleation properties of diesel and wood burning particles. *Atmos. Chem. Phys.*, 13(2):761–772, 2013. doi:10.5194/acp-13-761-2013.

Colberg, C. A., Luo, B. P., Wernli, H., Koop, T., and Peter, T. A novel model to predict the physical state of atmospheric $H_2SO_4/NH_3/H_2O$ aerosol particles. *Atmos. Chem. Phys.*, 3(4):909–924, 2003. doi:10.5194/acp-3-909-2003.

Collins, W. D., Rasch, P. J., Boville, B. A., Hack, J. J., McCaa, J. R., Williamson, D. L., Briegleb, B. P., Bitz, C. M., Lin, S.-J., and Zhang, M. The formulation and atmospheric simulation of the Community Atmosphere Model version 3 (CAM3). *J. Climate*, 19 (11):2144–2161, 2006. doi:10.1175/jcli3760.1.

Collins, W. J., Lamarque, J.-F., Schulz, M., Boucher, O., Eyring, V., Hegglin, M. I., Maycock, A., Myhre, G., Prather, M., Shindell, D., and Smith, S. J. AerChemMIP: quantifying the effects of chemistry and aerosols in CMIP6. *Geosci. Model Dev.*, 10(2): 585–607, 2017. doi:10.5194/gmd-10-585-2017.

Cziczo, D. J., Froyd, K. D., Gallavardin, S. J., Moehler, O., Benz, S., Saathoff, H., and Murphy, D. M. Deactivation of ice nuclei due to atmospherically relevant surface coatings. *Environ. Res. Lett.*, 4(4):044013, 2009. doi:10.1088/1748-9326/4/4/044013.

Cziczo, D. J., Froyd, K. D., Hoose, C., Jensen, E. J., Diao, M., Zondlo, M. A., Smith, J. B., Twohy, C. H., and Murphy, D. M. Clarifying the dominant sources and mechanisms of cirrus cloud formation. *Science*, 340(6138):1320–1324, 2013. doi:10.1126/science.1234145.

Dal Maso, M., Kulmala, M., Riipinen, I., Wagner, R., Hussein, T., Aalto, P. P., and Lehtinen, K. E. Formation and growth of fresh atmospheric aerosols: eight years of aerosol size distribution data from SMEAR II, Hyytiala, Finland. *Boreal environment research*, 10(5):323, 2005.

David, R. O., Marcolli, C., Fahrni, J., Qiu, Y., Perez Sirkin, Y. A., Molinero, V., Mahrt, F., Brühwiler, D., Lohmann, U., and Kanji, Z. A. Pore condensation and freezing is responsible for ice formation below water saturation for porous particles. *Proc. Natl. Acad. Sci. US*, 116(17):8184–8189, 2019. doi:10.1073/pnas.1813647116.

de Meij, A., Krol, M., Dentener, F., Vignati, E., Cuvelier, C., and Thunis, P. The sensitivity of aerosol in Europe to two different emission inventories and temporal distribution of emissions. *Atmos. Chem. Phys.*, 6(12):4287–4309, 2006. doi:10.5194/acp-6-4287-2006.

Dee, D. P., Uppala, S. M., Simmons, A. J., Berrisford, P., Poli, P., Kobayashi, S., Andrae, U., Balmaseda, M. A., Balsamo, G., Bauer, P., Bechtold, P., Beljaars, A. C. M., van de Berg, L., Bidlot, J., Bormann, N., Delsol, C., Dragani, R., Fuentes, M., Geer, A. J., Haimberger, L., Healy, S. B., Hersbach, H., Hólm, E. V., Isaksen, L., Kållberg, P., Köhler, M., Matricardi, M., McNally, A. P., Monge-Sanz, B. M., Morcrette, J.-J., Park, B.-K., Peubey, C., de Rosnay, P., Tavolato, C., Thépaut, J.-N., and Vitart, F. The ERA-interim reanalysis: configuration and performance of the data assimilation system. *Quarterly Journal of the Royal Meteorological Society*, 137(656):553–597, 2011. doi:10.1002/qj.828.

DeMott, P. J., Prenni, A. J., Liu, X., Kreidenweis, S. M., Petters, M. D., Twohy, C. H., Richardson, M., Eidhammer, T., and Rogers, D. Predicting global atmospheric ice nuclei distributions and their impacts on climate. *Proc. Natl. Acad. Sci.*, 107(25): 11217–11222, 2010. doi:10.1073/pnas.0910818107.

Dentener, F., Kinne, S., Bond, T., Boucher, O., Cofala, J., Generoso, S., Ginoux, P., Gong, S., Hoelzemann, J., Ito, A., et al. Emissions of primary aerosol and precursor gases in the years 2000 and 1750 prescribed data-sets for AeroCom. *Atmos. Chem. Phys.*, 6(12):4321–4344, 2006. doi:10.5194/acp-6-4321-2006.

Després, V. R., Huffman, J., Burrows, S. M., Hoose, C., Safatov, A., Buryak, G., Fröhlich-Nowoisky, J., Elbert, W., Andreae, M., Pöschl, U., and Jaenicke, R. Primary biological aerosol particles in the atmosphere: a review. *Tellus B: Chemical and Physical Meteorology*, 64(1):15598, 2012. doi:10.3402/tellusb.v64i0.15598.

Dey, S., Girolamo, L. D., Zhao, G., Jones, A. L., and McFarquhar, G. M. Satellite-observed relationships between aerosol and trade-wind cumulus cloud properties over the Indian Ocean. *Geophys. Res. Lett.*, 38(1), 2011. doi:10.1029/2010gl045588.

Dietmüller, S., Jöckel, P., Tost, H., Kunze, M., Gellhorn, C., Brinkop, S., Frömming, C., Ponater, M., Steil, B., Lauer, A., et al. A new radiation infrastructure for the Modular Earth Submodel System (MESSy, based on version 2.51). *Geosci. Model Dev.*, 9:2209–2222, 2016. doi:10.5194/gmd-9-2209-2016.

Durkee, P. A., Noone, K. J., Ferek, R. J., Johnson, D. W., Taylor, J. P., Garrett, T. J., Hobbs, P. V., Hudson, J. G., Bretherton, C. S., Innis, G., Frick, G. M., Hoppel, W. A., O'Dowd, C. D., Russell, L. M., Gasparovic, R., Nielsen, K. E., Tessmer, S. A., ström,

E., Osborne, S. R., Flagan, R. C., Seinfeld, J. H., and Rand, H. The impact of ship-produced aerosols on the microstructure and albedo of warm marine stratocumulus clouds: A test of MAST hypotheses 1i and 1ii. *J. Atmos. Sci.*, 57(16):2554–2569, 2000. doi:10.1175/1520-0469(2000)057<2554:tiospa>2.0.co;2.

Eck, T. F., Holben, B. N., Reid, J. S., Dubovik, O., Smirnov, A., O'Neill, N. T., Slutsker, I., and Kinne, S. Wavelength dependence of the optical depth of biomass burning, urban, and desert dust aerosols. *J. Geophys. Res. Atmos.*, 104(D24):31333–31349, 1999. doi:10.1029/1999jd900923.

Eyring, V., Righi, M., Lauer, A., Evaldsson, M., Wenzel, S., Jones, C., Anav, A., Andrews, O., Cionni, I., Davin, E. L., Deser, C., Ehbrecht, C., Friedlingstein, P., Gleckler, P., Gottschaldt, K.-D., Hagemann, S., Juckes, M., Kindermann, S., Krasting, J., Kunert, D., Levine, R., Loew, A., Mäkelä, J., Martin, G., Mason, E., Phillips, A. S., Read, S., Rio, C., Roehrig, R., Senftleben, D., Sterl, A., van Ulft, L. H., Walton, J., Wang, S., and Williams, K. D. ESMValTool (v1.0) – a community diagnostic and performance metrics tool for routine evaluation of Earth system models in CMIP. *Geosci. Model Dev.*, 9(5):1747–1802, 2016. doi:10.5194/gmd-9-1747-2016.

Fan, J., Wang, Y., Rosenfeld, D., and Liu, X. Review of aerosol–cloud interactions: Mechanisms, significance, and challenges. *J. Atmos. Sci.*, 73(11):4221–4252, 2016. doi:10.1175/jas-d-16-0037.1.

Feingold, G. On smoke suppression of clouds in Amazonia. *Geophys. Res. Lett.*, 32(2), 2005. doi:10.1029/2004gl021369.

Fountoukis, C., Nenes, A., Meskhidze, N., Bahreini, R., Conant, W. C., Jonsson, H., Murphy, S., Sorooshian, A., Varutbangkul, V., Brechtel, F., Flagan, R. C., and Seinfeld, J. H. Aerosol-cloud drop concentration closure for clouds sampled during the International Consortium for Atmospheric Research on Transport and Transformation 2004 campaign. *J. Geophys. Res. Atmos.*, 112(D10), 2007. doi:10.1029/2006jd007272.

Fowler, D., Pilegaard, K., Sutton, M., Ambus, P., Raivonen, M., Duyzer, J., Simpson, D., Fagerli, H., Fuzzi, S., Schjoerring, J., Granier, C., Neftel, A., Isaksen, I., Laj, P., Maione, M., Monks, P., Burkhardt, J., Daemmgen, U., Neirynck, J., Personne, E., Wichink-Kruit, R., Butterbach-Bahl, K., Flechard, C., Tuovinen, J., Coyle, M., Gerosa, G., Loubet, B., Altimir, N., Gruenhage, L., Ammann, C., Cieslik, S., Paoletti, E., Mikkelsen, T., Ro-Poulsen, H., Cellier, P., Cape, J., Horváth, L., Loreto, F., Niinemets, ., Palmer, P., Rinne, J., Misztal, P., Nemitz, E., Nilsson, D., Pryor, S., Gallagher, M., Vesala, T., Skiba, U., Brüggemann, N., Zechmeister-Boltenstern, S., Williams, J., O'Dowd, C., Facchini, M., de Leeuw, G., Flossman, A., Chaumerliac, N., and Erisman, J. Atmospheric composition change: Ecosystems–atmosphere interactions. *Atmos. Environ.*, 43(33):5193–5267, 2009. doi:10.1016/j.atmosenv.2009.07.068.

Freedman, M. A. Potential sites for ice nucleation on aluminosilicate clay minerals and related materials. *J. Phys. Chem. Lett.*, 6(19):3850–3858, 2015. doi:10.1021/acs.jpclett.5b01326.

Fuzzi, S., Baltensperger, U., Carslaw, K., Decesari, S., van der Gon, H. D., Facchini, M. C., Fowler, D., Koren, I., Langford, B., Lohmann, U., Nemitz, E., Pandis, S., Riipinen, I., Rudich, Y., Schaap, M., Slowik, J. G., Spracklen, D. V., Vignati, E.,

Wild, M., Williams, M., and Gilardoni, S. Particulate matter, air quality and climate: lessons learned and future needs. *Atmos. Chem. Phys.*, 15(14):8217–8299, 2015. doi:10.5194/acp-15-8217-2015.

Gasparini, B. and Lohmann, U. Why cirrus cloud seeding cannot substantially cool the planet. *J. Geophys. Res. Atmos.*, 121(9):4877–4893, 2016. doi:10.1002/2015JD024666.

Gasteiger, J., Groß, S., Sauer, D., Haarig, M., Ansmann, A., and Weinzierl, B. Particle settling and vertical mixing in the Saharan Air Layer as seen from an integrated model, lidar, and in situ perspective. *Atmos. Chem. Phys.*, 17(1):297–311, 2017. doi:10.5194/acp-17-297-2017.

Gentner, D. R., Isaacman, G., Worton, D. R., Chan, A. W. H., Dallmann, T. R., Davis, L., Liu, S., Day, D. A., Russell, L. M., Wilson, K. R., Weber, R., Guha, A., Harley, R. A., and Goldstein, A. H. Elucidating secondary organic aerosol from diesel and gasoline vehicles through detailed characterization of organic carbon emissions. *Proc. Natl. Acad. Sci.*, 109(45):18318–18323, 2012. doi:10.1073/pnas.1212272109.

Gettelman, A., Liu, X., Barahona, D., Lohmann, U., and Chen, C. Climate impacts of ice nucleation. *J. Geophys. Res. Atmos.*, 117(D20):D20201, 2012. doi:10.1029/2012JD017950.

Ghan, S. J. and Schwartz, S. E. Aerosol properties and processes: A path from field and laboratory measurements to global climate models. *Bull. Amer. Meteor. Soc.*, 88(7): 1059–1084, 2007. doi:10.1175/bams-88-7-1059.

Ghan, S. J., Liu, X., Easter, R. C., Zaveri, R., Rasch, P. J., Yoon, J.-H., and Eaton, B. Toward a minimal representation of aerosols in climate models: Comparative decomposition of aerosol direct, semidirect, and indirect radiative forcing. *J. Climate*, 25(19): 6461–6476, 2012. doi:10.1175/jcli-d-11-00650.1.

Ginoux, P., Chin, M., Tegen, I., Prospero, J. M., Holben, B., Dubovik, O., and Lin, S.-J. Sources and distributions of dust aerosols simulated with the GOCART model. *J. Geophys. Res. Atmos.*, 106(D17):20255–20273, 2001. doi:10.1029/2000jd000053.

Ginoux, P., Prospero, J. M., Torres, O., and Chin, M. Long-term simulation of global dust distribution with the GOCART model: correlation with North Atlantic Oscillation. *Environmental Modelling & Software*, 19(2):113–128, 2004. doi:10.1016/s1364-8152(03)00114-2.

Ginoux, P., Prospero, J. M., Gill, T. E., Hsu, N. C., and Zhao, M. Global-scale attribution of anthropogenic and natural dust sources and their emission rates based on MODIS Deep Blue aerosol products. *Rev. Geophys.*, 50(3):RG3005, 2012. doi:10.1029/2012RG000388.

Gläser, G., Kerkweg, A., and Wernli, H. The mineral dust cycle in EMAC 2.40: sensitivity to the spectral resolution and the dust emission scheme. *Atmos. Chem. Phys.*, 12(3): 1611–1627, 2012. doi:10.5194/acp-12-1611-2012.

Gliß, J., Mortier, A., Schulz, M., Andrews, E., Balkanski, Y., Bauer, S. E., Benedictow, A. M. K., Bian, H., Checa-Garcia, R., Chin, M., Ginoux, P., Griesfeller, J. J., Heckel, A., Kipling, Z., Kirkevåg, A., Kokkola, H., Laj, P., Sager, P. L., Lund, M. T., Myhre,

C. L., Matsui, H., Myhre, G., Neubauer, D., van Noije, T., North, P., Olivié, D. J. L., Rémy, S., Sogacheva, L., Takemura, T., Tsigaridis, K., and Tsyro, S. G. AeroCom phase III multi-model evaluation of the aerosol life cycle and optical properties using ground- and space-based remote sensing as well as surface in situ observations. *Atmos. Chem. Phys.*, 21(1):87–128, 2021. doi:10.5194/acp-21-87-2021.

Grawe, S., Augustin-Bauditz, S., Hartmann, S., Hellner, L., Pettersson, J. B. C., Prager, A., Stratmann, F., and Wex, H. The immersion freezing behavior of ash particles from wood and brown coal burning. *Atmos. Chem. Phys.*, 16(21):13911–13928, 2016. doi:10.5194/acp-16-13911-2016.

Groß, S., Freudenthaler, V., Schepanski, K., Toledano, C., Schäfler, A., Ansmann, A., and Weinzierl, B. Optical properties of long-range transported Saharan dust over Barbados as measured by dual-wavelength depolarization Raman lidar measurements. *Atmos. Chem. Phys.*, 15(19):11067–11080, 2015. doi:10.5194/acp-15-11067-2015.

Groß, S., Gasteiger, J., Freudenthaler, V., Müller, T., Sauer, D., Toledano, C., and Ansmann, A. Saharan dust contribution to the Caribbean summertime boundary layer–a lidar study during SALTRACE. *Atmos. Chem. Phys.*, 16(18):11535–11546, 2016. doi:10.5194/acp-16-11535-2016.

Gryspeerdt, E., Quaas, J., and Bellouin, N. Constraining the aerosol influence on cloud fraction. *J. Geophys. Res. Atmos.*, 121(7):3566–3583, 2016. doi:10.1002/2015jd023744.

Guelle, W., Schulz, M., Balkanski, Y., and Dentener, F. Influence of the source formulation on modeling the atmospheric global distribution of sea salt aerosol. *J. Geophys. Res. Atmos.*, 106(D21):27509–27524, 2001. doi:10.1029/2001jd900249.

Guenther, A., Hewitt, C. N., Erickson, D., Fall, R., Geron, C., Graedel, T., Harley, P., Klinger, L., Lerdau, M., Mckay, W. A., Pierce, T., Scholes, B., Steinbrecher, R., Tallamraju, R., Taylor, J., and Zimmerman, P. A global model of natural volatile organic compound emissions. *J. Geophys. Res.*, 100(D5):8873–8892, 1995. ISSN 0148-0227. doi:10.1029/94JD02950.

Guenther, A., Karl, T., Harley, P., Wiedinmyer, C., Palmer, P. I., and Geron, C. Estimates of global terrestrial isoprene emissions using MEGAN (model of emissions of gases and aerosols from nature). *Atmos. Chem. Phys.*, 6(11):3181–3210, 2006. doi:10.5194/acp-6-3181-2006.

Gutleben, M., Groß, S., Wirth, M., and Mayer, B. Radiative effects of long-range-transported Saharan air layers as determined from airborne lidar measurements. *Atmos. Chem. Phys.*, 20(20):12313–12327, 2020. doi:10.5194/acp-20-12313-2020.

Haarig, M., Walser, A., Ansmann, A., Dollner, M., Althausen, D., Sauer, D., Farrell, D., and Weinzierl, B. Profiles of cloud condensation nuclei, dust mass concentration, and ice-nucleating-particle-relevant aerosol properties in the Saharan Air Layer over Barbados from polarization lidar and airborne in situ measurements. *Atmos. Chem. Phys.*, 19(22):13773–13788, 2019. doi:10.5194/acp-19-13773-2019.

Han, J.-H., Hung, H.-M., and Martin, S. T. Size effect of hematite and corundum inclusions on the efflorescence relative humidities of aqueous ammonium nitrate particles. *J. Geophys. Res.*, 107(D10):AAC 3–1–AAC 3–9, 2002. ISSN 0148-0227. doi:10.1029/2001JD001054.

Harrison, A. D., Whale, T. F., Carpenter, M. A., Holden, M. A., Neve, L., O'Sullivan, D., Temprado, J. V., and Murray, B. J. Not all feldspars are equal: a survey of ice nucleating properties across the feldspar group of minerals. *Atmos. Chem. Phys.*, 16 (17):10927–10940, 2016. doi:10.5194/acp-16-10927-2016.

Hartigan, J. A. and Wong, M. A. Algorithm AS 136: A K-Means Clustering Algorithm. *Applied Statistics*, 28(1):100, 1979. doi:10.2307/2346830.

Hartmann, M., Blunier, T., Brügger, S., Schmale, J., Schwikowski, M., Vogel, A., Wex, H., and Stratmann, F. Variation of ice nucleating particles in the European Arctic over the last centuries. *Geophys. Res. Lett.*, 46(7):4007–4016, 2019. doi:10.1029/2019gl082311.

Heald, C. L., Ridley, D. A., Kroll, J. H., Barrett, S. R. H., Cady-Pereira, K. E., Alvarado, M. J., and Holmes, C. D. Contrasting the direct radiative effect and direct radiative forcing of aerosols. *Atmos. Chem. Phys.*, 14(11):5513–5527, 2014. doi:10.5194/acp-14-5513-2014.

Hendricks, J., Kärcher, B., and Lohmann, U. Effects of ice nuclei on cirrus clouds in a global climate model. *J. Geophys. Res. Atmos.*, 116(D18):D18206, 2011. doi:10.1029/2010JD015302.

Herich, H., Tritscher, T., Wiacek, A., Gysel, M., Weingartner, E., Lohmann, U., Baltensperger, U., and Cziczo, D. J. Water uptake of clay and desert dust aerosol particles at sub- and supersaturated water vapor conditions. *Phys. Chem. Chem. Phys.*, 11(36): 7804, 2009. doi:10.1039/b901585j.

Hess, M., Koepke, P., and Schult, I. Optical properties of aerosols and clouds: The software package OPAC. *Bull. Am. Meteorol. Soc.*, 79(5):831–844, 1998. doi:10.1175/1520-0477(1998)079<0831:OPOAAC>2.0.CO;2.

Heymsfield, A. J., Krämer, M., Luebke, A., Brown, P., Cziczo, D. J., Franklin, C., Lawson, P., Lohmann, U., McFarquhar, G., Ulanowski, Z., and Tricht, K. V. Cirrus clouds. *Meteor. Monogr.*, 58:21–226, 2017. doi:10.1175/amsmonographs-d-16-0010.1.

Hirsikko, A., Nieminen, T., Gagné, S., Lehtipalo, K., Manninen, H. E., Ehn, M., Hõrrak, U., Kerminen, V.-M., Laakso, L., McMurry, P. H., Mirme, A., Mirme, S., Petäjä, T., Tammet, H., Vakkari, V., Vana, M., and Kulmala, M. Atmospheric ions and nucleation: a review of observations. *Atmos. Chem. Phys.*, 11(2):767–798, 2011. doi:10.5194/acp-11-767-2011.

Holben, B. N., Eck, T. F., Slutsker, I., Tanré, D., Buis, J. P., Setzer, A., Vermote, E., Reagan, J. A., Kaufman, Y. J., Nakajima, T., Lavenu, F., Jankowiak, I., and Smirnov, A. AERONET– a federated instrument network and data archive for aerosol characterization. *Remote Sens. Environ.*, 66(1):1–16, 1998. ISSN 0034-4257. doi:10.1016/S0034-4257(98)00031-5.

Holben, B. N., Tanré, D., Smirnov, A., Eck, T. F., Slutsker, I., Abuhassan, N., Newcomb, W. W., Schafer, J. S., Chatenet, B., Lavenu, F., Kaufman, Y. J., Castle, J. V., Setzer, A., Markham, B., Clark, D., Frouin, R., Halthore, R., Karneli, A., O'Neill, N. T., Pietras, C., Pinker, R. T., Voss, K., and Zibordi, G. An emerging ground-based aerosol climatology: Aerosol optical depth from AERONET. *J. Geophys. Res.*, 106(D11): 12067–12097, 2001. ISSN 0148-0227. doi:10.1029/2001JD900014.

Hoose, C. and Möhler, O. Heterogeneous ice nucleation on atmospheric aerosols: a review of results from laboratory experiments. *Atmos. Chem. Phys.*, 12(20):9817–9854, 2012. doi:10.5194/acp-12-9817-2012.

Hoose, C., Lohmann, U., Erdin, R., and Tegen, I. The global influence of dust mineralogical composition on heterogeneous ice nucleation in mixed-phase clouds. *Environ. Res. Lett.*, 3(2):025003, 2008. doi:10.1088/1748-9326/3/2/025003.

Huneeus, N., Schulz, M., Balkanski, Y., Griesfeller, J., Prospero, J., Kinne, S., Bauer, S., Boucher, O., Chin, M., Dentener, F., Diehl, T., Easter, R., Fillmore, D., Ghan, S., Ginoux, P., Grini, A., Horowitz, L., Koch, D., Krol, M. C., Landing, W., Liu, X., Mahowald, N., Miller, R., Morcrette, J.-J., Myhre, G., Penner, J., Perlwitz, J., Stier, P., Takemura, T., and Zender, C. S. Global dust model intercomparison in AeroCom phase I. *Atmos. Chem. Phys.*, 11:7781–7816, 2011. doi:10.5194/acp-11-7781-2011.

Ignatius, K., Kristensen, T. B., Järvinen, E., Nichman, L., Fuchs, C., Gordon, H., Herenz, P., Hoyle, C. R., Duplissy, J., Garimella, S., Dias, A., Frege, C., Höppel, N., Tröstl, J., Wagner, R., Yan, C., Amorim, A., Baltensperger, U., Curtius, J., Donahue, N. M., Gallagher, M. W., Kirkby, J., Kulmala, M., Möhler, O., Saathoff, H., Schnaiter, M., Tomé, A., Virtanen, A., Worsnop, D., and Stratmann, F. Heterogeneous ice nucleation of viscous secondary organic aerosol produced from ozonolysis of α-pinene. *Atmos. Chem. Phys.*, 16(10):6495–6509, 2016. doi:10.5194/acp-16-6495-2016.

Ishizuka, M., Mikami, M., Leys, J., Yamada, Y., Heidenreich, S., Shao, Y., and McTainsh, G. H. Effects of soil moisture and dried raindroplet crust on saltation and dust emission. *J. Geophys. Res.*, 113(D24), 2008. doi:10.1029/2008jd009955.

Järvinen, E., Ignatius, K., Nichman, L., Kristensen, T. B., Fuchs, C., Hoyle, C. R., Höppel, N., Corbin, J. C., Craven, J., Duplissy, J., Ehrhart, S., Haddad, I. E., Frege, C., Gordon, H., Jokinen, T., Kallinger, P., Kirkby, J., Kiselev, A., Naumann, K.-H., Petäjä, T., Pinterich, T., Prevot, A. S. H., Saathoff, H., Schiebel, T., Sengupta, K., Simon, M., Slowik, J. G., Tröstl, J., Virtanen, A., Vochezer, P., Vogt, S., Wagner, A. C., Wagner, R., Williamson, C., Winkler, P. M., Yan, C., Baltensperger, U., Donahue, N. M., Flagan, R. C., Gallagher, M., Hansel, A., Kulmala, M., Stratmann, F., Worsnop, D. R., Möhler, O., Leisner, T., and Schnaiter, M. Observation of viscosity transition in alpha-pinene secondary organic aerosol. *Atmos. Chem. Phys.*, 16(7):4423–4438, 2016. doi:10.5194/acp-16-4423-2016.

Jensen, E. J., Pfister, L., Bui, T.-P., Lawson, P., and Baumgardner, D. Ice nucleation and cloud microphysical properties in tropical tropopause layer cirrus. *Atmos. Chem. Phys.*, 10(3):1369–1384, 2010. doi:10.5194/acp-10-1369-2010.

Jensen, E. J., Diskin, G., Lawson, R. P., Lance, S., Bui, T. P., Hlavka, D., McGill, M., Pfister, L., Toon, O. B., and Gao, R. Ice nucleation and dehydration in the Tropical Tropopause Layer. *Proc. Natl. Acad. Sci.*, 110(6):2041–2046, 2013. doi:10.1073/pnas.1217104110.

Jensen, E. J., van den Heever, S. C., and Grant, L. D. The life cycles of ice crystals detrained from the tops of deep convection. *J. Geophys. Res. Atmos.*, 123(17):9624–9634, 2018. doi:10.1029/2018jd028832.

Jiang, H., Xue, H., Teller, A., Feingold, G., and Levin, Z. Aerosol effects on the lifetime of shallow cumulus. *Geophys. Res. Lett.*, 33(14), 2006. doi:10.1029/2006gl026024.

Jickells, T. D., An, Z. S., Andersen, K. K., Baker, A. R., Bergametti, G., Brooks, N., Cao, J. J., Boyd, P. W., Duce, R. A., Hunter, K. A., Kawahata, H., Kubilay, N., laRoche, J., Liss, P. S., Mahowald, N., Prospero, J. M., Ridgwell, A. J., Tegen, I., and Torres, R. Global iron connections between desert dust, ocean biogeochemistry, and climate. *Science*, 308(5718):67–71, 2005. ISSN 0036-8075. doi:10.1126/science.1105959.

Jöckel, P., Tost, H., Pozzer, A., Brühl, C., Buchholz, J., Ganzeveld, L., Hoor, P., Kerkweg, A., Lawrence, M. G., Sander, R., Steil, B., Stiller, G., Tanarhte, M., Taraborrelli, D., van Aardenne, J., and Lelieveld, J. The atmospheric chemistry general circulation model ECHAM5/MESSy1: consistent simulation of ozone from the surface to the mesosphere. *Atmos. Chem. Phys.*, 6(12):5067–5104, 2006. doi:10.5194/acp-6-5067-2006.

Jöckel, P., Kerkweg, A., Buchholz-Dietsch, J., Tost, H., Sander, R., and Pozzer, A. Technical note: Coupling of chemical processes with the Modular Earth Submodel System (MESSy) submodel TRACER. *Atmos. Chem. Phys.*, 8(6):1677–1687, 2008. doi:10.5194/acp-8-1677-2008.

Jöckel, P., Kerkweg, A., Pozzer, A., Sander, R., Tost, H., Riede, H., Baumgaertner, A., Gromov, S., and Kern, B. Development cycle 2 of the modular earth submodel system (MESSy2). *Geosci. Model Dev.*, 3(2):717–752, 2010. doi:10.5194/gmd-3-717-2010.

Jöckel, P., Tost, H., Pozzer, A., Kunze, M., Kirner, O., Brenninkmeijer, C. A., Brinkop, S., Cai, D., Dyroff, C., Eckstein, J., et al. Earth system chemistry integrated modelling (ESCiMo) with the Modular Earth Submodel System (MESSy, version 2.51). *Geosci. Model Dev. Discuss.*, 9:1153–1200, 2016. doi:10.5194/gmd-9-1153-2016.

Johnson, M. S., Meskhidze, N., and Praju Kiliyanpilakkil, V. A global comparison of GEOS-Chem-predicted and remotely-sensed mineral dust aerosol optical depth and extinction profiles. *J. Adv. Model. Earth Syst.*, 4(3), 2012. ISSN 1942-2466. doi:10.1029/2011ms000109.

Joos, H., Spichtinger, P., Lohmann, U., Gayet, J.-F., and Minikin, A. Orographic cirrus in the global climate model ECHAM5. *J. Geophys. Res.*, 113(D18), 2008. doi:10.1029/2007jd009605.

Kaiser, C. *Including Coarse Mode Aerosol Microphysics in a Climate Model: Model Development and First Application*. PhD thesis, Ludwig-Maximilians-Universität München, 2016.

Kaiser, J. C., Hendricks, J., Righi, M., Riemer, N., Zaveri, R. A., Metzger, S., and Aquila, V. The MESSy aerosol submodel MADE3 (v2.0b): description and a box model test. *Geosci. Model Dev.*, 7:1137–1157, 2014. doi:10.5194/gmd-7-1137-2014.

Kaiser, J. C., Hendricks, J., Righi, M., Jöckel, P., Tost, H., Kandler, K., Weinzierl, B., Sauer, D., Heimerl, K., Schwarz, J. P., Perring, A. E., and Popp, T. Global aerosol modeling with MADE3 (v3.0) in EMAC (based on v2.53): model description and evaluation. *Geosci. Model Dev.*, 12(1):541–579, 2019. doi:10.5194/gmd-12-541-2019.

Kanji, Z. A., Florea, O., and Abbatt, J. P. D. Ice formation via deposition nucleation on mineral dust and organics: dependence of onset relative humidity on total particulate surface area. *Environ. Res. Lett.*, 3(2):025004, 2008. doi:10.1088/1748-9326/3/2/025004.

Kanji, Z. A., DeMott, P. J., Möhler, O., and Abbatt, J. P. D. Results from the university of toronto continuous flow diffusion chamber at ICIS 2007: instrument intercomparison and ice onsets for different aerosol types. *Atmos. Chem. Phys.*, 11(1):31–41, 2011. doi:10.5194/acp-11-31-2011.

Kanji, Z. A., Ladino, L. A., Wex, H., Boose, Y., Burkert-Kohn, M., Cziczo, D. J., and Krämer, M. Overview of ice nucleating particles. *Meteor. Monogr.*, 58:1.1–1.33, 2017. doi:10.1175/AMSMONOGRAPHS-D-16-0006.1.

Kanji, Z. A., Sullivan, R. C., Niemand, M., DeMott, P. J., Prenni, A. J., Chou, C., Saathoff, H., and Möhler, O. Heterogeneous ice nucleation properties of natural desert dust particles coated with a surrogate of secondary organic aerosol. *Atmos. Chem. Phys.*, 19(7):5091–5110, 2019. doi:10.5194/acp-19-5091-2019.

Kärcher, B. Cirrus clouds and their response to anthropogenic activities. *Curr. Clim. Change Rep.*, 3(1):45–57, 2017. doi:10.1007/s40641-017-0060-3.

Kärcher, B. and Burkhardt, U. A cirrus cloud scheme for general circulation models. *Quart. J. Roy. Meteor. Soc.*, 134(635):1439–1461, 2008. doi:10.1002/qj.301.

Kärcher, B. and Lohmann, U. A parameterization of cirrus cloud formation: Homogeneous freezing of supercooled aerosols. *J. Geophys. Res. Atmos.*, 107(D2):4010, 2002. doi:10.1029/2001JD000470.

Kärcher, B. and Lohmann, U. A parameterization of cirrus cloud formation: Heterogeneous freezing. *J. Geophys. Res. Atmos.*, 108(D14):4402, 2003. doi:10.1029/2002JD003220.

Kärcher, B., Hendricks, J., and Lohmann, U. Physically based parameterization of cirrus cloud formation for use in global atmospheric models. *J. Geophys. Res. Atmos.*, 111 (D1):D01205, 2006. doi:10.1029/2005JD006219.

Kärcher, B., Möhler, O., DeMott, P. J., Pechtl, S., and Yu, F. Insights into the role of soot aerosols in cirrus cloud formation. *Atmos. Chem. Phys.*, 7(16):4203–4227, 2007. doi:10.5194/acp-7-4203-2007.

Kerkweg, A., Buchholz, J., Ganzeveld, L., Pozzer, A., Tost, H., and Jöckel, P. Technical note: An implementation of the dry removal processes DRY DEPosition and SEDImentation in the Modular Earth Submodel System (MESSy). *Atmos. Chem. Phys.*, 6(12): 4617–4632, 2006a. doi:10.5194/acp-6-4617-2006.

Kerkweg, A., Sander, R., Tost, H., and Jöckel, P. Implementation of prescribed (OFFLEM), calculated (ONLEM), and pseudo-emissions (TNUDGE) of chemical species in the Modular Earth Submodel System (MESSy). *Atmos. Chem. Phys.*, 6(11):3603–3609, 2006b. doi:10.5194/acp-6-3603-2006.

Kim, J.-E., Alexander, M. J., Bui, T. P., Dean-Day, J. M., Lawson, R. P., Woods, S., Hlavka, D., Pfister, L., and Jensen, E. J. Ubiquitous influence of waves on tropical high cirrus clouds. *Geophys. Res. Lett.*, 43(11):5895–5901, 2016. doi:10.1002/2016gl069293.

Kirkby, J., Duplissy, J., Sengupta, K., Frege, C., Gordon, H., Williamson, C., Heinritzi, M., Simon, M., Yan, C., Almeida, J., Tröstl, J., Nieminen, T., Ortega, I. K., Wagner, R., Adamov, A., Amorim, A., Bernhammer, A.-K., Bianchi, F., Breitenlechner, M., Brilke, S., Chen, X., Craven, J., Dias, A., Ehrhart, S., Flagan, R. C., Franchin, A., Fuchs, C., Guida, R., Hakala, J., Hoyle, C. R., Jokinen, T., Junninen, H., Kangasluoma, J., Kim, J., Krapf, M., Kürten, A., Laaksonen, A., Lehtipalo, K., Makhmutov, V., Mathot, S., Molteni, U., Onnela, A., Peräkylä, O., Piel, F., Petäjä, T., Praplan, A. P., Pringle, K., Rap, A., Richards, N. A. D., Riipinen, I., Rissanen, M. P., Rondo, L., Sarnela, N., Schobesberger, S., Scott, C. E., Seinfeld, J. H., Sipilä, M., Steiner, G., Stozhkov, Y., Stratmann, F., Tomé, A., Virtanen, A., Vogel, A. L., Wagner, A. C., Wagner, P. E., Weingartner, E., Wimmer, D., Winkler, P. M., Ye, P., Zhang, X., Hansel, A., Dommen, J., Donahue, N. M., Worsnop, D. R., Baltensperger, U., Kulmala, M., Carslaw, K. S., and Curtius, J. Ion-induced nucleation of pure biogenic particles. *Nature*, 533(7604): 521–526, 2016. doi:10.1038/nature17953.

Kiselev, A., Bachmann, F., Pedevilla, P., Cox, S. J., Michaelides, A., Gerthsen, D., and Leisner, T. Active sites in heterogeneous ice nucleation—the example of K-rich feldspars. *Science*, 355:367–371, 2016. ISSN 0036-8075. doi:10.1126/science.aai8034.

Klingmüller, K., Metzger, S., Mohamed, A., Karydis, V. A., Stenchikov, G. L., Pozzer, A., and Lelieveld, J. Revised mineral dust emissions in the atmospheric chemistry–climate model EMAC (MESSy 2.52 DU_Astitha1 KKDU2017 patch). *Geosci. Model Dev.*, 11 (3):989, 2018. doi:10.5194/gmd-11-989-2018.

Knopf, D. A., Alpert, P. A., Wang, B., and Aller, J. Y. Stimulation of ice nucleation by marine diatoms. *Nat. Geosci.*, 4(2):88, 2011. doi:10.1038/NGEO1037.

Koehler, K. A., DeMott, P. J., Kreidenweis, S. M., Popovicheva, O. B., Petters, M. D., Carrico, C. M., Kireeva, E. D., Khokhlova, T. D., and Shonija, N. K. Cloud condensation nuclei and ice nucleation activity of hydrophobic and hydrophilic soot particles. *Phys. Chem. Chem. Phys.*, 11:7906–7920, 2009. doi:10.1039/B905334B.

Koehler, K. A., Kreidenweis, S. M., DeMott, P. J., Petters, M. D., Prenni, A. J., and Möhler, O. Laboratory investigations of the impact of mineral dust aerosol on cold cloud formation. *Atmos. Chem. Phys.*, 10(23):11955–11968, 2010. doi:10.5194/acp-10-11955-2010.

Koepke, P., Hess, M., Schult, I., and Shettle, E. P. *Global Aerosol Data Set.* MPI Meteorologie Hamburg Report No. 243, 1997.

Kojima, T., Buseck, P. R., Iwasaka, Y., Matsuki, A., and Trochkine, D. Sulfate-coated dust particles in the free troposphere over Japan. *Atmos. Res.*, 82(3):698–708, 2006. ISSN 0169-8095. doi:10.1016/j.atmosres.2006.02.024.

Koop, T., Luo, B., Tsias, A., and Peter, T. Water activity as the determinant for homogeneous ice nucleation in aqueous solutions. *Nature*, 406(6796):611, 2000. doi:10.1038/35020537.

Koop, T., Bookhold, J., Shiraiwa, M., and Pöschl, U. Glass transition and phase state of organic compounds: dependency on molecular properties and implications for secondary organic aerosols in the atmosphere. *Phys. Chem. Chem. Phys.*, 13(43):19238–19255, 2011. doi:10.1039/c1cp22617g.

Koren, I. Measurement of the effect of amazon smoke on inhibition of cloud formation. *Science*, 303(5662):1342–1345, 2004. doi:10.1126/science.1089424.

Krämer, M., Schiller, C., Afchine, A., Bauer, R., Gensch, I., Mangold, A., Schlicht, S., Spelten, N., Sitnikov, N., Borrmann, S., de Reus, M., and Spichtinger, P. Ice supersaturations and cirrus cloud crystal numbers. *Atmos. Chem. Phys.*, 9(11):3505–3522, 2009. doi:10.5194/acp-9-3505-2009.

Krämer, M., Rolf, C., Luebke, A., Afchine, A., Spelten, N., Costa, A., Meyer, J., Zöger, M., Smith, J., Herman, R. L., Buchholz, B., Ebert, V., Baumgardner, D., Borrmann, S., Klingebiel, M., and Avallone, L. A microphysics guide to cirrus clouds – part 1: Cirrus types. *Atmos. Chem. Phys.*, 16(5):3463–3483, 2016. doi:10.5194/acp-16-3463-2016.

Krämer, M., Rolf, C., Spelten, N., Afchine, A., Fahey, D., Jensen, E., Khaykin, S., Kuhn, T., Lawson, P., Lykov, A., Pan, L. L., Riese, M., Rollins, A., Stroh, F., Thornberry, T., Wolf, V., Woods, S., Spichtinger, P., Quaas, J., and Sourdeval, O. A microphysics guide to cirrus – part 2: Climatologies of clouds and humidity from observations. *Atmos. Chem. Phys.*, 20(21):12569–12608, 2020. doi:10.5194/acp-20-12569-2020.

Kristiansen, N. I., Stohl, A., Olivié, D. J. L., Croft, B., Søvde, O. A., Klein, H., Christoudias, T., Kunkel, D., Leadbetter, S. J., Lee, Y. H., Zhang, K., Tsigaridis, K., Bergman, T., Evangeliou, N., Wang, H., Ma, P.-L., Easter, R. C., Rasch, P. J., Liu, X., Pitari, G., Genova, G. D., Zhao, S. Y., Balkanski, Y., Bauer, S. E., Faluvegi, G. S., Kokkola, H., Martin, R. V., Pierce, J. R., Schulz, M., Shindell, D., Tost, H., and Zhang, H. Evaluation of observed and modelled aerosol lifetimes using radioactive tracers of opportunity and an ensemble of 19 global models. *Atmos. Chem. Phys.*, 16(5):3525–3561, 2016. doi:10.5194/acp-16-3525-2016.

Kuebbeler, M., Lohmann, U., Hendricks, J., and Kärcher, B. Dust ice nuclei effects on cirrus clouds. *Atmos. Chem. Phys.*, 14(6):3027–3046, 2014. doi:10.5194/acp-14-3027-2014.

Kulkarni, G., Sanders, C., Zhang, K., Liu, X., and Zhao, C. Ice nucleation of bare and sulfuric acid-coated mineral dust particles and implication for cloud properties. *J. Geophys. Res. Atmos.*, 119(16):9993–10011, 2014. doi:10.1002/2014jd021567.

Kulkarni, G., China, S., Liu, S., Nandasiri, M., Sharma, N., Wilson, J., Aiken, A. C., Chand, D., Laskin, A., Mazzoleni, C., Pekour, M., Shilling, J., Shutthanandan, V., Zelenyuk, A., and Zaveri, R. A. Ice nucleation activity of diesel soot particles at cirrus relevant temperature conditions: Effects of hydration, secondary organics coating, soot morphology, and coagulation. *Geophys. Res. Lett.*, 43(7):3580–3588, 2016. doi:10.1002/2016GL068707.

Kulmala, M., Petäjä, T., Ehn, M., Thornton, J., Sipilä, M., Worsnop, D., and Kerminen, V.-M. Chemistry of atmospheric nucleation: On the recent advances on precursor characterization and atmospheric cluster composition in connection with atmospheric new

particle formation. *Annu. Rev. Phys. Chem.*, 65(1):21–37, 2014. doi:10.1146/annurev-physchem-040412-110014.

Kumar, A., Marcolli, C., Luo, B., and Peter, T. Ice nucleation activity of silicates and aluminosilicates in pure water and aqueous solutions – part 1: The K-feldspar microcline. *Atmos. Chem. Phys.*, 18(10):7057–7079, 2018. doi:10.5194/acp-18-7057-2018.

Kurtén, T., Loukonen, V., Vehkamäki, H., and Kulmala, M. Amines are likely to enhance neutral and ion-induced sulfuric acid-water nucleation in the atmosphere more effectively than ammonia. *Atmos. Chem. Phys.*, 8(14):4095–4103, 2008. doi:10.5194/acp-8-4095-2008.

Laaksonen, A., Kulmala, M., O'Dowd, C. D., Joutsensaari, J., Vaattovaara, P., Mikkonen, S., Lehtinen, K. E. J., Sogacheva, L., Maso, M. D., Aalto, P., Petäjä, T., Sogachev, A., Yoon, Y. J., Lihavainen, H., Nilsson, D., Facchini, M. C., Cavalli, F., Fuzzi, S., Hoffmann, T., Arnold, F., Hanke, M., Sellegri, K., Umann, B., Junkermann, W., Coe, H., Allan, J. D., Alfarra, M. R., Worsnop, D. R., Riekkola, M. L., Hyötyläinen, T., and Viisanen, Y. The role of VOC oxidation products in continental new particle formation. *Atmos. Chem. Phys.*, 8(10):2657–2665, 2008. doi:10.5194/acp-8-2657-2008.

Ladino, L. A., Zhou, S., Yakobi-Hancock, J. D., Aljawhary, D., and Abbatt, J. P. D. Factors controlling the ice nucleating abilities of α-pinene SOA particles. *J. Geophys. Res. Atmos.*, 119(14):9041–9051, 2014. ISSN 2169-897X. doi:10.1002/2014JD021578.

Lamarque, J.-F., Bond, T. C., Eyring, V., Granier, C., Heil, A., Klimont, Z., Lee, D., Liousse, C., Mieville, A., Owen, B., Schultz, M. G., Shindell, D., Smith, S. J., Stehfest, E., Van Aardenne, J., Cooper, O. R., Kainuma, M., Mahowald, N., McConnell, J. R., Naik, V., Riahi, K., and van Vuuren, D. P. Historical (1850-2000) gridded anthropogenic and biomass burning emissions of reactive gases and aerosols: methodology and application. *Atmos. Chem. Phys.*, 10(15):7017–7039, 2010. doi:10.5194/acp-10-7017-2010.

Lauer, A., Hendricks, J., Ackermann, I., Schell, B., Hass, H., and Metzger, S. Simulating aerosol microphysics with the ECHAM/MADE GCM–Part I: Model description and comparison with observations. *Atmos. Chem. Phys.*, 5(12):3251–3276, 2005. doi:10.5194/acp-5-3251-2005.

Lauer, A., Eyring, V., Hendricks, J., Jöckel, P., and Lohmann, U. Global model simulations of the impact of ocean-going ships on aerosols, clouds, and the radiation budget. *Atmos. Chem. Phys.*, 7(19):5061–5079, 2007. doi:10.5194/acp-7-5061-2007.

Lebsock, M. D., Stephens, G. L., and Kummerow, C. Multisensor satellite observations of aerosol effects on warm clouds. *J. Geophys. Res.*, 113(D15), 2008. doi:10.1029/2008jd009876.

Levkov, L., Rockel, B., Kapitza, H., and Raschke, E. 3D mesoscale numerical studies of cirrus and stratus clouds by their time and space evolution. *Contrib. Atmos. Phys.*, 65 (1):35–58, 1992.

Li, C. Y., Ding, M., Yang, Y., Zhang, P., Li, Y., Wang, Y., Huang, L., Yang, P., Wang, M., Sha, X., Xu, Y., Guo, C., and Shan, Z. Portrait and classification of individual haze particulates. *J. Environ. Prot.*, 07(10):1355–1379, 2016. doi:10.4236/jep.2016.710118.

Lin, S.-J. and Rood, R. B. Multidimensional Flux-Form Semi-Lagrangian Transport Schemes. *Mon. Weather Rev.*, 124(9):2046–2070, 1996. doi:10.1175/1520-0493(1996)124<2046:mffslt>2.0.co;2.

Liss, P. S. and Merlivat, L. Air-sea gas exchange rates: Introduction and synthesis. In *The Role of Air-Sea Exchange in Geochemical Cycling*, pages 113–127. Springer Netherlands, 1986. doi:10.1007/978-94-009-4738-2_5.

Liu, X., Penner, J. E., Das, B., Bergmann, D., Rodriguez, J. M., Strahan, S., Wang, M., and Feng, Y. Uncertainties in global aerosol simulations: Assessment using three meteorological data sets. *J. Geophys. Res. Atmos.*, 112(D11):D11212, 2007. doi:10.1029/2006JD008216.

Liu, X., Penner, J. E., and Wang, M. Influence of anthropogenic sulfate and black carbon on upper tropospheric clouds in the NCAR CAM3 model coupled to the IMPACT global aerosol model. *J. Geophys. Res.*, 114(D3), 2009. doi:10.1029/2008jd010492.

Liu, X., Shi, X., Zhang, K., Jensen, E. J., Gettelman, A., Barahona, D., Nenes, A., and Lawson, P. Sensitivity studies of dust ice nuclei effect on cirrus clouds with the community atmosphere model CAM5. *Atmos. Chem. Phys.*, 12(24):12061–12079, 2012. doi:10.5194/acp-12-12061-2012.

Liu, X., Ma, P.-L., Wang, H., Tilmes, S., Singh, B., Easter, R. C., Ghan, S. J., and Rasch, P. J. Description and evaluation of a new four-mode version of the Modal Aerosol Module (MAM4) within version 5.3 of the Community Atmosphere Model. *Geosci. Model Dev.*, 9(2):505–522, 2016. doi:10.5194/gmd-9-505-2016.

Lohmann, U. and Diehl, K. Sensitivity studies of the importance of dust ice nuclei for the indirect aerosol effect on stratiform mixed-phase clouds. *J. Atmos. Sci.*, 63(3):968–982, 2006. doi:10.1175/jas3662.1.

Lohmann, U., Stier, P., Hoose, C., Ferrachat, S., Kloster, S., Roeckner, E., and Zhang, J. Cloud microphysics and aerosol indirect effects in the global climate model ECHAM5-HAM. *Atmos. Chem. Phys.*, 7(13):3425–3446, 2007. doi:10.5194/acp-7-3425-2007.

Lohmann, U., Spichtinger, P., Jess, S., Peter, T., and Smit, H. Cirrus cloud formation and ice supersaturated regions in a global climate model. *Environ. Res. Lett.*, 3(4): 045022, 2008. doi:10.1088/1748-9326/3/4/045022.

Lu, M.-L., Conant, W. C., Jonsson, H. H., Varutbangkul, V., Flagan, R. C., and Seinfeld, J. H. The marine stratus/stratocumulus experiment (MASE): Aerosol-cloud relationships in marine stratocumulus. *J. Geophys. Res. Atmos.*, 112(D10), 2007. doi:10.1029/2006jd007985.

Mahowald, N., Albani, S., Kok, J. F., Engelstaeder, S., Scanza, R., Ward, D. S., and Flanner, M. G. The size distribution of desert dust aerosols and its impact on the Earth system. *Aeolian Res.*, 15:53–71, 2014. doi:10.1016/j.aeolia.2013.09.002.

Mahowald, N. M., Kloster, S., Engelstaedter, S., Moore, J. K., Mukhopadhyay, S., McConnell, J. R., Albani, S., Doney, S. C., Bhattacharya, A., Curran, M., et al. Observed 20th century desert dust variability: impact on climate and biogeochemistry. *Atmos. Chem. Phys.*, 10(22):10875–10893, 2010. doi:10.5194/acp-10-10875-2010.

Mahrt, F., Marcolli, C., David, R. O., Grönquist, P., Meier, E. J. B., Lohmann, U., and Kanji, Z. A. Ice nucleation abilities of soot particles determined with the horizontal ice nucleation chamber. *Atmos. Chem. Phys.*, 18(18):13363–13392, 2018. doi:10.5194/acp-18-13363-2018.

Mahrt, F., Kilchhofer, K., Marcolli, C., Grönquist, P., David, R. O., Rösch, M., Lohmann, U., and Kanji, Z. A. The impact of cloud processing on the ice nucleation abilities of soot particles at cirrus temperatures. *J. Geophys. Res. Atmos.*, 125(3), 2020. doi:10.1029/2019jd030922.

Marcolli, C. Deposition nucleation viewed as homogeneous or immersion freezing in pores and cavities. *Atmos. Chem. Phys.*, 14(4):2071–2104, 2014. doi:10.5194/acp-14-2071-2014.

Marcolli, C. Pre-activation of aerosol particles by ice preserved in pores. *Atmos. Chem. Phys.*, 17(3):1595–1622, 2017. doi:10.5194/acp-17-1595-2017.

Martin, S. T. Phase transitions of aqueous atmospheric particles. *Chem. Rev.*, 100(9): 3403–3454, 2000. doi:10.1021/cr990034t. PMID: 11777428.

Martin, S. T., Han, J.-H., and Hung, H.-M. The size effect of hematite and corundum inclusions on the efflorescence relative humidities of aqueous ammonium sulfate particles. *Geophys. Res. Lett.*, 28(13):2601–2604, 2001. ISSN 0094-8276. doi:10.1029/2001GL013120.

Martin, S. T., Schlenker, J. C., Malinowski, A., Hung, H.-M., and Rudich, Y. Crystallization of atmospheric sulfate-nitrate-ammonium particles. *Geophys. Res. Lett.*, 30(21): 1–6, 2003. doi:10.1029/2003GL017930.

Martin, S. T., Hung, H.-M., Park, R. J., Jacob, D. J., Spurr, R. J. D., Chance, K. V., and Chin, M. Effects of the physical state of tropospheric ammonium-sulfate-nitrate particles on global aerosol direct radiative forcing. *Atmos. Chem. Phys.*, 4(1):183–214, 2004. doi:10.5194/acp-4-183-2004.

McGraw, Z., Storelvmo, T., Samset, B. H., and Stjern, C. W. Global radiative impacts of black carbon acting as ice nucleating particles. *Geophysical Research Letters*, 47(20): e2020GL089056, 2020. doi:10.1029/2020GL089056.

Metzger, A., Verheggen, B., Dommen, J., Duplissy, J., Prevot, A. S. H., Weingartner, E., Riipinen, I., Kulmala, M., Spracklen, D. V., Carslaw, K. S., and Baltensperger, U. Evidence for the role of organics in aerosol particle formation under atmospheric conditions. *Proc. Natl. Acad. Sci.*, 107(15):6646–6651, 2010. doi:10.1073/pnas.0911330107.

Metzger, S., Dentener, F., Pandis, S., and Lelieveld, J. Gas/aerosol partitioning: 1. a computationally efficient model. *J. Geophys. Res. Atmos.*, 107(D16):4312, 2002. doi:10.1029/2001JD001102.

Mitchell, D. L. and Finnegan, W. Modification of cirrus clouds to reduce global warming. *Environ. Res. Lett.*, 4(4):045102, 2009. doi:10.1088/1748-9326/4/4/045102.

Möhler, O., Linke, C., Saathoff, H., Schnaiter, M., Wagner, R., Mangold, A., Krämer, M., and Schurath, U. Ice nucleation on flame soot aerosol of different organic carbon content. *Meteorol. Z.*, 14(4):477–484, 2005. doi:10.1127/0941-2948/2005/0055.

Möhler, O., Field, P. R., Connolly, P., Benz, S., Saathoff, H., Schnaiter, M., Wagner, R., Cotton, R., Krämer, M., Mangold, A., and Heymsfield, A. J. Efficiency of the deposition mode ice nucleation on mineral dust particles. *Atmos. Chem. Phys.*, 6(10): 3007–3021, 2006. doi:10.5194/acp-6-3007-2006.

Möhler, O., Benz, S., Saathoff, H., Schnaiter, M., Wagner, R., Schneider, J., Walter, S., Ebert, V., and Wagner, S. The effect of organic coating on the heterogeneous ice nucleation efficiency of mineral dust aerosols. *Environ. Res. Lett.*, 3(2):025007, 2008. ISSN 1748-9326. doi:10.1088/1748-9326/3/2/025007.

Monerie, P.-A., Chevuturi, A., Cook, P., Klingaman, N. P., and Holloway, C. E. Role of atmospheric horizontal resolution in simulating tropical and subtropical South American precipitation in HadGEM3-GC31. *Geosci. Model Dev.*, 13(10):4749–4771, 2020. doi:10.5194/gmd-13-4749-2020.

Motos, G., Schmale, J., Corbin, J. C., Zanatta, M., Baltensperger, U., and Gysel-Beer, M. Droplet activation behaviour of atmospheric black carbon particles in fog as a function of their size and mixing state. *Atmos. Chem. Phys.*, 19(4):2183–2207, 2019. doi:10.5194/acp-19-2183-2019.

Mülmenstädt, J. and Feingold, G. The radiative forcing of aerosol–cloud interactions in liquid clouds: Wrestling and embracing uncertainty. *Curr. Clim. Change Rep.*, 4(1): 23–40, 2018. doi:10.1007/s40641-018-0089-y.

Muri, H., Kristjánsson, J. E., Storelvmo, T., and Pfeffer, M. A. The climatic effects of modifying cirrus clouds in a climate engineering framework. *J. Geophys. Res. Atmos.*, 119(7):4174–4191, 2014. doi:10.1002/2013jd021063.

Murphy, D. M. and Koop, T. Review of the vapour pressures of ice and supercooled water for atmospheric applications. *Q. J. R. Meteorol. Soc.*, 131(608):1539–1565, 2005. ISSN 0035-9009. doi:10.1256/qj.04.94.

Murray, B. J., Wilson, T. W., Dobbie, S., Cui, Z., Al-Jumur, S. M., Möhler, O., Schnaiter, M., Wagner, R., Benz, S., Niemand, M., Saathoff, H., Ebert, V., Wagner, S., and Kärcher, B. Heterogeneous nucleation of ice particles on glassy aerosols under cirrus conditions. *Nat. Geosci.*, 3(4):233–237, 2010. doi:10.1038/NGEO817.

Murray, B. J., O'Sullivan, D., Atkinson, J. D., and Webb, M. E. Ice nucleation by particles immersed in supercooled cloud droplets. *Chem. Soc. Rev.*, 41(19):6519, 2012. doi:10.1039/c2cs35200a.

Myhre, G., Samset, B. H., Schulz, M., Balkanski, Y., Bauer, S., Berntsen, T. K., Bian, H., Bellouin, N., Chin, M., Diehl, T., Easter, R. C., Feichter, J., Ghan, S. J., Hauglustaine, D., Iversen, T., Kinne, S., Kirkevåg, A., Lamarque, J.-F., Lin, G., Liu, X., Lund, M. T., Luo, G., Ma, X., van Noije, T., Penner, J. E., Rasch, P. J., Ruiz, A., Seland, Ø., Skeie, R. B., Stier, P., Takemura, T., Tsigaridis, K., Wang, P., Wang, Z., Xu, L., Yu, H., Yu, F., Yoon, J.-H., Zhang, K., Zhang, H., and Zhou, C. Radiative forcing of the direct aerosol effect from AeroCom phase II simulations. *Atmos. Chem. Phys.*, 13(4): 1853–1877, 2013. doi:10.5194/acp-13-1853-2013.

Nabat, P., Solmon, F., Mallet, M., Kok, J. F., and Somot, S. Dust emission size distribution impact on aerosol budget and radiative forcing over the Mediterranean region: a regional climate model approach. *Atmos. Chem. Phys.*, 12(21):10545–10567, 2012. doi:10.5194/acp-12-10545-2012.

Neale, R. B., Chen, C.-C., Gettelman, A., Lauritzen, P. H., Park, S., Williamson, D. L., Conley, A. J., Garcia, R., Kinnison, D., Lamarque, J.-F., Marsh, D., Mills, M., Smith, A. K., Tilmes, S., Vitt, F., Morrison, H., Cameron-Smith, P., Collins, W. D., Iacono, M. J., Easter, R. C., Ghan, S. J., Liu, X., Rasch, P. J., and Taylor, M. A. Description of the NCAR community atmosphere model (CAM 5.0). *NCAR Tech. Note NCAR/TN-486+ STR*, 1(1):1–12, 2010.

Nenes, A., Krom, M. D., Mihalopoulos, N., Van Cappellen, P., Shi, Z., Bougiatioti, A., Zarmpas, P., and Herut, B. Atmospheric acidification of mineral aerosols: a source of bioavailable phosphorus for the oceans. *Atmos. Chem. Phys.*, 11(13):6265–6272, 2011. doi:10.5194/acp-11-6265-2011.

Neubauer, D., Ferrachat, S., Drian, C. S.-L., Stier, P., Partridge, D. G., Tegen, I., Bey, I., Stanelle, T., Kokkola, H., and Lohmann, U. The global aerosol–climate model ECHAM6.3–HAM2.3 – part 2: Cloud evaluation, aerosol radiative forcing, and climate sensitivity. *Geosci. Model Dev.*, 12(8):3609–3639, 2019. doi:10.5194/gmd-12-3609-2019.

Nichman, L., Wolf, M., Davidovits, P., Onasch, T. B., Zhang, Y., Worsnop, D. R., Bhandari, J., Mazzoleni, C., and Cziczo, D. J. Laboratory study of the heterogeneous ice nucleation on black-carbon-containing aerosol. *Atmos. Chem. Phys.*, 19(19):12175–12194, 2019. doi:10.5194/acp-19-12175-2019.

Niehaus, J. and Cantrell, W. Contact freezing of water by salts. *J. Phys. Chem. Lett.*, 6 (17):3490–3495, 2015. doi:10.1021/acs.jpclett.5b01531.

Nordeng, T. E. Extended versions of the convective parametrization scheme at ECMWF and their impact on the mean and transient activity of the model in the tropics. *Research Department Technical Memorandum*, 206:1–41, 1994.

Onasch, T. B., Siefert, R. L., Brooks, S. D., Prenni, A. J., Murray, B., Wilson, M. A., and Tolbert, M. A. Infrared spectroscopic study of the deliquescence and efflorescence of ammonium sulfate aerosol as a function of temperature. *J. Geophys. Res.*, 104(D17): 21317–21326, 1999. ISSN 0148-0227. doi:10.1029/1999JD900384.

O'Sullivan, D., Marenco, F., Ryder, C. L., Pradhan, Y., Kipling, Z., Johnson, B., Benedetti, A., Brooks, M., McGill, M., Yorks, J., and Selmer, P. Models transport Saharan dust too low in the atmosphere: a comparison of the MetUM and CAMS forecasts with observations. *Atmos. Chem. Phys.*, 20(21):12955–12982, 2020. doi:10.5194/acp-20-12955-2020.

Pandey, R., Usui, K., Livingstone, R. A., Fischer, S. A., Pfaendtner, J., Backus, E. H. G., Nagata, Y., Fröhlich-Nowoisky, J., Schmüser, L., Mauri, S., Scheel, J. F., Knopf, D. A., Pöschl, U., Bonn, M., and Weidner, T. Ice-nucleating bacteria control the order and dynamics of interfacial water. *Sci. Adv.*, 2(4):e1501630, 2016. doi:10.1126/sciadv.1501630.

Pant, A., Parsons, M. T., and Bertram, A. K. Crystallization of aqueous ammonium sulfate particles internally mixed with soot and kaolinite: Crystallization relative humidities and nucleation rates. *J. Phys. Chem. A*, 110(28):8701–8709, 2006. ISSN 1089-5639. doi:10.1021/jp060985s.

Parajuli, S. P., Stenchikov, G. L., Ukhov, A., and Kim, H. Dust emission modeling using a new high-resolution dust source function in WRF-Chem with implications for air quality. *J. Geophys. Res. Atmos.*, 2019. doi:10.1029/2019jd030248.

Paramonov, M., David, R. O., Kretzschmar, R., and Kanji, Z. A. A laboratory investigation of the ice nucleation efficiency of three types of mineral and soil dust. *Atmos. Chem. Phys.*, 18(22):16515–16536, 2018. doi:10.5194/acp-18-16515-2018.

Park, R. J., Jacob, D. J., Field, B. D., Yantosca, R. M., and Chin, M. Natural and transboundary pollution influences on sulfate-nitrate-ammonium aerosols in the United States: Implications for policy. *J. Geophys. Res.*, 109(D15), 2004. doi:10.1029/2003jd004473.

Peckhaus, A., Kiselev, A., Hiron, T., Ebert, M., and Leisner, T. A comparative study of K-rich and Na/Ca-rich feldspar ice-nucleating particles in a nanoliter droplet freezing assay. *Atmos. Chem. Phys.*, 16(18):11477–11496, 2016. doi:10.5194/acp-16-11477-2016.

Penner, J. E., Chen, Y., Wang, M., and Liu, X. Possible influence of anthropogenic aerosols on cirrus clouds and anthropogenic forcing. *Atmos. Chem. Phys.*, 9(3):879–896, 2009. doi:10.5194/acp-9-879-2009.

Penner, J. E., Zhou, C., and Liu, X. Can cirrus cloud seeding be used for geoengineering? *Geophys. Res. Lett.*, 42(20):8775–8782, 2015. doi:10.1002/2015gl065992.

Penner, J. E., Zhou, C., Garnier, A., and Mitchell, D. L. Anthropogenic aerosol indirect effects in cirrus clouds. *J. Geophys. Res. Atmos.*, 123(20):11652–11677, 2018. ISSN 2169-897X. doi:10.1029/2018JD029204.

Petters, M. D. and Kreidenweis, S. M. A single parameter representation of hygroscopic growth and cloud condensation nucleus activity. *Atmos. Chem. Phys.*, 7(8):1961–1971, 2007. doi:10.5194/acp-7-1961-2007.

Petzold, A., Döpelheuer, A., Brock, C. A., and Schröder, F. In situ observations and model calculations of black carbon emission by aircraft at cruise altitude. *J. Geophys. Res. Atmos.*, 104(D18):22171–22181, 1999. doi:10.1029/1999jd900460.

Podglajen, A., Hertzog, A., Plougonven, R., and Legras, B. Lagrangian temperature and vertical velocity fluctuations due to gravity waves in the lower stratosphere. *Geophys. Res. Lett.*, 43(7):3543–3553, 2016. ISSN 0094-8276. doi:10.1002/2016GL068148.

Podglajen, A., Plougonven, R., Hertzog, A., and Jensen, E. Impact of gravity waves on the motion and distribution of atmospheric ice particles. *Atmos. Chem. Phys.*, 18(14):10799–10823, 2018. doi:10.5194/acp-18-10799-2018.

Prakash, P. J., Stenchikov, G., Kalenderski, S., Osipov, S., and Bangalath, H. The impact of dust storms on the Arabian Peninsula and the Red Sea. *Atmos. Chem. Phys.*, 15(1):199–222, 2015. doi:10.5194/acp-15-199-2015.

Quinn, P. K., Collins, D. B., Grassian, V. H., Prather, K. A., and Bates, T. S. Chemistry and related properties of freshly emitted sea spray aerosol. *Chem. Rev.*, 115(10):4383–4399, 2015. doi:10.1021/cr500713g.

Rayner, N. A., Parker, D. E., Horton, E. B., Folland, C. K., Alexander, L. V., Rowell, D. P., Kent, E. C., and Kaplan, A. Global analyses of sea surface temperature, sea ice, and night marine air temperature since the late nineteenth century. *J. Geophys. Res. Atmos.*, 108(D14), 2003. doi:10.1029/2002jd002670.

Reid, J. P., Bertram, A. K., Topping, D. O., Laskin, A., Martin, S. T., Petters, M. D., Pope, F. D., and Rovelli, G. The viscosity of atmospherically relevant organic particles. *Nat. Commun.*, 9(1):956, 2018. doi:10.1038/s41467-018-03027-z.

Riahi, K., Grübler, A., and Nakicenovic, N. Scenarios of long-term socio-economic and environmental development under climate stabilization. *Technol. Forecasting Social Change*, 74(7):887–935, 2007. doi:10.1016/j.techfore.2006.05.026.

Riahi, K., Rao, S., Krey, V., Cho, C., Chirkov, V., Fischer, G., Kindermann, G., Nakicenovic, N., and Rafaj, P. RCP 8.5—a scenario of comparatively high greenhouse gas emissions. *Clim. Chang.*, 109(1-2):33–57, 2011. doi:10.1007/s10584-011-0149-y.

Riccobono, F., Rondo, L., Sipilä, M., Barmet, P., Curtius, J., Dommen, J., Ehn, M., Ehrhart, S., Kulmala, M., Kürten, A., Mikkilä, J., Paasonen, P., Petäjä, T., Weingartner, E., and Baltensperger, U. Contribution of sulfuric acid and oxidized organic compounds to particle formation and growth. *Atmos. Chem. Phys.*, 12(20):9427–9439, 2012. doi:10.5194/acp-12-9427-2012.

Riemer, N., West, M., Zaveri, R. A., and Easter, R. C. Simulating the evolution of soot mixing state with a particle-resolved aerosol model. *J. Geophys. Res.*, 114(D9), 2009. doi:10.1029/2008jd011073.

Righi, M., Hendricks, J., and Sausen, R. The global impact of the transport sectors on atmospheric aerosol: simulations for year 2000 emissions. *Atmos. Chem. Phys.*, 13(19):9939–9970, 2013. doi:doi:10.5194/acp-13-9939-2013.

Righi, M., Hendricks, J., and Sausen, R. The global impact of the transport sectors on atmospheric aerosol in 2030-part 1: Land transport and shipping. *Atmos. Chem. Phys.*, 15(2):633–651, 2015. doi:doi:10.5194/acp-15-633-2015.

Righi, M., Hendricks, J., and Sausen, R. The global impact of the transport sectors on atmospheric aerosol in 2030–part 2: Aviation. *Atmos. Chem. Phys.*, 16(7):4481–4495, 2016. doi:doi:10.5194/acp-16-4481-2016.

Righi, M., Hendricks, J., Lohmann, U., Beer, C. G., Hahn, V., Heinold, B., Heller, R., Krämer, M., Ponater, M., Rolf, C., Tegen, I., and Voigt, C. Coupling aerosols to (cirrus) clouds in the global EMAC-MADE3 aerosol-climate model. *Geosci. Model Dev.*, 13(3):1635–1661, 2020. doi:10.5194/gmd-13-1635-2020.

Roeckner, E., Arpe, K., Bengtsson, L., Christoph, M., Claussen, M., Dümenil, L., Esch, M., Giorgetta, M. A., Schlese, U., and Schulzweida, U. The atmospheric general circulation model ECHAM-4: Model description and simulation of present-day climate. *MPI Report*, 1996.

Roeckner, E., Bäuml, G., Bonaventura, L., Brokopf, R., Esch, M., Giorgetta, M., Hagemann, S., Kirchner, I., Kornblueh, L., Manzini, E., Rhodin, A., Schlese, U., Schulzweida, U., and Tompkins, A. The atmospheric general circulation model ECHAM 5. PART I: Model description. *MPI Report*, 2003.

Roeckner, E., Brokopf, R., Esch, M., Giorgetta, M., Hagemann, S., Kornblueh, L., Manzini, E., Schlese, U., and Schulzweida, U. Sensitivity of simulated climate to horizontal and vertical resolution in the ECHAM5 atmosphere model. *J. Clim.*, 19(16): 3771–3791, 2006. doi:10.1175/JCLI3824.1.

Rogers, D. C., DeMott, P. J., Kreidenweis, S. M., and Chen, Y. Measurements of ice nucleating aerosols during SUCCESS. *Geophys. Res. Lett.*, 25(9):1383–1386, 1998. doi:10.1029/97gl03478.

Rogers, D. C., DeMott, P. J., and Kreidenweis, S. M. Airborne measurements of tropospheric ice-nucleating aerosol particles in the Arctic spring. *J. Geophys. Res. Atmos.*, 106(D14):15053–15063, 2001a. doi:10.1029/2000jd900790.

Rogers, D. C., DeMott, P. J., Kreidenweis, S. M., and Chen, Y. A continuous-flow diffusion chamber for airborne measurements of ice nuclei. *J. Atmos. Oceanic Technol.*, 18(5):725–741, 2001b. doi:10.1175/1520-0426(2001)018<0725:acfdcf>2.0.co;2.

Rotman, D. A., Tannahill, J. R., Kinnison, D. E., Connell, P. S., Bergmann, D., Proctor, D., Rodriguez, J. M., Lin, S. J., Rood, R. B., Prather, M. J., Rasch, P. J., Considine, D. B., Ramaroson, R., and Kawa, S. R. Global modeling initiative assessment model: Model description, integration, and testing of the transport shell. *J. Geophys. Res. Atmos.*, 106(D2):1669–1691, 2001. doi:10.1029/2000jd900463.

Rotman, D. A., Atherton, C. S., Bergmann, D. J., Cameron-Smith, P. J., Chuang, C. C., Connell, P. S., Dignon, J. E., Franz, A., Grant, K. E., Kinnison, D. E., Molenkamp, C. R., Proctor, D. D., and Tannahill, J. R. IMPACT, the LLNL 3-d global atmospheric chemical transport model for the combined troposphere and stratosphere: Model description and analysis of ozone and other trace gases. *J. Geophys. Res. Atmos.*, 109 (D4), 2004. doi:10.1029/2002jd003155.

Rumble, J. R. *CRC handbook of chemistry and physics.* CRC press, 98 edition, 2004.

Ryder, C. L., Highwood, E. J., Walser, A., Seibert, P., Philipp, A., and Weinzierl, B. Coarse and giant particles are ubiquitous in Saharan dust export regions and are radiatively significant over the Sahara. *Atmos. Chem. Phys.*, 19(24):15353–15376, 2019. doi:10.5194/acp-19-15353-2019.

Samset, B. H., Myhre, G., Herber, A., Kondo, Y., Li, S.-M., Moteki, N., Koike, M., Oshima, N., Schwarz, J. P., Balkanski, Y., Bauer, S. E., Bellouin, N., Berntsen, T. K., Bian, H., Chin, M., Diehl, T., Easter, R. C., Ghan, S. J., Iversen, T., Kirkevåg, A., Lamarque, J.-F., Lin, G., Liu, X., Penner, J. E., Schulz, M., Seland, Ø., Skeie, R. B., Stier, P., Takemura, T., Tsigaridis, K., and Zhang, K. Modelled black carbon radiative forcing and atmospheric lifetime in AeroCom Phase II constrained by aircraft observations. *Atmos. Chem. Phys.*, 14(22):12465–12477, 2014. doi:10.5194/acp-14-12465-2014.

Sander, R., Baumgaertner, A., Gromov, S., Harder, H., Jöckel, P., Kerkweg, A., Kubistin, D., Regelin, E., Riede, H., Sandu, A., Taraborrelli, D., Tost, H., and Xie, Z.-Q. The atmospheric chemistry box model CAABA/MECCA-3.0. *Geosci. Model Dev.*, 4(2): 373–380, 2011. doi:10.5194/gmd-4-373-2011.

Sander, R., Jöckel, P., Kirner, O., Kunert, A. T., Landgraf, J., and Pozzer, A. The photolysis module JVAL-14, compatible with the MESSy standard, and the JVal PreProcessor (JVPP). *Geosci. Model Dev.*, 7(6):2653–2662, 2014. doi:10.5194/gmd-7-2653-2014.

Sassen, K., Wang, Z., and Liu, D. Global distribution of cirrus clouds from CloudSat/cloud-aerosol lidar and infrared pathfinder satellite observations (CALIPSO) measurements. *J. Geophys. Res.*, 113, 2008. doi:10.1029/2008jd009972.

Saukko, E., Zorn, S., Kuwata, M., Keskinen, J., and Virtanen, A. Phase state and deliquescence hysteresis of ammonium-sulfate-seeded secondary organic aerosol. *Aerosol Sci. Technol.*, 49(7):531–537, 2015. doi:10.1080/02786826.2015.1050085.

Schill, G. P., De Haan, D. O., and Tolbert, M. A. Heterogeneous ice nucleation on simulated secondary organic aerosol. *Environ. Sci. Technol.*, 48(3):1675–1682, 2014. doi:10.1021/es4046428.

Schrod, J., Weber, D., Drücke, J., Keleshis, C., Pikridas, M., Ebert, M., Cvetković, B., Nickovic, S., Marinou, E., Baars, H., Ansmann, A., Vrekoussis, M., Mihalopoulos, N., Sciare, J., Curtius, J., and Bingemer, H. G. Ice nucleating particles over the Eastern Mediterranean measured by unmanned aircraft systems. *Atmos. Chem. Phys.*, 17(7): 4817–4835, 2017. doi:10.5194/acp-17-4817-2017.

Schrod, J., Kleinhenz, D., Hörhold, M., Erhardt, T., Richter, S., Wilhelms, F., Fischer, H., Ebert, M., Twarloh, B., Lunga, D. D., Jensen, C. M., Curtius, J., and Bingemer, H. G. Ice-nucleating particle concentrations of the past: insights from a 600-year-old Greenland ice core. *Atmos. Chem. Phys.*, 20(21):12459–12482, 2020. doi:10.5194/acp-20-12459-2020.

Schultz, M. G., Stadtler, S., Schröder, S., Taraborrelli, D., Franco, B., Krefting, J., Henrot, A., Ferrachat, S., Lohmann, U., Neubauer, D., Drian, C. S.-L., Wahl, S., Kokkola, H., Kühn, T., Rast, S., Schmidt, H., Stier, P., Kinnison, D., Tyndall, G. S., Orlando, J. J., and Wespes, C. The chemistry–climate model ECHAM6.3-HAM2.3-MOZ1.0. *Geosci. Model Dev.*, 11(5):1695–1723, 2018. doi:10.5194/gmd-11-1695-2018.

Schutgens, N. A. J., Gryspeerdt, E., Weigum, N., Tsyro, S., Goto, D., Schulz, M., and Stier, P. Will a perfect model agree with perfect observations? The impact of spatial sampling. *Atmos. Chem. Phys.*, 16(10):6335–6353, 2016. doi:10.5194/acp-16-6335-2016.

Schwarz, J. P., Weinzierl, B., Samset, B. H., Dollner, M., Heimerl, K., Markovic, M. Z., Perring, A. E., and Ziemba, L. Aircraft measurements of black carbon vertical profiles show upper tropospheric variability and stability. *Geophys. Res. Lett.*, 44(2):1132–1140, 2017. doi:10.1002/2016GL071241.

Seinfeld, J. H. and Pandis, S. N. *Atmospheric chemistry and physics: From air pollution to climate change.* John Wiley & Sons, 2016.

Shao, Y., Wyrwoll, K.-H., Chappell, A., Huang, J., Lin, Z., McTainsh, G. H., Mikami, M., Tanaka, T. Y., Wang, X., and Yoon, S. Dust cycle: An emerging core theme in earth system science. *Aeolian Res.*, 2(4):181–204, 2011. doi:10.1016/j.aeolia.2011.02.001.

Shao, Y., Zhang, J., Ishizuka, M., Mikami, M., Leys, J., and Huang, N. Dependency of particle size distribution at dust emission on friction velocity and atmospheric boundary-layer stability. *Atmos. Chem. Phys.*, 20(21):12939–12953, 2020. doi:10.5194/acp-20-12939-2020.

Shiraiwa, M., Li, Y., Tsimpidi, A. P., Karydis, V. A., Berkemeier, T., Pandis, S. N., Lelieveld, J., Koop, T., and Pöschl, U. Global distribution of particle phase state in atmospheric secondary organic aerosols. *Nat. Commun.*, 8:15002, 2017. doi:10.1038/ncomms15002.

Shpund, J., Khain, A., and Rosenfeld, D. Effects of sea spray on microphysics and intensity of deep convective clouds under strong winds. *J. Geophys. Res. Atmos.*, 124 (16):9484–9509, 2019. doi:10.1029/2018jd029893.

Small, J. D., Chuang, P. Y., Feingold, G., and Jiang, H. Can aerosol decrease cloud lifetime? *Geophys. Res. Lett.*, 36(16), 2009. doi:10.1029/2009gl038888.

Small, J. D., Jiang, J. H., Su, H., and Zhai, C. Relationship between aerosol and cloud fraction over Australia. *Geophys. Res. Lett.*, 38(2323), 2011. doi:10.1029/2011gl049404.

Smith, M. L., Bertram, A. K., and Martin, S. T. Deliquescence, efflorescence, and phase miscibility of mixed particles of ammonium sulfate and isoprene-derived secondary organic material. *Atmos. Chem. Phys.*, 12(20):9613–9628, 2012. doi:10.5194/acp-12-9613-2012.

Smith, M. L., You, Y., Kuwata, M., Bertram, A. K., and Martin, S. T. Phase transitions and phase miscibility of mixed particles of ammonium sulfate, toluene-derived secondary organic material, and water. *J. Phys. Chem. A*, 117(36):8895–8906, 2013. doi:10.1021/jp405095e. PMID: 23931697.

Spichtinger, P. and Cziczo, D. J. Impact of heterogeneous ice nuclei on homogeneous freezing events in cirrus clouds. *J. Geophys. Res.*, 115(D14), 2010. doi:10.1029/2009jd012168.

Spiro, P. A., Jacob, D. J., and Logan, J. A. Global inventory of sulfur emissions with 1°×1° resolution. *J. Geophys. Res.*, 97(D5):6023, 1992. doi:10.1029/91jd03139.

Stevens, B. and Feingold, G. Untangling aerosol effects on clouds and precipitation in a buffered system. *Nature*, 461(7264):607–613, 2009. doi:10.1038/nature08281.

Stevens, B., Giorgetta, M., Esch, M., Mauritsen, T., Crueger, T., Rast, S., Salzmann, M., Schmidt, H., Bader, J., Block, K., Brokopf, R., Fast, I., Kinne, S., Kornblueh, L., Lohmann, U., Pincus, R., Reichler, T., and Roeckner, E. Atmospheric component of the MPI-m earth system model: ECHAM6. *J. Adv. Model. Earth Syst.*, 5(2):146–172, 2013. doi:10.1002/jame.20015.

Stier, P., Feichter, J., Kinne, S., Kloster, S., Vignati, E., Wilson, J., Ganzeveld, L., Tegen, I., Werner, M., Balkanski, Y., Schulz, M., Boucher, O., Minikin, A., and Petzold, A. The aerosol-climate model ECHAM5-HAM. *Atmos. Chem. Phys.*, 5(4):1125–1156, 2005. doi:10.5194/acp-5-1125-2005.

Storelvmo, T., Kristjansson, J. E., Muri, H., Pfeffer, M., Barahona, D., and Nenes, A. Cirrus cloud seeding has potential to cool climate. *Geophys. Res. Lett.*, 40(1):178–182, 2013. doi:10.1029/2012gl054201.

Su, W., Loeb, N. G., Schuster, G. L., Chin, M., and Rose, F. G. Global all-sky shortwave direct radiative forcing of anthropogenic aerosols from combined satellite observations and GOCART simulations. *J. Geophys. Res. Atmos.*, 118(2):655–669, 2013. doi:10.1029/2012jd018294.

Sundqvist, H., Berge, E., and Kristjánsson, J. E. Condensation and cloud parameterization studies with a mesoscale numerical weather prediction model. *Mon. Weather Rev.*, 117(8):1641–1657, 1989. doi:10.1175/1520-0493(1989)117<1641:cacpsw>2.0.co;2.

Tang, I. N. and Munkelwitz, H. R. Composition and temperature dependence of the deliquescence properties of hygroscopic aerosols. *Atmospheric Environment. Part A. General Topics*, 27(4):467 – 473, 1993. ISSN 0960-1686. doi:https://doi.org/10.1016/0960-1686(93)90204-C.

Taylor, K. E. Summarizing multiple aspects of model performance in a single diagram. *J. Geophys. Res. Atmos.*, 106(D7):7183–7192, 2001. doi:10.1029/2000jd900719.

Tegen, I., Harrison, S. P., Kohfeld, K., Prentice, I. C., Coe, M., and Heimann, M. Impact of vegetation and preferential source areas on global dust aerosol: Results from a model study. *J. Geophys. Res. Atmos.*, 107(D21):14–1–14–27, 2002. doi:10.1029/2001JD000963.

Tegen, I., Werner, M., Harrison, S., and Kohfeld, K. Relative importance of climate and land use in determining present and future global soil dust emission. *Geophys. Res. Lett.*, 31(5):L05105, 2004. doi:10.1029/2003GL019216.

Textor, C., Schulz, M., Guibert, S., Kinne, S., Balkanski, Y., Bauer, S., Berntsen, T., Berglen, T., Boucher, O., Chin, M., Dentener, F., Diehl, T., Easter, R., Feichter, H., Fillmore, D., Ghan, S., Ginoux, P., Gong, S., Grini, A., Hendricks, J., Horowitz, L., Huang, P., Isaksen, I., Iversen, I., Kloster, S., Koch, D., Kirkevåg, A., Kristjansson, J. E., Krol, M., Lauer, A., Lamarque, J. F., Liu, X., Montanaro, V., Myhre, G., Penner, J., Pitari, G., Reddy, S., Seland, Ø., Stier, P., Takemura, T., and Tie, X. Analysis and quantification of the diversities of aerosol life cycles within AeroCom. *Atmos. Chem. Phys.*, 6(7):1777–1813, 2006. doi:10.5194/acp-6-1777-2006.

Tiedtke, M. A comprehensive mass flux scheme for cumulus parameterization in large-scale models. *Mon. Weather Rev.*, 117(8):1779–1800, 1989. doi:10.1175/1520-0493(1989)117<1779:acmfsf>2.0.co;2.

Tonttila, J., O'Connor, E. J., Niemelä, S., Räisänen, P., and Järvinen, H. Cloud base vertical velocity statistics: a comparison between an atmospheric mesoscale model and remote sensing observations. *Atmos. Chem. Phys.*, 11(17):9207–9218, 2011. doi:10.5194/acp-11-9207-2011.

Tost, H. *Global Modelling of Cloud, Convection and Precipitation Influences on Trace Gases and Aerosols*. PhD thesis, University of Bonn, Germany, 2006.

Tost, H., Jöckel, P., Kerkweg, A., Sander, R., and Lelieveld, J. Technical note: A new comprehensive SCAVenging submodel for global atmospheric chemistry modelling. *Atmos. Chem. Phys.*, 6(3):565–574, 2006a. doi:10.5194/acp-6-565-2006.

Tost, H., Jöckel, P., and Lelieveld, J. Influence of different convection parameterisations in a GCM. *Atmos. Chem. Phys.*, 6(12):5475–5493, 2006b. doi:10.5194/acp-6-5475-2006.

Tost, H., Jöckel, P., and Lelieveld, J. Lightning and convection parameterisations – uncertainties in global modelling. *Atmos. Chem. Phys.*, 7(17):4553–4568, 2007. doi:10.5194/acp-7-4553-2007.

Tröstl, J., Chuang, W. K., Gordon, H., Heinritzi, M., Yan, C., Molteni, U., Ahlm, L., Frege, C., Bianchi, F., Wagner, R., Simon, M., Lehtipalo, K., Williamson, C., Craven, J. S., Duplissy, J., Adamov, A., Almeida, J., Bernhammer, A.-K., Breitenlechner, M., Brilke, S., Dias, A., Ehrhart, S., Flagan, R. C., Franchin, A., Fuchs, C., Guida, R., Gysel, M., Hansel, A., Hoyle, C. R., Jokinen, T., Junninen, H., Kangasluoma, J., Keskinen, H., Kim, J., Krapf, M., Kürten, A., Laaksonen, A., Lawler, M., Leiminger, M., Mathot, S., Möhler, O., Nieminen, T., Onnela, A., Petäjä, T., Piel, F. M., Miettinen, P., Rissanen, M. P., Rondo, L., Sarnela, N., Schobesberger, S., Sengupta, K., Sipilä, M., Smith, J. N., Steiner, G., Tomè, A., Virtanen, A., Wagner, A. C., Weingartner, E., Wimmer, D., Winkler, P. M., Ye, P., Carslaw, K. S., Curtius, J., Dommen, J., Kirkby, J., Kulmala, M., Riipinen, I., Worsnop, D. R., Donahue, N. M., and Baltensperger, U. The role of low-volatility organic compounds in initial particle growth in the atmosphere. *Nature*, 533(7604):527–531, 2016. doi:10.1038/nature18271.

Twomey, S. The influence of pollution on the shortwave albedo of clouds. *J. Atmos. Sci.*, 34(7):1149–1152, 1977. doi:10.1175/1520-0469(1977)034<1149:tiopot>2.0.co;2.

Ueyama, R., Jensen, E. J., Pfister, L., Krämer, M., Afchine, A., and Schoeberl, M. Impact of convectively detrained ice crystals on the humidity of the tropical tropopause layer in boreal winter. *J. Geophys. Res. Atmos.*, 125(14), 2020. doi:10.1029/2020jd032894.

Uma, K. N. and Rao, T. N. Diurnal variation in vertical air motion over a tropical station, Gadanki (13.5°N, 79.2°E), and its effect on the estimation of mean vertical air motion. *J. Geophys. Res.*, 114(D20), 2009. doi:10.1029/2009jd012560.

Ushijima, S. B., Davis, R. D., and Tolbert, M. A. Immersion and contact efflorescence induced by mineral dust particles. *J. Phys. Chem. A*, 122(5):1303–1311, 2018. ISSN 1089-5639. doi:10.1021/acs.jpca.7b12075.

Vali, G., DeMott, P. J., Möhler, O., and Whale, T. F. Technical note: A proposal for ice nucleation terminology. *Atmos. Chem. Phys.*, 15(18):10263–10270, 2015. doi:10.5194/acp-15-10263-2015.

van der Werf, G. R., Randerson, J. T., Giglio, L., van Leeuwen, T. T., Chen, Y., Rogers, B. M., Mu, M., van Marle, M. J. E., Morton, D. C., Collatz, G. J., Yokelson, R. J., and Kasibhatla, P. S. Global fire emissions estimates during 1997–2016. *Earth Syst. Sci. Data*, 9(2):697–720, 2017. doi:10.5194/essd-9-697-2017.

Wagner, R., Kiselev, A., Möhler, O., Saathoff, H., and Steinke, I. Pre-activation of ice-nucleating particles by the pore condensation and freezing mechanism. *Atmos. Chem. Phys.*, 16(4):2025–2042, 2016. doi:10.5194/acp-16-2025-2016.

Wagner, R., Höhler, K., Huang, W., Kiselev, A., Möhler, O., Mohr, C., Pajunoja, A., Saathoff, H., Schiebel, T., Shen, X., and Virtanen, A. Heterogeneous ice nucleation of α-pinene soa particles before and after ice cloud processing. *J. Geophys. Res. Atmos.*, 122(9):4924–4943, 2017. ISSN 2169-897X. doi:10.1002/2016JD026401.

Walser, A., Sauer, D., Spanu, A., Gasteiger, J., and Weinzierl, B. On the parametrization of optical particle counter response including instrument-induced broadening of size spectra and a self-consistent evaluation of calibration measurements. *Atmos. Meas. Tech.*, 10(11):4341–4361, 2017. doi:10.5194/amt-10-4341-2017.

Wang, J., Hoffmann, A. A., Park, R. J., Jacob, D. J., and Martin, S. T. Global distribution of solid and aqueous sulfate aerosols: Effect of the hysteresis of particle phase transitions. *V*, 113(D11):D11206, 2008. doi:10.1029/2007JD009367.

Wang, M., Liu, X., Zhang, K., and Comstock, J. M. Aerosol effects on cirrus through ice nucleation in the community atmosphere model CAM5 with a statistical cirrus scheme. *J. Adv. Model. Earth Syst.*, 6(3):756–776, 2014. doi:10.1002/2014ms000339.

Weinzierl, B., Petzold, A., Esselborn, M., Wirth, M., Rasp, K., Kandler, K., Schütz, L., Koepke, P., and Fiebig, M. Airborne measurements of dust layer properties, particle size distribution and mixing state of Saharan dust during SAMUM 2006. *Tellus B: Chemical and Physical Meteorology*, 61(1):96–117, 2009. doi:10.1111/j.1600-0889.2008.00392.x.

Weinzierl, B., Sauer, D., Esselborn, M., Petzold, A., Veira, A., Rose, M., Mund, S., Wirth, M., Ansmann, A., Tesche, M., Gross, S., and Freudenthaler, V. Microphysical and optical properties of dust and tropical biomass burning aerosol layers in the Cape Verde region–an overview of the airborne in situ and lidar measurements during SAMUM-2. *Tellus B: Chemical and Physical Meteorology*, 63(4):589–618, 2011. doi:10.1111/j.1600-0889.2011.00566.x.

Weinzierl, B., Ansmann, A., Prospero, J. M., Althausen, D., Benker, N., Chouza, F., Dollner, M., Farrell, D., Fomba, W., Freudenthaler, V., Gasteiger, J., Groß, S., Haarig, M., Heinold, B., Kandler, K., Kristensen, T. B., Mayol-Bracero, O. L., Müller, T., Reitebuch, O., Sauer, D., Schäfler, A., Schepanski, K., Spanu, A., Tegen, I., Toledano, C., and Walser, A. The Saharan Aerosol Long-Range Transport and Aerosol–Cloud-Interaction Experiment: Overview and selected highlights. *Bull. Am. Meteorol. Soc.*, 98(7):1427–1451, 2017. doi:10.1175/BAMS-D-15-00142.1.

Welch, B. L. The generalization of Student's problem when several different population variances are involved. *Biometrika*, 34(1-2):28–35, 1947. doi:10.1093/biomet/34.1-2.28.

Welti, A., Lüönd, F., Stetzer, O., and Lohmann, U. Influence of particle size on the ice nucleating ability of mineral dusts. *Atmos. Chem. Phys.*, 9(18):6705–6715, 2009. doi:10.5194/acp-9-6705-2009.

Werner, F., Ditas, F., Siebert, H., Simmel, M., Wehner, B., Pilewskie, P., Schmeissner, T., Shaw, R. A., Hartmann, S., Wex, H., Roberts, G. C., and Wendisch, M. Twomey effect observed from collocated microphysical and remote sensing measurements over shallow cumulus. *J. Geophys. Res. Atmos.*, 119(3):1534–1545, 2014. doi:10.1002/2013jd020131.

West, R. E. L., Stier, P., Jones, A., Johnson, C. E., Mann, G. W., Bellouin, N., Partridge, D. G., and Kipling, Z. The importance of vertical velocity variability for estimates of the indirect aerosol effects. *Atmos. Chem. Phys.*, 14(12):6369–6393, 2014. doi:10.5194/acp-14-6369-2014.

Wex, H., DeMott, P. J., Tobo, Y., Hartmann, S., Rösch, M., Clauss, T., Tomsche, L., Niedermeier, D., and Stratmann, F. Kaolinite particles as ice nuclei: learning from the use of different kaolinite samples and different coatings. *Atmos. Chem. Phys.*, 14(11): 5529–5546, 2014. doi:10.5194/acp-14-5529-2014.

Whitby, E. R. and McMurry, P. H. Modal aerosol dynamics modeling. *Aerosol Sci. Technol.*, 27(6):673–688, 1997. doi:10.1080/02786829708965504.

Wilson, T. W., Ladino, L. A., Alpert, P. A., Breckels, M. N., Brooks, I. M., Browse, J., Burrows, S. M., Carslaw, K. S., Huffman, J. A., Judd, C., Kilthau, W. P., Mason, R. H., McFiggans, G., Miller, L. A., Nájera, J. J., Polishchuk, E., Rae, S., Schiller, C. L., Si, M., Temprado, J. V., Whale, T. F., Wong, J. P. S., Wurl, O., Yakobi-Hancock, J. D., Abbatt, J. P. D., Aller, J. Y., Bertram, A. K., Knopf, D. A., and Murray, B. J. A marine biogenic source of atmospheric ice-nucleating particles. *Nature*, 525(7568):234–238, 2015. doi:10.1038/nature14986.

Wise, M. E., Baustian, K. J., and Tolbert, M. A. Laboratory studies of ice formation pathways from ammonium sulfate particles. *Atmos. Chem. Phys.*, 9(5):1639–1646, 2009. doi:10.5194/acp-9-1639-2009.

Wu, C., Lin, Z., and Liu, X. The global dust cycle and uncertainty in CMIP5 (Coupled Model Intercomparison Project phase 5) models. *Atmos. Chem. Phys.*, 20(17):10401–10425, 2020. doi:10.5194/acp-20-10401-2020.

Xue, H., Feingold, G., and Stevens, B. Aerosol effects on clouds, precipitation, and the organization of shallow cumulus convection. *J. Atmos. Sci.*, 65(2):392–406, 2008. doi:10.1175/2007jas2428.1.

Yang, M., Huebert, B. J., Blomquist, B. W., Howell, S. G., Shank, L. M., McNaughton, C. S., Clarke, A. D., Hawkins, L. N., Russell, L. M., Covert, D. S., Coffman, D. J., Bates, T. S., Quinn, P. K., Zagorac, N., Bandy, A. R., de Szoeke, S. P., Zuidema, P. D., Tucker, S. C., Brewer, W. A., Benedict, K. B., and Collett, J. L. Atmospheric sulfur cycling in the southeastern Pacific – longitudinal distribution, vertical profile, and diel variability observed during VOCALS-REx. *Atmos. Chem. Phys.*, 11(10):5079–5097, 2011. doi:10.5194/acp-11-5079-2011.

Yu, H., Chin, M., Yuan, T., Bian, H., Remer, L. A., Prospero, J. M., Omar, A., Winker, D., Yang, Y., Zhang, Y., Zhang, Z., and Zhao, C. The fertilizing role of African dust in the Amazon rainforest: A first multiyear assessment based on data from cloud-aerosol lidar and infrared pathfinder satellite observations. *Geophys. Res. Lett.*, 42(6):1984–1991, 2015. doi:10.1002/2015GL063040.

Yuan, T., Remer, L. A., and Yu, H. Microphysical, macrophysical and radiative signatures of volcanic aerosols in trade wind cumulus observed by the A-train. *Atmos. Chem. Phys.*, 11(14):7119–7132, 2011. doi:10.5194/acp-11-7119-2011.

Zarzycki, C. M. and Bond, T. C. How much can the vertical distribution of black carbon affect its global direct radiative forcing? *Geophys. Res. Lett.*, 37(20), 2010. doi:10.1029/2010gl044555.

Zhang, K., O'Donnell, D., Kazil, J., Stier, P., Kinne, S., Lohmann, U., Ferrachat, S., Croft, B., Quaas, J., Wan, H., Rast, S., and Feichter, J. The global aerosol-climate model ECHAM-HAM, version 2: sensitivity to improvements in process representations. *Atmos. Chem. Phys.*, 12(19):8911–8949, 2012. doi:10.5194/acp-12-8911-2012.

Zhang, K., Wan, H., Liu, X., Ghan, S. J., Kooperman, G. J., Ma, P.-L., Rasch, P. J., Neubauer, D., and Lohmann, U. Technical note: On the use of nudging for aerosol–climate model intercomparison studies. *Atmos. Chem. Phys.*, 14(16):8631–8645, 2014. doi:10.5194/acp-14-8631-2014.

Zhang, Y., Macke, A., and Albers, F. Effect of crystal size spectrum and crystal shape on stratiform cirrus radiative forcing. *Atmos. Res.*, 52(1-2):59–75, 1999. doi:10.1016/S0169-8095(99)00026-5.

Zhou, C. and Penner, J. E. Aircraft soot indirect effect on large-scale cirrus clouds: Is the indirect forcing by aircraft soot positive or negative? *J. Geophys. Res. Atmos.*, 119 (19), 2014. doi:10.1002/2014JD021914.

Zhou, M. A normalized description of the direct effect of key aerosol types on solar radiation as estimated from Aerosol Robotic Network aerosols and Moderate Resolution Imaging Spectroradiometer albedos. *J. Geophys. Res. Atmos.*, 110(D19), 2005. doi:10.1029/2005jd005909.

Zhou, Y. and Savijärvi, H. The effect of aerosols on long wave radiation and global warming. *Atmos. Res.*, 135-136:102–111, 2014. doi:10.1016/j.atmosres.2013.08.009.

Zhu, J. and Penner, J. E. Radiative forcing of anthropogenic aerosols on cirrus clouds using a hybrid ice nucleation scheme. *Atmos. Chem. Phys.*, 20(13):7801–7827, 2020. doi:10.5194/acp-20-7801-2020.

Zwiers, F. W. and von Storch, H. Taking Serial Correlation into Account in Tests of the Mean. *J. Climate*, 8(2):336–351, 1995. ISSN 0894-8755. doi:10.1175/1520-0442(1995)008<0336:TSCIAI>2.0.CO;2.

Abbreviations

Acronyms

AC-GCM	Atmospheric chemistry general circulation model
AmSu	Crystalline ammonium sulfate
AOD	Aerosol optical depth
ASR	Ammonium-to-sulfate molar ratio
BC	Black carbon
BCair	Black carbon from aircraft emissions
CCN	Cloud condensation nuclei
CDNC	Cloud droplet number concentration
CMIP5	Coupled model intercomparison project, phase 5
CRE	Cloud radiative effect
DMS	Dimethyl sulfide
DRH	Deliquescence relative humidity
DU	Mineral dust
ECHAM5	5th generation European Centre Hamburg general circulation model
ECMWF	European Centre for Medium-Range Weather Forecasts
EMAC	ECHAM/MESSy atmospheric chemistry general circulation model
EQSAM	Equilibrium simplified aerosol model
ERF	Effective radiative forcing
ERF_{aci}	ERF due to aerosol–cloud interactions
ERF_{ari}	ERF due to aerosol–radiation interactions
$ERF_{ari+aci}$	ERF due to aerosol–radiation and aerosol–cloud interactions
ERH	Efflorescence relative humidity

GCM . . . . . General circulation model

glPOM . . . . . Glassy organics

ICNC . . . . . Ice crystal number concentration

INP . . . . . Ice nucleating particle

IPCC . . . . . Intergovernmental panel for climate change

IWC . . . . . Ice water content

LWC . . . . . Liquid water content

M2N . . . . . Mass-to-number conversion function

MADE3 . . . . . Modal aerosol dynamics model for Europe, adapted for global applications, 3rd generation

MBL . . . . . Marine boundary layer

MESSy . . . . . Modular Earth Submodel System

NPF . . . . . New particle formation

OA . . . . . Organic aerosol

PCF . . . . . Pore condensation and freezing

POM . . . . . Particulate organic matter

RE . . . . . Radiative effect

RF . . . . . Radiative forcing

RF_{aci} . . . . . RF due to aerosol–cloud interactions

RF_{ari} . . . . . RF due to aerosol–radiation interactions

RH . . . . . Relative humidity

SOA . . . . . Secondary organic aerosol

SS . . . . . Sea spray

TKE . . . . . Turbulent kinetic energy

TTL . . . . . Tropical tropopause layer

VOC . . . . . Volatile organic compounds

Variables

α . . . . . Ångstrom exponent

C_{cl} . . . . . Fractional cloud cover

D . . . . . Particle diameter

$\tilde{D}_g$ . . . . . Median particle diameter

f_{act} . . . . . Activated fraction of ice nucleating particles

k . . . . . Mode index

κ . . . . . Hygroscopicity parameter

m . . . . . Particle mass concentration

M_k . . . . . kth moment of the size distribution

N . . . . . Total number of particles

N_{ice} . . . . . Number concentration of ice crystals per freezing mode

n_N . . . . . Aerosol number size distribution function

ω . . . . . Vertical velocity

ω_{gw} . . . . . Gravity wave component of vertical velocity

ω_{ls} . . . . . Large-scale component of the vertical velocity

ω_{t} . . . . . Turbulent component of the vertical velocity

R_{ice} . . . . . Ice crystal radius

S_c . . . . . Critical supersaturation ratio of ice nucleating particles

S_{hom} . . . . . Critical supersaturation ratio at the homogeneous freezing threshold

S_i . . . . . Supersaturation ratio with respect to ice

σ_g . . . . . Geometric standard deviation or mode width

t . . . . . Time

T . . . . . Ambient temperature

τ . . . . . Optical thickness

T_g . . . . . Glass transition temperature

u . . . . . Wind friction velocity

u_{thr} . . . . . Threshold wind friction velocity

V . . . . . Particle volume concentration

Chemical compounds

CH_4 . . . . . Methane

Cl . . . . . Chloride

CO . . . . . Carbon monoxide

CO_2 . . . . . Carbon dioxide

H_2O . . . . . Water

H_2O_2 . . . . . Hydrogen peroxide

H_2SO_4 . . . . . Sulfuric acid

HCl . . . . . Hydrochloric acid

HNO_3 . . . . . Nitric acid

HOx . . . . . Hydrogen oxide radicals

N_2O . . . . . Nitrous oxide

N_2O_5 . . . . . Dinitrogen pentoxide

Na . . . . . Sodium

NaCl . . . . . Sodium chloride

NH_3 . . . . . Ammonia

NH_4 . . . . . Ammonium

$(NH_4)_2NO_4$ . . . . . Ammonium nitrate

$(NH_4)_2SO_4$ . . . . . Ammonium sulfate

NO_3 . . . . . Nitrate

NO_x . . . . . Nitrous oxides

O_3 . . . . . Ozone

OH . . . . . Hydroxyl radical

SO_2 . . . . . Sulfur dioxide

SO_4 . . . . . Sulfate

List of Figures

List of Tables

Danksagung

An dieser Stelle möchte ich mich bei allen Personen, die zur Erstellung dieser Doktorarbeit beigetragen haben, herzlich bedanken. Zuallererst gilt mein Dank Robert Sausen, der mir als mein Doktorvater diese Arbeit ermöglicht hat, sowie mich durch hilfreiche Diskussionen und Vorschläge während meiner Promotion unterstützt hat. Außerdem möchte ich mich bei meinem Zweitgutachter, George Craig, für dessen Unterstützung bedanken.

Ein besonderer Dank gilt meinem Betreuer, Johannes Hendricks, der mich durch zahlreiche Diskussionen und Anregungen entscheidend unterstützt hat und bei Fragen und Problemen ein wichtiger Ansprechpartner war. Dies trifft auch auf Mattia Righi zu, bei dem ich mich insbesondere für seine Unterstützung bei der Durchführung und Auswertung der Simulationen und für die Bereitstellung zahlreicher Werkzeuge und Skripte bedanke. Die Unterstützung durch das MESSy-Entwickler-Team und insbesondere durch Patrick Jöckel bei zahlreichen Fragen und Problemen im Umgang mit dem Modellsystem, war eine große Hilfe.

An dieser Stelle möchte ich mich bei den Koautorinnen und Koautoren für die Unterstützung bei der Erstellung der Publikation im Rahmen dieser Doktorarbeit bedanken: Johannes Hendricks und Mattia Righi (siehe oben); Bernd Heinold und Ina Tegen für die Unterstützung beim Modell-Tuning der Mineralstaubemissionen; Daniel Sauer, Adrian Walser und Bernadett Weinzierl für das Bereitstellen von flugzeuggestützten Messdaten und die Hilfe bei deren Auswertung; und bei Silke Groß für die Bereitstellung bodengestützter Lidar-Daten und die Unterstützung bei deren Analyse. Hier möchte ich auch Helmut Ziereis für die hilfreichen Kommentare zum Manuskript und außerdem für seine Unterstützung als Mentor in meinem Promotionskomitee danken. Weiterhin bedanke ich mich bei Axel Lauer und Klaus Klingmüller für die hilfreichen Diskussionen zur Publikation. Außerdem bedanke ich mich bei den AERONET Wissenschaftlerinnen und Wissenschaftlern und allen Beteiligten für den Aufbau und Unterhalt der 38 Messstationen, deren Daten für diese Publikation verwendet wurden.

Weiterhin möchte ich mich bei Jingmin Li und Monica Sharma für viele nützliche Diskussionen zur Aerosolmodellierung bedanken. Außerdem bedanke ich mich bei Christopher Kaiser, für Tipps und Diskussionen zur Weiterentwicklung von MADE3; bei Sabine Brinkop, für die Hilfe bei der Wolkendarstellung in EMAC; bei Thomas Popp, für die Hinweise zur Nutzung von Satellitendaten; und bei Bernd Kärcher, für die zahlreichen Diskussionen und Hinweise zu aktuellen Publikationen.

Mein Dank gilt außerdem allen Kolleginnen und Kollegen der ESM-Abteilung, insbesondere meinen Bürokolleginnen und Kollegen, und auch den anderen Doktorandinnen und Doktoranden am Institut. Die gegenseitige Motivation, die vielen nützlichen Tipps aber auch die gelegentlichen Süßigkeiten und zahlreichen gemeinsamen Events waren eine Bereicherung während meiner Promotion. Zuguterletzt bedanke ich mich bei meinen Eltern, deren Unterstützung und Motivation, insbesondere während der Zeit des Lockdowns, eine große Hilfe bei der Erstellung dieser Arbeit waren.

Die finanzielle Unterstützung dieser Doktorarbeit erfolgte durch das DLR-Programm für Verkehrsforschung (Projekte *Global model studies on the effects of transport-induced aerosols on ice clouds and climate* und *Transport und Klima* – TraK). Die hier ausgewerteten Modellsimulationen wurden auf dem Hochleistungsrechensystem für Erdsystemforschung HLRE-3 „Mistral“ des Deutschen Klimarechenzentrums (DKRZ) durchgeführt. Für die Datenauswertung kamen Python, gelegentlich das Earth System Model eValuation Tool (ESMValTool) v1.1.0 und vor allem die NCAR Command Language (NCL) zum Einsatz.